

014-78-1537

TECHNICAL  
LIBRARY

Optics Research

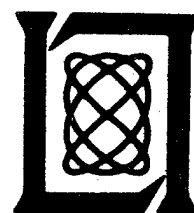
31 December 1977

Prepared  
under Electronic Systems Division Contract F19628-78-C-0002 by

**Lincoln Laboratory**

MASSACHUSETTS INSTITUTE OF TECHNOLOGY

LEXINGTON, MASSACHUSETTS



Approved for public release; distribution unlimited.

DTIC QUALITY INSPECTED 2

19970805 107

The work reported in this document was performed at Lincoln Laboratory, a center for research operated by Massachusetts Institute of Technology, with the support of the Department of the Air Force under Contract F19628-78-C-0002.

This report may be reproduced to satisfy needs of U.S. Government agencies.

The views and conclusions contained in this document are those of the contractor and should not be interpreted as necessarily representing the official policies, either expressed or implied, of the United States Government.

This technical report has been reviewed and is approved for publication.

**FOR THE COMMANDER**

*Raymond L. Loiselle*

Raymond L. Loiselle, Lt. Col., USAF  
Chief, ESD Lincoln Laboratory Project Office

Non-Lincoln Recipients

**PLEASE DO NOT RETURN**

Permission is given to destroy this document  
when it is no longer needed.

MASSACHUSETTS INSTITUTE OF TECHNOLOGY  
LINCOLN LABORATORY

OPTICS RESEARCH

1 JULY 1976 - 31 DECEMBER 1977

ISSUED 2 AUGUST 1978

~~DTIC QUALITY INSPECTED 8~~

Approved for public release; distribution unlimited.

LEXINGTON

MASSACHUSETTS

## A B S T R A C T

This report contains copies of journal articles, and papers appearing in conference proceedings describing optics research at Lincoln Laboratory during the period 1 July 1976 through 31 December 1977. Also included are preprints of articles accepted by journals and conference proceedings during this period as well as a list of meeting speeches given during this period.

Additional information on the Optics Program may be found in the ARPA/STO Program and ARPA/TTO Program HOWLS Semiannual Technical Summary Reports to DARPA; Navy HPL Program Semiannual Technical Summary Report to the Department of the Navy; Radar Measurements Semiannual Technical Summary Report to the BMDPO, Department of the Army; Tactical Systems and Technology Semiannual Technical Summary Report to the Air Force Systems Command; and Final Report to the National Science Foundation on Diode Laser System to Measure Trace Gases by Long-Path Infrared Absorption.

## CONTENTS

Published Journal Articles and Papers Appearing in Conference Proceedings

		Page	
Long-path monitoring: advanced instrumentation with a tunable diode laser	E. D. Hinkley R. T. Ku K. W. Nill J. F. Butler	Appl. Opt. <u>15</u> , No. 7, 1653-1655 (July 1976)	1
Long-Path Monitoring with Tunable Lasers	E. D. Hinkley R. T. Ku	Proc. 8th IMR Symposium, Gaithersburg, Maryland, 20-24 September 1976	5
Recent Developments in the Use of Tunable Semiconductor Lasers for Molecular Pollutant Detection	E. D. Hinkley R. T. Ku	In <u>Environmental Analysis</u> (Academic Press, New York, 1977)	9
High-sensitivity infrared heterodyne radiometer using a tunable-diode-laser local oscillator	R. T. Ku D. L. Spears	Opt. Lett. <u>1</u> , No. 3, 84-86 (September 1977)	23
Real Time Digital Recording of Thermovision Data	R. Cordova R. R. Parenti	Proc. 3rd Biennial Infrared Information Exchange, St. Louis, Missouri, 24-26 August 1976	27
Interferometric Evaluation of the Imaging Characteristics of Laser Beams Propagated Through the Turbulent Atmosphere	D. Kelsall	Phot. Sci. Eng. <u>21</u> , No. 3, 123-129 (May/June 1977)	33
Coherent Optical Radar	R. H. Kingston	Optics News (Summer 1977)	41
Advances in CO <sub>2</sub> Laser Stabilization Using the 4.3 $\mu$ m Fluorescence Technique	C. Freed R. G. O'Donnell	Proc. 2nd Frequency Standards and Metrology Symposium, Copper Mountain, Colorado, 5-7 July 1976	47
Progress in CO <sub>2</sub> Laser Stabilization	C. Freed	Proc. 31st Annual Symposium on Frequency Control, Atlantic City, New Jersey, 1-3 June 1977	53
Absolute Frequency Calibration of the CO <sub>2</sub> Isotope Laser Transitions	C. Freed R. G. O'Donnell A. H. M. Ross	IEEE Trans. Instrum. Meas. <u>IM-25</u> , No. 4, 431-437 (December 1976)	63
The dynamics of air breakdown initiated by a particle in a laser beam	D. E. Lencioni L. C. Pettingill	J. Appl. Phys. <u>48</u> , No. 5, 1848-1851 (May 1977)	71
Hole-boring in clouds by high-intensity laser beams: theory	R. C. Harney	Appl. Opt. <u>16</u> , No. 11, 2974-2978 (November 1977)	75

			<u>Page</u>
Thermal-blooming compensation: experimental observations using a deformable-mirror system	C. A. Primmerman D. G. Fouche	Appl. Opt. <u>15</u> , No. 4, 990-995 (April 1976)	81
Bandwidth specification for adaptive optics systems	D. P. Greenwood	J. Opt. Soc. Am. <u>67</u> , No. 3, 390-393 (March 1977)	87
Properties of phase conjugate optical systems	J. Herrmann	J. Opt. Soc. Am. <u>67</u> , No. 3, 290-295 (March 1977)	91
Tracking turbulence-induced tilt errors with shared and adjacent apertures	D. P. Greenwood	J. Opt. Soc. Am. <u>67</u> , No. 3, 282-290 (March 1977)	97
Simultaneous optical and x-ray imaging telescopes	R. C. Harney	Appl. Opt. <u>16</u> , No. 8, 2039 (August 1977)	107
Propagation of Ultrashort Light Pulses in a Resonant Medium	R. C. Harney	Physica <u>91A</u> , 469-479 (The Netherlands) (1978)	109
Active laser resonator control techniques	R. C. Harney	Appl. Opt. <u>17</u> , No. 11, 1671-1672 (June 1978)	121
A Compact 10.6 $\mu$ m Imaging Radar [U]	P. J. Berger S. Marcus J. Martin	Proc. 7th DoD Conference on Laser Technology [S], West Point, 4-6 June 1976	123

Journal Articles Accepted for Publication  
and Paper to Appear in Conference Proceedings

Thermal-Blooming Compensation Using the CLASP System	C. A. Primmerman F. B. Johnson I. Wigdor	Applied Optics	141
How Many Physically Significant Solutions are there to the Self-Induced Transparency Equations?	R. C. Harney	Proc. 4th Rochester Conference on Coherence and Quantum Optics, Rochester, New York, 8-10 June 1977	161
List of Unpublished Meeting Speeches			169

# ORGANIZATION

## OPTICS DIVISION

R. H. Rediker, *Head*  
G. F. Pippert, *Associate Head*  
J. M. McPhie, *Assistant*

## ADVANCED TECHNIQUES AND SYSTEMS

S. Edelberg, *Leader*  
J. E. Lowder, *Associate Leader*  
R. P. Espinola, *Assistant Leader*

Bicknell, W. E.	Johnson, J. Q.	McSheehy, R. B.
Billups, R. R.	Lencioni, D. E.	Pettingill, L. C.
Bloss, D. M.	Manlief, S. K.	Richardson, R. E.
Bradley, L. C.	Marshall, A. P.	Sanchez-Rubio, A.
Henshaw, P. D.		

## OPTO-RADAR SYSTEMS

A. B. Gschwendtner, *Leader*  
H. Kleiman, *Associate Leader*

Becherer, R. J.	Keicher, W. E.	Parenti, R. R.
Corbosiero, D. M.	Keyes, R. J.	Quist, T. M.
Cordova, R. J.	Marcus, S.	Sullivan, D. R.
Hamey, R. C.	Martin, J. S.	Veldkamp, W. B.
Hull, R. J.	Merrill, E. R.	Zieman, H. E.
Johns, T. W.		

## INFRARED RADAR

S. Y. Shey, *Leader*  
P. A. Ingwersen, *Associate Leader*  
I. J. Sullivan, *Associate Leader*

Bates, D. H.	Fulton, M. J.	Sasiela, R. J.
Bielinski, J. W.	Gruber, M.	Scouler, W. J.
Capes, R. N., Jr.	Gurski, T. R.	Sullivan, F. M.
Carter, G. M.	Ku, R. T.	Swezey, L. W.
Daley, J. A., Jr.	McPherson, R. D.	Teoste, R.
Dyer, A. C.	O'Donnell, R. G.	Valcourt, G. L., Jr.
Ferdinand, A. P., Jr.	Parker, A. C.	Zimmerman, M. D.
Freed, C.		

## APPLIED RADIATION

L. C. Marquet, *Leader*  
D. P. Greenwood, *Associate Leader*

Ariel, E. D.	Herrmann, J.	Lifshitz, J. R.
Berger, P. J.	Huber, E. E., Jr.	Morency, A. J.
Braman, C. E.	Humphreys, R. A.	Mudgett, D. A.
Brennan, M. J.	Johnson, F. B.	Perry, F. H.
Chaulk, L. W.	Kafalas, P.	Pirroni, J. S.
Clay, W. G.	Kelsall, D.	Pitts, R. F.
Coles, R. M.	Kilcline, C. W.	Primmerman, C. A.
Dickey, D. H.	Knopp, J.	Schroeder, M. E.
DiMarzio, E. W.	Kocher, D. G.	Simpson, E.
Grey, P. C.	Kramer, R.	

## Long-path monitoring: advanced instrumentation with a tunable diode laser

E. D. Hinkley, R. T. Ku, K. W. Nill, and J. F. Butler

E. D. Hinkley and R. T. Ku are with MIT Lincoln Laboratory, Lexington, Massachusetts 02173; the other authors are with Laser Analytics, Inc., Lexington, Massachusetts 02173.

Received 29 March 1976.

Sponsored by J. S. Garing, Air Force Geophysics Laboratory

Long-path monitoring of atmospheric carbon monoxide with high sensitivity and speed has recently been demonstrated using a tunable diode laser system.<sup>1,2</sup> This Communication describes significant progress in improving the multipollutant capability and operating simplicity of that monitoring technique. The improved capabilities result from integrating a newly developed, widely tunable diode laser with a variable temperature, stabilized, closed cycle refrigerator. With this single source it is possible to monitor any air pollutant whose absorption lines fall within bands of continuous tunability of the laser in the 9–12- $\mu\text{m}$  region. The instrument may also be used to measure high resolution (Doppler-limited) ir spectra for line strength calibration and identification of potential interferences. We illustrate its use for this purpose and estimate the monitoring sensitivity for several important pollutants, including ammonia, vinyl chloride, and ozone, based on laser spectroscopic measurements.

Tunable diode lasers are useful for long-path monitoring of air pollutants because their emission wavelengths can be made to coincide with ir absorption lines of most gases, their output can be sufficiently collimated for transmission over distances of several kilometers, and they are readily adaptable to field use. Application of an individual laser to more than one pollutant, however, has been limited by a somewhat narrow tuning range ( $\sim 30 \text{ cm}^{-1}$ ) and the need to maintain the diode at low temperature ( $< 20 \text{ K}$ ) for cw operation. A diode laser with significantly wider tunability was first developed in 1974 by Groves *et al.*<sup>3</sup> These lasers operated cw to a temperature of 80 K, with tuning over nearly  $280 \text{ cm}^{-1}$ . Using a simpler technique to be described below, we have developed lasers that possess extended wavelength tunability ( $300 \text{ cm}^{-1}$ )

and operate cw at temperatures as high as 100 K. Significantly, these lasers produce radiation in the important 8–12- $\mu\text{m}$  atmospheric window; and if liquid nitrogen is used to achieve operating temperature in a simpler (77 K) system, tuning over  $100 \text{ cm}^{-1}$  is still possible by varying the diode current.

Figure 1 illustrates temperature tuning of a diode laser fabricated by this new method, with nominal frequencies for monitoring several pollutant gases indicated. It is apparent that strong absorption lines of many important gases fall within the over-all tuning range of this laser; and it is worth noting that, with regard to long-path monitoring, atmospheric transmission over a 10-km sea level path is typically greater than 50% throughout the 8.7–12- $\mu\text{m}$  region,<sup>4</sup> making this an ideal spectral range for atmospheric long-path monitoring.

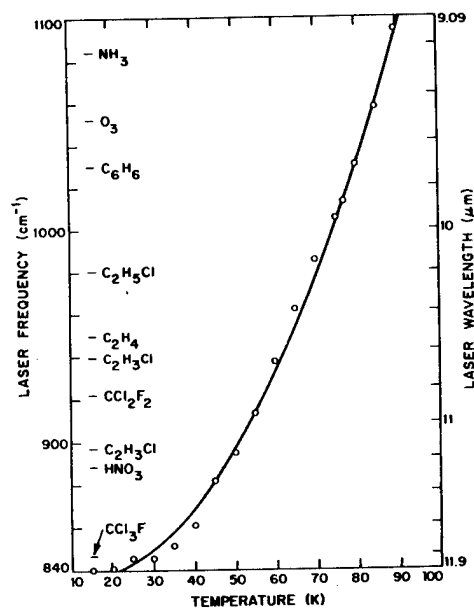


Fig. 1. Temperature tuning curve for the widely tunable diode laser. Strongly absorbing regions for some common pollutant gases are indicated.

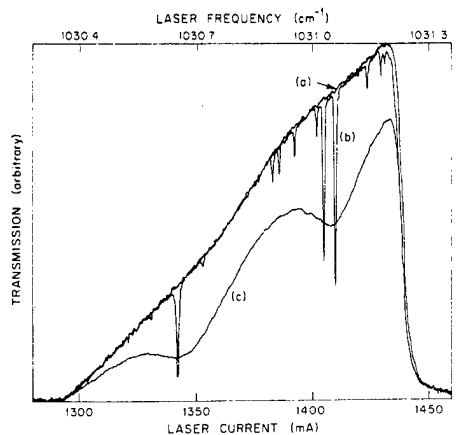


Fig. 2. Laser spectroscopy of  $\text{C}_2\text{H}_4$  using diode laser operating cw at 77 K (liquid nitrogen-cooled). Trace (a) is for the evacuated cell, (b) for 1 Torr  $\text{C}_2\text{H}_4$ , and (c) for 13,200 ppm  $\text{C}_2\text{H}_4$  in air at atmospheric pressure. Cell length is 30 cm.

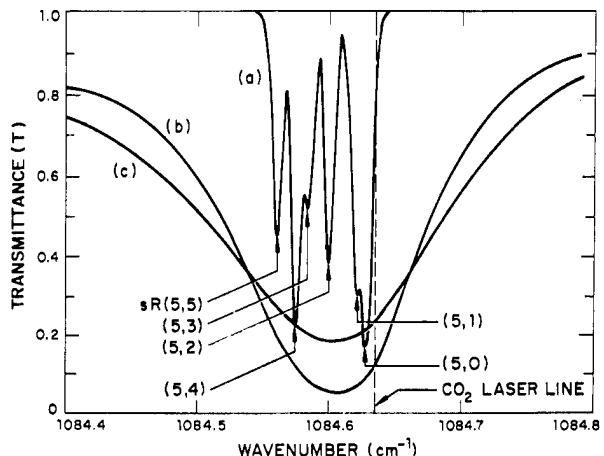


Fig. 3. Laser spectroscopy of  $\text{NH}_3$  using diode laser in closed cycle refrigerator, operating at approximately 90 K. Trace (a) represents 0.1 Torr  $\text{NH}_3$ , (b) is 0.46 Torr  $\text{NH}_3$  with 360 Torr air added, and (c) is 0.46 Torr  $\text{NH}_3$  with 750 Torr (1 atm) air added. The  $\text{CO}_2$  laser line is  $R(30)$  at  $1084.635 \text{ cm}^{-1}$ . Cell length is 30 cm.

Table I. Spectral Absorption Coefficient ( $k$ ) and Predicted Sensitivity for Measurement Over a 1-km Atmospheric Path for Several Pollutant Gases at the Indicated Frequencies ( $\nu$ )

Molecule	Formula	$\nu(\text{cm}^{-1})$	$k(\text{atm}^{-1} \text{ cm}^{-1})$	Sensitivity (ppb) <sup>a</sup>
Freon-11	$\text{CCl}_3\text{F}$	847	110	0.27
Freon-12	$\text{CCl}_2\text{F}_2$	921	275	0.11
Vinyl chloride	$\text{C}_2\text{H}_3\text{Cl}$	940	11	2.8
Ethylene	$\text{C}_2\text{H}_4$	950	42	0.71
Ozone	$\text{O}_3$	1052	22	1.3
Ammonia	$\text{NH}_3$	1085	93	0.33

<sup>a</sup> Sensitivity based on detecting 0.3% change in received laser power.<sup>1</sup>

Figure 2 illustrates application of the widely tunable laser operating at a base temperature of 77 K in a liquid nitrogen Dewar in calibrating sensitivity for laser monitoring and identifying potentially interfering species for a common pollutant, ethylene ( $\text{C}_2\text{H}_4$ ). In this procedure a pure sample of the pollutant is scanned with the laser, first at low pressure, then at atmospheric pressure, using air or nitrogen for the balance. At low pressure [trace (b)] the absorption lines are narrow and easily identified. Potential interferences from other constituents such as  $\text{H}_2\text{O}$ ,  $\text{CO}_2$ ,  $\text{CH}_4$ , etc. are identified by recording their low pressure absorption lines in the same region. Wavelengths for monitoring are selected to avoid absorption lines of any interfering gases. Having selected the optimum monitoring wavelength, the atmospheric pressure scan (c) then provides a quantitative measure of the attenuation coefficient per unit concentration. Relative frequency calibration is obtained by means of a Fabry-Perot etalon.<sup>5</sup>

Ammonia is another important gaseous pollutant in the troposphere and stratosphere for which sensitive monitoring instrumentation is urgently needed. Recently Schnell and Fischer<sup>6</sup> reported spectrophotometer measurements of the absorption coefficients for  $\text{NH}_3$  at several  $\text{CO}_2$  laser lines, which included one of the highest values ever obtained in the ir:  $120 \text{ atm}^{-1} \text{ cm}^{-1}$  at 360 Torr total pressure, for the  $R(30)$   $\text{CO}_2$  laser line at  $1084.635 \text{ cm}^{-1}$  ( $\sim 9.22 \mu\text{m}$ ). Because of the interest in detecting this pollutant by laser techniques, we have examined in detail the  $\text{NH}_3$  absorption in this region with the widely tunable diode laser of Fig. 1 and with a grating-tuned  $\text{CO}_2$  laser.<sup>7</sup> The resulting measurements are shown in Fig. 3. Trace (a) is a diode laser scan of the pure gas at 0.1 Torr pressure, which reveals absorption lines corresponding to the six  $sR(5,0)-sR(5,5)$   $\text{NH}_3$  transitions listed by Garing *et al.*<sup>8</sup> As far as we know, these lines have not been previously resolved. Trace (b) is a diode laser scan for 0.46 Torr  $\text{NH}_3$  in 360 Torr air. The absorption coefficient at the  $R(30)$   $\text{CO}_2$  laser line was found, by using the discretely tunable  $\text{CO}_2$  laser, to be  $120 \pm 10 \text{ atm}^{-1} \text{ cm}^{-1}$ , in agreement with Schnell and Fischer's measurement.<sup>6</sup> At line center ( $\nu = 1084.605 \pm 0.002 \text{ cm}^{-1}$ , determined by correlating the  $\text{CO}_2$  laser data and diode laser scans), the absorption coefficient is  $162 \text{ atm}^{-1} \text{ cm}^{-1}$ . A total pressure of 360 Torr corresponds to an altitude of 5 km above sea level. Schnell and Fischer did not report any measurements for atmospheric pressure; consequently, we performed the laser scan of Fig. 3(c) and also measured the absorption coefficient for  $\text{NH}_3$  at atmospheric pressure for the  $R(30)$   $\text{CO}_2$  laser line. The absorption coefficient at the  $R(30)$  line is  $75 \text{ atm}^{-1} \text{ cm}^{-1}$  vs  $93 \text{ atm}^{-1} \text{ cm}^{-1}$  at line center. Thus, the widely tunable diode laser has been useful for observing the transitions contributing to a strong absorption line of  $\text{NH}_3$  at atmospheric pressure and revealing the relative location of a fixed frequency laser line, which appears attractive for monitoring this gas at sea level and to altitudes of several kilometers.

Using this widely tunable diode laser mounted in a temperature stabilized, closed cycle refrigerator, we have investigated several other important molecular species listed in Table I. This table contains the largest values of atmospheric absorption coefficients measured for these gases at the indicated frequencies. Predictions of the corresponding sensitivities for a 1-km path are based on a state-of-the-art signal processing capability.<sup>1</sup>

The widely tunable diode lasers were fabricated by compositional interdiffusion (CID)—a new method for forming single heterojunctions without complex vapor<sup>9</sup> or liquid phase<sup>3</sup> epitaxial growth steps. An essential feature of CID, to be described in detail in a subsequent publication, is the use of a quaternary  $(\text{PbSe})_{1-x}(\text{SnTe})_x$  crystal, with  $x$  adjusted to obtain the desired emission frequency. The energy gap of

this quaternary alloy decreases by approximately 8 meV for each percent of SnTe. A heterojunction is formed when the crystal in annealed with a binary PbSe source, since SnTe volatilizes leaving a surface layer rich in the larger bandgap PbSe. Only a small depletion of the SnTe is required to establish an effective heterostructure, since the energy gap of the quaternary increases rapidly with decreasing SnTe content. A primary advantage of using the quaternary alloy is that lattice matching across the CID heterostructure can be achieved. Since the lattice constant of PbSe lies between that of SnSe (cubic phase) and SnTe,<sup>10</sup> a quaternary alloy with PbSe lattice constant can be chosen with an energy gap corresponding to laser emission frequencies between about 300–1400 cm<sup>-1</sup>. Though the present devices are not precisely lattice-matched, we estimate a mismatch of less than 0.1%.

In summary, we have shown that a new type of widely tunable semiconductor diode laser can permit sequential monitoring of many pollutant gases with a single device connected to a closed cycle refrigerator of adjustable temperature and can be useful for fundamental laboratory measurements as well. Moreover, for even simpler instrumentation involving only liquid nitrogen as the coolant, current tuning of the diode laser can still be used to reach a number of pollutants. This new development will greatly increase the usefulness and versatility of long-path monitoring for air quality assessment and model evaluation.

The Lincoln Laboratory portion of this work was supported by the National Science Foundation (RANN) and the U.S. Environmental Protection Agency.

## References

1. R. T. Ku, E. D. Hinkley, and J. O. Sample, *Appl. Opt.* **14**, 854 (1975).
2. R. T. Ku and E. D. Hinkley, "Long-Path Laser Monitoring of Atmospheric Carbon Monoxide—1975 Regional Air Pollution Study (St. Louis)," Technical Report to the U.S. Environmental Protection Agency (April 1976).
3. S. H. Groves, K. W. Nill, and A. J. Strauss, *Appl. Phys. Lett.* **25**, 331 (1974).
4. R. A. McClatchey and J. E. A. Selby, "Atmospheric Attenuation of Laser Radiation from 0.76 to 31.25  $\mu\text{m}$ ," AFCRL Report Tr-74-0003 to the Air Force Systems Command (3 January 1974).
5. E. D. Hinkley, K. W. Nill, and F. A. Blum, *Laser Spectroscopy of Atoms and Molecules*, H. Walther, Ed. (Springer-Verlag, Heidelberg, 1976), Chapter 2.
6. W. Schnell and G. Fischer, *Appl. Opt.* **14**, 2058 (1975); G. Fischer, Swiss Observatoire Cantonal; personal communication.
7. We are indebted to C. Freed of MIT Lincoln Laboratory for use of his CO<sub>2</sub> laser apparatus, and to W. A. McCleny of the U. S. Environmental Protection Agency for suggesting the spectroscopic study of ammonia.
8. J. S. Garing, H. H. Nielsen, and K. N. Rao, *J. Mol. Spectrosc.* **3**, 496 (1959).
9. J. N. Walpole, A. R. Calawa, R. W. Ralston, T. C. Harman, and J. P. McVittie, *Appl. Phys. Lett.* **23**, 620 (1973); J. N. Walpole, A. R. Calawa, T. C. Harman, and S. H. Groves, *Appl. Phys. Lett.* **28**, 552 (1976).
10. C. A. Kennedy and K. J. Linden, *J. Appl. Phys.* **41**, 252 (1970).

NATIONAL BUREAU OF STANDARDS SPECIAL PUBLICATION 464.  
Methods and Standards for Environmental Measurement,  
Proceedings of the 8th IMR Symposium,  
Held September 20-24, 1976, Gaithersburg, Md. (Issued November 1977).

## LONG-PATH MONITORING WITH TUNABLE LASERS<sup>1</sup>

E. D. Hinkley<sup>2</sup> and R. T. Ku

Massachusetts Institute of Technology  
Lincoln Laboratory  
Lexington, Massachusetts, 02173, USA

### 1. Introduction

By using a tunable laser whose signal is reflected from a distant target, differential absorption of the laser power can permit a quantitative determination to be made of the integrated pollutant concentration over the path due to a particular gaseous species. Many molecular pollutants, such as NO, NO<sub>2</sub>, SO<sub>2</sub>, CO, and O<sub>3</sub> [1]<sup>3</sup>, have already been monitored in the atmosphere using this technique, employing different types of tunable lasers in the ultraviolet, visible, and infrared regions of the electromagnetic spectrum. Integrated-path measurements such as these are important for studying various computer models being proposed for region-wide prediction of pollution levels, since their basic grid size is usually around 1 km.

Traditionally, pollutant concentrations have been measured by point-sampling instrumentation. However, the limitations of these standard methods become obvious in cases where the *average* pollutant concentration over a large area must be determined. In this paper, we describe a tunable laser system representing a development in the direction of a versatile and reliable monitor for such *in situ* ambient-air measurement. Moreover, with eventual utilization of the new widely-tunable diode lasers [2], it is possible to monitor several different pollutant gases simultaneously. A multipollutant capability is extremely useful since many pollutants interact with each other, and the time evolution of their concentrations can be incorporated into the mathematical models, along with meteorological and topological data, for advance prediction of air pollution levels.

We have developed a tunable semiconductor diode laser system for monitoring pollutants over long outdoor paths. The laser source is one of the Pb-salt types [3,4] which have several useful properties for field applications, such as small size, ruggedness, and ease of wavelength tunability. By chemically tailoring various combinations of Pb-salt compounds we can effectively cover the infrared wavelength range from 3 to 32  $\mu\text{m}$ . Many important atmospheric pollutants can be detected by lasers in this range. By using various PbS<sub>1-x</sub>Se<sub>x</sub> lasers, which operate in the 4-6.5  $\mu\text{m}$  range, we have monitored CO, H<sub>2</sub>O and NO over long paths. Once a laser is constructed to operate nominally and in the wavelength region where a particular pollutant has strong absorption lines, the laser can be tuned simply by varying the injection current or laser temperature.

<sup>1</sup>This work was supported by the National Science Foundation (RANN) and the U. S. Environmental Protection Agency.

<sup>2</sup>Present address: Laser Analytics, Inc., Lexington, Massachusetts

<sup>3</sup>Figures in brackets indicate literature references at the end of this paper.

## 2. Discussion

The essential components of the laser optical system are shown in figure 1. The diode laser is mounted in a closed-cycle cryogenic cooler, and its emission is collimated by an Al-coated parabolic mirror M-1, 12 cm in diameter. The beam is transmitted down-range to a remote retroreflector (hollow corner-cube) M-2 which reflects it back towards M-1, and then refocuses it onto the infrared detector situated behind a calibration cell. In order to minimize the effects of atmospheric turbulence on system sensitivity, a derivative spectroscopic technique is employed in which the laser is frequency-modulated at 10 kHz at the pollutant gas absorption line of interest.

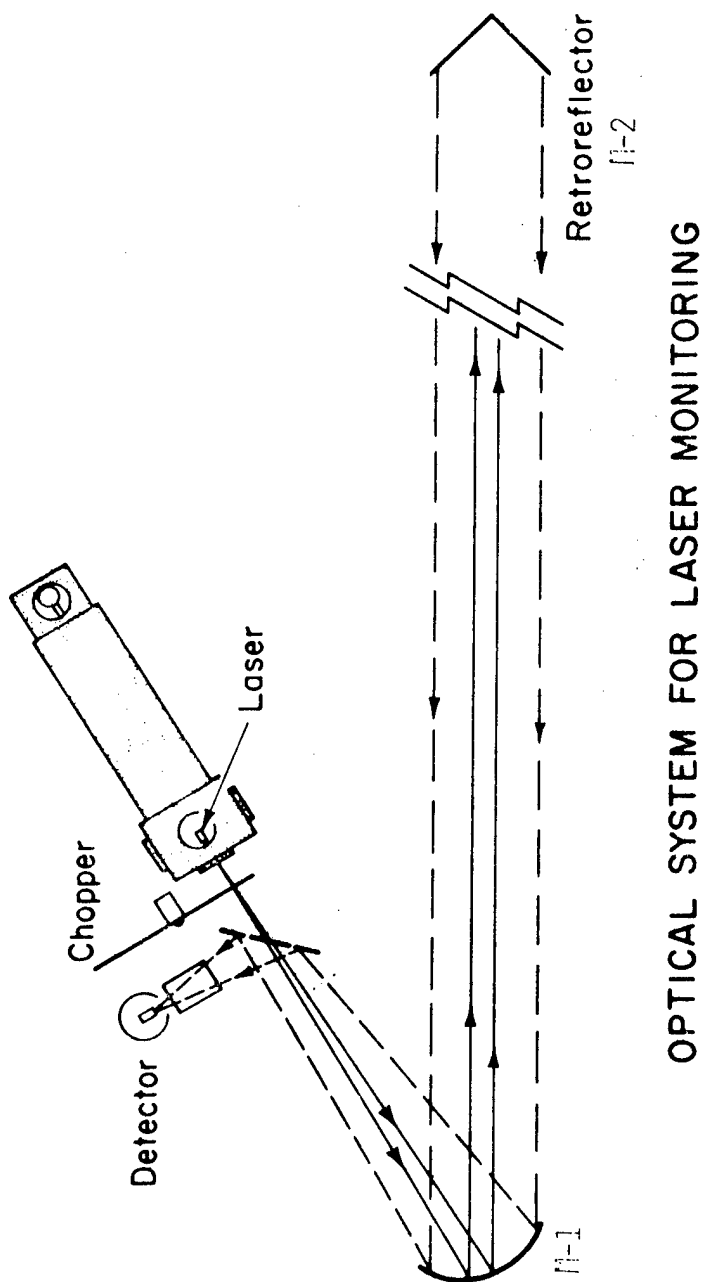


Figure 1. Long-path diode laser monitoring system.

This system was first used at our Laboratory's 300-meter test range in Bedford, Massachusetts, where an experimental detection limit of five parts per billion of CO was established [5]. An identical system was then incorporated into a mobile van which has since been utilized in St. Louis, Missouri, for atmospheric measurements of CO at various sites during the summers of 1974, 1975, and 1976, in conjunction with the Regional Air Pollution Study (RAPS) of the U. S. Environmental Protection Agency [6]. In addition, our mobile system has also been driven to Cambridge, Massachusetts for monitoring atmospheric NO in the vicinity of a traffic rotary.

The sensitivity and accuracy of these measurements are discussed, and the long-path measurements are compared with point sampling results in order to evaluate the potential of the long-path laser monitor for providing more reliable and acceptable quantitative measures for air quality.

### 3. Measurement Techniques

Tunable laser spectroscopic measurements in the laboratory are usually performed by propagating the laser radiation through an absorption cell. The change in laser power transmission during tuning can be used to obtain the absorption coefficients, line widths, and line shapes of the spectral lines. The experimentally-determined absorption coefficients can then be used to measure an unknown pollutant concentration using the amount of laser absorption in conjunction with Beer's Law.

Field measurements of ambient gases are similar to the laboratory procedures. The amount of absorption over a long atmospheric path can be related to the *average* pollutant concentration over that distance. In order to minimize atmospheric turbulence effects on laser beam propagation, a derivative spectroscopic technique can be employed [5]. Synchronous detection at a high a.c. modulation frequency, about the desired laser infrared frequency, provides the derivative of the absorption signal. Atmospheric effects are reduced by ratioing the derivative with the direct transmission signal. System "zero" is achieved by tuning the laser to line center (where the derivative/ratio signal should be zero) or by placing a retroreflector near the transmitting optics (to simulate a signal with effectively zero absorption).

Calibration is achieved by placing a known concentration of pollutant-N<sub>2</sub> mixture in the 10 cm cell. For example, if the monitored path outside is 610 meters, a calibration gas of 1,000 ppm mixture produces the same signal as 164 ppb over the long path. Linearity is confirmed by using several mixtures of different concentrations in the calibration cell. Inaccuracies in the measurements which occur as a drift of the zero-ppm signal and changes in linearity and repeatability of the calibration points, were mainly due to variations in the laser frequency. By proper controls, we have been able to reduce these effects to achieve an accuracy of  $\pm 5$  percent of the nominal reading.

### 4. Monitoring Results

In order to evaluate the measurement technique, "zero," and calibration procedures, comparative tests were made of pollutant variability using the long-path laser monitor and an air bag sampler which was filled during a traverse of the laser path. Results will be shown to support the validity of our measurement and calibration techniques.

The CO pollutant concentration was found to be quite dependent upon the location of the monitored area. For example, results will be shown for a generally low-concentration farm site in Illinois over which clouds of CO occasionally pass. In contrast, large changes in concentration were noted for an inner city site in St. Louis at various hours due largely to local traffic conditions. Significant spatial variations were also observed by means of a conventional point sampling instrument moved along a 1 km path, indicating the desirability for a long-path monitor for path-averaged pollutant measurements.

## 5. Conclusion

The long-path diode laser system has permitted unattended monitoring around the clock, with calibration checks reduced to two or three times a day. Although these results have demonstrated the feasibility and usefulness of long-path laser monitoring, several improvements must be made in future systems in order to increase reliability and provide legally-acceptable air quality measurements.

## References

- [1] Hinkley, E. D., Ku, R. T., and Kelley, P. L., *Laser Monitoring of the Atmosphere*, Chapter 6, edited by E. D. Hinkley, Springer-Verlag, Heidelberg (1976).
- [2] Hinkley, E. D., Ku, R. T., Nill, K. W., and Butler, J. F., *Appl. Opt.* 15, 1653 (1976).
- [3] Harman, T. C., *J. Phys. Chem. Soc. Suppl.* 32, 363 (1971).
- [4] Calawa, A. R., *J. Luminescence* 7, 77 (1973).
- [5] Ku, R. T., Hinkley, E. D., and Sample, J. O., *Appl. Opt.* 14, 854 (1975).
- [6] Ku, R. T. and Hinkley, E. D., M.I.T., Lincoln Laboratory Interim Technical Report, *Long-Path Monitoring of Atmospheric CO -- 1975 RAPS Study*, St. Louis, Missouri (1976).

Reprinted From  
ENVIRONMENTAL ANALYSIS  
© 1977  
Academic Press, Inc.  
New York San Francisco London

RECENT DEVELOPMENTS IN THE USE OF TUNABLE SEMICONDUCTOR LASERS  
FOR MOLECULAR POLLUTANT DETECTION<sup>1</sup>

E. D. Hinkley<sup>2</sup>

*Jet Propulsion Laboratory  
California Institute of Technology*

and

R. T. Ku

*Lincoln Laboratory  
Massachusetts Institute of Technology*

Tunable semiconductor diode lasers can be tailored to emit coherent radiation at wavelengths covering a wide region of the infrared "fingerprint" portion of the electromagnetic spectrum. With relatively large molecular absorption cross sections and generally acceptable specificity in this region of the spectrum, several important applications of these devices to gaseous pollutant detection have resulted. In addition to providing fundamental high-resolution infrared spectroscopic data for a number of molecular species, diode lasers have been used for low-pressure sampling, *in situ* source monitoring, long-path ambient-air monitoring, and passive infrared heterodyne detection. Recently there have been several new developments related to implementation of these devices for monitoring applications in the lower and upper atmospheres. In particular, one technological breakthrough with respect to the device itself has greatly increased the tunability of individual lasers. Other advancements to be discussed include laser spectroscopy of the free radical chlorine monoxide, heterodyne detection of stratospheric ozone lines, and long-path ambient-air monitoring at sea level. Finally, the implications of these recent advances for future monitoring instruments and systems are discussed.

---

<sup>1</sup>This work was supported by the National Aeronautics and Space Administration under Contract NAS 7-100, the National Science Foundation (RANN), and the U.S. Environmental Protection Agency.

<sup>2</sup>Present address: Laser Analytics, Inc., Lexington, Massachusetts 02173.

### I. INTRODUCTION

One of the most promising applications of tunable lasers is in the detection and measurement of ambient air pollutants; and many atmospheric pollutant gases such as NO,  $\text{C}_2\text{H}_4$ ,  $\text{SO}_2$ , CO, and  $\text{O}_3$  have already been detected by various tunable laser techniques (1). The most widely used tunable laser for this purpose is the Pb-salt semiconductor diode laser which can be tailored to emit coherent radiation over most of the infrared "fingerprint" region of the spectrum. Diode lasers are now available commercially, and cover the spectral region from 3 to 27  $\mu\text{m}$ . A photograph of one of these diode lasers is shown in Fig. 1.

Applications of tunable diode lasers in air pollution monitoring involve fundamental laboratory spectroscopy in addition to fieldable systems. In this paper we cover advances related to performance of the lasers themselves as well as their utility for the spectroscopic and field applications. In some instances, the fundamental spectroscopic information obtained in the laboratory by diode lasers can provide important data for the design and development of monitoring instrumentation using either tunable or fixed frequency lasers.

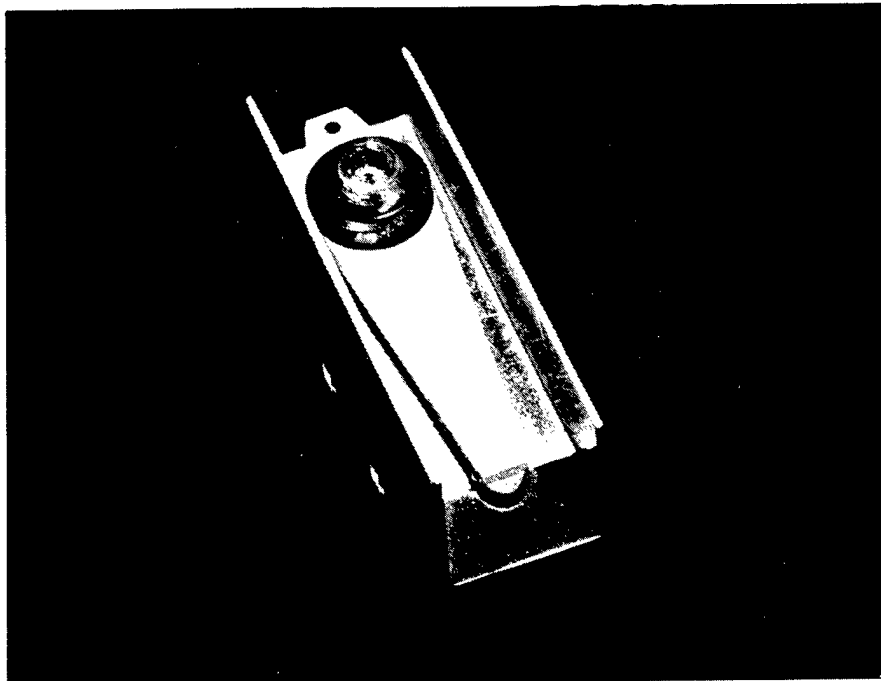


Fig. 1. Tunable semiconductor diode laser in standard package. Overall dimensions are 19.1 mm long, 6.4 mm wide, and 7.9 mm high. Typical laser length is 0.5 mm.

## II. WIDELY-TUNABLE DIODE LASERS

Tunable diode lasers are useful for monitoring air pollutants because their emission wavelengths can be made to coincide with infrared absorption lines of most gases, and their output can be sufficiently collimated for transmission over distances of several kilometers for field applications. The use of an individual laser for detection of more than one pollutant, however, has been limited by a somewhat narrow tuning range ( $\sim 30 \text{ cm}^{-1}$ ) and the need to maintain the diode at low temperature ( $< 20 \text{ K}$ ) for cw operation. A diode laser with significantly wider tunability was first developed in 1974 by Groves et al (2). These lasers operated cw to a temperature of 80 K, with tuning over nearly  $280 \text{ cm}^{-1}$ . Using a simpler technique of compositional interdiffusion (CID) (3), lasers have been developed that have extended wavelength tunability (to  $400 \text{ cm}^{-1}$ ) and operate cw at temperatures as high as 130 K. Even with liquid nitrogen to achieve operating temperature (77 K) in a simpler system, tuning over  $100 \text{ cm}^{-1}$  is possible by varying the diode laser current.

Figure 2 illustrates temperature tuning of a diode laser fabricated by this new method in the  $9-12 \mu\text{m}$  region, with nominal frequencies for monitoring several pollutant gases indicated.

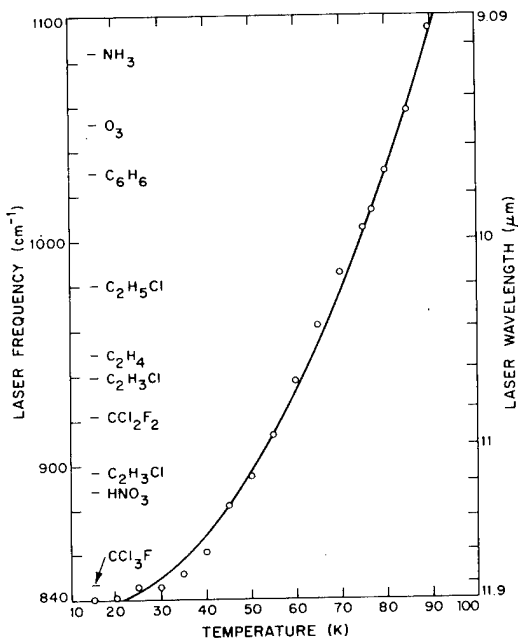


Fig. 2. Temperature-tuning curve for widely-tunable diode laser of  $(\text{PbSe})_{1-x}(\text{SnTe})_x$ . Strongly absorbing regions for some common pollutant gases are indicated.

Strong absorption lines of many important gases fall within the overall tuning range of this laser; and it is worth noting that, with regard to long-path monitoring, atmospheric transmission over a 10-km sea level path is typically greater than 50% through the 8.7-12  $\mu\text{m}$  region (4), making this an ideal spectral range for atmospheric long-path monitoring.

It is clear from Fig. 2 that the new widely-tunable lasers are important laboratory devices as well, where a large number of gases can be studied spectroscopically with a single diode laser. Results of diode laser spectroscopy on ethylene, vinyl chloride, ozone, ammonia, Freon-11, Freon-12 and ethyl alcohol have been obtained with the above laser in the 9-12  $\mu\text{m}$  region. Most of these data have been reported in Ref. 3.

In summary, this new type of widely tunable semiconductor diode laser can permit sequential monitoring of many pollutant gases with a single device installed in a closed cycle refrigerator of adjustable temperature, and can be useful for fundamental laboratory measurements as well. Moreover, for even simpler instrumentation involving only liquid nitrogen as the coolant, current tuning of the diode laser can still be used to reach strong spectral lines of a number of pollutants. This new development will greatly increase the usefulness and versatility of long-path air quality monitoring.

### III. SPECTROSCOPY

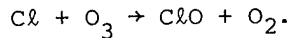
The introduction of a diode laser system as a commercial monochromator (5) has led to important fundamental measurements of gases and advances in the state-of-the-art of spectroscopy in general. Important advances in the understanding of the band structure of complex molecules such as sulfur hexafluoride for isotope separation applications have been made in the laser division of the Los Alamos Scientific Laboratory (6). Other diode laser isotopic spectroscopy carried out at the University of Bern may help to develop a new detector for  $^{14}\text{C}$  and  $^{14}\text{CO}_2$  (7), which are emitted in atomic power plants. Studies of line shapes and frequency shifts of spectral lines of sulfur dioxide attached to an argon matrix have been performed at the Swiss Federal Institute of Technology using tunable diode lasers (8). Finally, the use of expansion nozzles to form cooled molecular beams, thereby reducing Doppler effects to achieve sub-Doppler spectroscopy, has been pioneered by researchers at the University of Waterloo in Canada (9).

Laser spectroscopy, because of its very high resolution, requires new calibration techniques. The use of cells containing gases whose absorption line frequencies are precisely known is expanding, and recently researchers at the NOAA National Environmental Satellite Service and The Ohio State University reported calibration of  $\text{CO}_2$  spectra in the 14-15  $\mu\text{m}$  region for

this purpose (10). Accurately-calibrated CO<sub>2</sub> laser lines in the 9-12  $\mu\text{m}$  region have also been used. For a general review of infrared laser spectroscopy to 1975, see Ref. 11.

As an example of the way in which diode laser spectroscopy can benefit air pollution monitoring, consider the free radical chlorine monoxide (ClO) which many consider to be an important component of the stratosphere. There is, at the present time, considerable controversy surrounding the concentration of ClO in the upper atmosphere, and its potential to reduce the quantity of stratospheric ozone (12). Some ClO measurements already made have been found to differ by considerably more than an order of magnitude. A new study based on a remote optical laser technique should be highly desirable to resolve these discrepancies.

Chlorine monoxide is a highly reactive radical which cannot be prepared in high concentrations; consequently, laboratory measurements with most conventional spectrometers cannot resolve--or even quantitatively measure, as it turns out--the spectral signature of this gas. However, using a tunable PbSnTe diode laser, the ClO fundamental absorption band near 850  $\text{cm}^{-1}$  has been observed (13). The high resolution (less than  $10^{-4} \text{ cm}^{-1}$ ) of this tunable source was needed to resolve the narrow spectral lines at the low pressures for which ClO is relatively stable. The ClO for the measurement was generated in an apparatus schematically indicated in Fig. 3. Cl<sub>2</sub> and He passed through a microwave discharge to produce Cl atoms, which continued down the tube where they encountered a dilute mixture of O<sub>3</sub> in O<sub>2</sub> at approximately 7 torr pressure. ClO was formed by the reaction



For maximum sensitivity, the technique of derivative spectroscopy was used (11), with the diode laser wavelength modulated by superimposing on the steady excitation current a small, 100-Hz sinusoidal modulation. One of the ClO lines is shown in Fig. 4 along

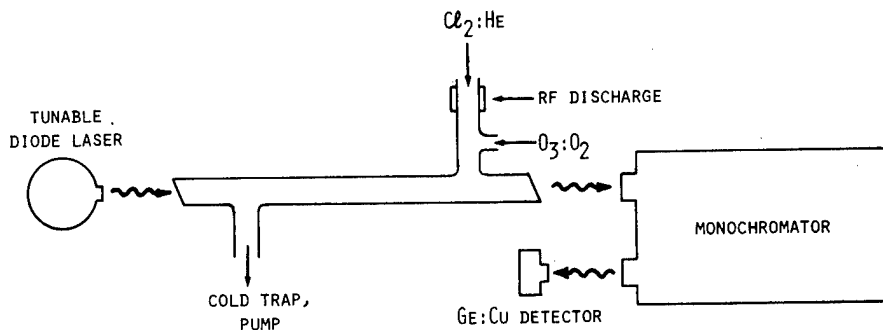


Fig. 3. Experimental setup for laser spectroscopy of ClO. [From Menzies *et al.* (13)].

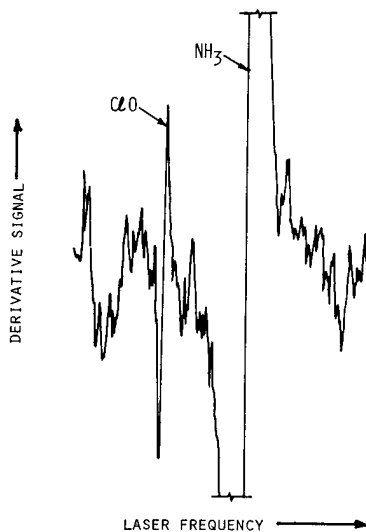


Fig. 4. Derivative spectrum of ClO line at  $847.00\text{ cm}^{-1}$  obtained with a tunable diode laser. Also shown is strong NH<sub>3</sub> reference line, sP(6,5), at  $847.04\text{ cm}^{-1}$ .

with a much stronger NH<sub>3</sub> line used for frequency (wavelength) calibration. By studying a number of ClO lines in this manner, and with the aid of recent microwave measurements of the ClO rotational constants for both the ground and first excited vibrational levels (14), Menzies *et al* have determined the infrared band center and rotational constants for the ClO fundamental vibration (13).

The importance of this research for the remote detection of ClO stems from the direct measurement of absorption cross sections and frequencies. They provide the basis for a theoretical understanding of the molecule, and from that we can then predict parameters for those lines which have not yet been observed, so that other lasers (e.g., the isotopic CO<sub>2</sub> laser) may be considered for monitoring this species.

#### IV. LONG-PATH MONITORING

Diode lasers have been used for measuring atmospheric carbon monoxide, nitric oxide, ethylene and water vapor. Path-lengths have been as long as 2 km (15). The CO measurements were performed mainly in St. Louis in conjunction with the Regional Air

Pollution Study of the U.S. Environmental Protection Agency (16). By comparing the long-path results with those of point-monitoring instruments, the laser measurement and calibration technique were confirmed. Nevertheless, at times there was marked disagreement between the point and long-path measurements, depending on the meteorological conditions and nature of the pollutant source. Continuous, long-path data were recorded over many days for use in the development of mathematical models for predicting air quality (16,17).

The essential components of the laser optical system are shown in Fig. 5. The diode laser was mounted in a closed-cycle refrigerator, and its emission collimated by an Al-coated parabolic mirror, 12 cm in diameter. The beam was transmitted down-range to a remote retroreflector (hollow corner-cube) which reflected it back towards the paraboloid, which refocused it onto the infrared detector situated behind a calibration cell. In order to minimize the effects of atmospheric turbulence on system sensitivity, a derivative spectroscopic technique was employed in which the laser was frequency-modulated at 10 kHz at the pollutant gas absorption line of interest (15).

Calibration was performed by placing a known concentration of pollutant- $N_2$  mixture in the 10 cm cell. For example, if the monitored path outside is 610 meters, a calibration gas of 1,000 ppm mixture produces the same signal as 164 ppb over the long path. Linearity was confirmed by using several different volumetric mixtures in the calibration cell. Inaccuracies in the measurements, which occur as a drift of the zero-ppm signal and changes in linearity and repeatability of the calibration points, were mainly due to variations in the laser frequency. By proper controls, these effects were reduced, and an accuracy of  $\pm 5\%$  of the nominal reading achieved.

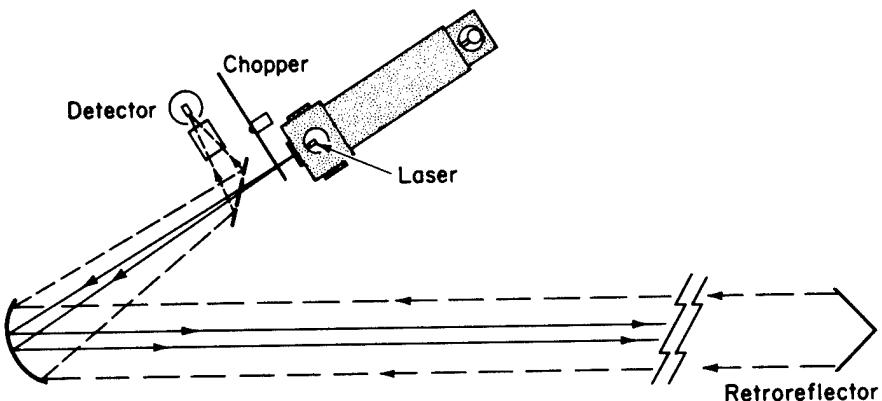


Fig. 5. Optical system for long-path monitoring.

As an example of monitoring in which there was an unexpected difference between the point and long-path measurements (17), Fig. 6(a) shows data for a 24-hour period on 8/2/75. Two sharp peaks were recorded by the laser monitor around 0800 CST; but, due to their fast rise and fall times, correlations with the RAMS hourly readings at 0800 and 0900 CST were poor. In order to check this apparent discrepancy, minute-by-minute readings from the point sampling instrument were obtained from the original computer data library. These, along with the laser data at a 1-sec time constant are shown in Fig. 6(b), where the correlation in both magnitude of CO concentration and time for each of the two "events" is excellent.

The long-path diode laser system has permitted unattended monitoring around the clock, with calibration checks reduced to two or three times a day. Although these results have demonstrated the feasibility and usefulness of long-path laser monitoring, several improvements must be made in future systems in order to increase reliability and provide legally-acceptable air quality measurements (17).

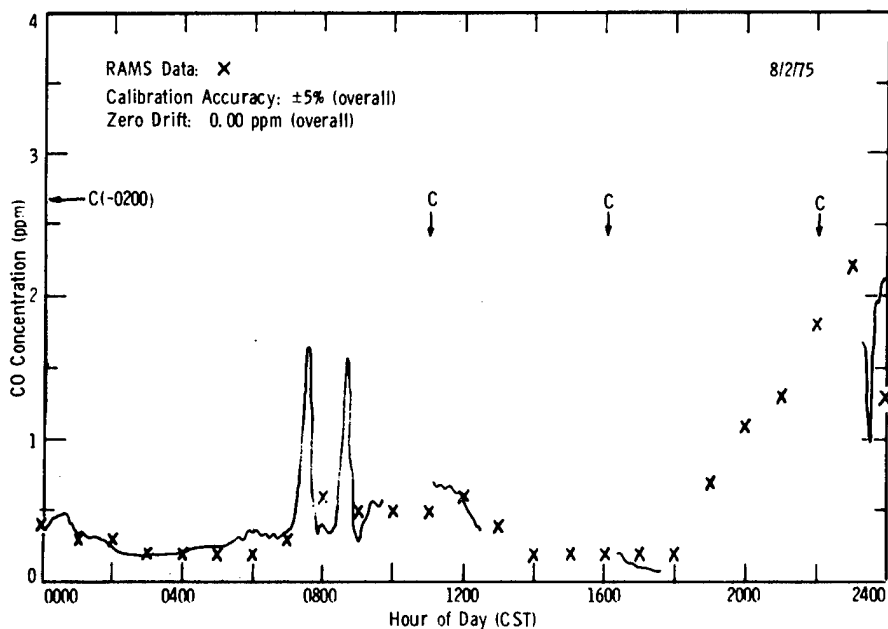


Fig. 6(a). Long-path CO monitoring at Regional Air Monitoring Site #108 in Granite City, Illinois on 2 August 1975, with RAMS data hourly averages. Total pathlength = 0.68 km.

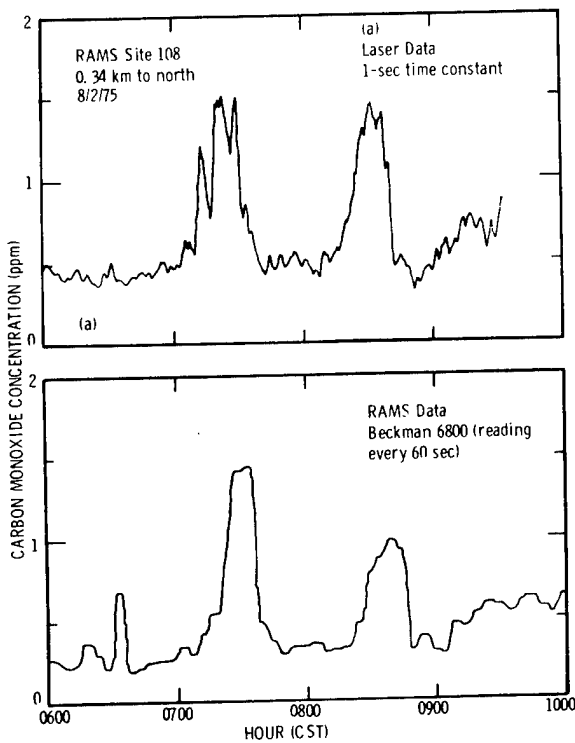


Fig. 6(b). Four-hour segment of Fig. 6(a) with RAMS data minute-by-minute averages.

##### V. SOURCE EFFLUENT MONITORING

The concentrations of pollutant gases emitted by sources is usually highest in the effluent stream near the source itself. Because of the higher concentrations, shorter pathlengths are usually adequate for sensitive detection of these pollutants. Monitoring of smokestacks and automobile exhausts by tunable diode lasers has already been discussed in the literature (1). Recently, however, Hanson and associates at Stanford University have shown that tunable semiconductor diode lasers can be used in combustion research as well. They reported (18) the detection of carbon monoxide in the flame of a propane gas jet, and determined its concentration. Moreover, by measuring the width of the CO lines they were able to determine the gas temperature.

##### VI. REMOTE HETERODYNE DETECTION

Because of the effects of pressure broadening on a spectral absorption line, it is possible to use lineshape information obtained in the manner of Fig. 7 to determine the concentration of a pollutant gas as a function of altitude. In Fig. 7(a) the technique of solar heterodyne radiometry is illustrated, in which the sun serves as the source of radiation and a laser local oscillator is used to measure the amount of the transmitted signal. By tuning the laser through a known absorption line of a

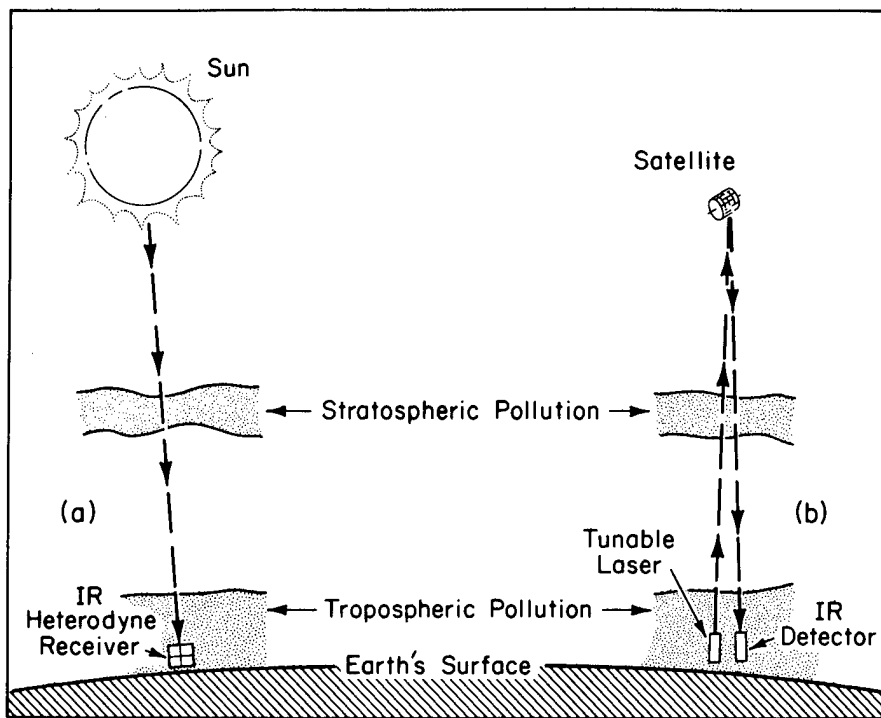


Fig. 7. Diagrams for long-path vertical profile monitoring of the atmosphere using (a) passive system with sun as radiation source and tunable-laser heterodyne detection, and (b) active, ground-based system employing cooperative satellite reflector.

pollutant present in the region between the receiver and the sun, a dip in the transmission will be observable. The same analysis applies over the two-way path of Fig. 7(b) involving a satellite reflector.

Two laser measurements based on the heterodyne technique of Fig. 7(a) have been performed during the past year. In early 1976, Menzies and Seals used several lines of a discretely-tunable  $\text{CO}_2$  laser to determine the height profile of ozone (19). More recently, Frerking and Muehlner of M.I.T. have performed the same measurement using a continuously-tunable semiconductor diode laser as local oscillator (20). Their apparatus consisted of a diode laser, beam splitter, infrared detector, and optics all attached to the cold head of a liquid nitrogen dewar, operating at 77 K. Figure 8 shows their results for ozone in the frequency range  $1010.9$  to  $1011.8 \text{ cm}^{-1}$ . Trace (a) is a fully-resolved ( $0.0001 \text{ cm}^{-1}$  resolution) direct absorption spectrum of ozone measured by transmitting the diode laser radiation through a laboratory gas cell. The heterodyne absorption signal from the sun is displayed in (b), which shows the same ozone

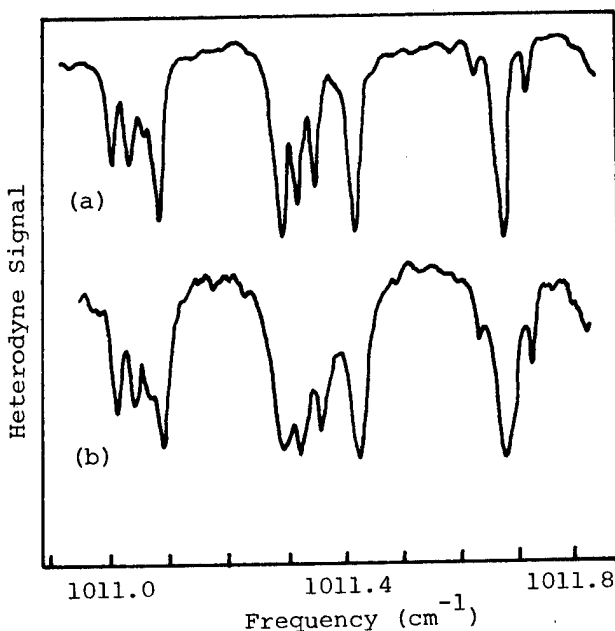


Fig. 8. Ozone spectra measured with a tunable diode laser. Trace (a) obtained in laboratory by direct absorption spectroscopy. Trace (b) was a measurement over the same spectral region using heterodyne detection with the sun as source of radiation, in the manner illustrated in Fig. 7(a). [Adapted from Frerking and Muehlner (20).]

absorption lines due to the presence of the gas in the stratosphere. The instrumental resolution in this case is  $0.006\text{ cm}^{-1}$  (180 MHz), limited by the bandwidth of the rf amplifier system. This result represents the first use of a tunable laser heterodyne receiver to trace out the continuous absorption profile of a molecule over a broad ( $0.8\text{ cm}^{-1}$  or 24 GHz) spectral range, as well as the first wide-scan spectroscopy of an atmospheric constituent with a tunable heterodyne receiver.

#### VII. CONCLUSION

With the commercial availability of tunable semiconductor diode lasers, there has been a remarkable series of developments and advances in the applications of these devices to environmental monitoring and related spectroscopy. Other device improvements need to be made, such as mode quality, power, stability, etc. and are being vigorously pursued; and it appears that these devices will prove to be even more useful in the years to come. The purpose of this paper is to point out the recent

advances in these tunable lasers and their applications, and, hopefully, have the reader develop new ideas for applications of the future.

## VIII. REFERENCES

1. For a comprehensive review of laser monitoring techniques and results to 1977, see "Laser Monitoring of the Atmosphere," (E.D. Hinkley, Ed.) Springer-Verlag, Heidelberg, 1976.
2. Groves, S.H., Nill, K.W., and Strauss, A.J., Appl. Phys. Lett. 25, 331 (1974).
3. Hinkley, E.D., Ku, R.T., Nill, K.W., and Butler, J.F., Appl. Optics 15, 1653 (1976).
4. McClatchey, R.A. and Selby, J.E.A., "Atmospheric Attenuation of Laser Radiation from 0.76 to 31.25  $\mu\text{m}$ ," AFCRL Report Tr-74-0003 to the Air Force Systems Command (1/3/74).
5. Model LS-3 Laser Source Spectrometer, manufactured by Laser Analytics, Inc., Lexington, MA 02173.
6. McDowell, R.S., Galbraith, H.W., Krohn, B.J., Cantrell, C.D., and Hinkley, E.D., Optics Comm. 17, 178 (1976).
7. Lehmann, B., Wahlen, M., Zumbrunn, R., and Oeschger, H., Appl. Phys., April, 1977.
8. Dubs, M. and Günthard, Hs. H., submitted for publication.
9. Gough, T.E., Miller, R., and Scoles, G., submitted for publication.
10. Knoll, J.S., Tettemer, G.L., Planet, W.G., Rao, K.N., Chen, D-W, and Pugh, L.A., submitted for publication.
11. Hinkley, E.D., Nill, K.W., and Blum, F.A., in "Laser Spectroscopy of Atoms and Molecules," (H. Walther, Ed.) Chapter 2, Springer-Verlag, Heidelberg, 1976.
12. Rowland, F.S. and Molina, M.J., Rev. Geophys. Space Phys. 13, 1 (1975).
13. Menzies, R.T., Margolis, J.S., Hinkley, E.D., and Toth, R.A., Appl. Optics, March, 1977.
14. Cohen, E. and Kakar, R., Jet Propulsion Laboratory, personal communication.
15. Ku, R.T., Hinkley, E.D., and Sample, J.O., Appl. Optics 14, 854 (1975).
16. Chaney, L.W., McClenney, W.A., and Ku, R.T., Paper 75-56.6 at the Air Pollution Control Association Annual Meeting, Boston, June, 1975.
17. Ku, R.T. and Hinkley, E.D., "Long-Path Monitoring of Atmospheric Carbon Monoxide:" Technical Report to the National Science Foundation (RANN) and U.S. Environmental Protection Agency, M.I.T. Lincoln Laboratory, April, 1976.
18. Hanson, R.K., Kuntz, P.A., and Kruger, C.H., Paper presented at Eastern States Section, Combustion Institute, Philadelphia, November, 1976.

19. Menzies, R.T. and Seals, Jr., R.K., submitted for publication.
20. Frerking, M.A. and Muehlner, D.J., Appl. Optics, March, 1977.

# High-sensitivity infrared heterodyne radiometer using a tunable-diode-laser local oscillator

R. T. Ku and D. L. Spears

Lincoln Laboratory, Massachusetts Institute of Technology, Lexington, Massachusetts 02173

Received June 10, 1977

A blackbody heterodyne radiometer using a widely tunable PbSnSe-diode laser as the local oscillator (LO) achieved signal-to-noise performance that was an order of magnitude better than previously reported and only a factor of 2.5 below that obtained with a CO<sub>2</sub> laser LO. The diode laser system performance was within a factor of 6 of an *ideal* radiometer. High-resolution blackbody heterodyne absorption spectra of ethylene at 10.6  $\mu\text{m}$  were obtained with a 0.4-sec post-detection integration time by tuning the diode LO in a closed-cycle cryogenic cooler.

Laser heterodyne radiometry has long been recognized as the completely *passive* method of detecting gas absorption and emission lines with high spectral resolution.<sup>1</sup> Menzies and Shumate<sup>2</sup> have recently reported laboratory detection of broadband emission signals from several pollutant gases using CO<sub>2</sub>- and CO-laser local oscillators. Emission lines from astronomical bodies have been detected near 10  $\mu\text{m}$  by using a CO<sub>2</sub>-laser heterodyne system.<sup>3</sup> These fixed-frequency gas-laser systems are limited by a dependence on an accidental coincidence of laser frequency with the characteristic gas line. Heterodyne systems would be much more versatile if a broadly tunable laser,<sup>4</sup> such as a semiconductor diode laser, could be used for the local oscillator (LO).

In this letter we report high-resolution spectroscopy of C<sub>2</sub>H<sub>4</sub> obtained with a diode-laser heterodyne system that has shown a sensitivity over an order of magnitude greater than previously<sup>5,6</sup> obtained with diode lasers, and within a factor of 2.5 of the quantum-noise-limited sensitivity we achieved with a CO<sub>2</sub>-laser LO. Although low-power tunable-diode lasers (<200  $\mu\text{W}$ ) have been used routinely for high-resolution infrared spectroscopy of many molecules (resolution <10<sup>-4</sup>  $\text{cm}^{-1}$ ),<sup>7</sup> and have been incorporated successfully in *active in situ* and long-path pollutant-monitoring systems,<sup>8-10</sup> their application as a *passive* heterodyne LO<sup>5,6</sup> has been limited, primarily as a result of relatively low diode-laser power level. Recently, diode-laser device improvement has increased the wavelength tunability to hundreds of wavenumbers and the power level to several milliwatts.<sup>11</sup> In addition, important advances<sup>12</sup> have been made in the wide-bandwidth heterodyne quantum sensitivity of HgCdTe photodiodes. These developments have stimulated interest in tunable-diode-laser local oscillators for heterodyne radiometer systems.

Figure 1 shows schematically the heterodyne setup, which utilized a 900°C blackbody source and a tunable 10- $\mu\text{m}$  PbSnSe-diode laser<sup>13</sup> LO mounted in a closed-cycle cooler. The LO wavelength was coarse tuned by adjusting the cooler temperature and fine tuned by adjusting laser current. A total tuning range from 920 to 980  $\text{cm}^{-1}$  was possible for cooler temperatures of 12

to 30 K. Laser radiation (polarized parallel to the diode junction plane) was combined with the thermal emission at the Ge beamsplitter and focused onto a state-of-the-art HgCdTe photodiode,<sup>12</sup> which has a bandwidth of over 1.5 GHz and an *effective heterodyne* quantum efficiency<sup>14</sup> ( $\eta_e$ ) of 0.45. A spike filter (10.45 to 10.68  $\mu\text{m}$ ) was used to limit the total blackbody radiation focused onto the detector. The RF signal generated by the photomixer was amplified by a low-noise (2.5-dB noise figure), wideband ( $B = 500$  MHz) preamplifier. The heterodyne signal was then square-law detected and fed into a lock-in amplifier, the output of which was plotted on the X-Y recorder as a function of laser current. A monochromator was used to examine the mode structure of the diode laser and provide wavelength calibration as a function of diode current. Precise diode frequency calibration was obtained by heterodyning the diode laser with an auxiliary CO<sub>2</sub> laser (not shown in Fig. 1). The IF noise from the preamplifier was monitored with a spectrum analyzer.

Heterodyne signal-to-noise ratio was found to be largely dependent on properties of the diode-laser LO, such as the power available at the photomixer and excess RF noise generated by the diode laser. A typical scan of heterodyne signal as a function of diode-laser current is shown in Fig. 2(a) for a diode laser with three or four dominant modes in the 20  $\text{cm}^{-1}$  (600 GHz) scan range. Note the occurrence of several very noisy regions (A, C, F, H), which are unsuitable for heterodyne detection and appear to be associated with mode switching and self-beating of laser modes. IF noise spectra in the 0 to 1 GHz region shown in Fig. 2(b) reveal quite different noise output in regions C and H as compared to that of region E, where the LO was relatively well behaved. In region C, strong self-beat signals were detected, and in region H, an excessively high "white" noise spectrum was seen. Mechanical vibration of the diode on the cooler cold head probably contributed in part to this noisy performance; however, the phenomenon is a general property of diode lasers, as we have seen similar effects with diodes mounted in a liquid-helium Dewar.

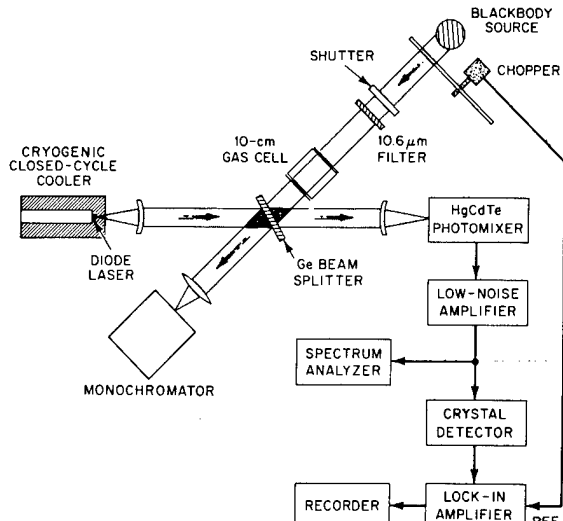


Fig. 1. Experimental setup used for diode-laser heterodyne radiometry.

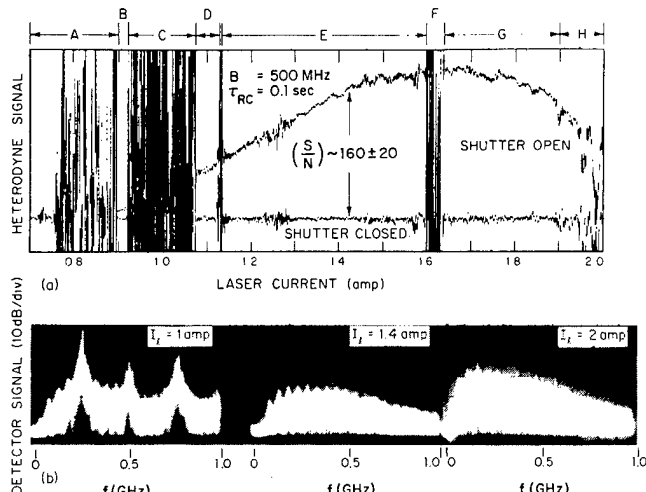


Fig. 2. (a) Heterodyne signal as a function of diode-laser local-oscillator (LO) current (i.e., wavelength). The amplifier noise level was about a factor of 2 less than the lowest level observed with LO on, as shown at 1.4 amp, with the shutter closed. (b) Preamplifier RF noise spectra in the 0 to 1 GHz region for three different laser currents showing LO noise (noise bandwidth = 100 kHz).

For Fig. 2(a), the best signal-to-noise ratio (SNR =  $160 \pm 20$ ) was found at  $I \approx 1.42$  amp (laser frequency  $\sim 942 \text{ cm}^{-1}$ ). This observed SNR is only a factor of 6 less than the theoretical SNR of 1000 calculated for an ideal ( $\eta_e = 1$ ) 10.6- $\mu\text{m}$  blackbody heterodyne radiometer from the expression,

$$\text{SNR} = 2\eta_e (B\tau_I)^{1/2} T_o [\exp(h\nu/kT_{BB} - 1)]^{-1};$$

and using our experimental parameters,  $T_{BB}$  = blackbody temperature (1173 K),  $B$  = IF bandwidth = 500 MHz,  $\tau_I$  = equivalent integration time =  $4\tau_{RC}$  of a 12-dB/oct lock-in amplifier<sup>15</sup> = 0.4 sec. A total transmission factor ( $T_o$ ) of 0.077 was due principally to the beamsplitter, filter, and chopper transmission factors of 0.36, 0.62, and 0.5, respectively. The above diode

laser's SNR performance is substantially better than that generally reported for systems using CO<sub>2</sub>-laser LO's, which is mainly due to the higher  $\eta_e$  (0.45) of our HgCdTe photodiode.<sup>16</sup> This result is very encouraging, since it was obtained with only 0.15 mW of diode-laser LO power on the photodiode and compares favorably with the best SNR value of  $420 \pm 20$  that we obtained with a CO<sub>2</sub>-laser LO. This quantum-noise-limited CO<sub>2</sub> LO performance required 0.4 mW of CO<sub>2</sub> power. The factor of  $\sim 2.5$  difference in SNR between the diode and the CO<sub>2</sub>-laser LO's is due primarily to insufficient diode-laser LO power. When the CO<sub>2</sub> LO power was reduced from 0.4 to 0.15 mW, the SNR dropped by about a factor of 2.

Kostiuk *et al.*<sup>17</sup> have discussed various degradation factors in practical heterodyne radiometers. They have shown that, for the case of insufficient LO power, the optimum beamsplitter transmission-reflection coefficients ( $T + R = 1$ ) should be in the 40 to 50% region. In our experimental setup (Fig. 1), 36% ( $R$ ) of the total thermal power was mixed with 64% ( $T$ ) of the LO. This arrangement is close to the optimum for a *single* detector. However, van de Stadt<sup>18</sup> has shown that a double-balanced heterodyne detection system can recover this beamsplitter loss factor. Indeed, we have confirmed this recovery factor with diode- and CO<sub>2</sub>-laser local oscillators. Two identical HgCdTe photodiodes and preamplifiers were placed at the outputs of a 50% beamsplitter. A wideband transformer was used to add the RF signals from the two preamplifiers. The SNR for this double-balanced detection scheme was about 1.85 times that obtained with a single detector; thus the beamsplitter loss factor of 0.5 was essentially recovered.

The best SNR region in Fig. 2(a) was used for heterodyne spectroscopy of ethylene. First, conventional diode-laser spectroscopy<sup>1</sup> was performed to locate the absorption of C<sub>2</sub>H<sub>4</sub> in this frequency region by placing a 10-cm gas cell in the diode laser beam. Figure 3(a) shows the transmission signal as a function of diode-laser current, where the dominant laser mode was tuned through several C<sub>2</sub>H<sub>4</sub> lines near 942 cm<sup>-1</sup>. Line-position and laser-tuning rates were established by heterodyne calibration with the P(22) line of a stabilized CO<sub>2</sub> laser. Figure 3(b) displays the line spectra obtained by tuning the diode-laser LO over the same range in a heterodyne absorption experiment where the C<sub>2</sub>H<sub>4</sub> cell was placed in front of the blackbody source. The total scan time in Fig. 3(b), and also in Fig. 3(a), was about 200 sec. The desired spectral resolution was achieved by reducing the IF bandwidth  $B$  accordingly. For Fig. 3(b),  $B$  was reduced to 300 MHz by placing a low-pass RF filter between the preamplifier and the RF detector. The observed spectral resolution from the line profile in Fig. 3(b) is approximately 600 MHz (0.02 cm<sup>-1</sup>), in agreement with the expected resolution of  $2B$ . The quality of the heterodyne spectra is very encouraging, as it was obtained passively, without transmitting the laser beam through the C<sub>2</sub>H<sub>4</sub> gas, and with only  $\tau_{RC} = 0.1$  sec. Total acquisition time of such heterodyne spectra could be greatly reduced with the aid of an RF filter bank<sup>3,5</sup> at the output of the preamplifier.

In summary, we have demonstrated that high-per-

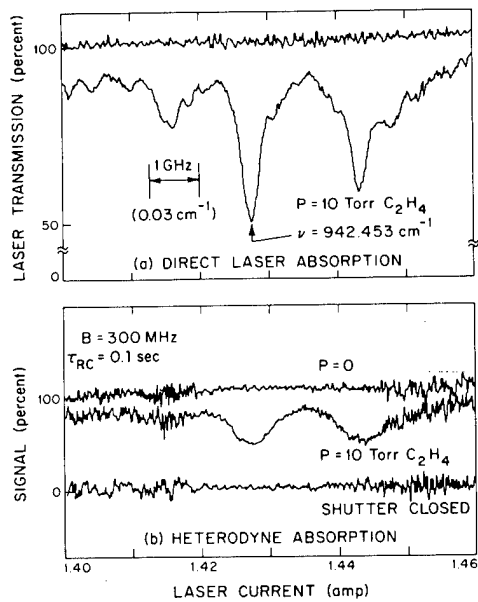


Fig. 3. (a) Direct diode-laser absorption scan of three  $C_2H_4$  lines near  $942\text{ cm}^{-1}$ . (b) Heterodyne absorption scan of the above lines with spectral resolution of  $2B = 600\text{ MHz}$  ( $0.02\text{ cm}^{-1}$ ).

formance heterodyne detection can be achieved using a widely tunable diode-laser L.O. Although some noisy frequency regions unsuitable for heterodyne operation were present in our diode laser, the diode-laser system did provide good heterodyne detectivity over many wavenumbers. With only moderate improvements in diode-laser output power and mode quality, their performance as heterodyne receiver L.O.'s should equal that of a  $CO_2$  laser, but with the advantage of wide tunability.

The views and conclusions contained in this document are those of the contractor and should not be interpreted as necessarily representing the official policies, either express or implied, of the United States Government.

This work was supported by the National Science

Foundation (RANN), the Environmental Protection Agency, and the Department of the Air Force.

## References

1. E. D. Hinkley and P. L. Kelley, *Science* **171**, 635 (1971).
2. R. T. Menzies and M. S. Shumate, *Science* **184**, 570 (1974).
3. A. L. Betz, M. A. Johnson, R. A. McLaren, and E. C. Sutton, *Astrophys. J.* **208**, L141 (1976).
4. *Tunable Lasers and Applications*, A. Mooradian, T. Jaeger, and P. Stokseth, eds. (Springer-Verlag, New York, 1976).
5. M. Mumma, T. Kostiuk, S. Cohen, D. Buhl, and P. C. von Thuna, *Nature* **253**, 514 (1975).
6. M. A. Frerking and D. J. Muehlner, *Appl. Opt.* **16**, 526 (1977).
7. E. D. Hinkley, K. W. Nill and F. A. Blum, in *Laser Spectroscopy of Atoms and Molecules*, H. Walther, ed. (Springer-Verlag, New York, 1976), chapter II.
8. E. D. Hinkley, R. T. Ku, and P. L. Kelley, in *Laser Monitoring of the Atmosphere*, E. D. Hinkley, ed. (Springer-Verlag, New York, 1976), chapter VI.
9. E. D. Hinkley, *Opt. Quant. Electron.* **8**, 155 (1976).
10. R. T. Ku, E. D. Hinkley and J. O. Sample, *Appl. Opt.* **14**, 854 (1976).
11. E. D. Hinkley, R. T. Ku, K. W. Nill, and J. F. Butler, *Appl. Opt.* **15**, 1653 (1976).
12. D. L. Spears, I. Melngailis, and T. C. Harman, *IEEE J. Quantum Electron.* **QE-11**, 79 (1975).
13. We are grateful to Laser Analytics, Inc., for providing the diode laser for this work.
14. B. J. Peyton, A. J. DiNardo, S. C. Cohen, J. H. McElroy, and R. J. Coates, *IEEE J. Quantum Electron.* **QE-11**, 569 (1975).
15. M. E. Tiuri, *IEEE Trans. Antennas Propag.* **AP-12**, 930 (1964).
16. The effective heterodyne quantum efficiency,  $\eta_e$ , can be substantially lower than the low-power, low-frequency quantum efficiency usually given for a device. The photodiodes used in this work had low-frequency quantum efficiencies in excess of 60%. However, other wide bandwidth devices with similar low-frequency values have shown  $\eta_e$  of only 8 to 10% [see D. L. Spears, *Solid State Research Report* 1976:3 (Lincoln Laboratory, MIT, Lexington, Mass., 1976), p. 5].
17. T. Kostiuk, M. J. Mumma, M. M. Abbas, and D. Buhl, *Infrared Phys.* **16**, 61 (1976).
18. H. van de Stadt, *Astron. and Astrophys.* **36**, 341 (1974).



## REAL TIME DIGITAL RECORDING OF THERMOVISION DATA

*Ronald Cordova and Ronald R. Parenti*

Massachusetts Institute of Technology, Lincoln Labs -  
Lexington, Massachusetts

### ABSTRACT

A direct, real time, video to digital data recording system has been developed at Lincoln Laboratory to record 10 $\mu$ m thermal imagery in conjunction with an AGA 680 LW camera. This device is now being used to study the thermal characteristics of various types of natural terrain for the purpose of developing tactical target acquisition techniques.

This data recording system consists of an Analog-Digital interface, NOVA 2/10 mini-computer and magnetic tape transport and is designed to record 16 frames per second at an 87 kHz digitization rate with 8 bit precision. Computer controlled timing circuits group pairs of 8 bit data points into a single 16 bit

NOVA compatible word in an intermediate buffer which is then transferred into core memory. A block of 5,476 data points is written onto standard 9 track magnetic tape at the end of each camera frame.

System initialization requires only the adjustment of the AGA display black level for normal picture quality. This correctly positions the digitization interval while the black level voltage provides the temperature offset; the discrete step size is normally set equal to the noise equivalent temperature of the Thermovision system. The final data format consists of a 74 x 74 picture element array with 0.2°C temperature resolution and 50°C dynamic range.

### INTRODUCTION

Lincoln Laboratory has been involved in the development of a variety of active and passive techniques to detect and locate man-made objects in natural terrain. This led to a requirement for a system capable of collecting quantitative data in the 8-12 $\mu$ m atmospheric window region. Since most experiments were to be performed at remote site locations, it was desirable to develop a method of digitizing and analyzing information in the field. The result was a real-time digitization system using state-of-the-art techniques to record data generated by a AGA 680 LW camera directly on a 9 track digital magnetic tape using a minicomputer as an intermediate storage buffer.

### DIGITIZATION ALTERNATIVES

The majority of the existing and proposed digitization methods fall into three general categories:

---

This work was sponsored by the Defense Advanced Research Projects Agency of the Department of Defense.

1. Calibrated film recording
2. Analog magnetic tape recording
3. Direct digital recording

The first two methods require an intermediate analog storage mechanism and post-experiment digitization at non-real-time rates; these techniques are presented schematically in Figures 1a and 1b. The film recording method has the advantages of simplicity

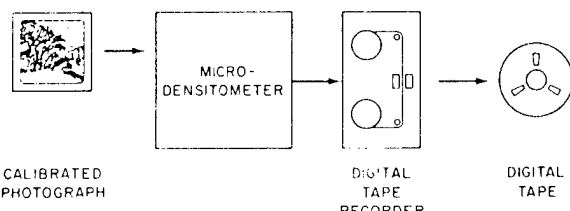
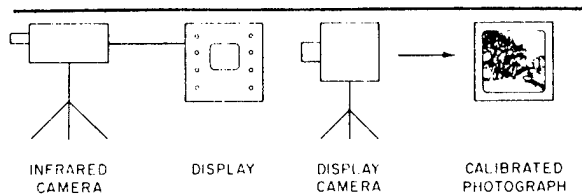


Fig. 1a

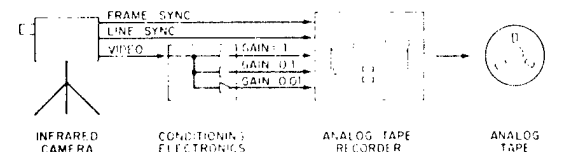


Fig. 1b

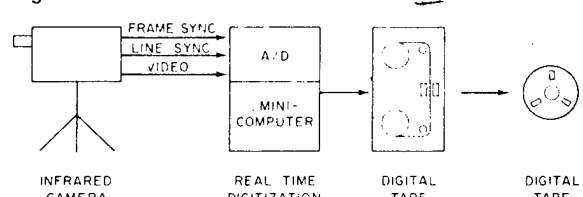


Fig. 1c

and economy for those laboratories with ready access to a microdensitometer. However, in many respects this is the least desirable of the three alternatives owing to the inherent non-linearity and low information density of photographic film or plates. Magnetic analog tape recording systems eliminate these problems, but still require two separate steps to produce a computer compatible digital tape.

Figure 1c illustrates the direct digitization concept. The infrared camera video is digitized in real-time by fast A/D converters and transferred directly to standard 9 track digital tape, thus eliminating the need for duplicate analog tape recorders at field sites and in

the laboratory. A key advantage of this system is the capability of instant data playback and analysis which is often vital in non-repeatable experimental situations.

## EQUIPMENT

The real-time infrared data collection system constructed by Lincoln Laboratory is pictured in Figure 2. It consists of five major components:

1. An AGA 680 LW camera operating in the 8-12  $\mu\text{m}$  spectral waveband. This device has an  $80^\circ \times 80^\circ$  lens with a 1.3 mr instantaneous field of view. The noise equivalent temperature of this unit is less than  $0.20^\circ\text{C}$ .
2. An analog to digital interface package containing a  $1\mu\text{s}$  8 bit A/D converter, a 16 bit hardware output buffer, and data clocking circuitry which generates 2,450 sixteen bit words during each camera frame.
3. A Data General NOVA 2/10 mini-computer with a 32,000 word memory. This device has a 16 bit parallel I/O central processor with a high speed direct memory access channel capable of transferring in excess of 500,000 words per second.
4. A Datum formatter-controller which converts the 16 bit NOVA words to the standard 8 bit IBM tape format.
5. A Wangco 9 track digital tape recorder operating at 1600 BPI density at 75 IPS. The maximum writing speed of this recorder is 120,000 eight bit words per second under continuous data transfer conditions.

Interaction with the NOVA computer for post-experiment data review and analysis is achieved

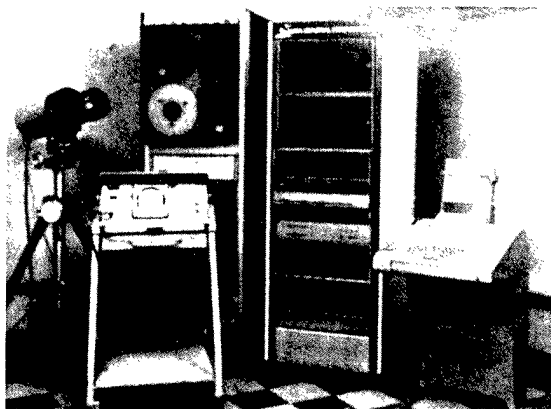


Fig. 2

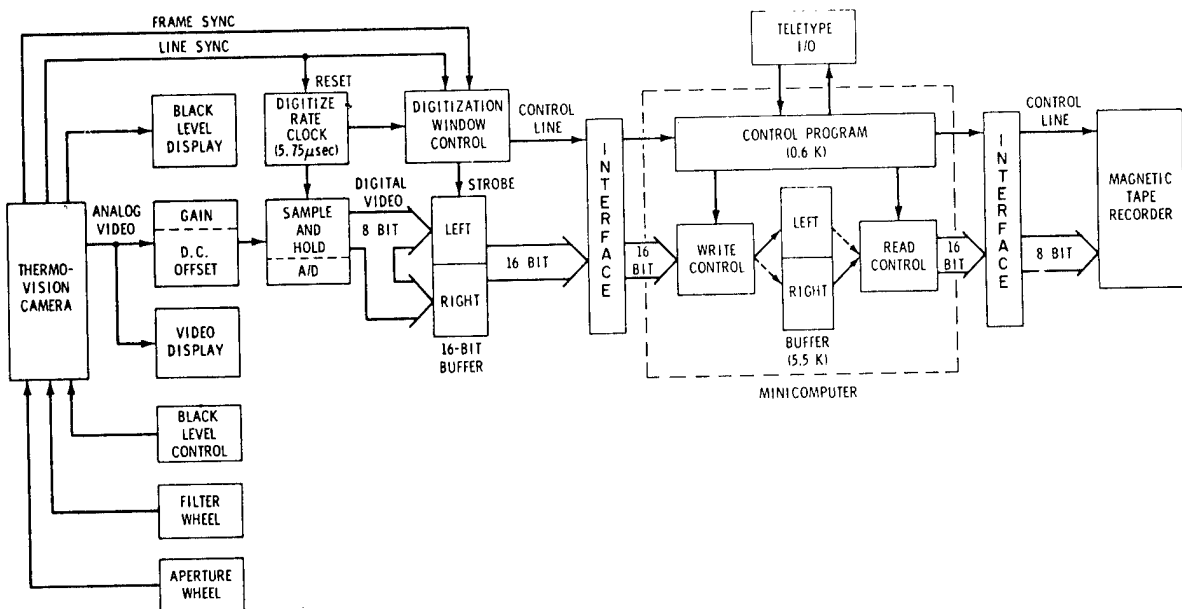


Fig. 3

through the use of a Teletype unit which is also shown in this figure. In addition to numerical output, crude gray scale pictures can be generated by the Teletype which can be compared with the AGA analog display for immediate conformation of proper system operation.

#### DATA RECORDING TECHNIQUE

The inherent spatial resolution of the AGA 680 camera yeilds a  $100 \times 100$  picture element field for a total of 10,000 discrete data points. However only 70 lines are generated by each frame; a complete infrared picture requires at least two or three interlaced scans out of a full 7 frame field<sup>1</sup>. The simplest and most direct method of digitizing these data involves a  $70 \times 70$  sampling each frame, producing a 4900 discrete element field with 1.9 mr resolution.

The collection of 70 data points during a  $400 \mu\text{s}$  line scan is equivalent to an instantaneous sampling rate in excess of 170 kHz, well above the upper writing speed limit of most commercially available digital tape recorders. On the other hand, state-of-the-art A/D converters and minicomputers with high speed data channels can easily digitize and store small blocks of data at rates up to 1 MHz. The key concept in the solution to the real time digital recording problem is the use of a dedicated minicomputer to temporarily store single frames of data prior to their transfer to magnetic tape. The result is that a 4900 element field can be recorded 16 times per second at a con-

stant 80 kHz data transfer rate, which is well within the capability of several moderately priced digital tape drives now available.

Figure 3 is a functional block diagram of the real-time recording system pictured in Figure 2. Video signals taken from the camera accessory plug are conditioned prior to recording by adjustment of the picture black level to produce a normal image on the AGA analog display. The signal then passes through the offset and gain circuit shown in Figure 4 which places it within the input range of the 8 bit analog to digital converter. The circuit gain is designed to match the digital step size to the noise equivalent temperature of the infrared system, resulting in a  $50^\circ\text{C}$  dynamic range with  $0.2^\circ\text{C}$  temperature resolution.

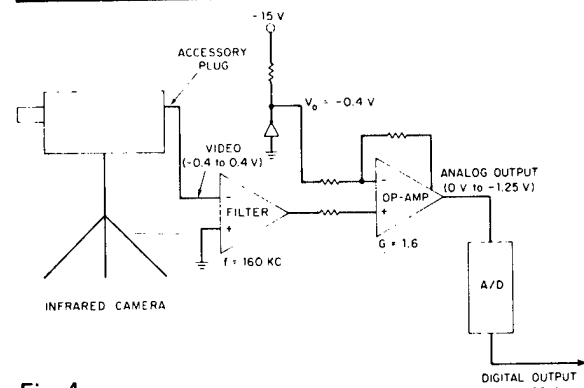


Fig. 4

A 16 bit hardware buffer follows the A/D converter allowing temporary storage of two 8 bit words for subsequent transfer to the 16 bit word length NOVA memory. The timing circuit described in Figure 5 receives the line and frame sync pulses from the AGA 680 unit and generates time gates regulating the flow of digitized information from the hardware interface to computer core memory during the camera's active scan period.

Computer input and output is handled by a high speed data channel which takes first priority in a control hierarchy which is shown in Figure 6. A data channel request generated either by the A/D interface or the magnetic tape drive controller momentarily halts all computer operations guaranteeing uninterrupted information transfer. A low priority software program continuously performs routine functions such as resetting flags and counters; its main task is the switching of the read and write buffer addresses when program interrupts signal that these functions have been completed. A total of 600 words of software memory is allocated to these control algorithms.

Two software buffers, each capable of storing a single frame of AGA data and occupying a total of 5500 words of NOVA memory, form the core of the real-time digital recording system. Data is written onto one memory block during the active scan period of the infrared camera while, simultaneously, the previous frame is read by the magnetic tape unit. Thus, data transfer to tape lags the camera video signal by a full frame, proceeding at an uninterrupted average rate of 78,400 eight bit words per second. Conversion of the NOVA 16 bit words to tape compatible 8 bit format is performed in the computer output interface by a commercially available formatter-controller.

### SYSTEM PERFORMANCE

The performance of the real-time digitization system can be summarized by the following list:

1.  $80^\circ \times 80^\circ$  field of view.
2. 1.9 mr instantaneous field of view.
3.  $70 \times 70$  data format.
4. 16 frame per second data rate.
5. 256 digital step precision (48 db S/N) giving a  $50^\circ\text{C}$  temperature dynamic range with  $0.2^\circ\text{C}$  resolution.
6. 9600 frame storage capacity allowing 10 minutes of continuous recording on a single 10 inch digital tape.

The picture quality achievable with this system

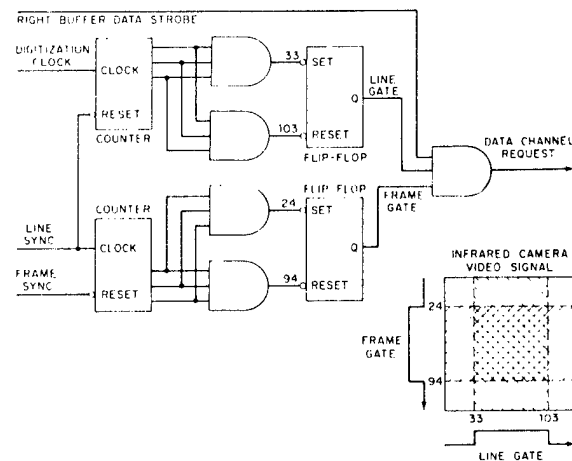


Fig. 5

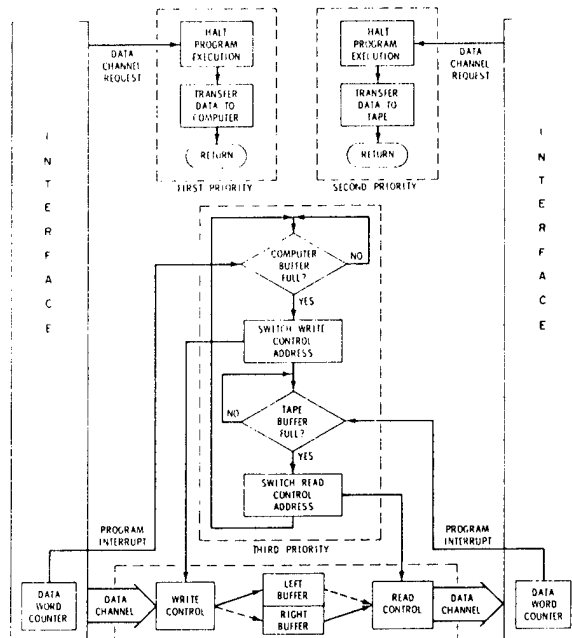


Fig. 6

can be best illustrated by the series of photographs appearing in Figure 7. Figure 7a was produced by an inexpensive computer terminal device, using the standard ASCII character set, to demonstrate the feasibility of producing crude gray scale images in the field. Figure 7b, 7c, and 7d were generated in the laboratory on a RAMTEK color monitor.

Finally, it should be noted that the  $70 \times 70$  data format currently employed does not represent the ultimate spatial resolution achievable with this system.

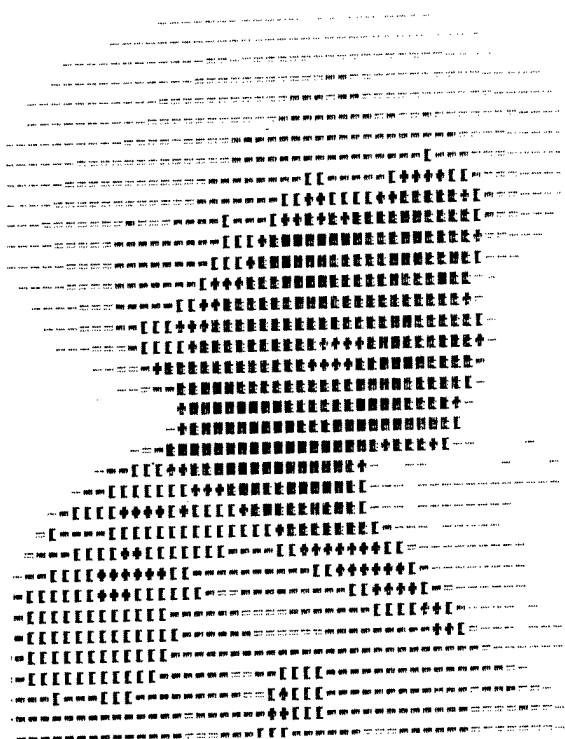


Fig. 7a

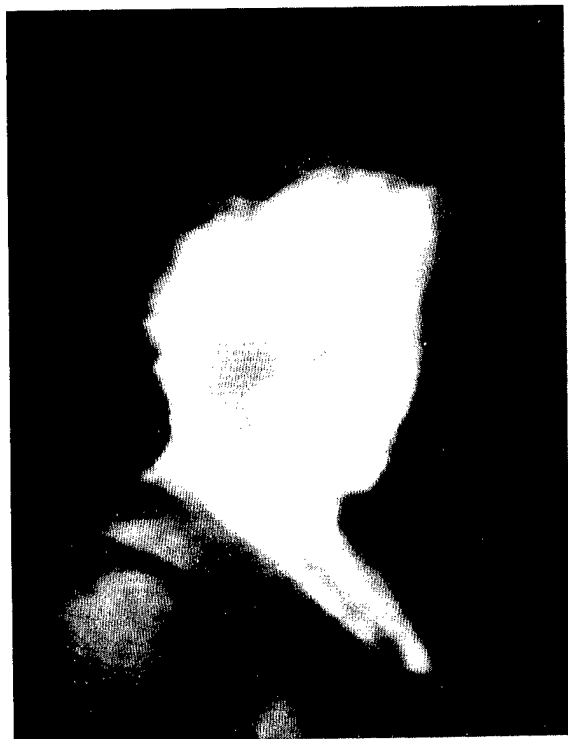


Fig. 7b



Fig. 7c



Fig. 7d

---

The utilization of an intermediate frame storage buffer effectively removes any digitization rate restrictions imposed by tape drive writing speed limitations, allowing data blocks of any size to be recorded as long as the average data transfer speed to tape is held 120,000 words per second. Plans are now being made to double the A/D digitization rate and to interlace two successive frames to produce a 140 x 140 data point field which would be recorded at a 4 field per second frame rate.

### CONCLUSIONS

A direct, real-time digitization system has been developed for the AGA 680 camera which records 16 frames per second with a 70 x 70 data point format

onto a standard 9 track digital tape. In its present configuration the recording capability is roughly comparable to that of an 80 kHz analog recorder, but offers the added advantage of providing the user with immediate post experiment data analysis. Although this prototype system cannot match the portability of the newer analog recorders, it is expected that advances in microprocessor and tape transport technology will make it possible to construct a rugged, lightweight, direct digitization unit in the very near future.

### ACKNOWLEDGMENTS

We are indebted to Mr. Harvey Buss for the development of the multicolor display algorithms used to generate the infrared images appearing in this report.

### REFERENCES

- 1 D. Dorratcague, "Thermovision Digital Data Processing", Proceedings of the Second Biennial Infrared Information Exchange, St. Louis, Missouri, August 27-29, 1974.

## Interferometric Evaluation of the Imaging Characteristics of Laser Beams Propagated Through the Turbulent Atmosphere\*

D. Kelsall

*Lincoln Laboratory, Massachusetts Institute of Technology, Lexington, Massachusetts*

Fast and continuously shearing, very stable, triangular interferometers for making accurate real-time measurements in field environments at visible and infrared wavelengths have been developed and used. The techniques employed are reviewed, an outline of their general properties is given, and some experimental work is described. The degradation of laser beams when propagated through a turbulent atmospheric medium has been measured. A series of modulation transfer function (MTF) measurements in wind tunnels and on jet aircraft has been carried out, and image analysis and evaluation of representative data will be discussed.

### Introduction

Optical image evaluation and in particular the measurement of the Optical Transfer Function (OTF) has usually involved sophisticated laboratory measurements, carried out under laboratory conditions, where steps to minimize vibration and air turbulence were necessary. One of the major objectives of the efforts devoted to developing the OTF measuring techniques over the last 30 years has been the setting up of accurate procedures and standards, so that optical systems or devices, whether mass-produced by an optical company or a specialized one-of-a-kind optical system, could be uniquely and accurately characterized.<sup>1-3</sup>

In practice, optical systems are very often set up and aligned in field environments, where they have different properties than when used in the laboratory. The measurement of performance may also include that of the environment, as well as including noise and disturbances arising from being used in a field situation. Thus, with the now widespread use of laser systems in many developments from alignment devices, communication systems, pollution-measuring projects, to propagation studies through the atmosphere, the need for

rapid, real-time, accurate field measurements of the OTF has arisen.

It was first shown by Hopkins<sup>4</sup> that the OTF can be directly measured by means of a lateral shearing interferometer, using a monochromatic light source. With the advent of lasers, emitting coherent radiation over a wide range of visible and infrared wavelengths, the interferometric technique appears to be ideally suited to OTF measurements at single wavelengths. Many interferometric systems have been described already in the literature,<sup>5-11</sup> although in most cases these instruments are not suitable for routine optical testing or for field use. More recently, a corner-cube shearing interferometer was constructed for making Modulation Transfer Function (MTF) measurements onboard a KC-135 jet aircraft.<sup>12</sup> In investigations into the characteristics of optical imaging through turbulent air paths, a series of experiments has been carried out by MIT Lincoln Laboratory in wind tunnels and from jet aircraft. In the present paper, a review of the shearing interferometric technique that has been developed for this purpose will be given, and a brief account of the type of data that has been obtained shown, to demonstrate the capability of this method to obtain OTF measurements in difficult field conditions.

Imaging through the turbulent atmosphere is such that the OTF rapidly changes from one instant to the next. In wind tunnels and in the turbulent air media around airborne jet aircraft for example, the optical degradation of a beam through such paths changes at least as fast as 1 msec in many instances. A common path lateral shearing triangular configuration interferometer has been developed which is extremely stable, even in environments where large vibrations are present, and requires no adjustment in use.<sup>13,14</sup> This fast scanning interferometer (FSI) continuously measures the complete OTF curve in about 1 msec, in real time, and allows recording of the OTF data at the rate of 14,400 complete curves every minute. Several instruments have been built for operation in either (or both) the visible or infrared wavelength region up to 10.6 microns. The present FSI units have been used only to obtain the MTF curve to date, but the systems also provide data to yield the phase transfer function. In ad-

Paper presented at the SPSE International Conference on Image Analysis and Evaluation, held in Toronto, Ontario, Canada, July 19-23, 1976. Received July 23, 1976.

\*This work was sponsored by the Department of the Air Force.

© 1977, Society of Photographic Scientists and Engineers.

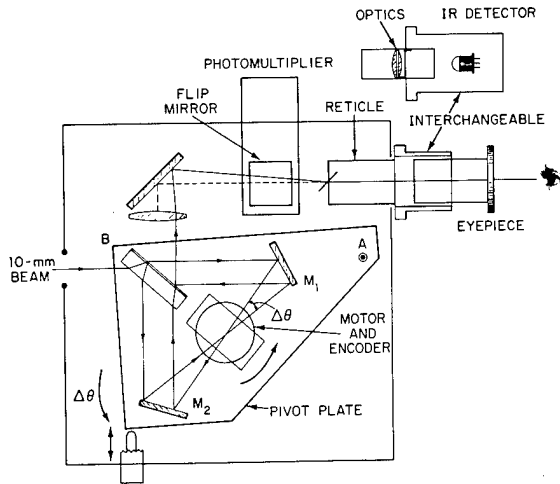


Figure 1. Optical diagram of FSI.

dition, the systems yield angle-of-arrival measurements, such as in those experiments involving propagation paths through the atmosphere, or where vibration of optical parts, tracker errors, or other disturbances may be producing wavefront tilts. The MTF data are independent of the wavefront tilt or pointing direction, and are not affected by such disturbances. A brief review of the FSI system is given here followed by a discussion of data obtained using this technique.

### Method of Operation of the FSI

The OTF can be measured directly using a lateral shearing interferometer which performs an autocorrelation operation on the complex amplitude over the pupil of a coherent optical beam.<sup>4</sup> The total flux in the interferogram,  $F(\delta, s, \phi)$  can be expressed as:

$$F(\delta, s, \phi) = 1 + |D(s, \phi)| \cos[k\delta + \chi(s, \phi)] \quad (1)$$

where  $k$  is the wavelength constant and  $\delta$  is the path difference in the interferometer between the two interfering beams. The two interfering beams are laterally displaced by an amount  $s$  (the shear) and  $\phi$  represents the direction of shear along a diameter of the entrance pupil to the interferometer (or azimuth angle). The shear parameter  $s$  is given by  $s = \lambda R / \sin \alpha$ , where  $\lambda$  is the radiation wavelength (in mm),  $R$  the spatial frequency in the image space (cycles/mm), and  $\alpha$  is the half-angular subtense in the image space.  $|D(s, \phi)|$  is the MTF and  $\chi(s, \phi)$  is the phase transfer function.

If in the triangular interferometer, both  $s$  and  $\delta$  are made to vary simultaneously and linearly with time at a uniform rate, then the total flux in the output interferogram (integrated over the complete sheared interferogram) produces a modulated carrier signal. The modulation of the carrier signal is a direct measure of the MTF and the phase (or zero crossing

points) of the carrier signal determines the phase component of the OTF. The carrier signal frequency itself depends upon the rate of change of  $k\delta$ . This technique is described in more detail in refs. 13 and 14.

In practice a collimated beam is divided into two parts at a beam splitter  $B$  and reflected at two mirrors  $M_1, M_2$  arranged to form a triangular interferometer (Fig. 1). These two beams traverse the triangular path in opposite directions, to recombine and interfere at the beam splitter where they produce an interferogram. The total flux in this exiting interferogram is collected and made to impinge on a radiation detector. A plane parallel micrometer plate, located between  $M_1$  and  $M_2$ , is rotated rapidly at high speed. As it does so the two beams traversing the interferometer are laterally sheared and undergo a relative path length ( $\delta$ ) change. The two beams make an angle  $\Delta\theta = \theta_1 - \theta_2$  to each other, and  $\Delta\theta$  is maintained constant as the micrometer plate rotates, although it can be easily and accurately changed by a micrometer which rotates the pivoted plate about a pivot point  $A$  on which the triangular interferometer is mounted. It can be shown<sup>13</sup> that the relative path difference  $\delta$  between the two beams traversing the micrometer plate as it rotates is given by

$$\delta = \{[(\mu - 1)t]/2\mu\} (\theta_1 + \theta_2) \cdot \Delta\theta \quad (2)$$

and that the total lateral shear  $s$  of the two beams is given by

$$s = 2\{[(\mu - 1)t]/(\mu h)\} (\theta_1 + \theta_2) \quad (3)$$

This of course is an approximation, assuming small angles of  $\theta$ , where  $\mu$  is refractive index of the shear plate,  $t$  is the plate thickness, and  $h$  is the beam diameter. Therefore both  $s$  and  $\delta$  vary linearly with  $\theta$ , the rotation of the shear plate, and the output signal from the interferometer consists of a signal having a constant carrier signal frequency (depending on the value of  $\Delta\theta$ ). The amplitude modulation of this signal yields the MTF and the phase of each cycle of the carrier signal frequency is a measure of the phase transfer function. The carrier signal frequency can be set at any level from zero to many hundred kilohertz by turning the pivot plate which determines the value of  $\Delta\theta$ . An encoder signal (216 KHz) and an index pulse (set to coincide with shear zero) are generated as the shear plate is rotated (by an encoder system coupled to the shear plate rotator motor), as well as standard IRIG time code signals, which are all recorded on an M magnetic tape recorder together with the MTF data. Thus accurate shear axis calibration, and location of the exact time an MTF curve was measured, can be determined, after inputting all the information recorded to a computer. Typical signals from the FSI, plus the IRIG B time code signals which are normally recorded on tape during measurements are shown in Fig. 2.

The FSI is designed primarily to operate with single wavelength lasers, at any wavelength in the visible and in the infrared, but the design is optimized for specific wavelengths and polarizations (or unpolarized radiation). (If the wrong wavelengths or polarizations are used, then errors due to ghost images, spurious signals, and decreased fringe visibility may arise.) Visible and infrared versions of the FSI must employ different optical materials, optical coatings, and detectors. In practice, a hybrid unit has been built in which only the pivot plate (on which the triangular optical components are mounted), and detector are changed to convert from visible to infrared operation. The same alignment is maintained.

The infrared FSI employs a ZnSe beam splitter, a ZnSe shear plate, a BaF<sub>2</sub> imaging lens, and a HgCdTe detector system. It operates exactly like the visible models of the interferometers except that the detector is located at the eyepiece position (with which it can be rapidly interchanged) indicated in Fig. 1. The compact infrared detector, mounted in a dewar, employs a demand-flow nitrogen gas cryogenic system, which is rugged and very stable, highly sensitive, and

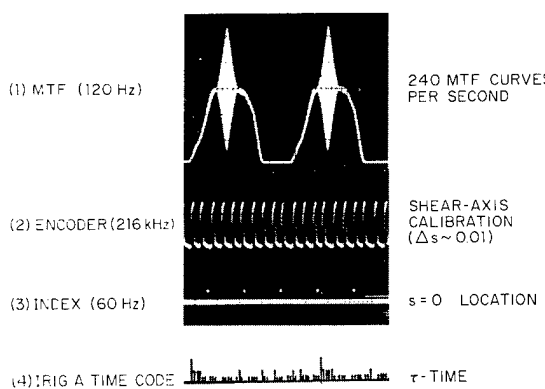


Figure 2. FSI signals recorded on tape.

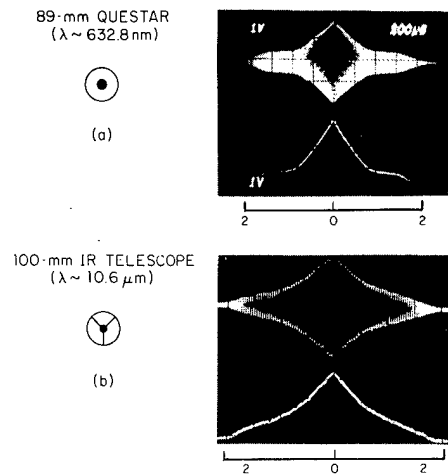


Figure 3. Real-time MTF display.

ready for operation within 30 sec of turning on the  $N_2$  supply. The signal from the infrared detector is fed to a matched preamplifier whose output can be looked at on an oscilloscope, or recorded on an FM magnetic tape recorder in the same way as the visible FSI. The recorded output MTF data from both visible and infrared versions of the FSI are treated in exactly the same way, and are first peak-detected electronically. In Fig. 3 MTF curves both before and after peak detection are shown for two different telescopes, one tested at 632.8 nm in the visible and the second at 10.6 microns. Thus real time MTF curves are immediately available and can be photographed from the oscilloscope. Rapid and accurate focusing of the telescope can be carried out in real time, and data taken directly from the oscilloscope, as shown in Fig. 4, where samples of MTF data from a fast defocus run are shown. This is particularly important where data, as is the case of propagation through the atmosphere is continually and rapidly changing. In certain experiments, a real time, on-line, signal averager can be used to smooth out rapid atmospheric fluctuations. The peak-detected data whether single scan or averaged MTF are then digitized and put into the computer.

#### White Light Operation

This particular technique to measure OTF functions in field environments has certain highly desirable properties. It is simple to operate, needs no internal alignment (it is a common path interferometer) over long periods of time (in terms of years), and essentially freezes out external vibrations because of the rapidity of scan and independence of the MTF envelope from the angle-of-arrival. The carrier frequency, which is determined by the pivot plate angle  $\Delta\theta$ , can be selected by a micrometer adjustment which rotates the pivot plate by an amount  $\Delta\theta$  (up to about  $\pm 4^\circ$ ). For a diffraction limited 89 mm diameter Questar telescope whose central obscuration is  $\alpha = 0.34$ , a series of MTF curves for increasing angles  $\Delta\theta$  of the pivot plate are shown in Fig. 5. The modulation envelope (which is the same for all angles of  $\Delta\theta$ —the only changes being in the carrier frequency), for the 4 right-hand curves (with low carrier signal frequency) is shown superimposed over them. The MTF (the modulation envelope) is independent of the carrier signal frequency, and the envelope is traced out by the peaks of the carrier signal.

Now consider the case where the light source is no longer a laser narrow band source, but a fairly wide band white light source. Providing the carrier signal frequency is kept very low (as on the right-hand side of Fig. 5) then the MTF can be obtained by tracing out the modulation envelope, with the second or third cycle (as the carrier signal frequency is changed by changing  $\Delta\theta$ , slowly turning the pivot plate). The condition (or tolerance) for doing this is easily calculated from Eqs. (2) and (3). Thus it is easily calculated that

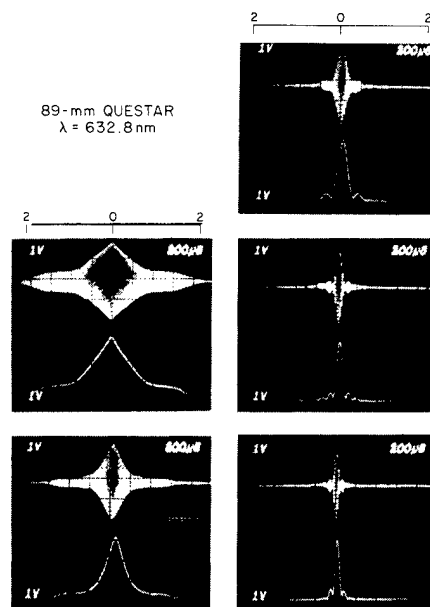


Figure 4. Fast defocus runs.

$$\frac{\Delta s}{s} = \frac{\Delta\delta}{\delta} = \frac{-1}{\mu} \cdot \frac{\Delta\mu}{(\mu - 1)} = \frac{-w}{\mu} \quad (4)$$

where  $\Delta\delta$  represents the maximum path length difference for the two wavelengths  $\lambda_1$  and  $\lambda_2$ , and  $\Delta s$  represents the maximum shear difference for the same two wavelengths. The bandwidth of the source light is  $\Delta\lambda = \lambda_2 - \lambda_1$  and  $\Delta\mu$  represents the variation in refractive index for the wavelengths  $\lambda_1$ ,  $\lambda_2$  of the glass of the shear plate—or more exactly  $w = \Delta\mu/(\mu - 1)$  is the dispersive power of the glass, which in practice should be chosen to be small. For a crown glass, taking  $w = 0.021$ , and  $\mu \sim 1.5$  the tolerance expression for Eq. (4) becomes

$$\frac{\Delta s}{s} = \frac{\Delta\delta}{\delta} = 0.014$$

This represents approximately a 1% error in both shear and path length. The effect of path length error contribution to an error in the MTF is now readily calculated from Eq. (1) as follows:

$$\frac{\Delta D(s, \phi)}{D(s, \phi)} = k \cdot \Delta\delta \cdot \sin k\delta$$

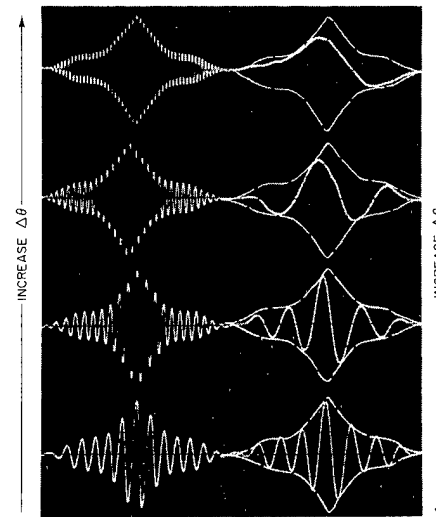


Figure 5. Variation of carrier frequency with pivot plate rotation ( $\Delta\theta$ ).

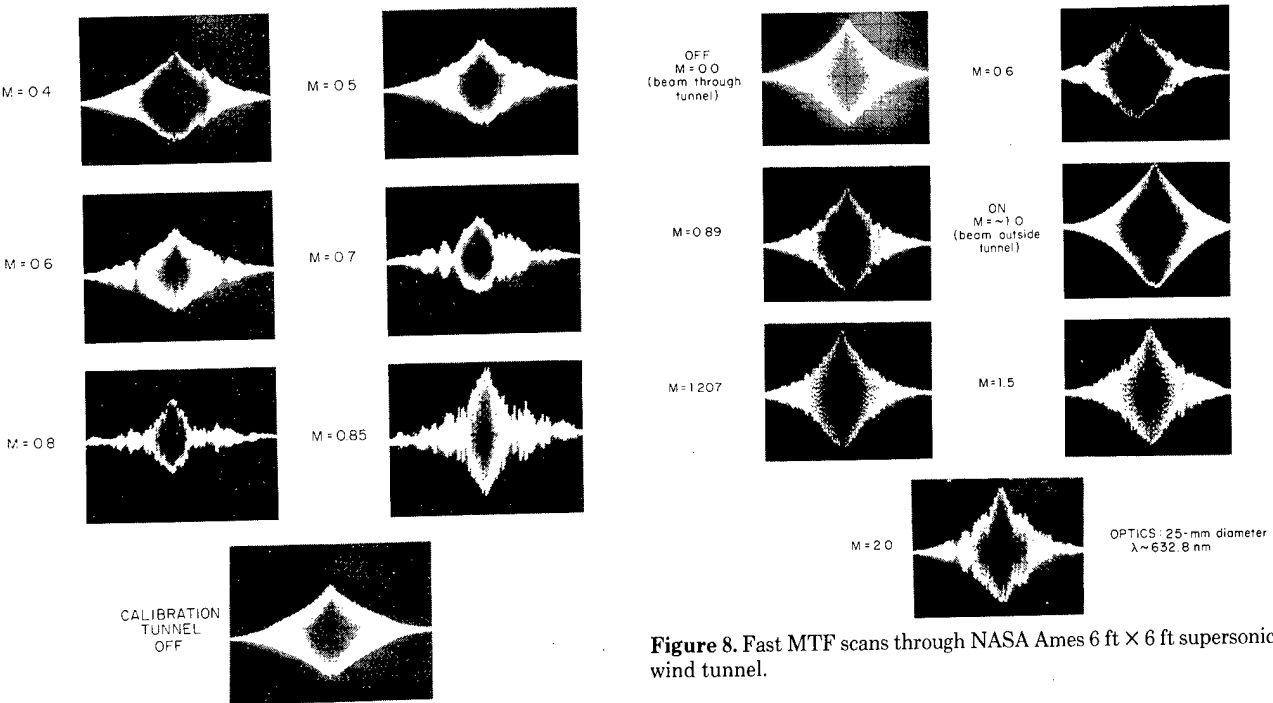


Figure 6. Fast MTF scans through NASA Ames 11 ft  $\times$  11 ft transonic wind tunnel.

where  $\Delta D(s, \phi)$  represents the error in the measured MTF. For example to estimate the error in the MTF due to this wide spectral source at  $s = 1$ , take the first cycle of the carrier signal (after the  $s = 0$  position) and assume this traces out the envelope of the MTF as it slides along the  $s$ -axis (as the carrier frequency changes). Putting  $\delta = 1 \lambda$ ,  $\Delta \delta = 0.014 \times \delta$  it follows that  $\Delta D(s, \phi) < 0.04$  (where for a circular aperture  $D(s, \phi) \leq 0.39$ ).

In this manner, the FSI system described here can be utilized, to look at star sources, in order to make MTF measurements through the earth's atmosphere. Some preliminary experiments have been carried out, but the intent here is

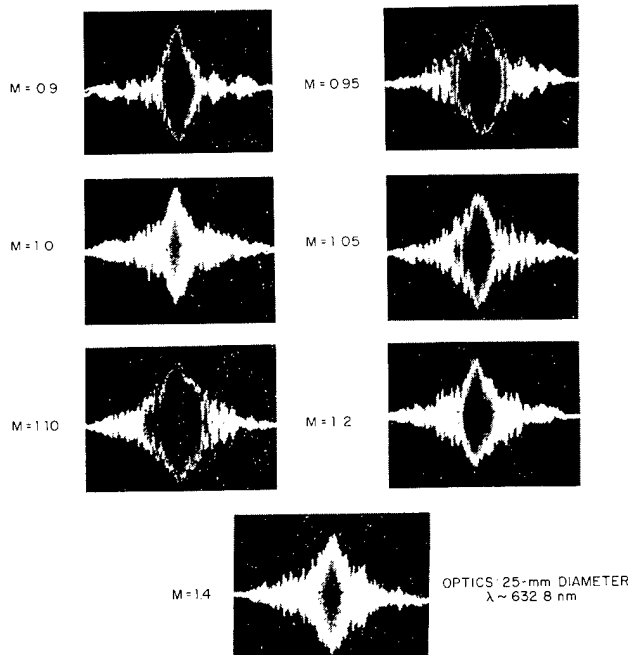


Figure 7. Fast MTF scan through NASA Ames 11 ft  $\times$  11 ft transonic wind tunnel.

Figure 8. Fast MTF scans through NASA Ames 6 ft  $\times$  6 ft supersonic wind tunnel.

simply to indicate how "white light" measurements can be made with this type of interferometer, and to indicate the accuracy of such measurements.

#### General Discussion

It has been recognized for many years that for optical systems there are several variables such as wavelength, best focal plane, field angle,  $F$  stop, for which the MTF must be measured. Not only does this imply that probably several hundreds of MTF curves are necessary for any one optical system, but in order to handle such a large amount of measured data, a compatible computing capability, coupled with rapid, continuous measurement, and large data handling capability are necessary.

While emphasis has been previously placed on "white light" measuring systems in the past, since "white light" in practice depends on the spectral composition (both of the sources, the transmission path, and the receiver), it is often more logical to measure the single spectral MTF over all wavelengths, and then compute "white light" performance according to the desired spectral composition for each case. The FSI interferometer discussed above, was primarily developed for use with single wavelength laser radiation.

In order to demonstrate the performance of the FSI in obtaining MTF data under adverse field conditions, a brief outline of two experiments to measure the optical degradation caused by a turbulent airflow is discussed.

The purpose in showing only samples of data from different experiments here is to give simply representative viewpoints of the types of measurements and methods of data reduction that are presently being employed. There is no intention here of reporting on these experiments, and therefore no details of this work are included here. Some data taken in wind-tunnel experiments, and on a Lear Jet airplane in flight will be outlined below.

#### MTF Measurements in Wind Tunnels

In an experiment to examine the optical characteristics of a 25-mm diameter HeNe laser beam passing through a wind tunnel, MTF measurements were made using the FSI system, as the operating conditions of the wind tunnel (changing airflow speed and the associated Reynolds number) were varied. Data for two different tunnels (a) the NASA-Ames 11 ft  $\times$  11 ft transonic tunnel and (b) the NASA-Ames 6 ft  $\times$  6 ft su-

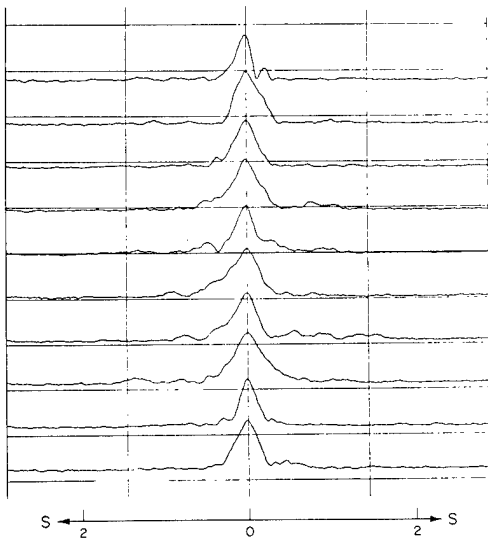


Figure 9. Computer write and average program output, wind-tunnel boundary layer, MTF measurements. (Turbulence generator: NASA PINS) (89-mm optics, 632.8 nm, M 0.9,  $R \sim 4 \times 10^6$ .)

personics wind tunnel are shown in Figs. 6-8 for a range of Mach number (airflow speeds) from zero to 2.0. The MTF measurements shown are single scan runs (showing 2 MTF curves back-to-back taken in less than 2 msec), and it is clear that while the turbulence in the tunnel is instantaneously "frozen" during the measurement, the temporal variations (over 1 msec time frames) are readily observed. In these runs the 6 ft  $\times$  6 ft tunnel is seen to have better imaging properties than the 11 ft  $\times$  11 ft tunnel. The performance of the 11 ft  $\times$  11 ft tunnel was seen to be poorest between 0.7 and 0.8 Mach numbers and then improved for higher airflow speeds.

In practice these data after being recorded on magnetic tape are processed by computer first to print out a series of MTF data and to take averages. A sample of the write and average program output for an MTF measurement conducted in the 6 ft  $\times$  6 ft wind tunnel is shown in Fig. 9. These printouts of 20 consecutive MTF curves shown here, allow a "quick-look" evaluation of the recorded MTF data. In the same format, averaged MTF data are also printed out. We may then select any samples of these data, and have the computer printout any individual MTF curve, compare it with a calibration curve or a series of other data measured as shown in Fig. 10, where

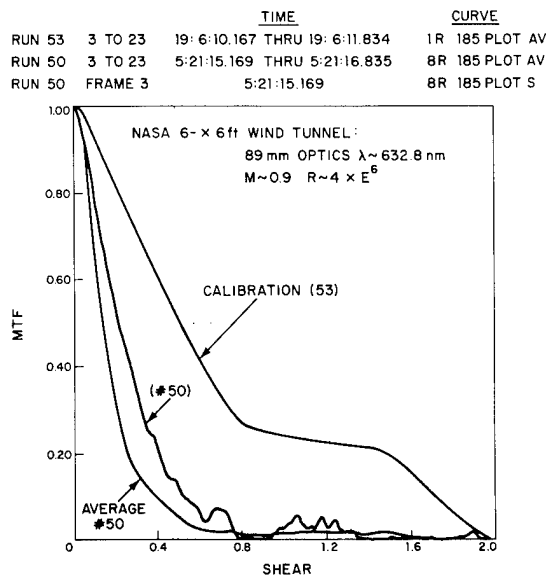


Figure 10. Computer MTF plots.

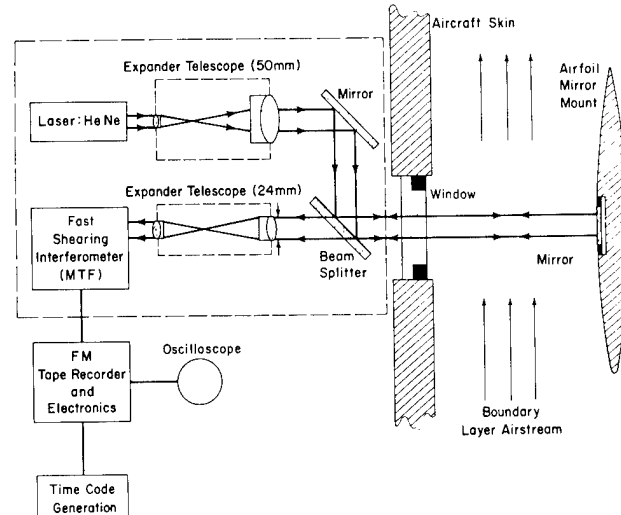


Figure 11. Optical schematic Lear jet experiment.



Figure 12. Lear jet with airfoil on side.

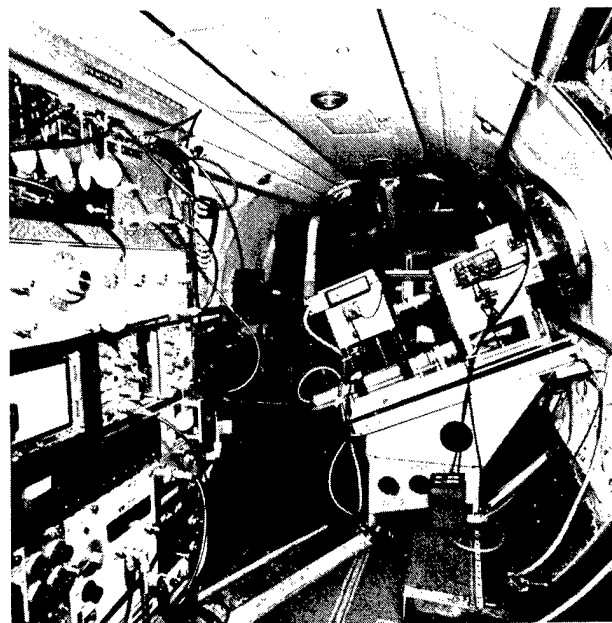


Figure 13. FSI inside Lear jet.

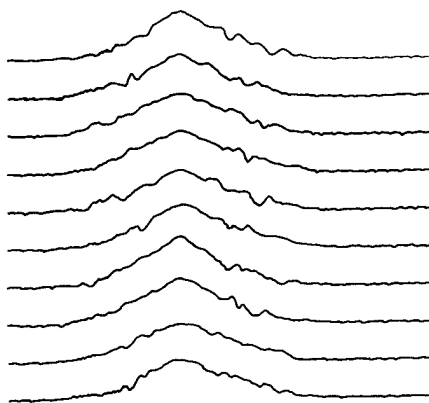


Figure 14. Lear jet fast scan MTF data Fr time 12:42:22.419.

a single scan, an averaged, and a calibration curve are compared. The computer keeps track of the time the data were taken, and prints out this information. In this way, a very large amount of data can be handled, processed and compiled.

#### MTF Measurements in a Lear Jet Airplane

In an experiment to explore the airflow near the skin of an airplane, the FSI was mounted in a Lear Jet aircraft and an airfoil mounted outside a window in the airstream to hold a small mirror about 25 cm away from the skin. An optical schematic (Fig. 11) shows how the optical degradation in the boundary layer airstream between this mirror and the aircraft window can be examined, obtaining MTF measurements. The diameter of the optical beam in this case was 24 mm. A photograph of the Lear Jet airplane is shown in Fig. 12 in which the airfoil mounted outside the window, located near the entry door can just be seen. The mounting of the FSI and the optics for the autocollimation system, and laser source are shown in Fig. 13. The electronics are mounted in the rack on the left.

The flight conditions could be varied, and the effect on the MTF could be observed in real time, focus adjustments quickly and accurately made, as well as recorded data being obtained for later data analysis. For Run 20 for example, two samples of single scan MTF data are shown in Figs. 14 and 15 (the flight conditions for this run (# 20) are indicated in Fig. 16) plotted out by the computer. In Fig. 14, only a small degradation of the MTF was observed, but in Fig. 15 only 1.416 sec later (see the time printouts) a very large degradation was observed—even though no change in flight conditions occurred. The highest MTF data for any given flight condition could be readily chosen (selecting a frame, and line number from print outs such as in Fig. 14), and the resultant curve printed out by the computer on a larger scale, as shown in Fig. 16 in which selected curves for 7 different flight conditions are

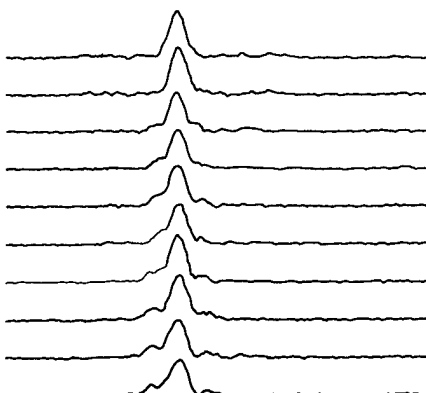


Figure 15. Lear jet fast scan MTF data Fr time 12:42:23.835.

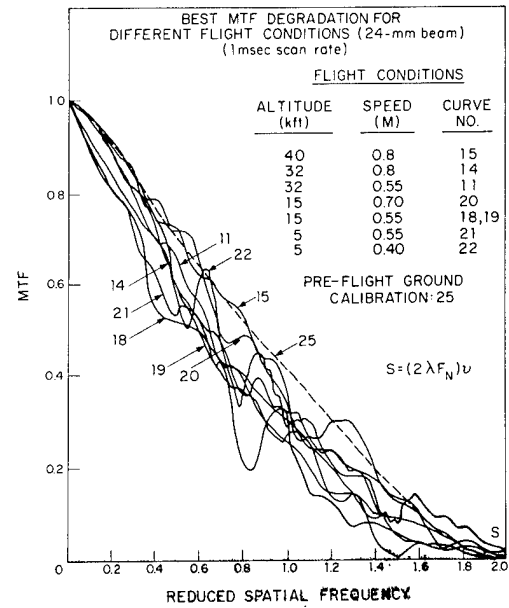


Figure 16. Lear jet-MTF boundary layer measurements: Flight 5L.

shown compared to one another. In the same manner, averages of 50 single scan curves were taken by the computer and a series of averaged MTF curves for the same flight conditions as in Fig. 16 are shown in Fig. 17.

In these two experiments outlined above, it was essential to have real time and very rapid presentation of MTF data and to be able to check alignment and adjust for best focus (this takes literally just one or two seconds) during the course of the experiments. Selected intervals of good data could then be recorded for later data reduction and analysis. Once the data have been inputted to the computer, statistical analysis, Fourier transforms, fluctuation spectra, etc., are readily obtained.

#### Conclusion

The fast scanning interferometric technique has been used for making many MTF measurements in a field environment, for a number of different experiments, providing a large amount of reliable and accurate data. A brief review of its general properties, and two examples of experiments recently

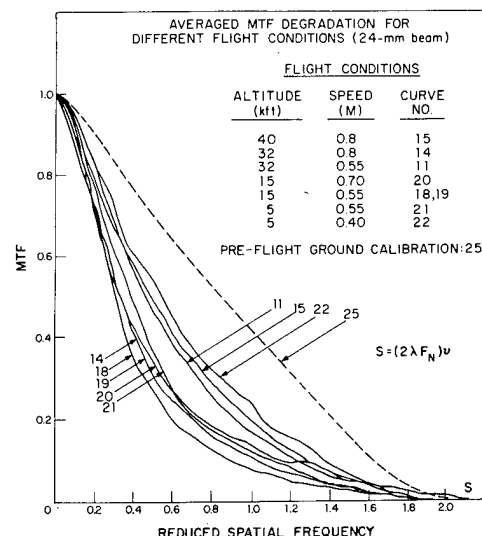


Figure 17. Lear jet-MTF Boundary layer measurements: Flight 5L.

carried out have been described here. While the main use for which it has been used in our case has been to explore the characteristics of turbulent atmospheric airflow, making MTF measurements, and using laser single wavelength sources, it can have a much wider use in the optical field. Complete OTF measurements can be made, it can be used with multiple wavelength lasers, or white light sources, and can provide very accurate and rapid angle-of-arrival measurements. On-line signal processing electronics can be readily employed, and it is very suitable for subsequent computer data processing of the measured data, generating and handling a very large amount of data in a short time. Accuracy of the MTF data—providing accurate alignment of all the external optics and systems (under test) is carried out—is about  $\pm 1\%$ . Thus it would appear that it would be very useful if adapted to an automated optical lens test facility, where a wide range of MTF data must be measured, reduced and analyzed, almost instantly—or at least in the order of seconds or minutes—for a large range of optical parameters.

**Acknowledgments.** Much of the work discussed here has

involved a great deal of help and effort in the laboratory, by the data analysis facility, and by Lincoln Laboratory field site personnel in carrying out field measurements in wind tunnels and on the Lear Jet airplane. I am indebted in particular to J. R. Theriault, E. J. Casazza in the laboratory, and to D. A. Page and Dr. L. D. Weaver at the field sites.

## References

1. K. Rosenhauer and K. J. Rosenbruch, *Reports on Progress in Physics* **30** (1): 1(1967).
2. K. Murata, *Progress in Optics* **V**: 201(1966).
3. See *Proc. SPIE*, **46**: 59-84(1974).
4. H. H. Hopkins, *Opt. Acta* **2**: 23(1955).
5. L. R. Baker, *Proc. Phys. Soc.* **B68**: 871(1955).
6. D. Kelsall, *Proc. Phys. Soc.* **73**: 465(1959).
7. P. Hariharan and D. Sen, *Proc. Phys. Soc.* **75**: 434(1960).
8. T. Tsurata, *J. Opt. Soc. Am.* **53**: 1156(1963).
9. A. J. Montgomery, *J. Opt. Soc. Am.* **54**: 191(1964).
10. W. H. Steel, *Opt. Acta* **11**: 9(1964).
11. J. C. Wyant, *Appl. Optics* **14**: 1613(1975).
12. D. Kelsall, *J. Opt. Soc. Am.* **63**: 1472(1973).
13. D. Kelsall, *Appl. Optics* **12**: 1398(1973).
14. D. Kelsall, *Proc. SPIE* **46**: 124(1974).

# Coherent Optical Radar

R. H. KINGSTON

The term, "optical radar," seems at first to be a misnomer, since "radar" (radio detection and ranging systems) was coined to describe systems using radio frequency or microwave radiation. In truth, however, if we allow the *ra* to stand for electromagnetic radiation, we would note that the first radar experiment was carried out in 1849. In that year Fizeau, using a light beam passing through a cogged wheel, measured the time delay over an 8.6-km path by reflecting the beam off a mirror at the end of the path and adjusting the wheel speed to obtain maximum transmission of the return beam through the adjacent cogged opening. Actually, Fizeau was measuring not range but the velocity of light, which he determined to within five per cent of the currently accepted value. In any event, this is still the earliest recorded experiment using pulsed electromagnetic radiation to measure the time delay over an extended distance. Despite these early beginnings, the use of light for range measurements has been limited. One of the few applications that comes to mind is the measurement of cloud heights by using a pulsed flashlamp. All of which brings us to the key word in our title, "coherent."



Obviously, coherent optical radar refers to lasers, but what is the true significance to radar operation of this coherent nature of laser radiation? The answer is twofold, and it involves two distinct kinds of co-

herence, *spatial* and *temporal*. It is the spatial coherence of the laser that first made optical radar an attractive range-measuring device. The reason, by analogy to the microwave case, is the high "antenna gain" available from a near-diffraction-limited optical wave. Put another way, the laser radiation is limited to a small number of *spatial* modes of the electromagnetic field, whereas incoherent or thermal radiation occupies all available modes, as we learned in the derivation of Planck's radiation law. As a result, coherent optical energy can be collimated into a beam of diameter  $d$ , whose angular spread in the far field may be as small as  $\lambda/d$ . In contrast, the energy in a diffraction-limited beam from a thermal source is roughly the energy emitted from an area,  $\lambda^2$ , of the hot radiating medium. The result of this extreme brightness is the feasibility of optical ranging on satellites and on corner reflectors placed on the moon.<sup>1</sup>

We now consider the second type of coherence, *temporal*. Spatial coherence is measured in terms of the approach to diffraction-limited behavior; temporal coherence is measured in terms of the coherence time or its inverse, the spectral linewidth. Most solid lasers have relatively short coherence times, on the order of nanoseconds or less, since many different frequency modes of the laser cavity are excited because of the broad spectral bandwidth of the laser transition. These frequency modes usually satisfy the resonance criterion of an integral number of half wavelengths over the cavity length, and they may supply energy to the same spatial mode. Single-frequency operation is either impossible or extremely low in efficiency. The broad frequency distribution of the modes can be used to advantage, however, if the modes are "locked." In this technique, either internal nonlinear effects or external modulation at the mode-separation frequency (the spectral-free range) of

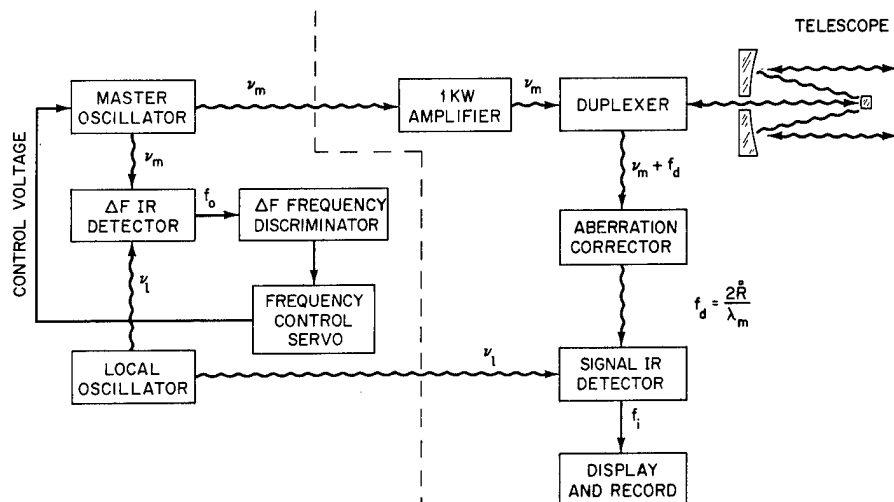


Figure 1. Block diagram of laser radar system. Solid lines are electrical paths; wavy lines, optical.

the cavity causes a coupling of the modes such that the electric field in all modes adds up coherently at one point in time and space. The resultant power output is a series of extremely narrow pulses of length equal to the reciprocal of the spectral bandwidth. Pulse lengths in the picosecond range, equivalent to a fraction of a millimeter, have been generated in this manner.<sup>2</sup>

The multifrequency behavior still limits the detection system to a measurement of the return energy, not the amplitude and phase of the reflected wave, as in microwave radar systems. This ability to detect "coherently," that is, to measure amplitude and phase, is essential for measurement of target velocity by the Doppler effect and also yields orders-of-magnitude improvement in sensitivity in the infrared, where simple "photon counters" or incoherent detectors are not only inefficient but also suffer from solar scatter and thermal-background energy interfering with the desired signal. Fortunately, the carbon dioxide laser, operating at a wavelength of  $10.6 \mu\text{m}$ , has ample power output for radar use and also may be operated at a single very stable frequency. In addition,

highly efficient broadband detectors<sup>3</sup> are available for coherent detection of the return signal. In fact, this paper is devoted to a discussion of such a *coherent* radar, where we use the term to indicate that the amplitude and phase of the return wave are measured by the detection system.

The coherent detection technique, also called heterodyne detection, is based on the beat frequency obtained between an optical local oscillator and the signal, both of which strike the detector. Photodetectors in general produce an output current (or voltage) proportional to the incident optical power. The detector current,  $i_d$ , is thus given by

$$i_d : E^2,$$

where  $E$  is the optical electrical field. In incoherent detection, the detected current from the signal competes with the "shot" noise associated with the photon-counting process as well as with noise generated in the following amplifier stages. In coherent detection, the current is again proportional to the square of the electrical field, but in this case we may write

$$i_d : E^2 = (E_s + E_{lo})^2 \\ = E_s^2 + 2E_{lo}E_s + E_{lo}^2,$$

where  $E_s$  and  $E_{lo}$  are the signal

The author is with the Lincoln Laboratory, Massachusetts Institute of Technology, Lexington, Massachusetts 02173.

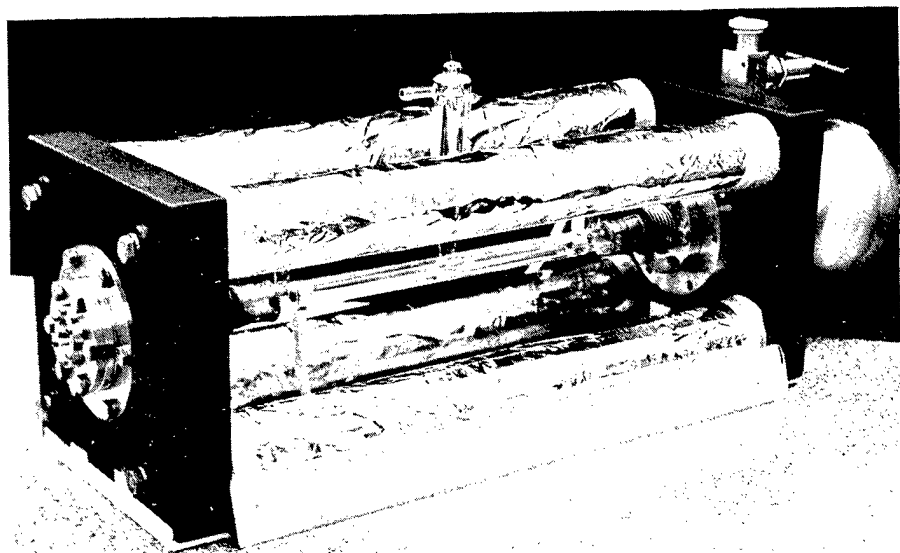


Figure 2. Stable CO<sub>2</sub> laser oscillator. Granite end plates and shielded super-invar spacer rods yield excellent stability. The spherical gas reservoir allows sealed-off operation for several months.

and local oscillator fields. Now  $E_{lo}$  is much greater than  $E_s$ , so that the important terms are  $E_{lo}^2$ , which produces a dc current plus a current fluctuating at twice the local-oscillator frequency, and  $2E_{lo}E_s$ , which is a current at the intermediate or difference frequency plus a current at the sum of the signal and local-oscillator frequencies. The two currents at the optical frequencies may be ignored; the dc term from  $E_{lo}^2$  is the limiting shot-noise source, and the intermediate frequency term is an *exact* replica in amplitude and phase of the signal wave but displaced in frequency to the rf part of the spectrum. Since the intermediate frequency current is proportional to the local oscillator field, the local-oscillator power may be raised to a level such that noise in the following amplifier stages is negligible compared to the fundamental shot-noise produced by the local oscillator. The output signal-to-noise power is given by  $P_{sig}/hvB$ , where  $B$  is the spectral bandwidth of the optical signal and, by the heterodyne process, the rf bandwidth of the intermediate frequency output power. A detailed analysis<sup>4</sup> shows that such a coherent detection system also couples to only one spatial mode of the electromagnetic field. Put another way, the receiver

beamwidth with an aperture of diameter  $d$  is approximately  $\lambda/d$ .

### THE RADAR SYSTEM

The carbon dioxide laser radar system we shall describe combines modern laser and detector technology with astronomical concepts, some dating back to previous centuries. Figure 1 is a schematic diagram showing the major components of the system. The master and local oscillators are the key to coherent operation of the system, since they are highly stable, single-frequency lasers<sup>5</sup> of the type shown in Fig. 2. The two oscillators are offset in frequency by 10 MHz, the local oscillator used as a reference standard, and the master oscillator slaved by a frequency-discriminator servo loop, which drives a piezoelectric cavity tuner in the laser. The local oscillator best serves as the stable reference, since its required output power, less than a watt, permits a compact laser design, while backscatter from the detector system, which can cause frequency pulling, is minimal. In contrast, the master oscillator must supply 10 W to the amplifier, thus necessitating a larger and more vibration-sensitive structure; backscatter from the active amplifier could cause serious frequency shifting if the laser were not exter-

nally stabilized. Since the output frequency from the detector is the difference between the signal and the local-oscillator frequencies, the 10-MHz offset is convenient for observing stationary targets for calibration purposes. The detector sensitivity,  $10^{-19}$  W/Hz, is within a factor of 5 of the theoretical value,  $hv$ . This means that, for a 1-msec pulse, requiring a 1-kHz bandwidth, the minimum detectable power is  $10^{-16}$  W. An incoherent detector at this wavelength, measuring only the pulse envelope, would require 100 times as much power for the same output signal-to-noise ratio. This marked advantage of the coherent detector results from the internal conversion gain discussed previously. Only at wavelengths of 1  $\mu$ m or shorter are equivalent internal detector gains available by using either photomultipliers or avalanche photodiodes.

Figure 3 is a cutaway view of the radar system showing the stable oscillators in acoustically shielded boxes with the 1-kW amplifier in the background. This latter device is a low-pressure flowing gas laser which amplifies continuously, raising the master oscillator power from 10 W to powers from 100 to 1000 W.<sup>6</sup> The duplexer, in the circular housing just at the output of the amplifier, is somewhat akin to Fizeau's cogged wheel in that it is a slotted rotating disk, which transmits the laser beam 25 per cent of the time, and the remainder of the time reflects the signal onto the detector. Before striking the detector, the received wave is reflected from a computer-controlled mirror, designated the aberration corrector. When one observes satellites with this system, the velocity of the target is such that the transmit beam must *lead* in angle by an amount  $v/c$ , and, on reception, the viewing path must *lag* by another increment  $v/c$ , where  $v$  is the velocity normal to the line of sight. Thus, if the radar system has been boresighted on a stationary target, the aberration corrector must cause the

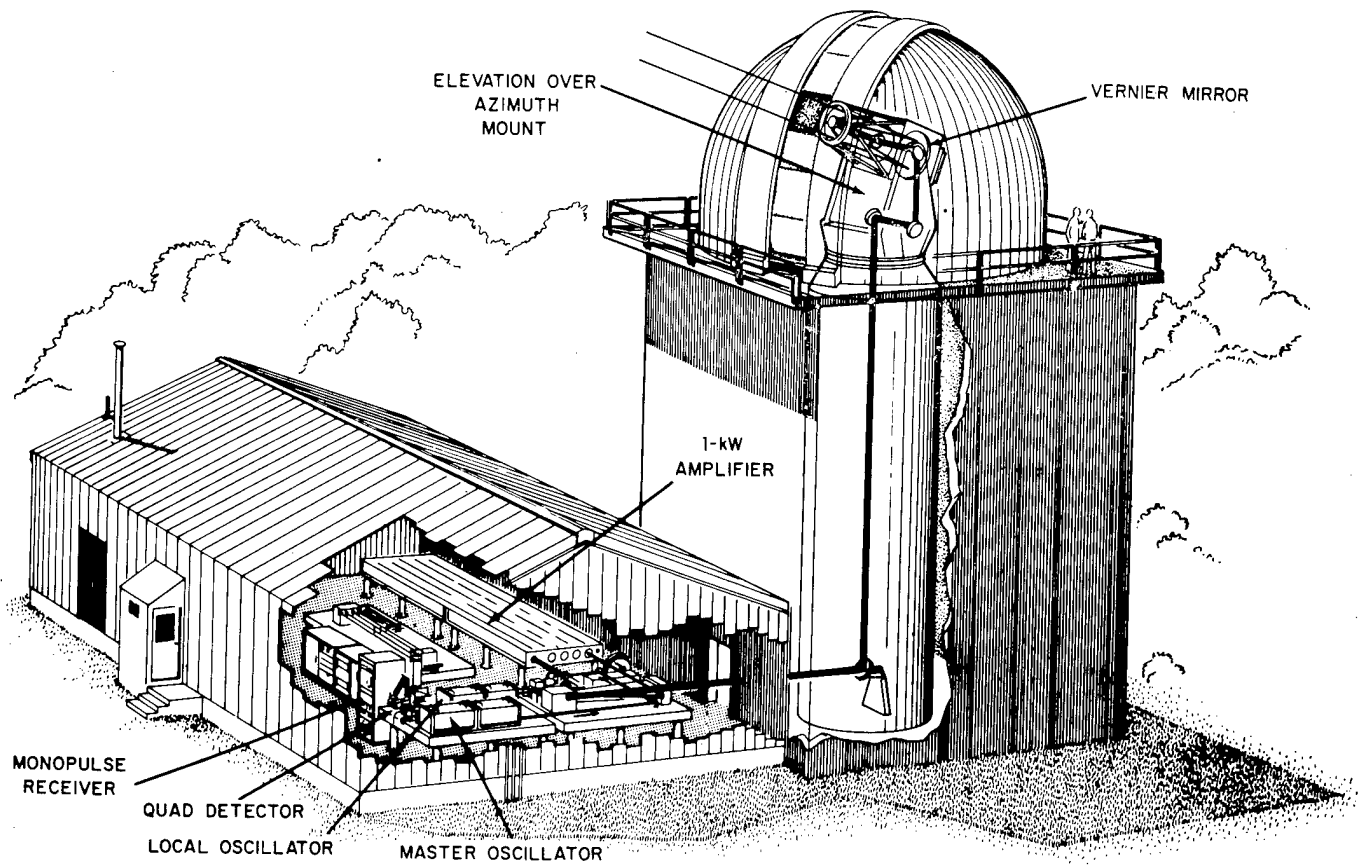


Figure 3. Cutaway view of radar system. The afocal telescope has a 1.2-m primary and 15-cm secondary.

receive path to deviate by  $2 v/c$  to maintain boresight on a moving object. In the case of a satellite,  $2 v/c$  has a value of approximately 50  $\mu\text{rad}$  at the point of closest approach. Since the transmitter-receiver half-power beamwidth is 10  $\mu\text{rad}$  for the 1.2-m-aperture telescope, the aberration correction is essential for most satellite observations. It is interesting that this aberration effect was used in 1725 by Bradley in an early measurement of the velocity of light before Fizeau's work. In Bradley's case, the observer (the earth in its orbit) was moving with respect to the stationary stellar source.

## SOME EXPERIMENTAL RESULTS

Our radar system has been used to make observations on GEOS-III, a NASA geodetic satellite equipped with a solid-cube corner retroreflector fabricated from Irtran II. This point source has been used to de-

termine the tracking capability of the radar as well as the frequency stability of the lasers and the associated velocity, or Doppler-measuring precision. For precision tracking, error signals from the quad detector indicated in Fig. 3 are used to drive the vernier mirror shown at the telescope elevation axis. The main mount is driven by a computer-smoothed input from a local microwave radar, which has an angular fluctuation of the order of 50  $\mu\text{rad}$  or 5 optical beamwidths. Using the error-sensing technique in Fig. 4, one can reduce the angular fluctuation or tracking precision to approximately 1  $\mu\text{rad}$ , or one tenth the beamwidth.<sup>7</sup> The target-return beam pattern is shown distorted to represent the effects of the atmosphere, the dominant one being wavefront tilt or angle-of-arrival fluctuations. In fact, for astronomical "seeing" of 2 arc sec or 10  $\mu\text{rad}$ , the atmospherically induced angle fluc-

tuations are of similar magnitude, that is, close to a full beamwidth in our system. Since the frequency content of the angular fluctuation, determined by the angular track rate and the local winds, is mostly below 10 Hz, the detection system can track out these slow changes and maintain the radar beam on the target. At the same time as this precision angle measurement is being made, Doppler data from the target can be processed to determine the radial velocity. Since the Doppler shift is 2 kHz per cm/sec and typical satellite velocities are 8 km/sec, the frequency shift may be over 1000 MHz for low elevation angles, with the shift passing through zero at the closest approach point. The output spectra for a sequence of pulses is shown in Fig. 5. These data were taken near closest approach at a Doppler shift of 64 MHz, a range of 1006 km, and a pulse length of 4 msec. By orbit fitting, the main frequency

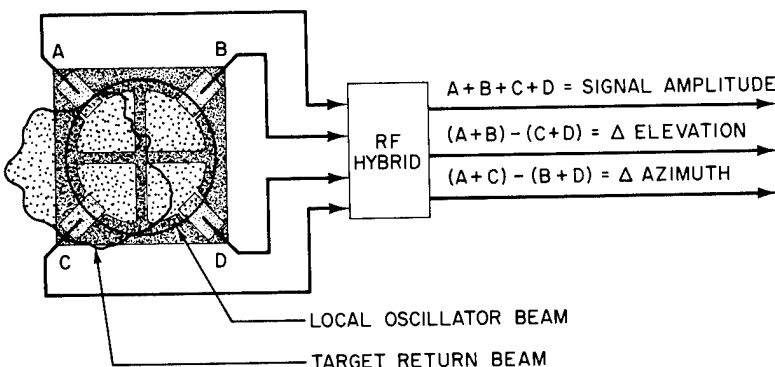


Figure 4. Quadrant or monopulse detector array. The circular mercury cadmium telluride structure has a diameter of 0.3 mm.

shift has been removed and the residual, 8 kHz or 4 cm/sec, is the absolute velocity error for the orbit segment observed. It should be noted that, at this point in the satellite path, the radial velocity is changing rapidly and the Doppler frequency changes at 10 MHz/sec. Thus, during the 4-msec pulse, the frequency shifts by 40 kHz. This shift is also removed in the data processing so that the individual spectra, which are plotted on a log scale, should ideally be the transform of a square single-frequency pulse, or a  $(\sin x/x)^2$  function, and should be fixed in center frequency. System and laser oscillator stabilities actually result in an rms jitter of about 250 Hz and a spectral spread roughly twice the theoretical value of 500 Hz at the first minima.

This jitter, however, corresponds to a velocity precision of 1.25 mm/sec, a rather impressive value. It is, in fact, interesting to turn the problem around and use the radar as a way of measuring short-term laser stability.<sup>8</sup> Although stabilities may be measured by beating two lasers together, the independence of the individual frequency fluctuations is always in question. Using the radar, one actually observes the beat between the reference stable laser and itself with an interposed delay of the round-trip time to the target, in our example here, of 6.7 msec. The experiments thus establish that the laser short-term stability is of the order of one part in  $10^{11}$ , since the oscillator frequency is  $3 \times 10^{13}$  Hz.

### CONCLUSION

One topic we have not discussed is the ranging capability of our radar, which is limited by the long transmitted pulse to precisions of the order of hundreds of kilometers, commensurate with the millisecond waveform length. Although we might obtain much better range measurements with a shorter pulse, the peak-power limit from the amplifier, about 10 kW, would result in poor sensitivity, since coherent radar sensitivity is determined by the energy per pulse. Put another way, the shorter the pulse at the same power level, the broader the required receiver bandwidth and the greater the competing noise. Fortunately, there is a convenient way to obtain excellent

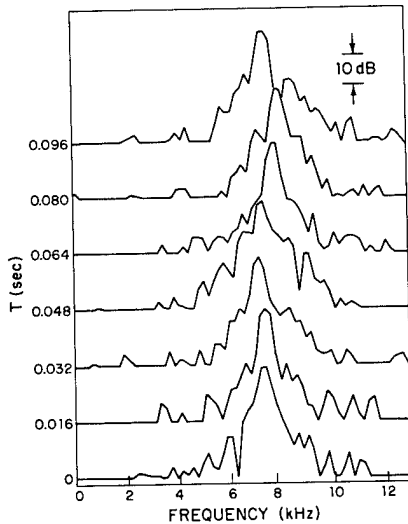


Figure 5. Frequency spectra for several received pulses. The vertical scale is logarithmic.

range precision with a long transmitted pulse by taking advantage of the coherent nature of the radar. This technique, known as "chirp" radar, uses a linear fm sweep of the transmit frequency during the pulse. By suitable processing of the return swept signal, either in a dispersive network or by cross-correlation techniques, the range may be measured to a time accuracy roughly equal to the inverse of the frequency-sweep width.<sup>9</sup> As an example, a 500-MHz-wide chirp yields a range precision of approximately 30 cm. Of course, to obtain such performance requires a laser amplifier with commensurate bandwidth. Our present device is limited to about 50 MHz because of the low gas pressure. Such devices as the waveguide or capillary laser<sup>10</sup> operate at higher pressures, and the resultant line broadening, 500 MHz at 100 Torr, should yield adequate bandwidth for precision ranging.

This work was sponsored by the Advanced Research Projects Agency of the Department of Defense.

### REFERENCES

1. W. Koechner, *Solid State Laser Engineering* (Springer-Verlag, New York, 1975) p. 559.
2. A. J. DeMaria, W. H. Glenn, M. J. Brienza, and M. E. Mack, Proc. IEEE **57**, 2 (1969).
3. D. L. Spears, *Infrared Phys.* **17**, 5 (1977).
4. A. E. Siegman, Proc. IEEE **54**, 1350 (1966); R. J. Keyes and R. H. Kingston, *Phys. Today*, **25**, 48 (1972).
5. C. Freed, *IEEE J. Quantum. Electron.* **QE-4**, 404 (1968).
6. P. A. Miles and J. W. Lotus, *IEEE J. Quantum. Electron.* **QE-4**, 811 (1968).
7. R. Teoste, W. J. Scouler, and D. L. Spears, "Coherent Tracking with a 10.6  $\mu\text{m}$  Radar," 1977 IEEE/OSA Conference on Laser Engineering and Applications, Washington, D.C. (June 2, 1977).
8. T. R. Gurski, *J. Opt. Soc. Am.* **66**, 1133A (1976).
9. W. E. Bicknell, L. R. Tomasetta, and R. H. Kingston, *IEEE J. Quantum. Electron.* **QE-11**, 308 (1975).
10. M. B. Klein and R. L. Abrams, *IEEE J. Quantum. Electron.* **QE-11**, 609 (1975).

# Advances in CO<sub>2</sub> Laser Stabilization Using the 4.3 μm Fluorescence Technique\*

Charles Freed and Robert G. O'Donnell  
M.I.T. Lincoln Laboratory, Lexington, MA, USA

Received: November 17, 1976

## Abstract

Significant improvement in signal-to-noise ratios is achieved with new, low pressure CO<sub>2</sub> stabilization cells external to the lasers. A time domain fractional frequency stability of  $\sigma_y(\tau) \simeq 6 \times 10^{-12} \tau^{-1/2}$  was measured with independently line-center locked 1.5 metre grating controlled CO<sub>2</sub> lasers. Accurate, repeatable determination of pressure shift is demonstrated.

## Introduction

At the 1976 Boulder Conference on Precision Electromagnetic Measurements we described [1] the absolute frequency calibration of CO<sub>2</sub> isotope laser transitions with the two channel laser heterodyne system shown in Figure 1. This paper will discuss the stabilization technique and the frequency stability achieved with the equipment indicated in Figure 1.

It was previously shown [2, 3] that CO<sub>2</sub> lasers can be frequency stabilized by using the standing-wave saturation resonances in a low-pressure, room-temperature, pure CO<sub>2</sub> absorber via the intensity changes observed in the collisionally-coupled spontaneous emission band at 4.3 μm. It was also demonstrated that the frequency shift due to changes in pressure is very small in CO<sub>2</sub>, typically about 100 Hz/mTorr.<sup>†</sup>

In the initial experiments, a short gas cell with a total absorption path of about 3 cm was placed inside the cavity of each stable CO<sub>2</sub> laser [3, 4] with a Brewster angle window separating the cell from the laser gain tube. Pure CO<sub>2</sub> gas at various pressures was introduced inside the sample cell. A sapphire window at the side of the sample cell allowed the observation of the 4.3 μm

spontaneous emission signal with a liquid-nitrogen-cooled InSb detector. The detector element was about 1.5 cm from the path of the laser beam in the sample cell. In order to reduce the broadband noise caused by background radiation, the detector placement was chosen to be at the center of curvature of a gold-coated spherical mirror which was internal to the gas absorption cell. Essentially identical experimental arrangements of CO<sub>2</sub> lasers, internal absorption cells, and InSb 4.3 μm fluorescence detectors have been used in more recent experiments by Petersen *et al.* [5] Meyer and Rhodes [6] and also by Woods and Joliffe [7] who used similar but external absorption cells.

## Signal-to-Noise Ratio at 4.3 μm

In the CO<sub>2</sub> isotope calibration system shown by Figure 1, we use improved CO<sub>2</sub> stabilization cells external to the lasers.

In the new design, the low pressure gas cell, the LN<sub>2</sub> (liquid nitrogen) cooled radiation collector, and the IR detector are all integral parts of one evacuated housing assembly. This arrangement minimizes signal absorption by windows and eliminates all other sources of absorption. Because of the vacuum enclosure, diffusion of other gases into the low-pressure gas reference cell is almost completely eliminated; therefore, the time period available for continuous use of the reference gas cell is greatly increased and considerably less time has to be wasted on repumping and refilling procedures. One LN<sub>2</sub> fill will last at least 24 hours. Figure 2 schematically illustrates the new external reference gas cell used in the 4.3 μm fluorescence stabilization loop.

With the new cells significantly larger signal collection efficiency is achieved simultaneously with a great reduction of noise due to background radiation, which is the primary limit for high-quality InSb photovoltaic detectors. We have evaluated and tested several large area InSb detectors and determined that LN<sub>2</sub>-cooled background greatly diminished 1/f noise in addition to the expected reduction in white noise due to the lower

\* This work was sponsored by the Advanced Research Projects Agency of the Department of Defense and in part by U.S. Energy Research and Development Administration

† 1 Torr = 1 mmHg = 101325/760 pascal (Pa).

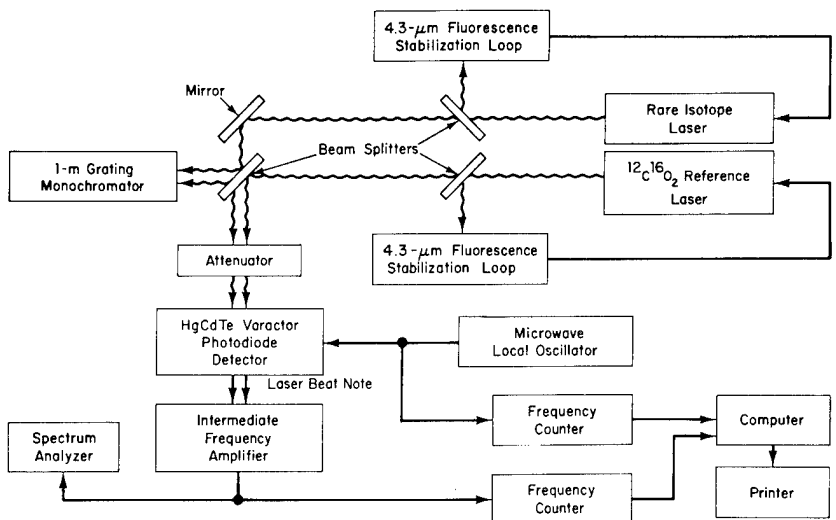


Fig. 1. Two-channel heterodyne system used to determine  $\text{CO}_2$  isotope laser frequencies

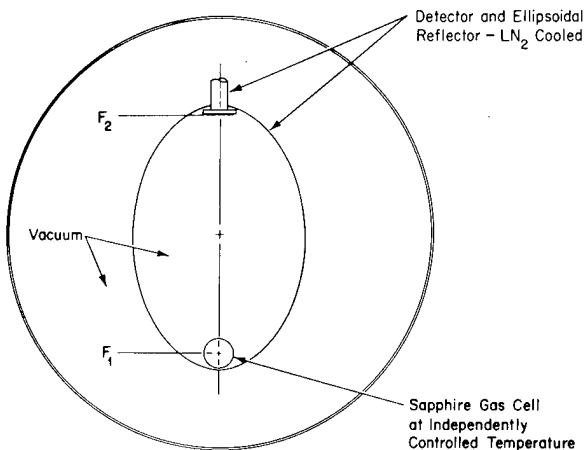


Fig. 2. Schematic illustration of the new external  $\text{CO}_2$  reference gas cell

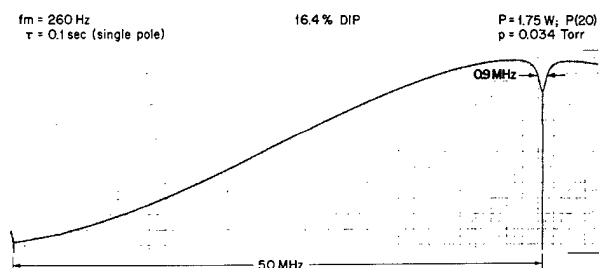


Fig. 3. Recorder tracing of the  $4.3 \mu\text{m}$  intensity change signal as a function of laser frequency tuning in the  $\text{P}(20)$  transition at  $10.59 \mu\text{m}$

temperature background radiation. In comparison with previously published results, we obtained more than two orders of magnitude improvement of the signal-to-noise ratio in measuring the  $4.3 \mu\text{m}$  fluorescence.

Figure 3 shows a typical recorder tracing of the observed  $4.3 \mu\text{m}$  intensity change as the laser frequency

is tuned across the  $10.59 \mu\text{m}$   $\text{P}(20)$  line profile with 0.034 Torr pressure of  $\text{CO}_2$  absorber gas. The standing wave saturation resonance appears in the form of a narrow resonant 16.4% "dip" in the  $4.3 \mu\text{m}$  signal intensity. The broad background curve is due to the laser power variation as the frequency is swept within its oscillation bandwidth. Since collision broadening in the  $\text{CO}_2$  absorber is about 7.6 MHz/Torr FWHM) (full width half maximum), [2, 6] in the limit of very low gas cell pressure the linewidth is determined primarily by power broadening and by the molecular transit time across the diameter of the incident beam. The potentially great improvements in signal-to-noise ratio, in power and transit time broadening and in short-term laser stability were the motivating factors that led to the choice of stabilizing cells external to the laser's optical cavity.

The one disadvantage inherent with the use of external stabilizing cells is that appropriate precautions must be taken to avoid optical feedback into the lasers to be stabilized.

For frequency reference and long-term stabilization it is convenient to obtain the derivative of the  $4.3 \mu\text{m}$  emission signal as a function of frequency. This  $4.3 \mu\text{m}$  signal derivative may be readily obtained by a small dithering of the laser frequency as we slowly tune across the resonance in the vicinity of the absorption line center frequency. With the use of standard phase-sensitive detection techniques we can then obtain the  $4.3 \mu\text{m}$  derivative signal to be used as a frequency discriminator. Figure 4 shows such a  $4.3 \mu\text{m}$  derivative signal as a function of laser tuning near the center frequency of the  $10.59 \mu\text{m}$   $\text{P}(20)$  transition.

Figure 4 also illustrates the signal and noise level amplitudes we have chosen to define the signal-to-noise (S/N) ratios of the frequency discriminants in this paper. More than half of the noise was caused by background photon current noise  $i_p^2 = 2eI_p\Delta f$ , with the remainder primarily due to residual  $1/f$  noise. As Figure 4 shows, the noise levels were chosen near the peak-to-peak rather than the rms value. A single RC filter with a 0.1 s risetime

was used to measure all the  $4.3 \mu\text{m}$  signal and noise results shown in this paper. Thus, the S/N data presented here were obtained with a noise bandwidth which was twenty times wider than the one we have used in our previously published experiments [2, 4]. Obviously, we could have shown much larger S/N values by using longer noise averaging times; nevertheless the wide bandwidth data are considered more appropriate for usability in closed loop stabilization schemes.

Figure 5 shows another  $4.3 \mu\text{m}$  derivative signal with a  $\pm 20 \text{ kHz}$  frequency dither which we used to lock one laser to the center of the P(20) absorption profile. Figure 6 shows the spectrum analyzer display of the beat note of two lasers. One of the lasers was line-center locked by using the discriminant shown in Figure 5, while the other laser was free running with a frequency offset of about 8 MHz. If both lasers are synchronously modulated at a 260 Hz rate with a  $\pm 20 \text{ kHz}$  peak deviation of the  $10.59 \mu\text{m}$  P(20) signal, the beat note appears as a relatively narrow single spectral line shown in the left half of Figure 6. The right half of Figure 6 illustrates a typical FM signal spectrum which results when the modulation signal is disconnected from the free running laser. The lasers remained locked to the line center with as little as  $\pm 2 \text{ kHz}$  frequency dither. Respective rise times of 0.001 and 0.03 to 1.5 s were used in the phase sensitive detector and in the high voltage integrating amplifier of the servo loop [8].

Figure 7 illustrates the signal, noise and S/N obtained with  $\pm 100 \text{ kHz}$  dithering of the laser. Figure 8 provides a summary of the signal-to-noise ratios as a function of peak frequency deviation at a 260 Hz rate. The results summarized in Figure 8 were obtained with a  $^{12}\text{C}^{16}\text{O}_2$   $10.59 \mu\text{m}$  P(20) laser power of about 1.75 watts. The absorption cell diameter, the beam diameter (at the 1/e field) and beam divergence were about 22.2 mm, 11.8 mm and  $1.5 \times 10^{-3}$  rad, respectively. The  $\text{CO}_2$  cell pressure was purposefully chosen to be about 0.034 Torr to provide

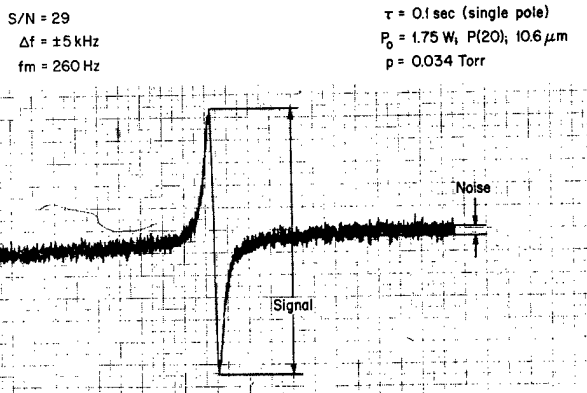


Fig. 4. Recorder tracing of the  $4.3 \mu\text{m}$  derivative signal as a function of laser frequency tuning near the center frequency of the P(20) transition at  $10.59 \mu\text{m}$ ; the frequency dither is set to  $\pm 5 \text{ kHz}$  at a 260 Hz rate

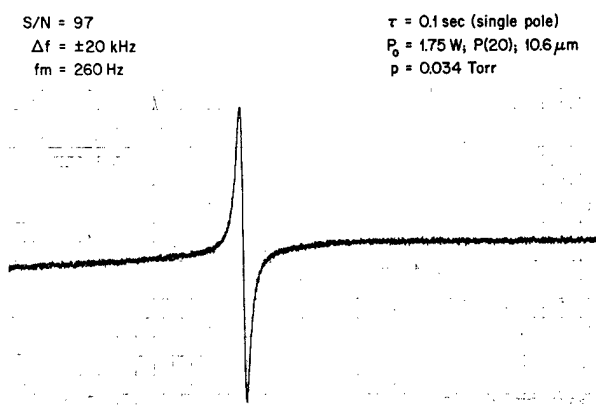


Fig. 5. Recorder tracing of the  $4.3 \mu\text{m}$  derivative signal as a function of laser frequency tuning near the center frequency of the P(20) transition at  $10.59 \mu\text{m}$ ; the frequency dither is set to  $\pm 20 \text{ kHz}$  at a 260 Hz rate

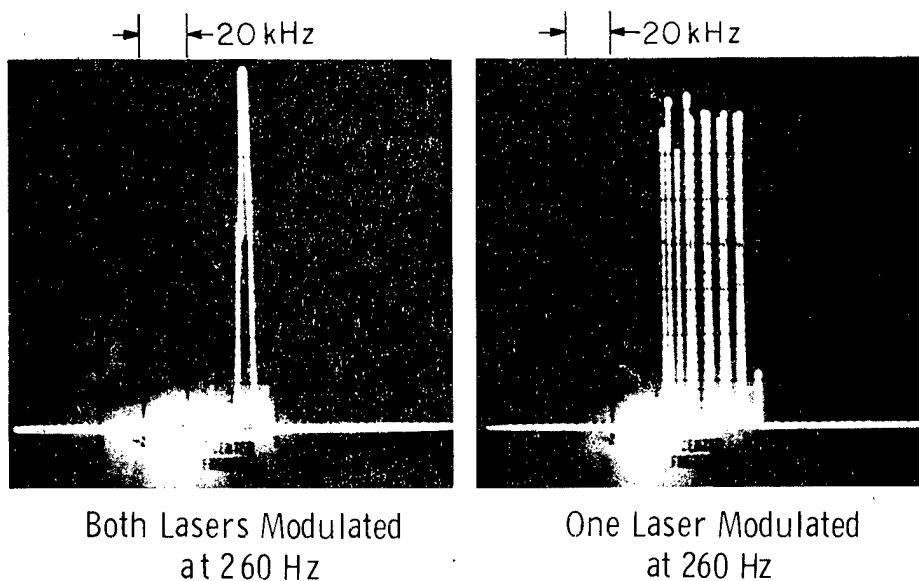


Fig. 6. Spectrum analyzer display of the beat note of two lasers with one laser locked to the line center and the other offset by 8 MHz and free running

S/N = 480  
 $\Delta f = \pm 100 \text{ kHz}$   
 $f_m = 260 \text{ Hz}$

$\tau = 0.1 \text{ sec (single pole)}$   
 $P_0 = 1.75 \text{ W}$ ; P(20);  $10.6 \mu\text{m}$   
 $p = 0.034 \text{ Torr}$

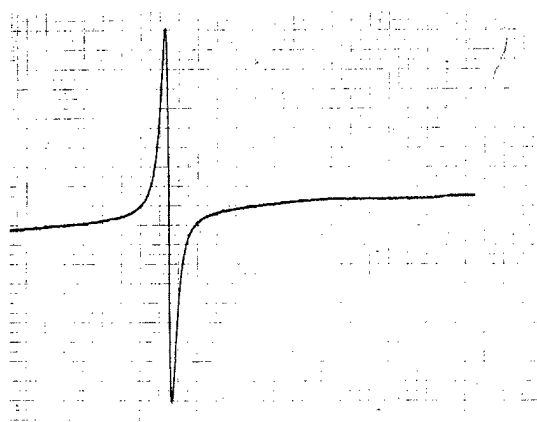


Fig. 7. Recorder tracing of the  $4.3 \mu\text{m}$  derivative signal as a function of laser frequency tuning near the center frequency of the P(20) transition at  $10.59 \mu\text{m}$ ; the frequency dither is set to  $\pm 100 \text{ kHz}$  at a  $260 \text{ Hz}$  rate

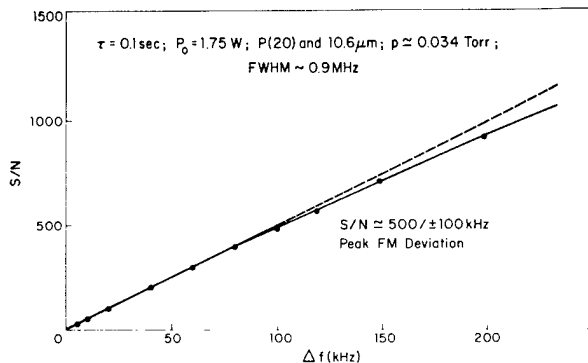


Fig. 8. Signal-to-noise ratio as a function of peak frequency dither at a  $260 \text{ Hz}$  rate

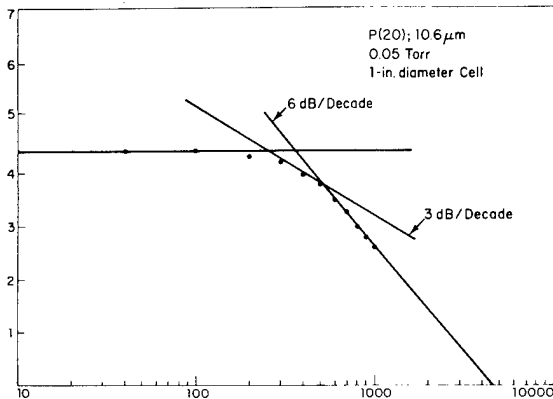


Fig. 9.  $4.3 \mu\text{m}$  signal as a function of modulator frequency (Hz)

Table 1. Sample Size,  $m$ , as a Function of Sample Time,  $\tau$ .

$\tau$ (seconds)	0.1	0.2	0.4	0.7	1.0	2	5	10	25	50	100	250	500	1000
$m$	101	101	101	101	101	51	26	26	11	3	3	3	3	2

easy comparison with previously published results [2, 4, 5, 6].

The relatively slow decay [9, 10] of the spontaneous  $4.3 \mu\text{m}$  radiation arising from the  $(00^01) \rightarrow (00^00)$  transition seriously limits the maximum frequency that can be effectively used to modulate the  $\text{CO}_2$  lasers. Figure 9 clearly illustrates the loss of the  $4.3 \mu\text{m}$  signal with increasing modulation frequency. The  $4.3 \mu\text{m}$  decay rate is primarily determined by cell pressure and geometry. Consideration of detector  $1/f$  noise may well dictate an optimum modulating frequency which is higher than would be indicated by considering the signal alone. As an example, Figure 10 shows the signal, noise and S/N as a function of modulation frequency for one of our reference cells. From Figure 10 it is clear that at  $0.034 \text{ Torr}$  pressure the optimum modulating frequency is approximately  $500 \text{ Hz}$ , in spite of some loss of signal at this frequency.

### Frequency Stability and Reproducibility

In order to investigate in the most direct fashion the various parameters affecting frequency stability, we carried out extensive measurements of the Allan Variance on the  $2,697.86 \text{ MHz}$  beat frequency between the  $^{12}\text{C}^{16}\text{O}_2$   $00^01-[10^00, 02^00]_1$  band P(20) and the  $^{13}\text{C}^{18}\text{O}_2$   $00^01-[10^00, 02^00]_1$  band R(24) laser transitions [11]. By using two different  $\text{CO}_2$  isotope lines, frequency pulling due to optical feedback was avoided and the  $2,697 \text{ MHz}$  beat frequency output of the  $\text{HgCdTe}$  photodiode was directly measured by a microwave frequency counter; thus only two independently lockable lasers and a single microwave frequency counter were utilized in the experiments to be described in this section. (Note that Figure 1 indicates a separate microwave local oscillator and a second counter; neither of these were necessary for the stability measurements.)

Since each laser was assumed to contribute equally to the instability, the measured Allan Variance was divided by  $\sqrt{2}$  times the laser frequency ( $2.8306 \times 10^{13} \text{ Hz}$ ) in order to derive the fractional frequency stability for a single laser as a function of sample time,  $\tau$  (gating time of the frequency counter).

In compliance with the "Truth in Packaging" dictates [12] that the sample size,  $m$ , be stated with the results, Table 1 gives the sample size,  $m$ , for each observation time,  $\tau$ , used to obtain the Allan Variance.

The stability of the lasers may be best summarized by Figure 11 where each circle or cross represents an Allan Variance measurement based on a sample size,  $m$ , as specified in Table 1 above.

The fractional stability of the beat note of the two lasers under free running conditions is denoted by crosses and may be reasonably well approximated by  $\sigma_y$ .

(unlocked)  $\simeq 10^{-10} \times \tau^{0.72}$  which of course indicates the drift rate of the lasers relative to each other.

The circles represent the results obtained with each laser independently locked to its own reference absorption cell filled with 40 mTorr of  $^{12}\text{C}^{16}\text{O}_2$  and  $^{13}\text{C}^{18}\text{O}_2$ , respectively.

As Figure 11 indicates, there were three consecutive sets of measurements made, each based on  $m$  samples for any given observation time,  $\tau$ . The locked laser stability may be described by  $\sigma_y$  (locked)  $\simeq 6 \times 10^{-12} \tau^{-1/2}$ .

Thus, the instability of the lasers became less than  $1 \times 10^{-12}$  for sample times  $\tau \geq 40$  seconds. A fractional stability of  $10^{-12}$  corresponds to  $\sigma_y \simeq 28$  Hz fluctuation in the laser frequency. Since the piezoelectric mirror tuning rate is about 200 kHz/volt, the phase sensitive detector output stability (drift) must be less than  $150 \mu\text{v}$  to achieve  $1 \times 10^{-12}$  long-term stability. Such low, long-term drift was clearly beyond the capability of the ten-year-old lock-in amplifiers used to obtain these results; therefore, the measurement of longer term stability with larger sample sizes was not seriously pursued in the current phase of our experiments. However, the stability we did obtain was quite sufficient to carry out accurate and reproducible measurement of pressure shift in  $\text{CO}_2$ .

In the pressure shift experiments both lasers are locked to their individual reference cells, and the shift in the beat frequency is measured as a function of pressure change in one of the cells, with the pressure held constant in the second cell in order to obtain a stable reference laser frequency.

Figure 12 shows the last two digits of the  $2,697,862 \pm 6$  kHz beat frequency of the  $^{12}\text{C}^{16}\text{O}_2$  laser  $00^01-[10^00, 02^00]_1$ -band P(20) and the  $^{13}\text{C}^{18}\text{O}_2$  laser  $00^01-[10^00, 02^00]_1$ -band R(24) transitions as a function of pressure in the  $^{12}\text{C}^{16}\text{O}_2$  reference cell. Each circle in Figure 12 is based on an observation time of  $\tau = 10$  s and a sample size of  $m = 26$ . As Figure 12 indicates, two independent, consecutive sets of measurements give results which are barely distinguishable from each other and are within one  $\sigma_y(\tau)$  of the solid line. A straight line fitting (by the least-squares method) of the data between 0 and 60 mTorr yields a  $-108.6 \pm 21.3$  Hz/mTorr frequency change with increasing pressure in the  $^{12}\text{C}^{16}\text{O}_2$  reference cell (red shift). The pressure shift becomes larger and non-

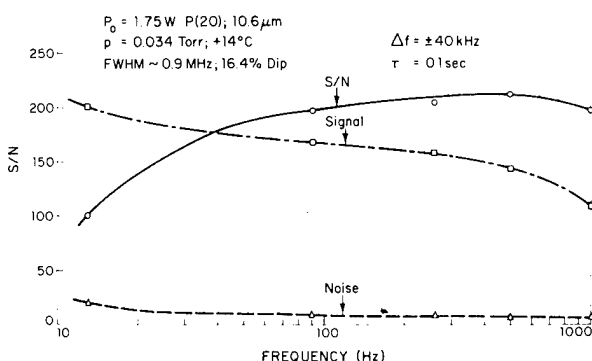


Fig. 10. Signal, noise and signal-to-noise ratio as a function of modulation frequency for a 22.2 mm diameter cell filled with 0.034 Torr  $\text{CO}_2$

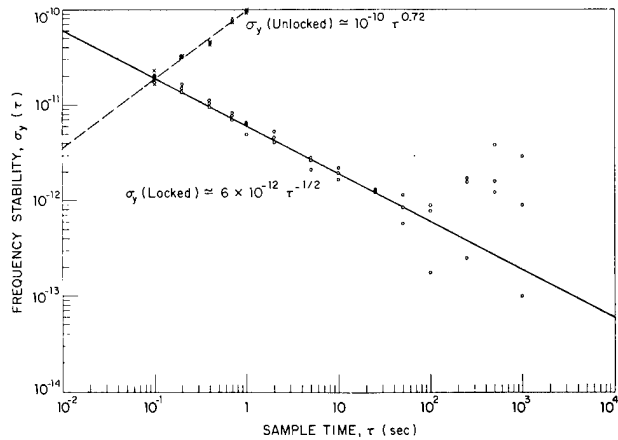


Fig. 11. Time domain stability of grating controlled  $\text{CO}_2$  lasers

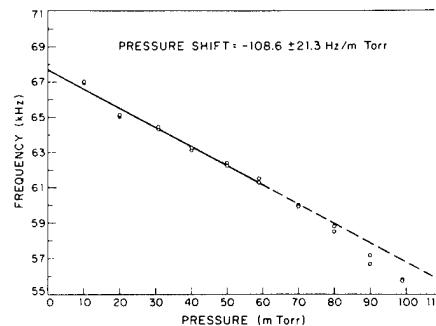


Fig. 12. Variation of the  $2,697,862 + 6$  kHz beat frequency as a function of pressure change in the  $^{12}\text{C}^{16}\text{O}_2$  reference cell for the  $00^01-[10^00, 02^00]_1$  band P(20) transition

linear at higher pressures, but for the purpose of frequency stabilization only the low pressure region is of interest. It is rather interesting to note that our original 1970 estimate [2, 3] was also about 100 Hz/mTorr red shift for the same P(20) laser transition.

Analogous data for the  $^{13}\text{C}^{18}\text{O}_2$   $00^01-[10^00, 02^00]_1$ -band R(24) transition gave a 168.6 Hz/mTorr red shift in the 0-60 mTorr pressure range. Neither repeated breaking and resetting of the frequency-lock, nor refilling of the lasers and the reference cells altered the results shown in Figures 11 and 12.

## Conclusions

The data presented in this paper clearly show significant advances in  $\text{CO}_2$  laser stabilization using the  $4.3 \mu\text{m}$  fluorescence technique. The time-domain frequency stability data of Figure 11 are quite consistent with the spectral density measurements presented at the Seminar on Frequency Standards and Metrology in Quebec (see Figure 5) [4]. It is noteworthy that the frequency stability

shown in this paper was achieved with relatively large, 1.5 metre, grating controlled, LR-35 invar lasers (see Figure 3 in Ref. [4]) with  $\pm 100$  kHz synchronous frequency modulation of the outputs. We have previously demonstrated far better spectral purity with smaller, superinvar [13, 14] cavity lasers (see Figures 1 and 4 in Ref. [4]). In the next phase of our experiments the use of superinvar lasers in conjunction with larger diameter stabilizing cells and ultra-stable electronics will undoubtedly result in at least one order of magnitude improvement over the time domain stability shown in Figure 11.

*Acknowledgments.* The authors are deeply appreciative to A.H.M. Ross for many helpful discussions, and to D.L. Spears for providing the fast HgCdTe varactor photodiodes.

## References

1. Freed, C., O'Donnell, R.G., Ross, A.H.M.: IEEE Trans. Instrum. Meas. *IM-25*, 431 (1976)
2. Freed, C., Javan, A.: Appl. Phys. Lett. *17*, 53 (1970)
3. Freed, C., Javan, A.: Standing-wave saturation resonances in room temperature  $\text{CO}_2$   $10.6 \mu\text{m}$  absorption lines. Paper 4.4 presented at the 1970 Sixth International Quant. Elect. Conference, September 1970, Kyoto, Japan
4. Freed, C.: Designs and experiments relating to stable lasers. Proceedings of the Frequency Standards and Metrology Seminar, Quebec, Canada 1971, p. 226.
5. Petersen, F.R., McDonald, D.G., Cupp, J.D., Danielson, B.L.: Accurate rotational constants, frequencies, and wavelengths from  $^{12}\text{C}^{16}\text{O}_2$  lasers stabilized by saturated absorption. Proc. of the Laser Spectroscopy Conference, Vail Colorado, 1973, p. 555
6. Meyer, T.W.: Line broadening and collisional studies of  $\text{CO}_2$  using the techniques of saturation spectroscopy. Ph.D. Thesis, U. of California, Lawrence Livermore Laboratory, UCRL-51561, April 1974
7. Woods, P.T., Joliffe, B.W.: J. of Physics E: *9*, 395 (1976)
8. The authors gratefully appreciate the correspondence and circuit diagrams which John Hall (of JILA, U of Colorado) provided. However, because of significant differences in detectors, piezoelectrics and modulation frequencies, we designed and constructed new circuitry specially tailored to the components we use.
9. Kovacs, M., Ramachandra Rao, D., Javan, A.: J. Chem. Phys. *48*, 3339 (1968)
10. Doyennette, L., Margottin-Maclou, M., Gueguen, H., Carion, A., Henry, L.: J. Chem. Phys. *60*, 697 (1974)
11. Freed, C., O'Donnell, R.G., Ross, A.H.M.: J. Molecular Spectrosc. *49*, 439 (1974)
12. Barnes, J.A., Chi, A.R., Cutler, L.S., Healey, D.J., Leeson, D.B., McGunigal, T.E., Mullen, J.A., Jr., Smith, W.L., Sydnor, R.L., Vessot, R.F.C., Winkler, G.M.R.: IEEE Trans. Instrum. Meas. *IM-20*, 105 (1971)
13. Freed, C.: IEEE J. Quan. Elect. *QE-4*, 404 (1968)
14. Berthold, J.W., III, Jacobs, S.F., Norton, M.A.: Appl. Opt. *15*, 1898 (1976)

Charles Freed  
 Massachusetts Institute of Technology  
 Lincoln Laboratory  
 Lexington, Massachusetts 02173

### Summary

A family of stable CO<sub>2</sub> lasers have been under development at M.I.T., Lincoln Laboratory for the past few years. These lasers are used in a variety of applications and under different operating conditions.

Stability data have been obtained for free-running, offset-locked and line-center stabilized lasers. Measurements of spectral purity (frequency domain), and of the fractional frequency stability (time domain) of the laser beat notes will be presented.

A two-channel, line-center stabilized CO<sub>2</sub> laser heterodyne frequency calibration system will also be described, together with the latest data obtained for the various CO<sub>2</sub> isotope laser transitions. The new data are 10<sup>3</sup> to 10<sup>6</sup> times more accurate than previously published results and will provide secondary frequency references over a wide portion of the infrared spectrum.

**Key Words:** Stable CO<sub>2</sub> lasers, short-term stability, long-term stability, pressure shift, CO<sub>2</sub> isotope constants.

### Introduction

This paper reviews the stability obtained with various CO<sub>2</sub> lasers and under different operating conditions. New results are emphasized while previously published details on laser design, experimental procedure and long-term stabilization are left to the references.

In the first part of the paper results obtained with free-running lasers are described. The second part concentrates on line-center locked CO<sub>2</sub> lasers and some of their applications.

### Open Loop Stability

In this section we shall first describe lasers and results applicable to high resolution optical radars. Figure 1 shows the basic laser structure which was previously described in greater detail.<sup>1,2</sup> Figure 2 illustrates the real time power spectrum of the beat note between two free running lasers, similar to the one shown in Figure 1. This figure and the conditions under which it was obtained was also published previously<sup>2</sup> and is repeated here for completeness sake. Figure 3 shows a real time power spectrum similar to the one in Figure 2, but measured under somewhat noisier environmental conditions.

The mostly discrete modulation sidebands in Figure 3 are primarily due to line frequency harmonics, structure vibrations, acoustic noise and optical feedback from the detector. Note, that the modulation sidebands in Figure 3 may be enclosed under a Gaussian envelope with  $\sigma \approx 209$  Hz. Although laser stabilities

are most conveniently measured by heterodyning two lasers, the results are not altogether foolproof because the disturbances causing frequency jitter of the lasers may be at least partially correlated. In an optical radar one may compare the laser with its own output delayed by the round trip time to and from the target. Hence, effects due to disturbances with correlation times less than the round trip time of the transmitted signal will be included in the measured beat note spectrum.

Figure 4 shows a block diagram of a 10.6  $\mu$ m laser radar at the Lincoln Laboratory Firepond Facility<sup>3,4,5,6</sup> in Westford, MA. In Figure 4 wavy and solid lines denote optical and electrical signal paths, respectively. The 0.5 meter local and the 1.5 meter master oscillators are similar to the one shown in Figure 1. The higher power master oscillator is offset-locked to the local oscillator using a stable 10 MHz frequency discriminator and a frequency control servo loop with unity gain at 3 kHz. Figure 5 shows the real time power spectrum of the 10 MHz beat note of the two offset-locked lasers. The analyzer resolution in Figure 5 is set to 0.02 Hz; thus the observed narrowness of the beat note spectrum indicates that the master oscillator tracked the local oscillator within less than one part in 10<sup>15</sup> during the 50 sec observation period required to obtain a high resolution measurement such as shown in Figure 5.

The 10.6  $\mu$ m laser radar shown in Figure 4 has been used to make observations on GEOS-III, a NASA geodetic satellite equipped with an IRTRAN II solid cube corner retro-reflector. Radar returns from GEOS-III have been used to determine the radial velocity of the satellite using Doppler measurements, and to set an upper bound to the laser oscillator instability.

A logarithmic display of the power spectra of a consecutive sequence of radar return signals is shown in Figure 6. Table I summarizes the applicable operating conditions.

The returns in Figure 6 were obtained near the closest approach of the satellite, corresponding to a Doppler shift of 64 MHz. At this point of the orbit the Doppler frequency was changing by 10 MHz/sec. This change in frequency amounted to a 40 kHz shift during the 0.004 sec radar transmission. This frequency shift, together with the main Doppler shift was removed by orbit-fitting in the computerized processing of the data. Thus the individual spectra of the radar returns shown in Figure 6 should ideally approach a  $(\sin x/x)^2$  distribution corresponding to the Fourier transform of the 10.6  $\mu$ m single frequency 0.004 sec radar pulse. The spectral width one may observe on the returns in Figure 6 is approximately twice the theoretical 500 Hz that should occur between the first minima. The excess width and smearing of the return spectra is due to instabilities and jitter in the entire, rather complex system, including the laser

\* This work was sponsored by the Advanced Research Projects Agency of the Department of Defense and also by the U. S. Energy Research and Development Administration.

oscillators. Needless to say, the system performance is steadily improving as the operating conditions and components giving rise to instabilities are gradually corrected; however, even the present level of performance corresponds to an orbital velocity precision of 1.25 mm/sec, and one may put an upper bound of about one part in  $10^{11}$  on the short-term stability of the laser oscillators.

#### Open-Loop Stability Of Microwave Self-Beats

The results in the remainder of this paper were obtained with grating controlled lasers, which have been previously described.<sup>2,7</sup> Such a grating controlled laser is shown in Figure 7.

Microwave (or lower) frequency generation may be achieved with a single laser filled with a mixture of  $\text{CO}_2$  isotopes. The spectral purity and long-term stability of the (self-) beat notes obtained in this way may only be compared to stabilized oscillators of the highest quality. Figure 8 shows the spectrum analyzer display of the 3165 MHz self-beat of the  $^{14}\text{C}^{16}\text{O}_2$   $00^01-[10^00, 02^00]_{\text{II}}$  P(10) and the  $^{12}\text{C}^{16}\text{O}_2$   $00^01-[10^00, 02^00]_{\text{I}}$  R(18) transitions. Time domain frequency stability measurements of the same 3165 MHz beat note are shown in Figure 9. In order to obtain the fractional frequency stability, the measured Allan Variance was divided by  $\sqrt{2}$  times the laser frequency. Table II gives the sample size,  $m$ , for each observation time,  $\tau$ , used to obtain the Allan Variance.

Figure 10 shows an even better frequency stability measurement of the 593 MHz beat note between the  $^{14}\text{C}^{16}\text{O}_2$   $00^01-[10^00, 02^00]_{\text{II}}$  P(38) and the  $^{12}\text{C}^{16}\text{O}_2$   $00^01-[10^00, 02^00]_{\text{I}}$  P(16) laser transitions. Each data point in Figures 9 and 10 is based on an independent set of consecutive  $m$  samples. Table III shows the sample size,  $m$ , for each observation time,  $\tau$ , of Figure 10.

The spectral purity of Figures 8, 9 and 10 is explained by the fact that the fractional frequency stability at the microwave beat frequency will be identical to the fractional stability of the laser frequency itself. It should be clear by now that short-term stabilities of  $10^{-11}$  to  $10^{-13}$  may be routinely achieved with well designed and acoustically shielded  $\text{CO}_2$  lasers.

Two additional facts are noteworthy in Figures 9 and 10. The frequency stability gets better for shorter observation times, a very desirable requirement in radar-like applications. As a matter of fact, inadequate frequency resolution of our present equipment prevented meaningful measurements of the Allan Variance for observation times less than 1 sec in cases like the ones illustrated by Figures 9 and 10. A second noteworthy feature of such self-beats is that they may be utilized for direct comparison of optical and microwave frequency domains.

#### Long-Term Stability and Some Of Its Applications

It was previously shown<sup>8,9</sup> that  $\text{CO}_2$  lasers can be frequency stabilized by using the standing-wave saturation resonances in a low-pressure, room-temperature, pure  $\text{CO}_2$  absorber via the intensity changes observed in the collisionally-coupled spontaneous emission band at  $4.3 \mu\text{m}$ . More recently, significant improvement in signal-to-noise ratios with new, low pressure  $\text{CO}_2$  stabilization cells external to the lasers was also demonstrated<sup>10</sup>.

The experimental results in the remaining part of this paper were obtained with the two-channel line-

center stabilized  $\text{CO}_2$  isotope calibration system which was previously described<sup>7</sup>. Figure 11 shows the block diagram of this system.

In order to investigate in the most direct fashion the various parameters affecting long-term frequency stability, we carried out extensive measurements of the Allan Variance on the 2,697.86 MHz beat frequency between the  $^{12}\text{C}^{16}\text{O}_2$   $00^01-[10^00, 02^00]_{\text{I}}$  band P(20) and the  $^{13}\text{C}^{18}\text{O}_2$   $00^01-[10^00, 02^00]_{\text{I}}$  band R(24) laser transitions<sup>7</sup>. By using two different  $\text{CO}_2$  isotope lines, frequency pulling due to optical feedback was reduced and the 2,698 MHz beat frequency output of the HgCdTe photodiode was directly measured by a microwave frequency counter; thus only two independently lockable lasers and a single microwave frequency counter were utilized in the experiments to be described in this section (note that Figure 11 indicates a separate microwave local oscillator and a second counter; neither of these were necessary for the stability measurements).

Since each laser was assumed to contribute equally to the instability, the measured Allan Variance was divided by  $\sqrt{2}$  times the laser frequency ( $2.8306 \times 10^{13} \text{ Hz}$ ) in order to derive the fractional frequency stability for a single laser as a function of sample time,  $\tau$ , (gating time of the frequency counter).

The stability of the lasers may be best summarized by Figure 12 where each circle or cross represents an Allan Variance measurement based on a sample size,  $m$ , as specified in Table IV.

The fractional stability of the beat note of the two lasers under free running conditions is denoted by crosses and may be reasonably well approximated by  $\sigma_y$  (unlocked)  $\approx 10^{-10} \times \tau^{0.72}$  which of course indicates the drift rate of the lasers relative to each other.

The circles represent the results obtained with each laser independently locked to its own reference absorption cell filled with 40 mTorr of  $^{12}\text{C}^{16}\text{O}_2$  and  $^{13}\text{C}^{18}\text{O}_2$ , respectively.

As Figure 12 indicates, there were three consecutive sets of measurements made, each based on  $m$  samples for any given observation time,  $\tau$ . The locked laser stability may be described by  $\sigma_y$  (locked)  $\approx 6 \times 10^{-12} \times \tau^{-1/2}$ .

Thus, the instability of the lasers became less than  $1 \times 10^{-12}$  for sample times  $\tau \geq 40$  seconds. A fractional stability of  $10^{-12}$  corresponds to  $\sigma_y \approx 28 \text{ Hz}$  fluctuation in the laser frequency. Since the piezoelectric mirror tuning rate is about 200 kHz/volt, the phase sensitive detector output stability (drift) must be less than 150  $\mu\text{v}$  to achieve  $1 \times 10^{-12}$  long-term stability. Such low, long-term drift was clearly beyond the capability of the ten year old lock-in amplifiers used to obtain these results; therefore, the measurement of longer term stability with larger sample sizes was not seriously pursued in the current phase of our experiments. However, the stability we did obtain was quite sufficient to carry out accurate and reproducible measurements of pressure shift in  $\text{CO}_2$ .

In the pressure shift experiments both lasers are locked to their individual reference cells, and the shift in the beat frequency is measured as a function of pressure change in one of the cells, with the pressure held constant in the second cell in order to obtain a stable reference laser frequency.

Figure 13 shows the last two digits of the  $2.697.862 \pm 6 \text{ kHz}$  beat frequency of the  $^{12}\text{C}^{16}\text{O}_2$  laser

00°1-[10°0, 02°0]<sub>I</sub> band P(20) and the  $^{13}\text{C}^{18}\text{O}_2$  laser 00°1-[10°0, 02°0]<sub>I</sub> band R(24) transitions as a function of pressure in the  $^{12}\text{C}^{16}\text{O}_2$  reference cell. Each circle in Figure 13 is based on an observation time of  $\tau = 10$  seconds and a sample size of  $m = 26$ . As Figure 13 indicates, two independent, consecutive sets of measurements give results which are barely distinguishable from each other and are within one  $\sigma_y(\tau)$  of the solid line. A straight line fitting (by the least-squares method) of the data between 0 and 60 mTorr yields a -108.6 Hz/mTorr frequency change with increasing pressure in the  $^{12}\text{C}^{16}\text{O}_2$  reference cell (red shift). The pressure shift becomes larger and nonlinear at higher pressures, but for the purpose of frequency stabilization only the low pressure region is of interest. It is rather interesting to note that our original 1970 estimate<sup>2,8</sup> was also about 100 Hz/mTorr red shift for the same P(20) laser transition.

Analogous data for the  $^{13}\text{C}^{18}\text{O}_2$  00°1-[10°0, 02°0]<sub>I</sub> band R(24) transition gave a 168.6 Hz/mTorr red shift in the 0 - 60 mTorr pressure range. Neither repeated breaking and resetting of the frequency lock, nor refilling of the lasers and the reference cells altered the results shown in Figures 12 and 13.

In the final portion of this paper new results relating to  $\text{CO}_2$  isotope lasers will be given. We have previously reported<sup>11,12</sup> on the determination of transition frequencies, band centers and rotational constants of  $^{12}\text{C}^{18}\text{O}_2$ ,  $^{13}\text{C}^{16}\text{O}_2$  and  $^{13}\text{C}^{18}\text{O}_2$  isotope lasers with accuracies of about 3 MHz.

Optical heterodyne techniques were used to generate beat frequencies between two lasers filled with different  $\text{CO}_2$  isotopes. The rotational constants are computed by fitting the measured difference frequencies in a least-squares sense to the expansion of the line frequencies

$$\nu = \nu_0 + B_u [J'(J'+1) - J(J+1)] - (B_l - B_u) J(J+1) - D_u [J'^2(J'+1)^2 - J(J+1)^2] + (D_l - D_u) J^2(J+1)^2 + H_u [J'^3(J'+1)^3 - J^3(J+1)^3] - (H_l - H_u) J^3(J+1)^3 - L_u [\dots] \quad (1)$$

where  $J' = J-1$  for a P(J) line and  $J' = J+1$  for an R(J) line.

The experimental procedure is similar in principle to the one previously described<sup>12,13</sup>, and this paper will only list the latest results which are summarized in Table V.

The band centers and rotational constants of  $^{12}\text{C}^{16}\text{O}_2$  listed in Table V were originally determined by Petersen et al.<sup>13</sup>, and were used as fixed references in the computation of vibrational - rotational constants of the other  $\text{CO}_2$  isotopes in Table V. Upon completion of our data taking in the near future, we shall relax this restriction, and will simultaneously determine the rotational constants of all the isotopes since our measurements include much higher J-transitions than reported previously<sup>13</sup>. Thus the constants listed in Table V should not be considered as the final results of our isotope measurements; however, they do represent an approximately  $10^3$  - fold improvement over our previously published data for  $^{13}\text{C}^{16}\text{O}_2$  and  $^{13}\text{C}^{18}\text{O}_2$  and an even greater improvement for  $^{14}\text{C}^{16}\text{O}_2$ . Figure 14 graphically illustrates the lasing transitions of the  $\text{CO}_2$  isotopes listed in Table V and the spectral region they occupy.

### Conclusion

Even the few examples given in this paper make it quite clear that the spectral purity, frequency stability and resetability, together with the availability of well over a thousand lasing transitions uniquely endow the  $\text{CO}_2$  system for direct use in high resolution spectroscopy, or as secondary frequency standard in heterodyne spectroscopy with tunable lasers, or in precision IR synthesis which involves frequency mixing.

A systematic and precise evaluation of the band centers, rotational constants, and lasing transition frequencies of the  $\text{CO}_2$  isotopes is under way. These data will also be of great value in evaluating the potential function under the influence of which the nuclei are moving.

### Acknowledgments

The author is deeply appreciative to R. G. O'Donnell for assistance in all phases of the stability and isotope measurements and to many other colleagues who contributed to the design of the 10.6  $\mu\text{m}$  radar and who provided the data relating to the GEOS-III experiments.

### References

1. C. Freed, "Design and Short-Term Stability of Single-Frequency  $\text{CO}_2$  Lasers", *IEEE J. Quan. Elect.* QE-4, 404-408 (June 1968).
2. C. Freed, "Designs and Experiments Relating to Stable Lasers", "Proceedings of the Frequency Standards and Metrology Seminar, University Laval, Quebec, Canada, 226-261 (1 September 1971).
3. R. H. Kingston and L. J. Sullivan, "Coherent Infrared Radar", *SPIE 69*, 10-13 (1975).
4. T. R. Gurski, "Laser Frequency Stability Limitations On A 10.6  $\mu\text{m}$  Laser Radar", paper presented at OSA, Tucson, Arizona (18-22 October 1976).
5. R. H. Kingston, "Coherent Optical Radar" (1977) to be published.
6. R. Teoste, W. J. Scouler and D. L. Spears, "Coherent Monopulse Tracking With a 10.6  $\mu\text{m}$  Radar", Paper 9.5 presented at the CLEA Conference in Washington, D. C. (1-3 June 1977).
7. C. Freed, R. G. O'Donnell and A. H. M. Ross, "Absolute Frequency Calibration of the  $\text{CO}_2$  Isotope Laser Transitions", *IEEE Trans. Instrum. Meas.* IM-25, 431-437 (December 1976).
8. C. Freed and A. Javan, "Standing-Wave Saturation Resonances in the 10.6  $\mu\text{m}$  Transitions Observed In A Low-Pressure Room-Temperature Absorber Gas", *Appl. Phys. Lett.* 17, 53-56 (15 July 1970).
9. C. Freed and A. Javan, "Standing-Wave Saturation Resonances in Room Temperature  $\text{CO}_2$  10.6  $\mu\text{m}$  Absorption Lines", Paper 4.4 presented at the 1970 Sixth International Quan. Elect. Conference, Kyoto, Japan (September 1970).
10. C. Freed, "Frequency Stabilization of  $\text{CO}_2$  Lasers", *Proc. of the 29th Annual Symposium on Frequency Control*, Atlantic City, NJ, 330-337 (28-30 May 1975).
11. C. Freed, D. L. Spears, R. G. O'Donnell,

and A. H. M. Ross, "Precision Heterodyne Calibration", Proc. of the Laser Spectroscopy Conference, Vail, Colorado (25-29 June 1973). Also in Laser Spectroscopy, 171-191, Plenum Press, 1975 (R. A. Brewer and A. Mooradian, Editors).

12. C. Freed, A. H. M. Ross and R. G. O'Donnell, "Determination of Laser Line Frequencies and Vibrational-Rotational Constants of the  $^{12}\text{C}^{18}\text{O}_2$ ,  $^{13}\text{C}^{16}\text{O}_2$  and  $^{13}\text{C}^{18}\text{O}_2$  Isotopes from Measurements of CW Beat Frequencies with Fast HgCdTe Photodiodes and Microwave Frequency Counters", J. Molecular Spectrosc. 49, 439 (1974).

13. F. R. Petersen, D. G. McDonald, J. D. Cupp and B. L. Danielson, "Accurate Rotational Constants, Frequencies, and Wavelengths from  $^{12}\text{C}^{16}\text{O}_2$  Lasers Stabilized by Saturated Absorption", Proc. of the Laser Spectroscopy Conference, Vail, Colorado (25-29 June 1973).

10.6  $\mu\text{m}$  LASER RADAR OBSERVATION OF GEOS-III SATELLITE

RANGE:	1007 km
DOPPLER VELOCITY:	-318 m/sec
ELEVATION:	56.11°
PULSE DURATION:	0.004 sec
PULSE REPETITION RATE:	62.5/sec (0.016 sec)
FULL SPECTRAL WIDTH OF SIGNAL RETURNS:	$\Delta\nu = 693 (\pm 99) \text{ Hz}$ 10 db BELOW PEAK
AVERAGE PULSE TO PULSE JITTER:	209 Hz

TABLE I

$\tau$ (seconds)	1	2	4	5	7	10
m	101	51	51	51	26	26

Sample size, m, as a function of sample time,  $\tau$ , for  $v_{\text{beat}} \approx 3165 \text{ MHz}$ .

TABLE II

$\tau$ (seconds)	1	2	5	10	25
m	101	51	26	26	11

Sample size, m, as a function of sample time,  $\tau$ , for  $v_{\text{beat}} \approx 593 \text{ MHz}$ .

TABLE III

$\tau$ (seconds)	0.1	0.2	0.4	0.7	1.0	2	5	10	25	50	100	250	500	1000
m	101	101	101	101	101	51	26	26	11	3	3	3	3	2

Sample Size, m, as a Function of Sample Time,  $\tau$ , for  $v_{\text{beat}} \approx 2698 \text{ MHz}$

TABLE IV

VIBRATIONAL - ROTATIONAL CONSTANTS OF  $\text{CO}_2$  ISOTOPE LASER TRANSITIONS

Isotope Constants in MHz	$^{12}\text{C}^{16}\text{O}_2$	$^{13}\text{C}^{16}\text{O}_2$	$^{13}\text{C}^{18}\text{O}_2$	$^{14}\text{C}^{16}\text{O}_2$
$V(0)_{001-\text{I}}$	28 808 813.8	27 383 792.4	27 838 551.2	25 965 920.7
$V(0)_{001-\text{II}}$	31 889 960.2	30 508 659.6	30 785 884.8	29 460 002.6
$B_{001}$	11 606.2072	11 610.1771	10 319.0962	11 613.6722
$B_I$	11 697.5697	11 683.4536	10 403.4743	11 674.7428
$B_{II}$	11 706.3645	11 719.3785	10 398.9836	11 727.0591
$D_{001}$	$3.9883 \times 10^{-3}$	$3.9923 \times 10^{-3}$	$3.1451 \times 10^{-3}$	$3.9879 \times 10^{-3}$
$D_I$	$3.4462 \times 10^{-3}$	$3.6126 \times 10^{-3}$	$2.7147 \times 10^{-3}$	$3.8183 \times 10^{-3}$
$D_{II}$	$4.7115 \times 10^{-3}$	$4.7567 \times 10^{-3}$	$3.6544 \times 10^{-3}$	$4.8317 \times 10^{-3}$
$H_{001}$	$5.15 \times 10^{-10}$	$1.012 \times 10^{-9}$	$-8.12 \times 10^{-10}$	$2.852 \times 10^{-9}$
$H_I$	$5.730 \times 10^{-9}$	$7.159 \times 10^{-9}$	$1.807 \times 10^{-9}$	$3.7293 \times 10^{-8}$
$H_{II}$	$6.984 \times 10^{-9}$	$9.022 \times 10^{-9}$	$4.018 \times 10^{-9}$	$1.6284 \times 10^{-8}$

$c = 299 792 458 \text{ m/sec}$

TABLE V

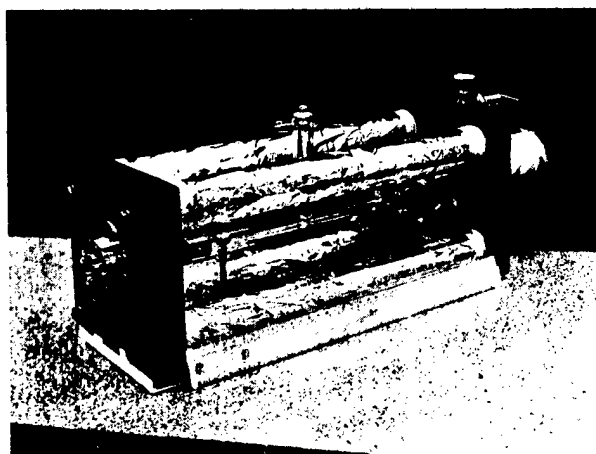


FIG. 1 0.5 meter, internal mirror, piezoelectrically tuned stable  $\text{CO}_2$  laser.

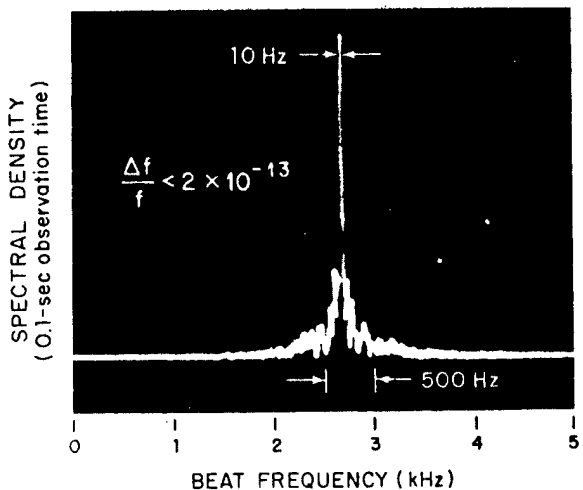
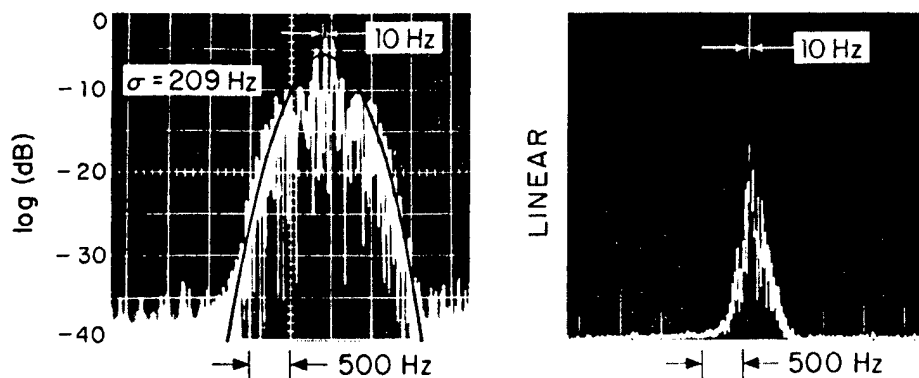
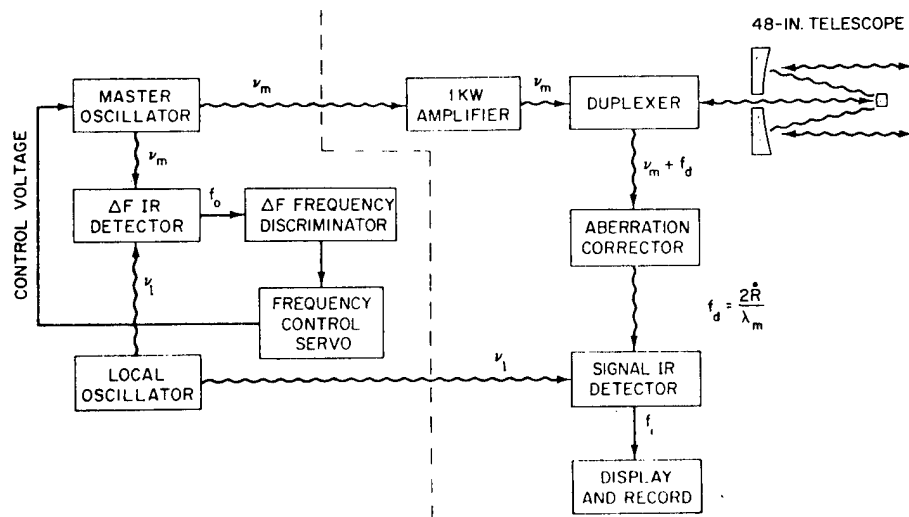


FIG. 2. Real-time spectral density of the beat note of two free running, 0.5 meter stable  $\text{CO}_2$  lasers for 0.1 second observation time; horizontal scale: 500 Hz/cm; resolution 10 Hz.



BEAT NOTE SPECTRA OF TWO CO<sub>2</sub> LASERS

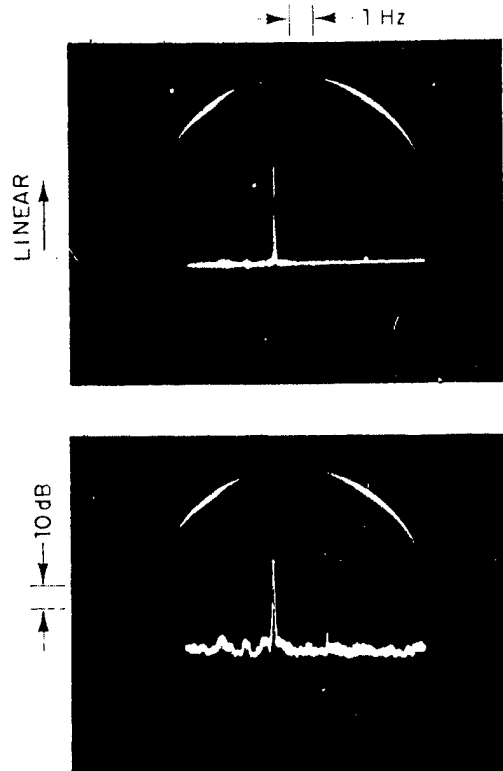
FIG. 3 A beat note similar to Figure 2 but measured under somewhat noisier environmental conditions.



INFRARED RADAR SYSTEM BLOCK DIAGRAM

FIG.4 10.6 μm radar system block diagram.

-5-7481



RF SPECTRUM OF  $\text{CO}_2$  LASER BEAT  
WITH FREQUENCY SERVO  
(0.02 Hz Resolution)

FIG. 5 10 MHz beat note of two offset-locked lasers;  
spectrum analyzer resolution set to 0.02 Hz.

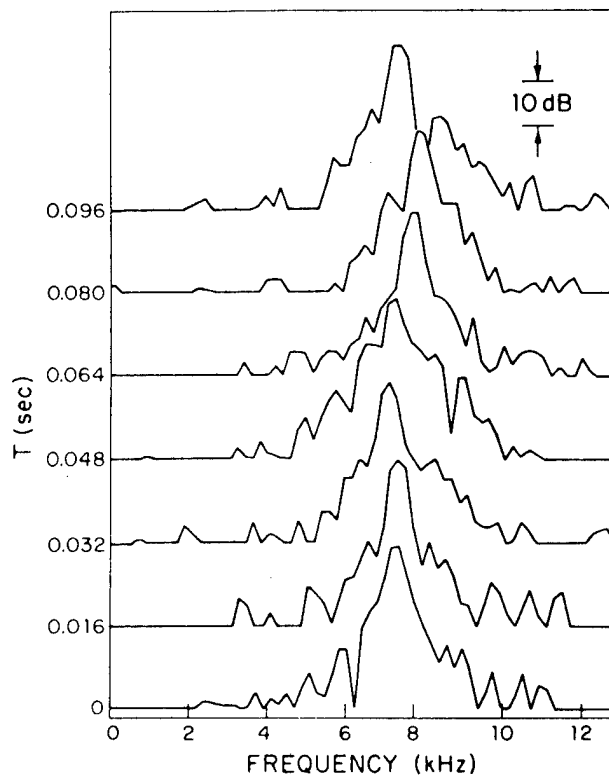
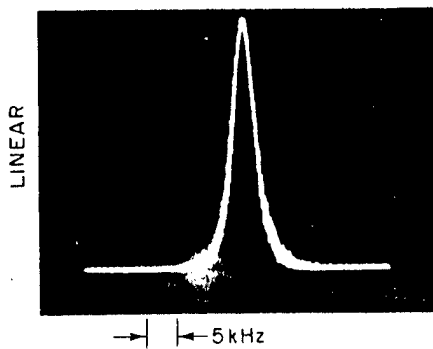


FIG. 6 10.6  $\mu\text{m}$  radar return spectra from GEOS III  
geodetic satellite.



Fig. 7. 1.5 meter, internal-grating-controlled, piezoelectrically tuned  
stable  $\text{CO}_2$  laser.



3,165 MHz BEAT FREQUENCY OF A  
 $^{12}\text{C}^{16}\text{O}_2$  00 $^{\circ}$ 1 - [10 $^{\circ}$ 0, 02 $^{\circ}$ 0] $_{\text{II}}$  band R(18) TRANSITION  
 WITH A  $^{14}\text{C}^{16}\text{O}_2$  LASER LINE

I.F. BANDWIDTH : 3 kHz

Fig. 8. Spectrum analyzer display of 3,165 MHz beat frequency of the  $^{14}\text{C}^{16}\text{O}_2$  00 $^{\circ}$ 1 - [10 $^{\circ}$ 0, 02 $^{\circ}$ 0] $_{\text{II}}$  band P(10) and the  $^{12}\text{C}^{16}\text{O}_2$  00 $^{\circ}$ 1 - [10 $^{\circ}$ 0, 02 $^{\circ}$ 0] $_{\text{I}}$  band R(18) transitions; I. F. Bandwidth: 3 kHz.

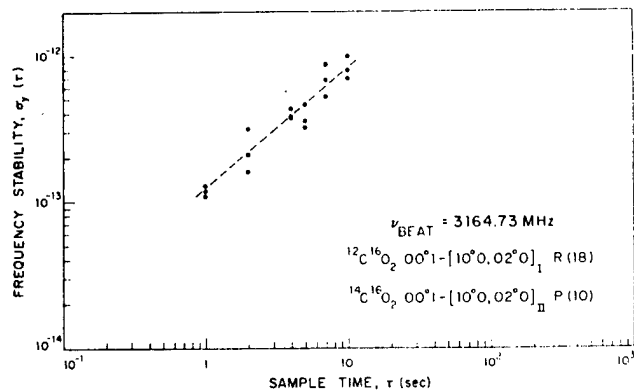


FIG. 9 Time domain stability of the beat note shown in Figure 8.

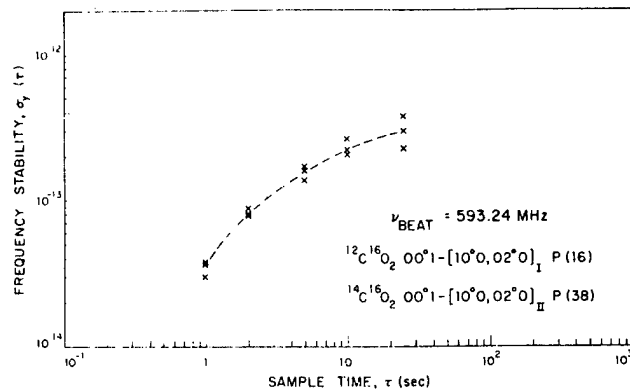


FIG. 10 Time domain stability of the 593.24 MHz self-beat in a  $^{14}\text{C}^{16}\text{O}_2$  -  $^{12}\text{C}^{16}\text{O}_2$  combination laser.

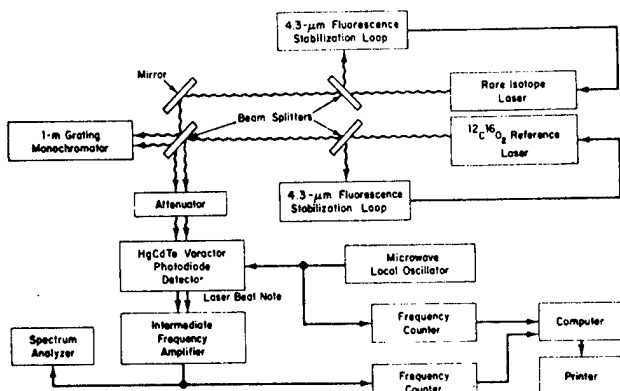


FIG. 11 Two-channel heterodyne system used to determine  $\text{CO}_2$  isotope laser frequencies.

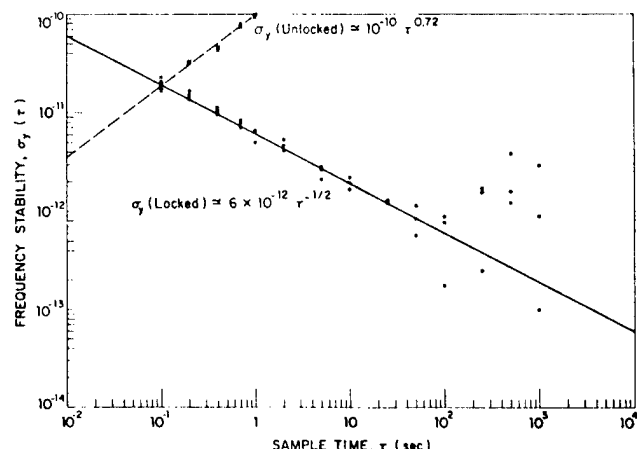


FIG. 12 Time domain stability of independently lock-ed grating controlled  $\text{CO}_2$  lasers.

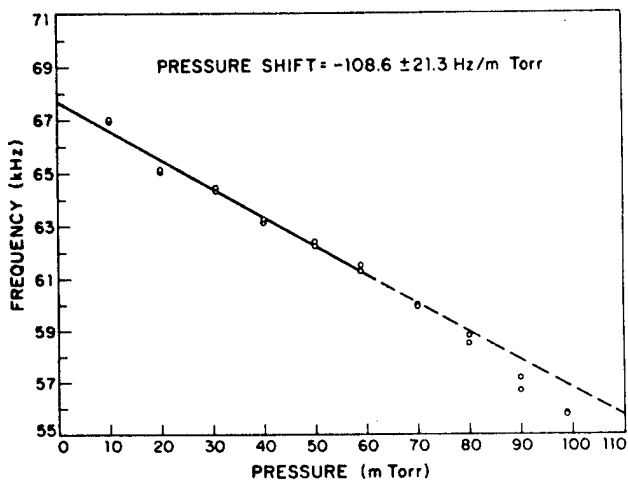


FIG. 13 Variation of the  $2,697,862 \pm 6$  kHz beat frequency as a function of pressure change in the  $^{12}\text{C}^{16}\text{O}_2$  reference cell for the  $00^01 - [10^00, 02^00]_1$  band P (20) transition.

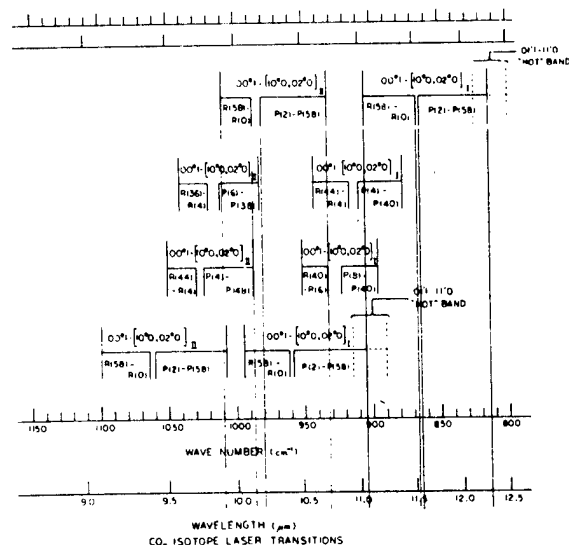


FIG. 14 Comparison of the frequency and wavelength domains of rare  $\text{CO}_2$  isotope lasers with  $^{12}\text{C}^{16}\text{O}_2$ .

# Absolute Frequency Calibration of the CO<sub>2</sub> Isotope Laser Transitions

CHARLES FREED, SENIOR MEMBER, IEEE, ROBERT G. O'DONNELL, AND A. H. M. ROSS

**Abstract**—The frequencies of rare CO<sub>2</sub> isotope lasers are measured by comparison with <sup>12</sup>C<sup>16</sup>O<sub>2</sub> reference lines and with each other. Improved heterodyne techniques are used to generate difference frequencies in a liquid-nitrogen-cooled HgCdTe varactor photodiode. Microwave frequency counter measurements of the difference frequencies are then used to calculate the band centers, rotational constants and transition frequencies with an estimated accuracy of less than a few kilohertz. Selected applications of CO<sub>2</sub> isotope lasers in precision heterodyne calibration, spectroscopy, microwave and IR synthesis are described.

## INTRODUCTION

THIS PAPER will concentrate on new results relating to CO<sub>2</sub> isotope lasers [1]. At the June 1973 Laser Spectroscopy Conference in Vail, CO, we reported

Manuscript received June 29, 1976. This work was supported by the Advanced Research Project Agency of the Department of Defense and in part by the U.S. Energy Research and Development Administration.

C. Freed and R. G. O'Donnell are with the M.I.T. Lincoln Laboratory, Lexington, MA 02173.

A. H. M. Ross is with the Department of Physics, University of California, Los Angeles, CA 90024.

on the determination of transition frequencies, band centers and rotational constants of <sup>12</sup>C<sup>18</sup>O<sub>2</sub>, <sup>13</sup>C<sup>16</sup>O<sub>2</sub>, and <sup>13</sup>C<sup>18</sup>O<sub>2</sub> isotope lasers [2], [3] with accuracies of about 3 MHz. At least a 1000-fold improvement in accuracy has been achieved with the experimental apparatus currently in use. Also, hundreds of new lasing transitions have been observed in <sup>16</sup>O<sup>12</sup>C<sup>18</sup>O, <sup>16</sup>O<sup>13</sup>C<sup>18</sup>O, and <sup>14</sup>C<sup>16</sup>O<sub>2</sub>, and measurements of <sup>14</sup>C<sup>18</sup>O<sub>2</sub> and <sup>16</sup>O<sup>14</sup>C<sup>18</sup>O lasers will be carried out in the near future.

## CURRENT EXPERIMENTS

Optical heterodyne techniques [2]–[5] are used to generate beat frequencies between two lasers either filled with different CO<sub>2</sub> isotopes, or if the same isotope is used the difference frequencies between adjacent rotational transitions are measured. The band centers are determined by two heterodyne comparisons with the <sup>12</sup>C<sup>16</sup>O<sub>2</sub> lines measured by Evenson *et al.* [6]. The rotational constants are computed by fitting the measured difference frequencies

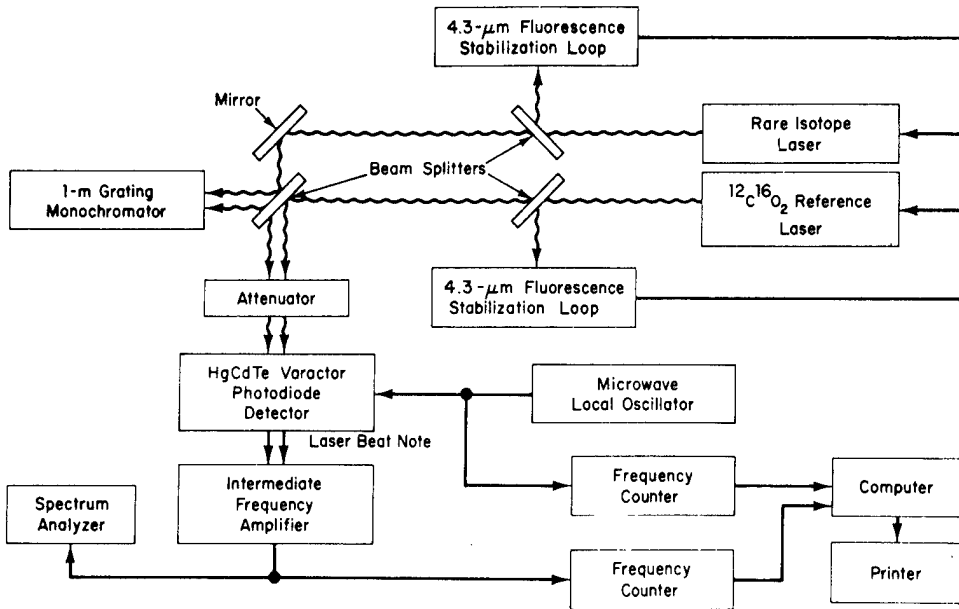


Fig. 1. Experimental setup used to determine the  $\text{CO}_2$  isotope laser frequencies.

in a least squares sense to the expansion of the line frequencies

$$\begin{aligned}
 f = & f_0 + B_u [J'(J'+1)] - J(J+1) \\
 & - (B_l - B_u) J(J+1) \\
 & - D_u [J'^2(J'+1)^2 - J^2(J+1)^2] \\
 & + (D_l - D_u) J^2(J+1)^2 + H_u [J'^3(J'+1)^3] \\
 & - J^3(J+1)^3 - (H_l - H_u) J^3(J+1)^3 - L_u [\dots] \quad (1)
 \end{aligned}$$

where  $J' = J - 1$  for a  $P(J)$  line and  $J' = J + 1$  for an  $R(J)$  line. Fig. 1 shows a block diagram of the experimental apparatus.

The experimental procedure is similar in principle to the one previously described [2], [3]; therefore, this paper will emphasize the improvements achieved and avoid repetition of every detail.

Refinements in our standard grating controlled laser design [2], [3], [7] resulted in greatly improved laser output with tap-water cooling. About 150 transitions lasing in the  $\text{TEM}_{00q}$  mode could be obtained with a pure  $\text{CO}_2$  isotope fill, including many from the  $01^11 - 11^10$  "hot band". Several hundred lasing transitions were available from a single laser filled with mixed isotopes.

The 1000-fold improvement in the accuracy of frequency measurements was primarily due to active long-term stabilization of the lasers to the natural line centers of low pressure room temperature  $\text{CO}_2$  absorption cells external to the lasers. In previous papers with A. Javan we have shown [8], [9] that  $\text{CO}_2$  lasers can be frequency-stabilized in any lasing transition by using the standing-wave saturation resonances in a low pressure, room temperature pure  $\text{CO}_2$  absorber via the intensity changes observed in the entire collisionally coupled spontaneous emission band at  $4.3 \mu\text{m}$ . It was also demonstrated that the frequency shift due to changes in pressure is very small in  $\text{CO}_2$ , typically much less than 100 Hz/mtorr.

In the experimental setup shown in Fig. 1, vastly improved  $\text{CO}_2$  stabilization cells external to the lasers are

used [10]. In the new design, the low pressure gas cell, the  $\text{LN}_2$ -cooled radiation collector, and the IR detector are all integral parts of one evacuated housing assembly which also minimizes signal absorption by windows and eliminates all other sources of absorption. Because of the vacuum enclosure, diffusion of other gases into the low-pressure gas reference cell is almost completely eliminated; therefore, the time period available to use the reference gas cell has greatly increased and considerably less time has to be wasted on repumping and refilling procedures. Also, one  $\text{LN}_2$  fill will last at least 18 h. In addition to greatly improved reliability and maintenance we have also obtained [10] at least two orders of magnitude improvement of the signal-to-noise ratio in measuring the  $4.3\text{-}\mu\text{m}$  fluorescence.

The improvements in laser stability also necessitated the use of highly stabilized microwave oscillators and frequency counters to measure both the intermediate and the local oscillator frequencies. The frequency counts were directly fed into a computer for further processing of the data.

No description of our experimental setup can be complete without specially mentioning the remarkable performance achieved with the improved, high speed, high quantum efficiency  $\text{HgCdTe}$  photodiodes developed by D. L. Spears at Lincoln Laboratory. We achieve mixing of the microwave local oscillator, or its harmonics, with the  $\text{CO}_2$  laser beats directly in these  $\text{HgCdTe}$  photodiodes. The generation of harmonics and the mixing of the microwave signals closely correspond to varactor diode behavior [11]. Fig. 2 illustrates a typical microwave frequency beat signal obtained by varactor harmonic mixing and frequency down-conversion in such a photodiode. Fig. 2 shows a 52-dB signal-to-noise ratio with a 10-kHz noise bandwidth for the  $24\ 410.301\text{-MHz}$  beat frequency of the  $^{16}\text{O}^{12}\text{C}^{18}\text{O}$   $00^11 - [10^0, 02^0]_1$  band  $P(12)$  and the  $^{12}\text{C}^{16}\text{O}_2$   $00^11 - [10^0, 02^0]_1$  band  $P(6)$  transitions; this represents a 16-dB increase in signal-to-noise ratio when compared to our

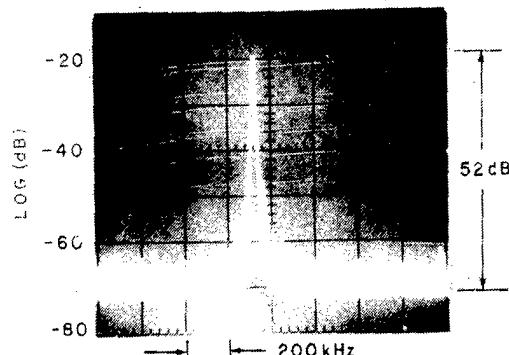


Fig. 2. 24,410.301-MHz beat frequency of the  $^{16}\text{O}^{12}\text{C}^{18}\text{O}$  laser  $00^1 - [10^0, 02^0]$ , band P(12) and the  $^{12}\text{C}^{16}\text{O}_2$  laser  $00^1 - [10^0, 02^0]$ , band P(6) transitions.

Power levels into photodiode:

$^{12}\text{C}^{16}\text{O}_2$  Laser: 0.42 mW

$^{16}\text{O}^{12}\text{C}^{18}\text{O}$  Laser: 0.48 mW

Noise bandwidth: 10 kHz

Second harmonic of microwave LO is used.

previously published results [2], [3]. Greater detection sensitivity was due in part to improvements in detector technology and in part to special, low microwave loss dewar and signal-duplexer design. The two detectors presently in use have been installed well over two years ago and both can detect the up to 60-GHz ( $2 \text{ cm}^{-1}$ ) beat frequencies of adjacent  $\text{CO}_2$  rotational transitions with over 30-dB signal-to-noise ratio.

Table I shows a set of 20 beat frequencies measured between the indicated  $^{16}\text{O}^{12}\text{C}^{18}\text{O}$  isotope transitions and adjacent  $^{12}\text{C}^{16}\text{O}_2$  laser lines used as reference. The measured difference frequencies were fitted in a least squares sense to the expansion of the line frequencies shown previously in (1). The  $^{12}\text{C}^{16}\text{O}_2$  reference frequencies were computed from the constants recently published by Petersen [5] and his coworkers at the NBS in Boulder, CO.

Table II shows the band centers and rotational constants of  $^{16}\text{O}^{12}\text{C}^{18}\text{O}$  determined from the twenty beat frequencies listed in Table I. The results in Tables I and II show more than  $10^4$  improvement over the data previously available for this isotope. We expect another order of magnitude improvement because the data of Table I were taken prior to installation of the improved laser stabilization equipment [10].

Hundreds of laser lines have been observed in  $^{16}\text{O}^{12}\text{C}^{18}\text{O}$  and in  $^{16}\text{O}^{13}\text{C}^{18}\text{O}$  isotopes since both even and odd rotational transitions are allowed for a linear molecule in which one of the atoms is replaced by an isotopic substitute. Our current emphasis, however, lies in the determination of the  $^{14}\text{CO}_2$  laser transitions because of the rich spectrum they provide in the vicinity of  $12 \mu\text{m}$ . Some of the  $01^1 - 11^1$  "hot band" lines we observe are near  $12.4 \mu\text{m}$  in  $^{14}\text{C}^{16}\text{O}_2$  lasers. Fig. 3 illustrates the relative positions of lasing transitions in  $^{14}\text{C}^{16}\text{O}_2$ ,  $^{16}\text{O}^{13}\text{C}^{18}\text{O}$ ,  $^{16}\text{O}^{12}\text{C}^{18}\text{O}$  and  $^{12}\text{C}^{16}\text{O}_2$  isotopes. We previously published [2], [3] a similar chart for the  $^{13}\text{C}^{18}\text{O}_2$ ,  $^{13}\text{C}^{16}\text{O}_2$  and  $^{12}\text{C}^{18}\text{O}_2$  isotopes.

It is thus clear that the spectral purity, frequency stability, and resettability together with the availability of well over a thousand lasing transitions uniquely endow the  $\text{CO}_2$  system for either direct use in high resolution spectroscopy, or as a secondary frequency standard in hetero-

TABLE I  
Difference Frequencies Measured Between  $^{16}\text{O}^{12}\text{C}^{18}\text{O}$  and  $^{12}\text{C}^{16}\text{O}_2$  Lasing Transitions

Isotope	Reference	Measured	Meas.-Calc.	
	Line	$f(\text{I}) - f(\text{R})$ (MHz)	(kHz)	
I	P(36)	I	23093.872213	0.319
I	F(30)	I	24056.453370	-4.910
I	P(28)	I	24281.326590	11.685
I	F(26)	I	24458.722416	-9.601
I	P(12)	I	24410.301202	-0.837
I	F(20)	I	24293.464805	7.006
I	R(22)	I	15492.423925	-6.201
I	F(24)	I	14661.591163	2.163
I	R(26)	I	13801.985927	-3.534
I	B(28)	I	12914.731880	4.148
I	R(30)	I	12000.945390	1.706
I	F(32)	I	11061.821500	-1.943
II	P(24)	II	-13727.654393	-0.455
II	F(23)	II	12200.062893	-1.532
II	P(21)	II	12550.189553	9.409
II	F(20)	II	-12234.574563	-1.442
II	P(19)	II	13033.172350	-2.832
II	R(13)	II	3066.650077	-3.714
II	R(15)	II	6484.301600	7.754
II	B(19)	II	13634.173280	-7.108
Standard deviation =		8.226 kHz		

TABLE II  
Band Centers and Rotational Constants (in MHz) for  $^{16}\text{O}^{12}\text{C}^{18}\text{O}$

NU	=	28968012.096378	$\pm 2.425\text{E-}02$
NU	=	32158350.546717	$\pm 9.860\text{E-}02$
B	=	10951.024273309	$\pm 3.579\text{E-}04$
001			
B - E	=	96.700681735529	$\pm 1.40\text{E-}04$
I 001			
B - B	=	84.981411491412	$\pm 8.990\text{E-}04$
II 001			
D	=	3.5527097121690D-03	$\pm 4.490\text{E-}07$
001			
D - E	=	-4.8755934078738D-04	$\pm 2.277\text{E-}07$
I 001			
D - D	=	5.4516002699856D-04	$\pm 2.481\text{E-}06$
II 001			
H	=	9.7056436467953D-10	$\pm 2.468\text{E-}10$
001			
B - R	=	2.2601804334360D-09	$\pm 1.079\text{E-}10$
I 001			
B - B	=	5.1398380543550D-09	$\pm 2.109\text{E-}09$
II 001			

dyne spectroscopy with tunable lasers, or in precision IR synthesis which involves frequency mixing. Examples of such uses will be given in the remaining part of this paper.

#### CO<sub>2</sub> LASER APPLICATIONS IN IR SPECTROSCOPY AND SYNTHESIS

The examples described in this section have been selected because of some personal interest or involvement of the author and are not meant to be all inclusive. By comparison with selected, doubled CO<sub>2</sub> transitions [12] the entire CO laser spectrum may be also utilized as a secondary frequency standard in the 4.9 to 7.5- $\mu\text{m}$  portion of the infrared spectrum. With the sole exception of the saturation resonance stabilization technique using the 4.3- $\mu\text{m}$  spontaneous emission, all other aspects of this paper can

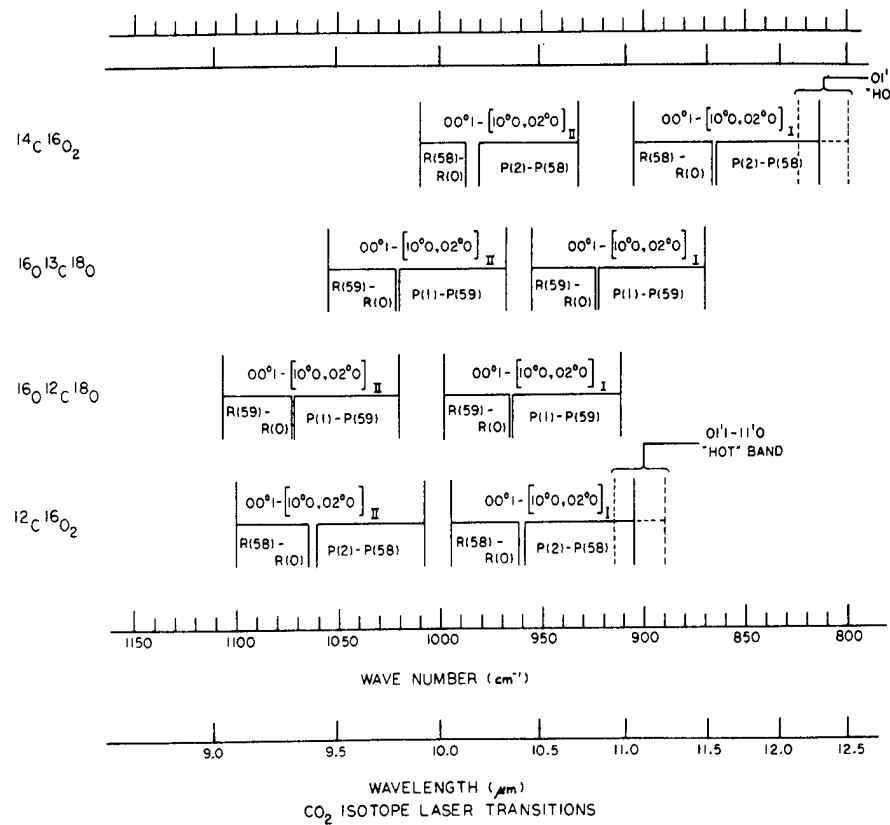


Fig. 3. Comparison of the frequency domain of rare  $\text{CO}_2$  isotope lasers with  $^{12}\text{C}^{16}\text{O}_2$ .

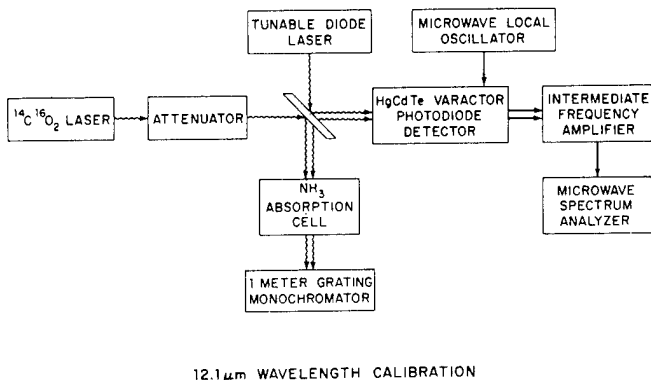


Fig. 4. Experimental setup used to calibrate  $\text{NH}_3$  absorption lines at  $12.1 \mu\text{m}$ .

be easily extended to the molecular CO laser system. Stable, sealed-off CO laser operation has been previously demonstrated [13]. The Lamb dip in CO lasers [14] can be used to set the laser transitions well within 1 MHz of line center. The HgCdTe varactor photodiodes are just as useful at CO wavelengths. Indeed, microwave frequency beats between CO laser transitions equivalent to the one shown in Fig. 2 have been previously described [2], [12], [15], [16].

Fig. 4 illustrates probably the most precise measurement method available to date in the calibration of absorption spectra. In the experimental arrangement of Fig. 4, the outputs of a tunable diode laser and a  $^{14}\text{C}^{16}\text{O}_2$  laser are combined by a beam splitter. One part of the combined

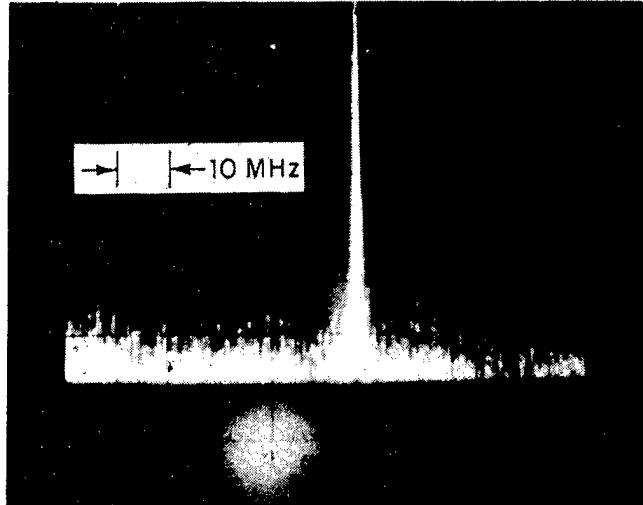


Fig. 5. Spectrum analyzer display of a 6775-MHz beat frequency between a  $^{14}\text{C}^{16}\text{O}_2$  laser transition and a tunable diode laser probe held to one of the  $\text{NH}_3$  absorption lines near  $12.1 \mu\text{m}$ .

radiation is heterodyned on a fast HgCdTe varactor photodiode [11], and the beatnote displayed and measured by a microwave spectrum analyzer (or counter). The other part of the combined laser radiation is used to probe an absorption cell, which in this particular experiment was filled with  $\text{NH}_3$  at a pressure of 5 torr.

Fig. 5 shows a heterodyne beat frequency of 6775 MHz between the  $^{14}\text{C}^{16}\text{O}_2$  laser and the diode laser tuned to one of the  $\text{NH}_3$  absorption lines near  $12.1 \mu\text{m}$ . With the  $\text{CO}_2$

TABLE III  
Beat Frequency Generation in the 0- to 2000-MHz Range by  
Synthesis of  $^{12}\text{C}^{16}\text{O}_2$  and  $^{16}\text{O}^{12}\text{C}^{18}\text{O}$  Isotope Laser Transitions

$\Delta\nu$ (MHz)	$\pm n \times \nu_{^{12}\text{C}^{16}\text{O}_2}$	$\pm n \times \nu_{^{16}\text{O}^{12}\text{C}^{18}\text{O}}$
3.590500	- 1 * 16012C160 (0001,1000 P ( 6)	- 1 * 16012C180 (0001,1000 P ( 13)
27.790000	- 1 * 16012C160 (0001,0200 R ( 8)	- 1 * 16012C180 (0001,0200 P ( 3)
68.384400	- 1 * 16012C160 (0001,1000 R ( 14)	- 1 * 16012C180 (0001,1000 R ( 7)
144.304800	- 1 * 16012C160 (0001,1000 R ( 16)	- 1 * 16012C180 (0001,1000 R ( 9)
197.785900	- 1 * 16012C160 (0001,1000 R ( 4)	1 * 16012C180 (0001,1000 P ( 11)
285.483700	- 1 * 16012C160 (0001,1000 R ( 12)	1 * 16012C180 (0001,1000 R ( 5)
248.712600	- 1 * 16012C160 (0001,1000 R ( 8)	- 1 * 16012C180 (0001,1000 P ( 15)
262.406100	- 1 * 16012C160 (0001,0200 R ( 24)	- 1 * 16012C180 (0001,0200 R ( 11)
356.102700	- 1 * 16012C160 (0001,1000 R ( 2)	1 * 16012C180 (0001,1000 P ( 9)
386.221600	- 1 * 16012C160 (0001,1000 R ( 10)	1 * 16012C180 (0001,1000 R ( 3)
391.546300	- 1 * 16012C160 (0001,1000 R ( 18)	- 1 * 16012C180 (0001,1000 R ( 11)
489.692100	- 1 * 16012C160 (0001,1000 R ( 8)	1 * 16012C180 (0001,1000 R ( 1)
518.390200	- 1 * 16012C160 (0001,1000 R ( 0)	1 * 16012C180 (0001,1000 P ( 6)
538.247100	- 1 * 16012C160 (0001,1000 R ( 10)	- 1 * 16012C180 (0001,1000 P ( 17)
550.550800	- 1 * 16012C160 (0001,1000 R ( 60)	- 1 * 16012C180 (0001,1000 R ( 54)
568.188400	- 1 * 16012C160 (0001,1000 R ( 2)	1 * 16012C180 (0001,1000 P ( 4)
573.327800	- 1 * 16012C160 (0001,1000 R ( 58)	1 * 16012C180 (0001,1000 R ( 52)
581.483900	- 1 * 16012C160 (0001,1000 R ( 4)	1 * 16012C180 (0001,1000 P ( 2)
672.434700	- 1 * 16012C160 (0001,1000 R ( 20)	- 1 * 16012C180 (0001,1000 R ( 13)
872.840600	- 1 * 16012C160 (0001,1000 P ( 12)	- 1 * 16012C180 (0001,1000 P ( 19)
985.995100	- 1 * 16012C160 (0001,1000 R ( 22)	- 1 * 16012C180 (0001,1000 R ( 15)
1163.742900	- 1 * 16012C160 (0001,0200 R ( 34)	- 1 * 16012C180 (0001,0200 R ( 20)
1253.120000	- 1 * 16012C160 (0001,1000 P ( 14)	- 1 * 16012C180 (0001,1000 P ( 21)
1331.221500	- 1 * 16012C160 (0001,1000 R ( 24)	- 1 * 16012C180 (0001,1000 R ( 17)
1369.368300	- 1 * 16012C160 (0001,0200 R ( 60)	- 1 * 16012C180 (0001,0200 R ( 42)
1526.584100	- 1 * 16012C160 (0001,0200 R ( 42)	- 1 * 16012C180 (0001,0200 R ( 27)
1532.085300	- 1 * 16012C160 (0001,0200 R ( 50)	1 * 16012C180 (0001,0200 R ( 34)
1679.691900	- 1 * 16012C160 (0001,1000 P ( 16)	- 1 * 16012C180 (0001,1000 P ( 23)
1680.857900	- 1 * 16012C160 (0001,1000 R ( 62)	- 1 * 16012C180 (0001,1000 R ( 56)
1688.788900	- 1 * 16012C160 (0001,1000 R ( 56)	1 * 16012C180 (0001,1000 R ( 50)
1707.075200	- 1 * 16012C160 (0001,1000 R ( 26)	- 1 * 16012C180 (0001,1000 R ( 19)
1948.147600	- 1 * 16012C160 (0001,0200 R ( 6)	- 1 * 16012C180 (0001,0200 P ( 5)
2011.583500	- 1 * 16012C160 (0001,0200 R ( 10)	1 * 16012C180 (0001,0200 P ( 1)
2034.739500	- 1 * 16012C160 (0001,0200 R ( 56)	1 * 16012C180 (0001,0200 R ( 39)
2112.482400	- 1 * 16012C160 (0001,1000 R ( 28)	- 1 * 16012C180 (0001,1000 R ( 21)
2153.141800	- 1 * 16012C160 (0001,1000 P ( 18)	- 1 * 16012C180 (0001,1000 P ( 25)
2546.332500	- 1 * 16012C160 (0001,1000 R ( 30)	- 1 * 16012C180 (0001,1000 R ( 23)
2674.033500	- 1 * 16012C160 (0001,1000 P ( 20)	- 1 * 16012C180 (0001,1000 P ( 27)
2793.931300	- 1 * 16012C160 (0001,1000 R ( 54)	1 * 16012C180 (0001,1000 R ( 48)
2815.512100	- 1 * 16012C160 (0001,1000 R ( 64)	- 1 * 16012C180 (0001,1000 R ( 58)
2913.889200	- 1 * 16012C160 (0001,0200 R ( 36)	1 * 16012C180 (0001,0200 R ( 22)

laser stabilized to its line center and the diode laser locked to the absorption line to be measured, heterodyne calibration can provide an accuracy not presently available by any other method.

At Kitt Peak National Observatory, in a whole series of beautiful experiments, heterodyne detection was used to measure CO<sub>2</sub> emission lines in the atmospheres of Venus and Mars. The observed frequencies have been combined with a knowledge of the CO<sub>2</sub> transition rest frequencies and the center of mass velocity of the planet to determine the line-of-sight wind velocities in the upper atmosphere of Venus [18], [19].

In heterodyne experiments with CO<sub>2</sub> lasers it is often advantageous to use a local oscillator with a precisely known offset frequency. For instance knowledge of the 910.365-MHz beat frequency between the  $^{13}\text{C}^{16}\text{O}_2$  [10°, 02°]I P(16) and the  $^{12}\text{C}^{16}\text{O}_2$  01<sup>11</sup> – 11<sup>10</sup> band P(31) transitions provided a convenient choice in the observation of hot band emission lines in the atmosphere of Mars [19].

The computerized setup shown in Fig. 1 gives great flexibility in the processing and use of accumulated experimental results. For example, Table III shows the beat frequencies from 0 to 2000 MHz, computed and sorted for the  $^{12}\text{C}^{16}\text{O}_2$  and  $^{16}\text{O}^{12}\text{C}^{18}\text{O}$  isotopes.

Microwave (or lower) frequency generation may be achieved with a single laser filled with a mixture of CO<sub>2</sub> isotopes. The spectral purity and long term stability of the (self-) beatnotes obtained in this way may only be com-

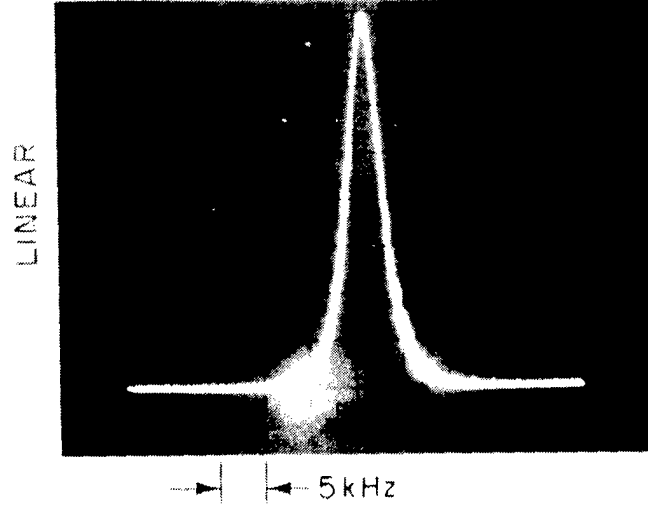


Fig. 6. Spectrum analyzer display of 3,165-MHz beat frequency of the  $^{14}\text{C}^{16}\text{O}_2$  00<sup>1</sup> – [10°, 02°]II band P(10) and the  $^{12}\text{C}^{16}\text{O}_2$  00<sup>1</sup> – [10°, 02°]I R(18) transitions.

pared to stabilized oscillators of the highest quality. Fig. 6 shows the spectrum analyzer display of the 3165-MHz self-beat frequency of the  $^{14}\text{C}^{16}\text{O}_2$  00<sup>1</sup> – [10°, 02°]II P(10) and the  $^{12}\text{C}^{16}\text{O}_2$  00<sup>1</sup> – [10°, 02°]I R(18) transitions. The spectral purity of such self-beats is explained by the fact that the fractional frequency stability at the microwave beat frequency will be identical to the stability of the laser frequency itself. Short-term stabilities of  $10^{-11}$  to  $10^{-13}$  are routinely achieved with well designed and

TABLE IV

Computerized IR Synthesis at 16  $\mu\text{m}$  to Find All Possible  $\text{CO}_2$  Isotope Line Combinations for which the Difference Frequency Between Frequency Doubled  $^{14}\text{C}^{16}\text{O}_2$  and Any Other  $\text{CO}_2$  Transition Will Fall Within  $625.0 \pm 0.1 \text{ cm}^{-1}$

$\nu_S (\text{cm}^{-1})$	$=$	$2 \times \nu_{^{14}\text{C}^{16}\text{O}_2}$	$-1 \times \nu_{\text{CO}_2}$
624.901199	=	2 * 16014C160 (0001,1000 P ( 62)	-1 * 18012C180 (0001,1000 R ( 56)
624.901502	=	2 * 16014C160 (0001,1000 P ( 8)	-1 * 18012C180 (0001,0200 R ( 16)
624.920791	=	2 * 16014C160 (0001,1000 P ( 58)	-1 * 16013C180 (0001,0200 R ( 22)
624.923799	=	2 * 16014C160 (0001,1000 P ( 44)	-1 * 16013C160 (0001,0200 R ( 18)
624.949936	=	2 * 16014C160 (0001,1000 P ( 34)	-1 * 16013C180 (0001,0200 R ( 47)
624.956395	=	2 * 16014C160 (0001,1000 P ( 34)	-1 * 18013C180 (0001,0200) R ( 38)
624.960880	=	2 * 16014C160 (0001,1000 P ( 22)	-1 * 16012C180 (0001,0200) P ( 2)
624.965292	=	2 * 16014C160 (0001,1000 P ( 42)	-1 * 16012C180 (0001,0200) P ( 44)
624.968260	=	2 * 16014C160 (0001,1000 P ( 32)	-1 * 16012C180 (0001,0200) P ( 24)
624.976181	=	2 * 16014C160 (0001,1000 P ( 20)	-1 * 16012C160 (0001,0200) R ( 14)
624.977011	=	2 * 16014C160 (0001,1000 P ( 6)	-1 * 16012C180 (0001,0200) R ( 40)
624.982866	=	2 * 16014C160 (0001,1000 P ( 30)	-1 * 16013C180 (0001,0200) R ( 64)
624.999227	=	2 * 16014C160 (0001,1000 R ( 0)	-1 * 18012C180 (0001,0200) R ( 42)
625.000768	=	2 * 16014C160 (0001,1000 P ( 18)	-1 * 18012C180 (0001,0200) P ( 8)
625.013035	=	2 * 16014C160 (0001,1000 P ( 32)	-1 * 16013C180 (0001,0200) R ( 55)
625.019624	=	2 * 16014C160 (0001,1000 P ( 50)	-1 * 16012C180 (0001,0200) P ( 59)
625.024311	=	2 * 16014C160 (0001,1000 P ( 42)	-1 * 16013C160 (0001,0200) R ( 24)
625.032336	=	2 * 16014C160 (0001,1000 P ( 26)	-1 * 18012C180 (0001,0200) P ( 26)
625.035214	=	2 * 16014C160 (0001,1000 P ( 2)	-1 * 16012C180 (0001,0200) R ( 54)
625.046729	=	2 * 16014C160 (0001,1000 P ( 28)	-1 * 16012C160 (0001,0200) P ( 4)
625.051687	=	2 * 16014C160 (0001,1000 P ( 46)	-1 * 16013C160 (0001,0200) R ( 12)
625.065110	=	2 * 16014C160 (0001,1000 P ( 12)	-1 * 16012C180 (0001,0200) R ( 22)
625.077193	=	2 * 16014C160 (0001,1000 P ( 60)	-1 * 16012C180 (0001,1000) R ( 62)
625.087914	=	2 * 16014C160 (0001,1000 P ( 64)	-1 * 16013C160 (0001,0200) P ( 30)

CO<sub>2</sub> ISOTOPE LASER FREQUENCY SYNTHESIS

$$\nu_S \approx 625.0 \pm 0.1 \text{ cm}^{-1}$$

$$\nu_S \approx 18.750 \pm 0.003 \text{ THz}$$

$$\lambda_S \approx 16.00000 \pm 0.00256 \mu\text{m}$$

acoustically shielded CO<sub>2</sub> lasers in a normal laboratory environment [20].

Table IV illustrates IR synthesis at 16  $\mu\text{m}$ , in which the computer was given the task to find all possible CO<sub>2</sub> isotope line combinations for which the difference frequency between frequency doubled  $^{14}\text{C}^{16}\text{O}_2$  transitions and any other CO<sub>2</sub> transition will fall within  $625.0 \pm 0.1 \text{ cm}^{-1}$ . (It should be noted, however, that Table IV was computed from our preliminary spectrometer measurements on  $^{14}\text{C}^{16}\text{O}_2$  and should not be considered final and accurate, but rather as an example of methodology.)

## CONCLUSIONS

Rare CO<sub>2</sub> isotopes can provide a many-fold expansion of the already highly useful spectral range of CO<sub>2</sub> lasers. In terms of number of lasing transitions, power output, gain, stability, and sealed-off cw operation characteristics, rare isotope lasers are generally similar to the commonly used  $^{12}\text{C}^{16}\text{O}_2$  lasers. Since sealed-off CO<sub>2</sub> laser operating life times of over 10 000 h have been reported by a number of laboratories, the additional cost of a few torr-liters of isotope required for a properly designed laser is not significant.

Even the few examples given in this paper make it quite clear that the spectral purity, frequency stability and re-settability together with the availability of well over a thousand lasing transitions uniquely endow the CO<sub>2</sub> system for either direct use in high resolution spectroscopy

or as a secondary frequency standard in heterodyne spectroscopy with tunable lasers, or in precision IR synthesis which involves frequency mixing.

A systematic and precise evaluation of the band centers, rotational constants, and lasing transition frequencies of the CO<sub>2</sub> isotopes is under way. These data will also be of great value in evaluating the potential function under the influence of which the nuclei are moving.

## ACKNOWLEDGMENT

The author is deeply appreciative to K. Nill for collaboration in heterodyne spectroscopy with a tunable diode laser, and to D. L. Spears for providing the fast HgCdTe varactor photodiodes.

## REFERENCES

- [1] For a review of previous work on CO<sub>2</sub> isotope lasers see the introduction in [2] or [3].
- [2] C. Freed, D. L. Spears, R. G. O'Donnell, and A. H. M. Ross, "Precision heterodyne calibration," in *Proc. Laser Spectroscopy Conf.*, (Vail, CO), June 25-29, 1973. Also in *Laser Spectroscopy*, R. A. Brewer and A. Mooradian, Eds. New York: Plenum Press, 1975, pp. 171-191.
- [3] C. Freed, A. H. M. Ross, and R. G. O'Donnell, "Determination of laser line frequencies and vibrational-rotational constants of the  $^{12}\text{C}^{18}\text{O}_2$ ,  $^{13}\text{C}^{16}\text{O}_2$ , and  $^{13}\text{C}^{18}\text{O}_2$  isotopes from measurements of CW beat frequencies with fast HgCdTe photodiodes and microwave frequency counters," *J. Molecular Spectrosc.*, vol. 49, p. 439, 1974.
- [4] T. J. Bridges and T. Y. Chang, "Accurate rotational constants of

<sup>12</sup>C<sup>16</sup>O<sub>2</sub> from measurements of CW beats in bulk GaAs between CO<sub>2</sub> vibrational-rotational laser lines," *Phys. Rev. Lett.*, vol. 22, pp. 811-814, Apr. 21, 1969.

[5] F. R. Petersen, D. G. McDonald, J. D. Cupp, and B. L. Danielson, "Accurate rotational constants, frequencies, and wavelengths from <sup>12</sup>C<sup>16</sup>O<sub>2</sub> lasers stabilized by saturated absorption," in *Proc. Laser Spectroscopy Conf.*, Vail, CO., June 25-29, 1973.

[6] K. M. Evenson, J. S. Wells, F. R. Petersen, B. L. Danielson, and G. W. Day, "Accurate frequencies of molecular transitions used in laser stabilization: the 3.39- $\mu$ m transition in CH<sub>4</sub> and the 9.33- and 10.18- $\mu$ m transitions in CO<sub>2</sub>," *Appl. Phys. Lett.*, vol. 22, pp. 192-195, Feb. 15, 1973.

[7] C. Freed, "Designs and experiments relating to stable lasers," in *Proc. Frequency Standards and Metrology Seminar* (University Laval, Quebec, P.Q., Canada), pp. 226-261, Sept. 1, 1971.

[8] C. Freed and A. Javan, "Standing-wave saturation resonances in the 10.6  $\mu$ m transitions observed in a low-pressure room-temperature absorber gas," *Appl. Phys. Lett.*, vol. 16, pp. 53-56, July 15, 1970.

[9] —, "Standing-wave saturation resonances in room temperature CO<sub>2</sub> 10.6  $\mu$ m absorption lines," Paper 4.4 presented at the 6th Int. Quantum Electronics Conf., Sept. 1970, Kyoto, Japan.

[10] C. Freed, "Frequency stabilization of CO<sub>2</sub> lasers," in *Proc. 29th Annu. Symp. Frequency Control* (Atlantic City, NJ, May 28-30, 1975), pp. 330-337, 1975.

[11] D. L. Spears and C. Freed, "HgCdTe varactor photodiode detection of CW CO<sub>2</sub> laser beats beyond 60 GHz," *Appl. Phys. Lett.*, vol. 23, p. 445, 1973.

[12] R. S. Eng, H. Kildal, J. C. Mikkelsen, and D. L. Spears, "Determination of absolute frequencies of <sup>12</sup>C<sup>16</sup>O and <sup>13</sup>C<sup>16</sup>O laser lines," *Appl. Phys. Lett.*, vol. 24, pp. 231-233, 1974.

[13] C. Freed, "Sealed-off operation of stable CO lasers," *Appl. Phys. Lett.*, vol. 18, pp. 458-461, 1974.

[14] C. Freed and H. A. Haus, "Lamb dip in CO lasers," *IEEE J. Quantum Electron.*, vol. QE-9, pp. 219-226, 1973.

[15] H. Kildal, R. S. Eng, and A. H. M. Ross, "Heterodyne measurements of <sup>12</sup>C<sup>16</sup>O laser frequencies and improved Dunham coefficients," *J. Molecular Spectrosc.*, vol. 53, pp. 479-488, 1974.

[16] A. H. M. Ross, R. S. Eng, and H. Kildal, "Heterodyne measurements of <sup>12</sup>C<sup>18</sup>O, and <sup>13</sup>C<sup>18</sup>O laser frequencies; Mass dependence of Dunham coefficients," *Optics Commun.*, vol. 12, pp. 433-438, Dec. 1974.

[17] C. Freed and K. Nill, "12.2  $\mu$ m wavelength calibration," Semiannual Report in Support of the Jumper Program for Laser Isotope Separation, pp. 70-78, Dec. 1975.

[18] A. L. Betz, M. A. Johnson, R. A. McLaren, and E. C. Sutton, "Heterodyne detection of CO<sub>2</sub> emission lines and wind velocities in the atmosphere of Venus," to be published.

[19] —, "Infrared heterodyne spectroscopy of CO<sub>2</sub> in the atmosphere of Mars," to be published.

[20] C. Freed, "Design and short-term stability of single-frequency CO<sub>2</sub> lasers," *IEEE J. Quant Electron.*, vol. QE-4, p. 404, 1968.

# The dynamics of air breakdown initiated by a particle in a laser beam\*

D. E. Lencioni and L. C. Pettingill

Massachusetts Institute of Technology, Lincoln Laboratory, Lexington, Massachusetts 02173

(Received 11 October 1976; accepted for publication 4 January 1977)

An experimental study was made of air breakdown induced by a single 50- $\mu\text{m}$  particle at the focus of a 5- $J$  pulsed 10.6- $\mu\text{m}$  laser beam. The breakdown thresholds for 50- $\mu\text{m}$  carbon and NaCl particles were  $\approx 5 \times 10^7$  and  $8 \times 10^7$   $\text{W/cm}^2$ . The dynamics of plasma formation were studied with an image-converter camera. At low intensities the plasma grew as an axisymmetric volume surrounding the particle. At higher intensities the plasma formed as a thin disk which propagated towards the laser. The growth rates were measured as a function of beam intensity. The transmitted laser energy was measured as a function of beam parameters and compared to an idealized dynamics model.

PACS numbers: 52.50.Jm, 42.68.Rp, 42.60.He

It has been established experimentally<sup>1-6</sup> and theoretically<sup>7,8</sup> that the threshold for laser-induced breakdown in air can be lowered substantially by the presence of dust particles in the laser beam. In this paper we give the results of an experimental study of air breakdown triggered by a single 50- $\mu\text{m}$  carbon particle positioned at the center of a focused 10.6- $\mu\text{m}$  laser beam. Results are given for the effects of spot size on the breakdown threshold, the growth dynamics of the breakdown within the laser beam, and the extinction of the laser beam due to the breakdown plasma.<sup>9</sup>

The experimental apparatus is shown in Fig. 1. The laser beam was provided by a Febetron- $\text{CO}_2$  laser operated in the short-pulse mode.<sup>10</sup> The pulse shape for this device consisted of a 150-nsec spike and, with  $\text{N}_2$  in the lasing mixture, a 2- $\mu\text{sec}$  tail (Fig. 2). The peak output power was  $\approx 10$  MW. The beam was focused with spherical mirrors. 50- $\mu\text{m}$  particles were dropped into the focal volume from an activated dispenser through a hypodermic needle. When a particle was at a pre-selected position in the beam, HeNe laser light was scattered through a microscope system into a PM tube and initiated the experimental triggering sequence. The position of the particle was observed from a back-lighted micrograph obtained by firing a nanolight. With this technique particles could be positioned consistently to within a particle diameter. An image-converter camera, with exposure times down to 10 nsec, was used to obtain time-resolved information on the growth of the breakdown in the beam. The transmitted beam was reimaged and magnified 9 $\times$  at a pair of photon drag detectors to obtain the radial and temporal dependence of the transmitted beam.

The laser-intensity profile at focus was determined from a set of burns of known relative intensity obtained by inserting a diffraction grating in the beam. Also, measurements of the magnified focal plane were made directly with a pair of coaxial annular detectors. The focal spot was approximately Gaussian in shape with a divergence  $D/F \approx 10$  mrad where  $D$  is the  $e^{-1}$  diameter at focus and  $F$  is the mirror focal length.

Figure 3 shows a back-lighted micrograph of a particle taken 6  $\mu\text{sec}$  after being hit by the laser beam incident from the left. This shows what happens to a particle at below threshold intensity. The laser beam heats

one side of the particle to incandescence. The resulting vaporization causes the particle to jet.<sup>11</sup> From the measured velocities it was determined that the particle motion at the peak laser intensity was  $\approx 1 \mu\text{m}$ , which had negligible effect on the breakdown threshold measurements.

The breakdown thresholds (50% probability of breakdown) for 50- $\mu\text{m}$  carbon and NaCl particles were  $\approx 5 \times 10^7$  and  $8 \times 10^7$   $\text{W/cm}^2$ . These are well below the threshold for clean air,<sup>2,12,13</sup>  $3 \times 10^9$   $\text{W/cm}^2$ . As was shown in Refs. 2 and 6, the aerosol breakdown thresholds depend on the size of the particles, with smaller particles having larger thresholds. For single 50- $\mu\text{m}$  carbon particles the threshold was measured for three focal spot diameters (4, 1, and 0.55 mm) and was found to be insensitive to spot size, as would be expected for spots much larger than the particle size.

Figure 4 shows a series of image-converter frames which illustrate the growth of a breakdown at near-threshold intensity. The dashed white lines mark the

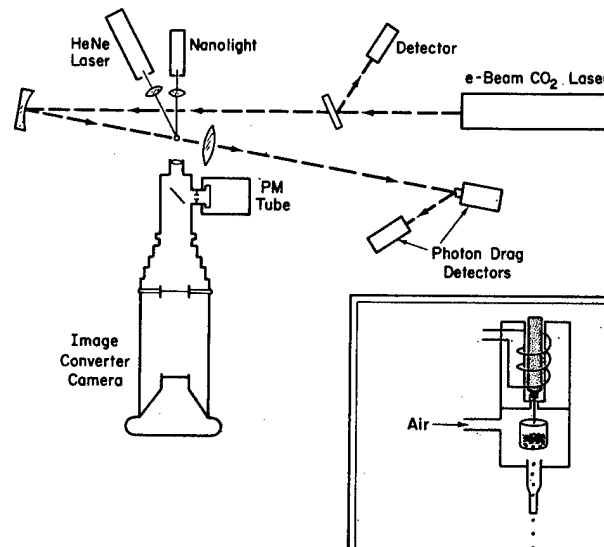


FIG. 1. Experimental apparatus used to study breakdown dynamics. Time-resolved information on the growth dynamics was obtained with the image-converter camera. Particles were placed at a spot in the focal volume with the activated particle dropper shown in the inset.

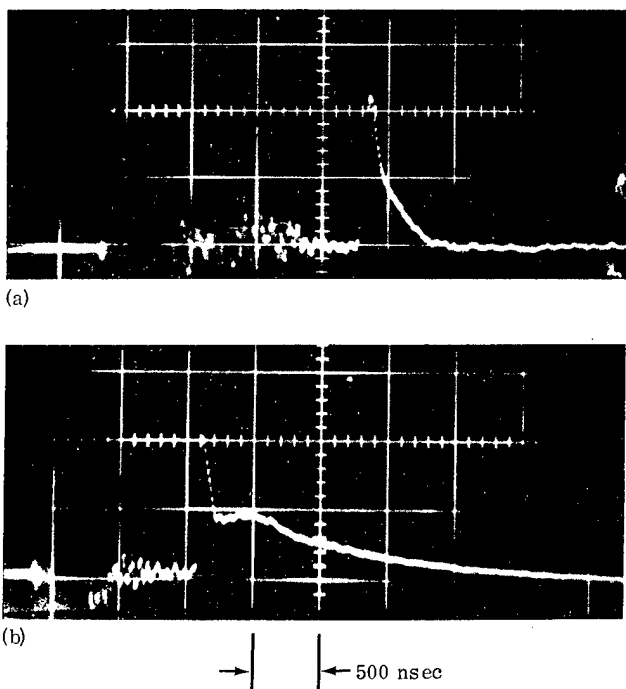


FIG. 2. Laser pulse shape (a) with no  $N_2$  and (b) with  $N_2$  in the lasing mixture.

$e^{-1}$  diameter of the beam which was 1 mm. The laser beam was incident from the left. The four frames were taken on four separate shots at the indicated exposure

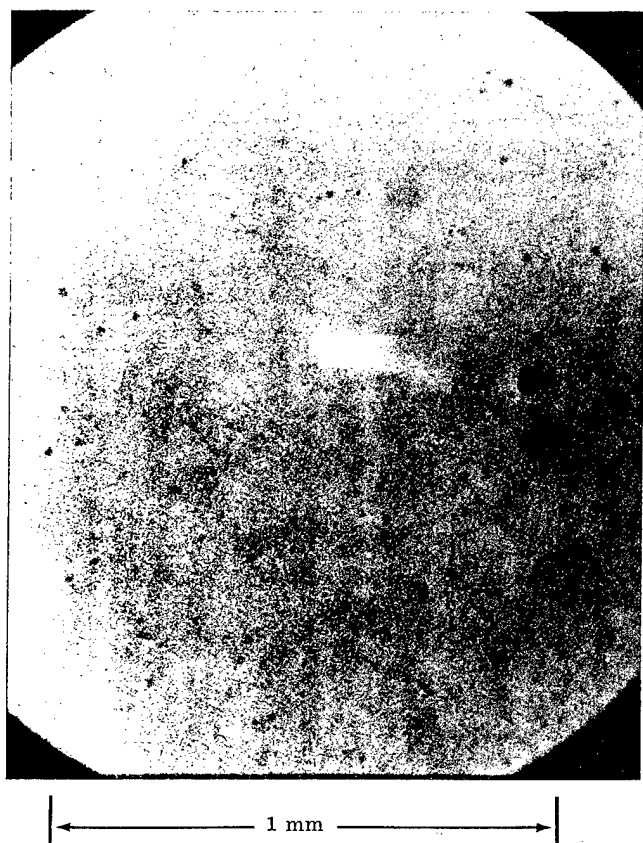


FIG. 3. Back-lighted micrograph of a 50- $\mu m$  carbon particle taken 6  $\mu sec$  after being hit by a laser pulse incident from the left.

$$\bar{I} = 2.4 \times 10^7, I_0 = 4.8 \times 10^7 \text{ W/cm}$$

$\tau$  (nsec)

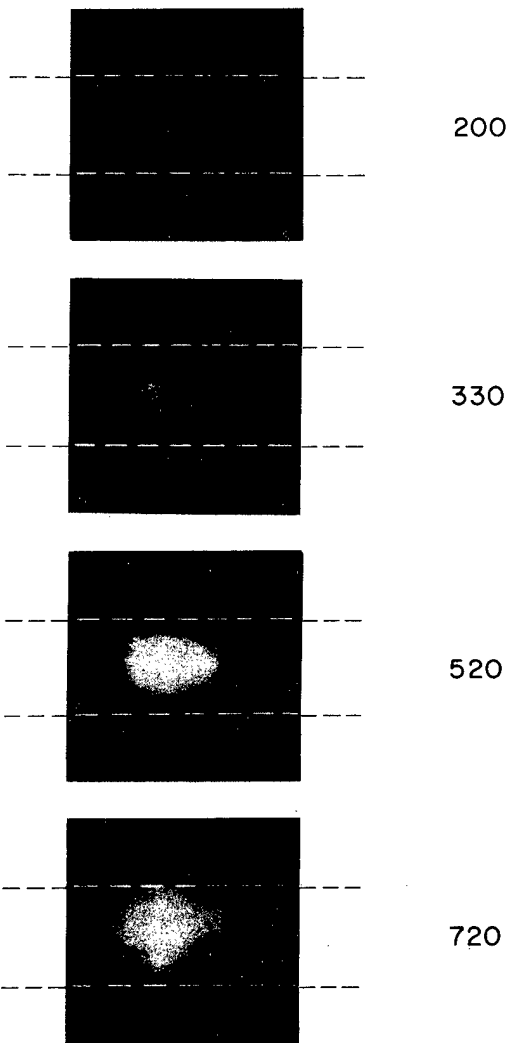


FIG. 4. Series of image-converter frames illustrating breakdown growth at near-threshold intensity. Dashed lines show  $e^{-1}$  diameter of the laser beam which was incident from the left.

times relative to the start of the pulse. The breakdown initiated near the peak laser intensity and grew radially and axially as a volume absorbing plasma. The axial velocity was slightly larger than the radial velocity which had an initial value  $\approx 1.4 \times 10^5$  cm/sec. The velocities were observed to decrease by  $\approx 25\%$  after  $\approx 300$  nsec due probably to the fall off in laser intensity. Note that the particle remains visible in each of the frames.

At high laser intensities the character of the breakdown growth changed abruptly. This is illustrated in Fig. 5 where the intensity was increased above threshold by a factor of 5. The top frame is a time-integrated photograph of the breakdown. In the remaining frames the white dot indicates the position of the particle. For these higher intensities the breakdown developed as a thin absorbing front which propagated towards the laser and grew radially. This type of breakdown growth is

characteristic of the laser-supported denotation wave (LSD) described by Raizer.<sup>14</sup>

The radial and axial velocities obtained from data of this type are shown in Fig. 6 as a function of intensity. At lower intensities both velocity components increased approximately linearly with intensity. At higher intensities the axial velocity varied roughly as  $I^{1/3}$  which is in agreement with planar LSD wave theory.<sup>14</sup>

The extinction of laser intensity by the breakdown plasma for a spot diameter of 1 mm was measured directly by reimaging the focal spot with magnification on two photon drag detectors, one giving the power transmitted through the central disk of radius  $r = 0.023$  cm and the other giving the power through concentric annulus with the outer radius being 0.067 cm. A comparison was made of the arrival time of the luminous front at a given radius within the beam with the time for the cutoff of laser power within that radius. For most

$$\bar{I} = 1.7 \times 10^8 \text{ W/cm}^2$$

$$I_0 = 2.4 \times 10^8 \text{ W/cm}^2$$

$$\tau \text{ (nsec)}$$

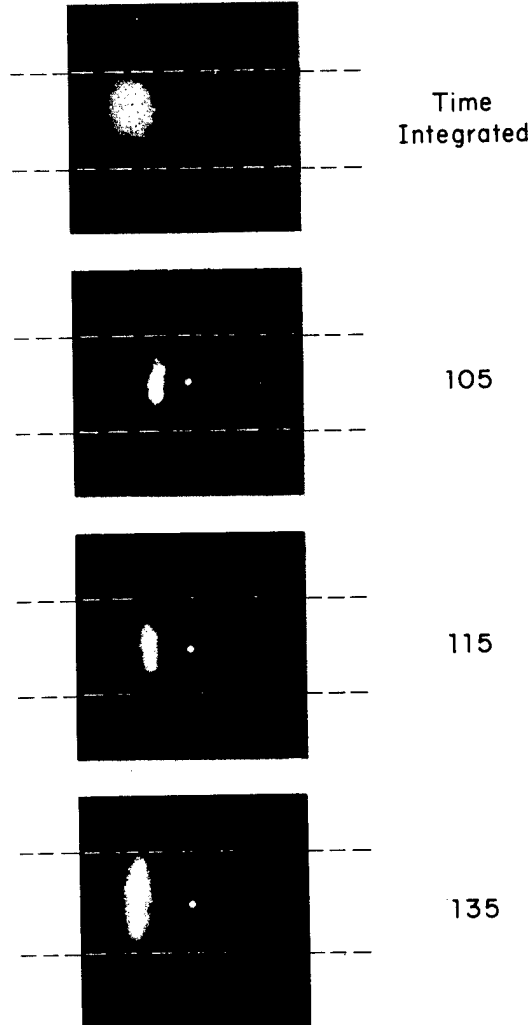


FIG. 5. Breakdown dynamics at five times threshold intensity.

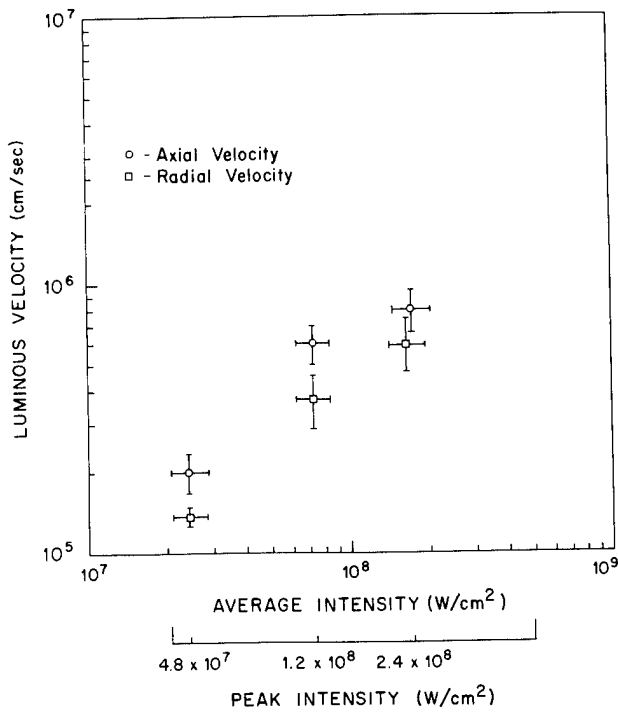


FIG. 6. Axial and radial velocities of particle-initiated breakdown within the beam.

conditions the two times are the same, indicating total laser extinction within the luminous region. However, at low intensity or for small plasma dimensions the cutoff of the laser energy occurred  $\approx 150$  nsec after the arrival of the luminous front, indicating a relatively long absorption depth in the plasma. This is consistent with the character of the breakdown development at low intensities, e.g., Fig. 4. The absorption depths within the breakdown plasma was estimated (neglecting reflective losses) by comparing the luminous thickness with the

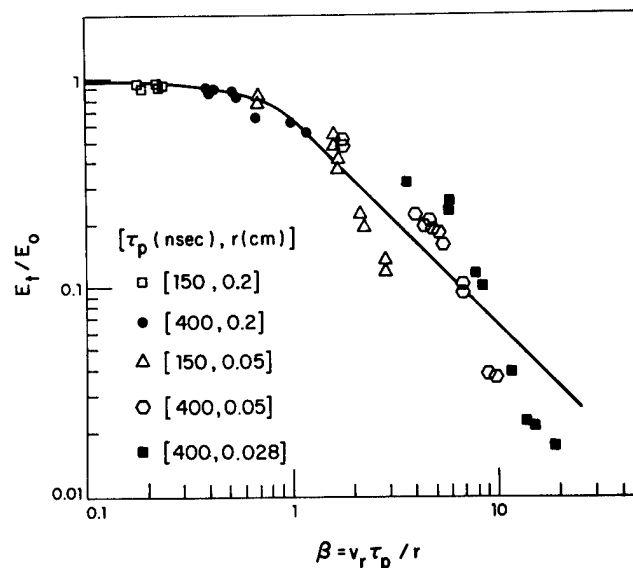


FIG. 7. Fractional energy transmission as a function of beam size  $r$ , pulse length  $\tau_p$ , and beam intensity  $I$ , where  $v_r(I)$  is the radial growth rate at intensity  $I$ . The solid curve is theoretical.

transmitted intensity. At near-threshold intensities  $\delta \approx 0.5$  mm, and at higher intensities  $\delta \approx 0.15$  mm.

These results for the finite radial growth rates indicate that the total energy transmitted through a beam with a particle-induced breakdown should be a strong function of the beam diameter and pulse length. For example, for a large beam and a short pulse length the breakdown does have a chance to grow substantially and causes little attenuation even though a fully developed breakdown has been initiated. These statements can be made more quantitative in terms of an idealized model for the effects of the finite radial growth rate in which we consider a uniform laser beam of radius  $r$  and a rectangular pulse shape of pulse length  $\tau_p$ . If the plasma, assumed to be opaque, grows at a constant radial velocity  $v_r(I)$ , the beam will be cutoff at time  $\tau_c = r/v_r(I)$ . The transmitted energy  $E_t$  is

$$E_t = E_0(1 - \frac{1}{3}\beta^2), \quad \tau_p < \tau_c$$

and

$$E_t = 2E_0/3\beta, \quad \tau_p > \tau_c,$$

where  $E_0$  is the total pulse energy and  $\beta = v_r(I)\tau_p/r$ .

This effect was studied directly by measuring the transmitted energy as a function of the incident pulse energy for three different spot sizes and two pulse lengths. A short pulse length was obtained by removing the  $N_2$  from the lasing mixture. These data are shown in Fig. 7 where the fraction of transmitted energy is shown as a function of the parameter  $\beta$ . The values of  $v_r(I)$  used in the parameter  $\beta$  were obtained from Fig. 6.

The solid curve shows the theoretical model which, even though idealized, is in close agreement with the data.

## ACKNOWLEDGMENTS

The authors would like to thank Dr. Seymour Edelberg for his interest and helpful suggestions and D. P. DeGloria for his technical assistance.

\*Work supported by the Advanced Research Projects Agency of the Department of Defense.

<sup>1</sup>L. C. Marquet, R. J. Hull, and D. E. Lencioni, IEEE J. Quantum Electron. QE-8, 564 (1972).

<sup>2</sup>D. E. Lencioni, Appl. Phys. Lett. 23, 12 (1973).

<sup>3</sup>J. E. Lowder and H. Kleiman, J. Appl. Phys. 44, 5504 (1973).

<sup>4</sup>D. E. Lencioni, Appl. Phys. Lett. 25, 15 (1974).

<sup>5</sup>D. C. Smith and R. T. Brown, J. Appl. Phys. 46, 1146 (1975).

<sup>6</sup>D. E. Lencioni, AGARD Conf. Proc. 183, 31-1 (1976).

<sup>7</sup>G. H. Canavan and P. E. Nielsen, Appl. Phys. Lett. 22, 409 (1973).

<sup>8</sup>F. V. Bunkin and V. V. Savranskii, Sov. Phys.-JETP 38, 1091 (1974).

<sup>9</sup>D. E. Lencioni and L. C. Pettingill, Bull. Am. Phys. Soc. 19, 163 (1974); Lincoln Laboratory Optics Research Report No. 2, 1973 (unpublished).

<sup>10</sup>S. Marcus, Appl. Phys. Lett. 21, 18 (1972).

<sup>11</sup>D. E. Lencioni and J. E. Lowder, IEEE J. Quantum Electron. QE-10, 235 (1974).

<sup>12</sup>G. H. Canavan, W. A. Proctor, P. E. Nielsen, and S. D. Rockwood, IEEE J. Quantum Electron. QE-8, 564 (1972).

<sup>13</sup>N. Kroll and K. M. Watson, Phys. Rev. A 5, 1883 (1972).

<sup>14</sup>Y. P. Raizer, Sov. Phys.-JETP 21, 1009 (1965).

# Hole-boring in clouds by high-intensity laser beams: theory

R. C. Harney

The physics of hole-boring in clouds and fogs by high-intensity ir laser beams is investigated in a zeroth-order approximation. Simple analytical expressions are obtained which describe the phenomena of interest. Application of these expressions to various types of clouds and fogs yields order-of-magnitude estimates of the laser powers required to bore holes of a given size and quality. The power requirements for hole-boring through light ground fogs or thin overcasts are in excess of 100 kW, while hole-boring through thicker overcasts will require laser powers much in excess of 10 MW. Dispersal of ground fogs over an extended area will require laser powers in the  $10^8$ – $10^9$ -W range and thus may not be cost effective simply in terms of energy consumption.

## Introduction

The possible application of high-intensity laser beams to boring holes in clouds or dispersing fogs has received considerable attention because of its obvious potential impacts on long distance communications and transportation safety. Numerous theoretical calculations<sup>1–4</sup> and experiments<sup>5–8</sup> have already been performed with varying degrees of sophistication. However, few of these, if any, have seriously addressed the laser requirements for hole-boring or fog dissipation in practical applications. Consequently, it may be useful at this point to analyze the problem of hole-boring from an elementary point of view to place the problem in its proper technological perspective.

In this paper we examine the physics of hole-boring in a zeroth-order approximation to obtain a few simple analytical expressions describing the phenomena of interest. These simple expressions are then applied to hole-boring in three different types of clouds to obtain order-of-magnitude estimates of the laser powers required to bore a given size and quality of hole. The results indicate that hole-boring through light fogs and thin overcasts will require powers at least of the order of 100 kW, while hole-boring through moderate to heavy overcasts will require powers in excess of 10 MW. Dispersal of ground fog over an extended area will require laser powers in the  $10^8$ – $10^9$ -W range and thus may not be cost effective simply in terms of energy consumption.

## Theory

Fogs and clouds are composed of fine droplets of water roughly spherical in shape. Droplet diameters range from submicrometer to a few tens of micrometers with mean droplet diameters in the 1–5- $\mu\text{m}$  range.<sup>9</sup> The total water content in a cloud may vary from 0.01 g/m<sup>3</sup> to 10 g/m<sup>3</sup>.

Consider a single droplet of water of radius  $R$  immersed in a laser beam of intensity  $I$  and 10.6- $\mu\text{m}$  wavelength. If the diameter of the droplet is of the order of or smaller than the absorption length of the laser radiation, the droplet will be uniformly heated throughout its volume. As will be seen shortly, this condition is valid for the majority of droplets in almost any cloud. Consequently, the rate of energy deposition in the droplet due to absorption of the laser light is proportional to the volume of the droplet and to the laser intensity:

$$\left. \frac{dE}{dt} \right|_{\text{dep}} = \frac{4\pi}{3} KR^3 I, \quad (1)$$

where  $K$  is the absorption coefficient. Although  $K$  is in actuality a function of  $R$ , in the zeroth-order approximation characteristic of this paper we will assume it to be a constant with a value,  $K \sim 10^3 \text{ cm}^{-1}$ .<sup>10,11</sup> The absorption length is the inverse of  $K$ , so Eq. (1) is valid for droplets with diameters of the order of 10  $\mu\text{m}$  or less. Neglecting heat transfer to the surrounding air and the changing surface energy of the droplet, the rate of energy loss of the droplet is proportional to the mass loss through vaporization:

$$\left. \frac{dE}{dt} \right|_{\text{vap}} = H \frac{dM}{dt} = 4\pi R^2 H \rho \frac{dR}{dt}, \quad (2)$$

where  $H$  is the heat of vaporization of water (2300 J/g) and  $\rho$  is the density of water (1 g/cm<sup>3</sup>). In the adiabatic approximation the rate of energy loss equals the rate of energy deposition. Consequently,

The author is with MIT Lincoln Laboratory, Lexington, Massachusetts 02173.

Received 25 April 1977.

$$\frac{KR\dot{I}}{3} = H\rho \frac{dR}{dt}; \quad (3)$$

or upon integration

$$R(t) = R_o \exp \left[ -\frac{K}{3H\rho} \int_0^t I(t) dt \right]. \quad (4)$$

The vaporization time  $t_v$  may be defined as the time required for the droplet to shrink to some arbitrary fraction of its original volume when exposed to a constant intensity  $I_o$ . A volume reduction of  $e^{-10}$  will reduce all droplets less than 50- $\mu\text{m}$  diam to submicrometer diameters. Since this is mathematically convenient, we will use this factor. From Eq. (4) we now find

$$\ln \frac{R}{R_o} = \frac{-10}{3} = -\frac{KI_o t_v}{3H\rho}, \quad (5)$$

or

$$t_v = \frac{10H\rho}{KI_o} \sim \frac{25}{I_o} \text{ sec} \quad (6)$$

when  $I_o$  is expressed in  $\text{W/cm}^2$ . A minimum possible value for  $t_v$  can be obtained from hydrodynamic considerations. Regardless of the energy deposited, the droplet of vapor cannot expand significantly faster than the sound speed  $C_s$ . For a vapor density reduction of  $10^3$ ,  $C_s = 3 \times 10^4 \text{ cm/sec}$ , and  $R_o = 5 \mu\text{m}$ , we find

$$t_{v\min} \sim \frac{10R_o}{C_s} \sim 2 \times 10^{-7} \text{ sec.} \quad (7)$$

Consequently, increasing the intensity beyond  $10^8 \text{ W/cm}^2$  will have little effect on  $t_v$ .

Now consider a laser beam incident on a cloud of droplets. Initially ( $t = 0$ ) the laser beam is attenuated due to both absorption and scattering. The intensity as a function of distance into the cloud is given by

$$I(x,0) = I_o \exp(-\alpha x), \quad (8)$$

where  $\alpha$  is the extinction coefficient. As with  $K$ ,  $\alpha$  is a function of the distribution of particle diameters. We will assume it to be a constant in time, depending only on the water content  $Q(\text{g/m}^3)$  of the cloud. Thus,

$$\alpha = \langle \epsilon N \pi R_o^2 \rangle = \frac{3Q}{4\rho} \left\langle \frac{\epsilon}{R_o} \right\rangle \sim 10^{-3} Q \text{ cm}^{-1}, \quad (9)$$

where  $\epsilon$  is the Mie efficiency factor ( $\sim 0.3$ ) and  $N$  is the number density of droplets. A value  $R_o \sim 2 \mu\text{m}$  was chosen because droplets in this size range have the most influence on  $\alpha$ .<sup>8,10,11</sup>

The absorption of the laser light causes droplets in the cloud to vaporize. However, because the intensity falls off with distance into the cloud, droplets at the front of the cloud vaporize before droplets at the back of the cloud. The result is a vaporization front which propagates at some velocity  $V$  through the cloud in the direction of the laser beam. Consider a droplet which is a small distance  $dx$  into the cloud. At  $t = t_v$  this droplet will only be partially vaporized, with a radius given by

$$\begin{aligned} R(t_v) &= R_o \exp \left[ -\frac{K}{3H\rho} \int_0^{t_v} I_o \exp(-\alpha dx) dt \right] \\ &= R_o \exp \left[ -\frac{KI_o}{3H\rho} \int_0^{t_v} (1 - \alpha dx) dt \right] \\ &= R_o \exp \left[ -\frac{KI_o}{3H\rho} (t_v - \alpha t_v dx) \right]. \end{aligned} \quad (10)$$

Since at  $t = t_v$  the droplets at  $x = 0$  have just vaporized, they no longer attenuate the beam. Consequently, the droplets at  $x = dx$  will vaporize at time  $t'$  given by

$$\begin{aligned} R(t') &= R_o \exp \left( -\frac{KI_o}{3H\rho} t_v \right) \\ &= R_o \exp \left[ -\frac{KI_o}{3H\rho} (t_v - \alpha t_v dx) - \frac{KI_o}{3H\rho} \int_{t_v}^{t'} dt \right]. \end{aligned} \quad (11)$$

Equation (11) simplifies to

$$\exp \left[ \alpha t_v dx \frac{KI_o}{3H\rho} - (t' - t_v) \frac{KI_o}{3H\rho} \right] = 1, \quad (12)$$

which implies

$$\alpha t_v dx - (t' - t_v) = 0. \quad (13)$$

Consequently, we see that the vaporization front moves with velocity

$$V = \frac{dx}{(t' - t_v)} = \frac{1}{\alpha t_v} \sim 40 \frac{I_o}{Q} \text{ cm/sec}, \quad (14)$$

where we have used our earlier estimates of  $\alpha$  and  $t_v$ . It should be noted that the speed of light sets an upper limit to  $V$ .

If there is a wind in the cloud, droplets will continually move into the laser beam. Even in the absence of a real wind, heating-induced convection and/or Brownian motion will cause an effective wind. If we assume the laser has been on for a time long compared with  $t_v$  (thus we may consider the steady-state solution) and label the wind velocity  $U$ , we find the following simple results. At the front of the cloud the time required for vaporization of the droplets is  $t_v$ . Here the droplets will travel a distance  $U t_v$  into the laser beam before vaporizing. At a distance  $x$  into the cloud, the time required for vaporization of the droplets is  $t_v + x/V$ . At this point the droplets can penetrate a distance  $U t_v + xU/V$  into the laser beam. This behavior is shown schematically in Fig. 1. After the water vapor has been carried out of the laser beam by the wind, it will gradually lose its accumulated heat energy and recondense into droplets. The phenomenon of recondensation has no effect on hole-boring but is of prime importance in fog dispersal, which will be discussed later.

Clearly, if any of the laser beam is to penetrate the cloud completely, the quantity  $U t_v + L U/V$ , where  $L$  is the thickness of the cloud, must be smaller than the beam diameter  $D$ . Thus

$$U t_v + L (U/V) = U t_v (1 + \alpha L) < D. \quad (15)$$

Expressing this inequality in terms of the laser intensity yields

$$I_o > \frac{25U}{D} (1 + 10^{-3} Q L) \text{ W/cm}^2 \quad (16)$$

as the minimum intensity which will bore a hole (of zero size at the back of the cloud) in a given cloud. However,

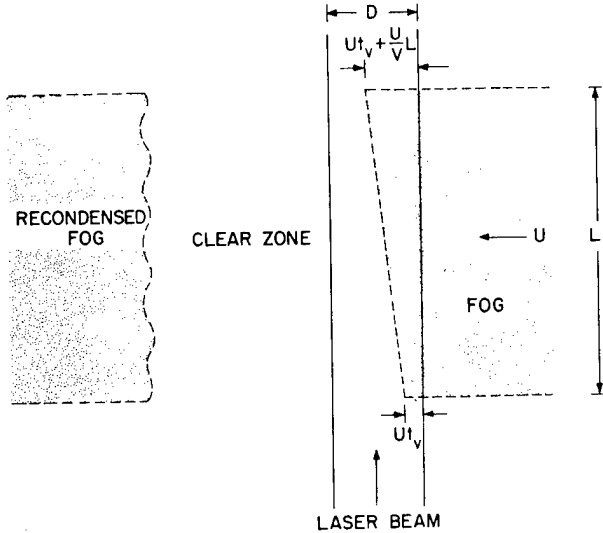


Fig. 1. Schematic of the clearing profile of a cw laser beam. The fog thickness is  $L$ ; the laser beam diameter,  $D$ ; the wind speed,  $U$ ; the vaporization front velocity,  $V$ ; and the vaporization time,  $t_v$ .

in most practical applications, the hole size at the rear of the cloud must be an appreciable fraction of the beam size. This causes an increase in the required intensity by a factor  $(1 - D_e)^{-1}$ , where  $D_e$  is the required hole size expressed as a fraction of the laser beam size. In practical applications, the factor may be as large as 100.

The relations derived above serve to define the behavior of cw laser beams in clouds and fogs. However, we can also discuss the behavior of pulsed laser beams in terms of the same quantities,  $t_v$  and  $V$ . If the pulse duration  $t_p$  is longer than the time required for the vaporization front to be initiated and propagate completely through the cloud,  $t_v + L/V$ , the laser pulse may be effectively treated as a cw beam. After the pulse is over, the hole will be filled in completely by the wind in a time  $t_f = D/U$ .

Consider a pulse of duration  $t_p = t_v + L/V = t_v(1 + \alpha L)$ , which is sufficiently short that the effects of wind may be neglected ( $t_p \ll D/U$ ). Substituting the expression for  $t_v$  we obtain

$$I_o t_p > 25(1 + \alpha L) J/cm^2 \quad (17)$$

as the minimum pulse energy density required to bore a hole. If  $\alpha L \gg 1$ , this reduces to

$$I_o t_p > 25\alpha L = 0.025LQ \text{ J/cm}^2. \quad (18)$$

It is interesting to note that this is 12.5 times the total heat of vaporization of the water contained in a 1-cm<sup>2</sup> column through the cloud.

If  $t_p < t_v + L/V$ , the laser pulse cannot bore a complete hole before the pulse is over. Consider first the case  $t_p < t_{v\min}$ . This limit is applicable to mode-locked or Q-switched laser pulses. In this case no vaporization at all can occur before the pulse is over. However, it still may be possible to deposit enough energy in the droplets so they will vaporize after the pulse is over. For a

complete hole to be bored, the total energy deposited in a droplet at the rear of the cloud must exceed the total vaporization energy of the droplet. This requirement yields the following equation:

$$E_{\text{dep}} = \frac{4\pi R_o^3}{3} K I_o \exp(-\alpha L) t_p > \frac{4\pi R_o^3}{3} \rho H, \quad (19)$$

which implies

$$I_o > \frac{H\rho}{Kt_p} \exp(\alpha L) \sim \frac{2.3}{t_p} \exp(10^{-3}QL) \text{ W/cm}^2. \quad (20)$$

A moving vaporization front will still occur, although it will propagate at a velocity just slightly less than the speed of light. For these ultrashort pulses, if  $H\rho/Kt_p < I_o < \exp(\alpha L)H\rho/Kt_p$ , a hole of length  $L'$  will be bored

$$L' = \frac{1}{\alpha} \ln \left( \frac{I_o K t_p}{H \rho} \right). \quad (21)$$

If  $I_o < H\rho/Kt_p$ , no hole at all will be bored.

For pulses of duration  $t_{v\min} < t_p < t_v$ , no clearing will take place. Droplets at the front of the cloud will be reduced in size but not to the point of complete vaporization. For pulses with durations  $t_v < t_p < t_v + L/V$ , some complete vaporization will occur at the front of the cloud; but a complete hole will not be bored. The length of the hole that will be cleared in this case is given by

$$L' = V(t_p - t_v). \quad (22)$$

Single laser pulses are likely to have little utility in hole-boring applications. However, long trains of repetitive laser pulses may find application. Consider first a train of intensity  $[I_o > \exp(\alpha L)H\rho/Kt_p]$ , ultrashort ( $t_p < t_{v\min}$ ) laser pulses of separation  $t_s$ . The relationship of  $t_s$  and  $t_p$  is clarified in Fig. 2. The first pulse of this train will have bored a complete hole after a time of the order of  $t_{v\min}$  has elapsed. If the pulse separation is such that  $t_{v\min} < t_s < t_f - L/c$ , the wind cannot have completely closed the hole; and a fraction of the second pulse will pass through the cloud unattenuated with the remainder of the pulse serving to reopen the part of the original hole which had been closed. Each succeeding pulse in the train will behave just like the second pulse. If the pulse separation is such that  $t_f - L/c < t_s < t_f$ , the hole formed by the first pulse will be closed but not completely filled with fresh droplets. Consequently,

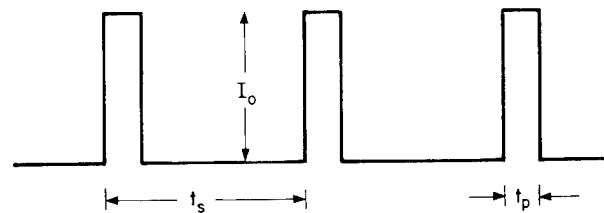


Fig. 2. Characteristic quantities of a laser pulse train.  $I_o$  is the peak intensity;  $t_s$ , the pulse separation;  $t_p$ , the pulse duration. Although a rectangular pulse train is indicated, the relations in the text should be valid for pulses of any shape.

a second pulse of much lower intensity can open the hole again (albeit after the pulse is over). If  $t_s > t_f$ , the hole will be completely filled, and the situation regarding the second pulse is as if the first pulse had never happened. If the pulse intensity is less than that required to bore a hole completely with a single pulse, i.e.,  $I_o < \exp(\alpha L) \cdot H_p / Kt_p$ , and the pulse separation is less than the hole filling time  $t_s < t_f$ , it is possible for a train of pulses to open gradually and maintain a hole as long as the average intensity exceeds the cw limit minimum. For  $\alpha L \gg 1$ , we have the relation

$$I_o \frac{t_p}{t_s} > \frac{10H_p \alpha L U}{KD}. \quad (23)$$

If we now consider pulses with duration  $t_p > t_{v\min}$ , the requirement for maintaining a hole is again that the average intensity exceed the cw limit minimum. Since the phenomenon of hole-boring is a process linear in the intensity, this is to be expected.

### Applications

In the preceding section it was argued that, in boring and maintaining a hole, pulse trains must meet average requirements identical to those of the cw limit. When considering single laser pulses, only long pulses (which can be treated as a cw beam) or very short intense pulses are capable of hole-boring. Consequently, in making estimates of the laser requirements for hole-boring we need consider only the cw and short-pulse limits. Due to the extreme approximations made in the derivations only order of magnitude accuracy can be expected. However, this should be more than adequate for establishing the practicality of hole-boring. We shall consider three kinds of clouds: thin ground fog, moderate overcast, and thunderheads. These examples cover wide ranges of propagation distances, water contents, and wind speeds and should give good indications of where hole-boring may be expected to be practical. For all calculations we will assume a beam diameter  $D = 100$  cm. We begin in the cw case.

**Light Ground Fog ( $Q \sim 0.1$ ,  $L \sim 10^4$  cm,  $U \sim 30$  cm/sec)**

From Eq. (9),  $\alpha \sim 10^{-4}$  cm $^{-1}$ .  
 From Eq. (16),  $I_o > 15$  W/cm $^2$ .  
 Total power is  $I_o D^2 > 150$  kW.  
 From Eq. (14),  $V > 5 \times 10^3$  cm/sec.  
 From Eq. (6),  $t_v < 2.2$  sec.

These results are valid if the beam is on longer than  $t_v + L/V$ , which is roughly 4.2 sec at the minimum intensity.

**Moderate Overcast ( $Q \sim 1$ ,  $L \sim 10^5$  cm,  $U \sim 300$  cm/sec)**

$\alpha \sim 10^{-3}$  cm $^{-1}$ .  
 $I_o > 6.6$  kW/cm $^2$ .  
 Total power > 66 MW.  
 $V > 1.4 \times 10^5$  cm/sec.  
 $t_v < 7$  msec.

These results are valid if the beam is on longer than 0.7 sec at the minimum intensity.

**Thunderhead ( $Q \sim 10$ ,  $L \sim 10^6$  cm,  $U \sim 3000$  cm/sec)**

$\alpha \sim 10^{-2}$  cm $^{-1}$ .  
 $I_o > 6$  MW/cm $^2$ .  
 Total power > 60 GW.  
 $V > 1.2 \times 10^8$  cm/sec.  
 $t_v < 10^{-5}$  sec.

These results are valid if the beam is on longer than 8 msec at the minimum intensity.

Now we examine the ultrashort pulse limit, that is,  $t_p < 10^{-7}$  sec.

### Light Ground Fog

$\alpha L = 1$ .  
 $I_o t_p > 6.3$  J/cm $^2$ .  
 Total energy > 63 kJ.

### Moderate Overcast

$\alpha L = 100$ .  
 $I_o t_p > 6 \times 10^{43}$  J/cm $^2$ .  
 Total energy >  $6 \times 10^{47}$  J.

These values are so large (the explosion of 1 Mton of TNT yields only about  $10^{16}$  J) that we need not continue further in this limit.

### Discussion

It should be noted that these results do not include the (possibly large) factor  $(1 - D_e)^{-1}$ . Consequently it appears that cw hole-boring through ground fogs will require laser powers in excess of 100 kW, while cw hole-boring in moderate to heavy overcasts will require laser powers very much greater than 10 MW and exceeding 10 GW in the limiting example of a thunderhead. Short-pulse hole-boring in light ground fogs will require pulse energies much in excess of 10 kJ, while short-pulse hole-boring in any clouds other than light ground fogs requires incomprehensibly large pulse energies.

In the preceding calculations we have completely neglected the deleterious effects of thermal blooming.<sup>12</sup> In dry air, thermal blooming becomes important at intensities above 100 W/cm $^2$ . However, in the moist air of a vaporized cloud, thermal blooming could become important at 1-W/cm $^2$  intensities or less. Thermal blooming in the near field can be readily corrected using coherent optical adaptive techniques (COAT).<sup>13</sup> Strong blooming occurring in the far field, as would be encountered in vertical hole-boring through high clouds, cannot be completely corrected. The effect of thermal blooming is to reduce the beam intensity, thus requiring an increased initial intensity to bore a hole. Since thermal blooming is a nonlinear process, it is entirely possible that in some situations even an infinitely large initial intensity could not bore a hole. Beam slewing, which is frequently used to reduce the effects of thermal blooming, acts like an increased wind and consequently is not very helpful as far as hole-boring is concerned. The severely detrimental effects of thermal blooming dictate that hole-boring may not be feasible in light to moderate overcasts even if it were possible in the absence of thermal blooming.

An important application of high-intensity lasers which is closely related to hole-boring is the dissipation of fog over large areas. As mentioned earlier, recondensation is of critical importance in this application. The rate of recondensation depends on factors as diverse as the dust content of the fog, the number of submicron droplets which remain after passage through the laser beam, the amount of heat which the water vapor has absorbed, the air and ground temperatures, and the wind speed and turbulence levels. Consequently, it is not amenable to simple analysis. However, it seems probable that recondensation will occur within a few minutes after leaving the laser beam.

Let us consider the requirements for clearing a runway of dimensions (100 m by 3000 m) of a light ground fog ( $Q \sim 0.1$ ,  $U \sim 100$  cm/sec) which is 100 m thick. Neglecting recondensation and assuming a rectangular laser beam with dimensions 100 cm by 100 m placed across the short end of the runway with the wind direction perpendicular to the laser beam, we can easily calculate that an intensity of  $50 \text{ W/cm}^2$  is required to dissipate the fog at the laser beam. This corresponds to a total laser power of 50 MW. However, it would take 3000 sec (50 min) for the wind to move a distance of 3000 m. Thus, it seems probable that recondensation will take place within a few hundred meters of the laser array. To maintain the clear zone for the length of the runway a number of laser arrays must be located down the length of the runway. Side winds caused by laser heating-induced convection will have effects similar to recondensation. Higher winds may reduce these problems but will require much higher initial laser powers. Consequently, it seems clear that total laser powers of the order of  $10^8$ – $10^9$  W are necessary for fog dispersal on the scale of an airport runway. Since these powers must be maintained for extended periods (possibly hours) it is important to realize that  $10^9$  W is equivalent to the output of a large electrical generating plant. Given this large energy requirement, the application of lasers to fog dissipation is probably not cost

effective even if it were, in principle, technologically feasible.

### Conclusions

In the preceding sections simple analytical expressions have been obtained in a zeroth-order approximation which describe the phenomena involved in cloud hole-boring by high-intensity lasers. The validity of the analysis is demonstrated by the fact that all the phenomena predicted by the simple analysis have been anticipated by the more sophisticated analyses of others. Application of the relations arising from the simple analysis to typical fogs and clouds indicates that hole-boring in light fogs and very thin overcasts will require laser powers in excess of 100 kW. Problems associated with thermal blooming indicate that hole-boring in moderate to heavy overcasts may not be feasible regardless of the laser power available. The energy requirements to dissipate fog over large areas such as airport runways are so large ( $\sim 10^9$  W) that the application is probably not cost effective.

This work was sponsored by the Advanced Research Projects Agency of the Department of Defense.

### References

1. F. A. Williams, *Int. J. Heat Mass Transfer* **8**, 575 (1965).
2. G. W. Sutton, *AIAA J.* **8**, 1907 (1970).
3. S. L. Glickler, *Appl. Opt.* **10**, 644 (1971).
4. S. M. Bedair and S. S. Aly, *Infrared Phys.* **15**, 233 (1975).
5. G. J. Mullaney, W. H. Christiansen, and D. A. Russell, *Appl. Phys. Lett.* **13**, 145 (1968).
6. P. Kafalas and A. P. Ferdinand, *Appl. Opt.* **12**, 29 (1973).
7. P. Kafalas and J. Herrmann, *Appl. Opt.* **12**, 772 (1973).
8. J. E. Lowder, H. Kleiman, and R. W. O'Neil, *J. Appl. Phys.* **45**, 221 (1974).
9. R. G. Eldridge, *J. Meteorol.* **18**, 671 (1961).
10. T. S. Chu and D. Hogg, *Bell Syst. Tech. J.* **10**. T. S. Chu and D. C. Hogg, *Bell Syst. Tech. J.* **47**, 723 (1968).
11. D. B. Rensch and R. K. Long, *Appl. Opt.* **9**, 1563 (1970).
12. J. Wallace and M. Camac, *J. Opt. Soc. Am.* **60**, 1587 (1970).
13. J. E. Pearson, *Opt. Eng.* **15**, 151 (1976).

# Thermal-blooming compensation: experimental observations using a deformable-mirror system

C. A. Primmerman and D. G. Fouche

A laboratory experiment has demonstrated the effectiveness of compensating for forced-convection-dominated cw thermal blooming by using a deformable mirror to add phase corrections to the laser beam. In agreement with theoretical predictions, the peak focal-plane irradiance has been increased by a factor of 3 under severely bloomed conditions.

## I. Introduction

As a laser beam passes through an absorbing medium, it heats the medium causing the index of refraction along its path to change. The induced index-of-refraction gradients, in turn, cause the beam to be spread or bloomed. This phenomenon of thermal blooming is well known and has been studied both theoretically and experimentally for a variety of different conditions.<sup>1</sup> Recently it has been suggested that one could compensate for thermal blooming by using an adaptive-optics system to add appropriate phase corrections at the beam transmitter.<sup>2</sup> In this article we report experimental evidence conclusively demonstrating that this technique may be used to compensate for the blooming of a cw slewed laser beam.

## II. Deformable-Mirror System

We apply phase corrections to a laser beam by means of a deformable-mirror system developed by Itek Corporation.<sup>3</sup> The deformable mirror uses a novel design in that instead of having discrete actuators, it consists of a monolithic disk of piezoelectric crystal into which is placed an array of electrodes. There are fifty-seven electrodes which, energized with up to  $\pm 1500$  V, can produce surface deformations of  $\pm 0.5 \mu\text{m}$  over an active area 1.5 in. (3.8 cm) in diameter. The mirror surface is a metalized glass disk cemented on the piezoelectric crystal.

The electrodes may be individually actuated so that any phase profile consistent with the maximum deformation and the spatial-frequency limitation imposed by the finite number of actuators may be put

on the mirror. But for the experiment reported here, the relative voltages of the electrodes were fixed by a resistive network to give the relative phase profile shown in Fig. 1. This profile closely matches that calculated by Bradley and Herrmann<sup>2</sup> to give the maximum correction for a truncated Gaussian beam undergoing forced-convection-dominated thermal blooming, if only corrections through third order are taken into account. Thus, the profile of Fig. 1 includes refocus and third-order spherical, coma, and astigmatism terms; it does not include tilt, since tilt produces only a shift of the beam and no change in intensity. In these experiments we manually varied the amplitude of the deformation from flat to about  $2\lambda$  peak to peak, but did not vary the shape.

## III. Experimental Conditions

The experimental arrangement is shown in Fig. 2. We use a cw argon-ion laser that produces a Gaussian beam with up to 2 W of useful power at 5145 Å; the beam is assumed to have uniform phase. The beam is expanded to make the  $1/e^2$  diameter 3.8 cm, is truncated at this diameter, and is reflected from the deformable mirror. The beam is then contracted and is slewed through the absorption cell by a variable-speed slewing mirror. In the focal plane just beyond the cell we have a row of 50- $\mu\text{m}$  pinholes at a slight angle to the slewed beam. By detecting the light coming through these pinholes we can measure both the intensity and the shape of the bloomed beam as it leaves the gas cell. The optics are such that with the absorption cell empty the focal-spot diameter is within  $\sim 10\%$  of the diffraction limit.

The gas cell is filled with a few Torr of  $\text{NO}_2$ , enough to absorb  $\sim 50\%$  of the incident radiation in the 1.5-m long tank, and 1 atm of a nonabsorbing buffer gas. Since we are interested in studying the thermal blooming of a slewed beam (that is, one in which forced convection is the dominant cooling

The authors are with Massachusetts Institute of Technology, Lincoln Laboratory, Lexington, Massachusetts 02173.

Received 3 December 1975.

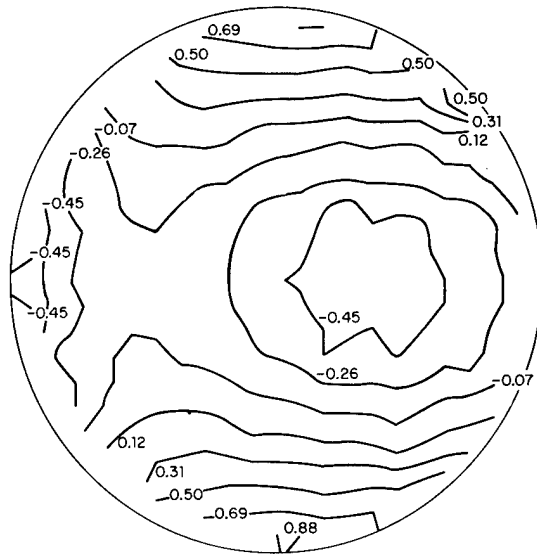


Fig. 1. Actual surface contour on the deformable mirror as measured interferometrically. The profile was chosen to match that determined by computational analysis of the laser-beam propagation. Contours are labeled in units of wavelength.

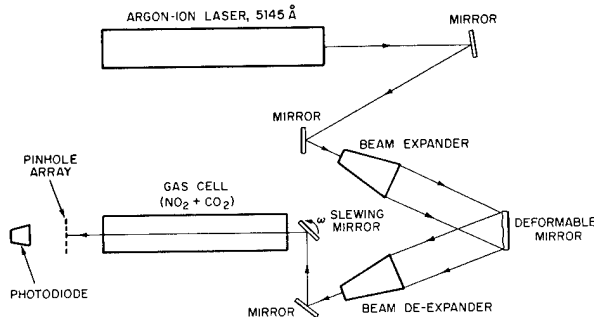


Fig. 2. Experimental arrangement.

mechanism), the gas cell is mounted vertically to minimize free-convection cooling, and  $\text{CO}_2$  is used as the buffer gas to reduce conduction cooling. Mounting the gas cell vertically effectively eliminates free-convection effects; but, unfortunately conduction effects are not always negligible and must be taken into account.

As shown by Bradley and Herrmann,<sup>2</sup> the propagation of a slewed beam through an absorbing medium can be characterized by the four dimensionless numbers:

$$\begin{aligned} \text{absorption number} - N_A &\equiv \alpha R; \\ \text{Fresnel number} - N_F &\equiv k a^2 / R; \\ \text{slewing number} - N_\omega &\equiv \omega R / v; \\ \text{distortion number} - N_D &\equiv (1/\rho c_p \epsilon_0) (\partial \epsilon / \partial T) \\ &\quad (\alpha P k R / av); \end{aligned}$$

where  $\alpha$  is the absorption coefficient,  $R$  is the range,  $k$  is the wavenumber,  $a$  is the  $1/e$  radius at the cell entrance,  $\omega$  is the slewing frequency,  $v$  is the constant

cross-wind velocity,  $P$  is the incident power, and  $(1/\rho c_p \epsilon_0) (\partial \epsilon / \partial T)$  is a constant characterizing the change in index of refraction of the heated gas. For our laboratory experiment an additional dimensionless number is required as a measure of the importance of conduction compared to forced convection:

$$\text{conduction number} - N_C \equiv \kappa / \sqrt{2av},$$

where  $\kappa$  is the thermal diffusivity.

The actual experimental conditions are given by the following set of parameters:

$$\begin{aligned} \alpha &= 4.6 \times 10^{-3} \text{ cm}^{-1}; \\ R &= 150 \text{ cm}; \\ k &= 1.22 \times 10^5 \text{ cm}^{-1}; \\ a &= 0.25 \text{ cm}; \\ \omega &= 0-0.2 \text{ rad/sec (variable)}; \\ v &= 0-3 \text{ cm/sec (variable)}; \\ P &= 0.03-1 \text{ W (variable)}; \\ (1/\rho c_p \epsilon_0) (\partial \epsilon / \partial T) &= 1.95 \times 10^{-5} \text{ J}^{-1} \text{ cm}^3; \\ \kappa &= 0.11 \text{ cm}^2 \text{-sec}^{-1}; \\ N_A &= 0.69; \\ N_F &= 45; \\ N_\omega &= 7.5-30 \text{ (variable)}; \\ N_D &= 686P/v \text{ (variable)}; \\ N_C &= 0.1-\infty \text{ (variable).} \end{aligned}$$

The three basic variables in this experiment are the input power at the cell entrance  $P$ , the slew frequency  $\omega$ , and the constant cross-wind velocity  $v$ , which can be varied independently of  $\omega$  by changing the distance from the slewing mirror to the cell entrance. These variables enable us to test the dependence of the thermal-blooming corrections on the dimensionless numbers  $N_\omega$ ,  $N_D$ ,  $N_C$ . We can also vary  $N_A$  and  $N_F$ , but in these experiments no attempt has

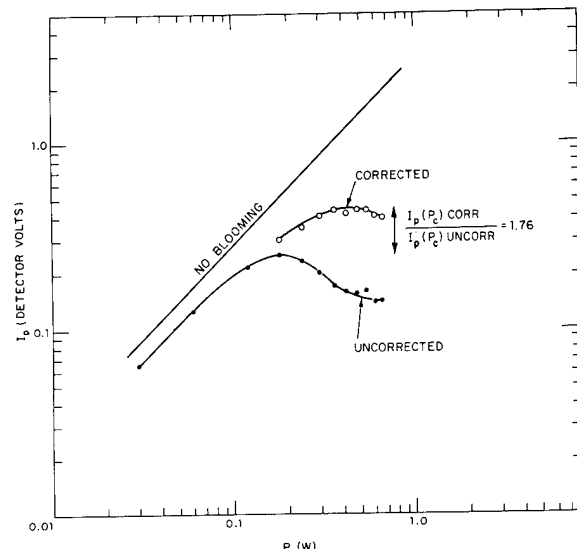


Fig. 3. Peak focal-plane intensity vs input power for corrected and uncorrected beams. The straight line would be the intensity if there were absorption but no blooming.  $v = 1.65 \text{ cm/sec}$ ,  $N_C = 0.19$ ,  $N_\omega = 10$ . Other parameters are listed in the text.

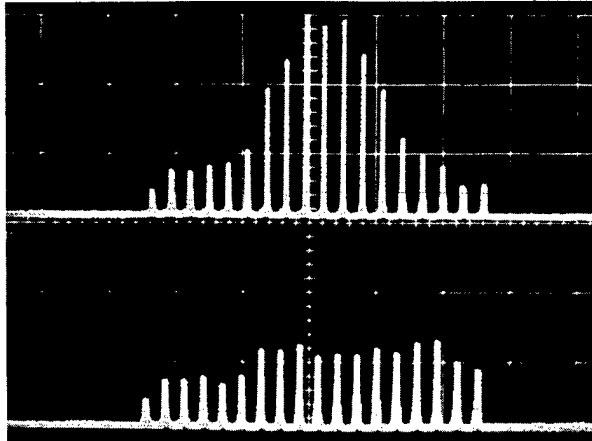


Fig. 4. Intensity through pinhole array for severely bloomed conditions at  $P = 0.45$  W. Lower curve: uncorrected beam. Upper curve: corrected beam. Parameters as in Fig. 3.

been made to study systematically the effect of these parameters on phase correction for thermal blooming.

#### IV. Experimental Results

##### A. Results of Varying Power

In Fig. 3 we show the measured peak focal-plane intensity plotted against input power for the uncorrected beam, the corrected beam, and the hypothetical situation of absorption with no blooming. Varying the power is equivalent to varying the distortion number, since  $N_D \propto P$ . The uncorrected curve was taken with the deformable mirror in the flat condition; the corrected curve was obtained by adjusting the amplitude of the mirror deformation to get the maximum possible intensity to each power.

The uncorrected curve exhibits the classic thermal-blooming behavior: the intensity first increases with increasing power and then, after a certain critical power  $P_c$ , decreases with further increases in the input power. As expected, the corrected curve shifts upward to higher intensities and outward to higher critical power. We observe that the maximum intensity increases 76% over the uncorrected case and that at certain powers there is a factor of 3 increase in intensity. This result is representative: we have consistently achieved improvements in maximum intensity of  $\sim 70\%$ . We also observe that the critical power increases by almost a factor of 2.5. A reasonable figure of merit in atmospheric propagation is  $I_p(P_c)P_c$ , the maximum intensity times the critical power. On the basis of this figure of merit we have achieved fourfold improvement using our deformable-mirror system.

Figure 4 shows oscilloscope traces of the detector voltage as the beam sweeps across our pinhole array. The spike amplitudes are proportional to beam irradiance, and the envelope of spikes gives the profile of the beam perpendicular to the slew direction. (From the widths of the spikes, unresolved in this photograph, we can also obtain the profile of the beam par-

allel to the slew direction.) The lower trace shows the severely bloomed beam at  $P = 0.45$  W; the upper trace shows the corrected beam at the same power. We see that the peak intensity has increased by almost a factor of 3 and that the beam shape has been greatly improved.

Figure 5 shows photographs of the beam in the focal plane. In the top picture we see the characteristic crescent-shaped bloomed beam. In the next

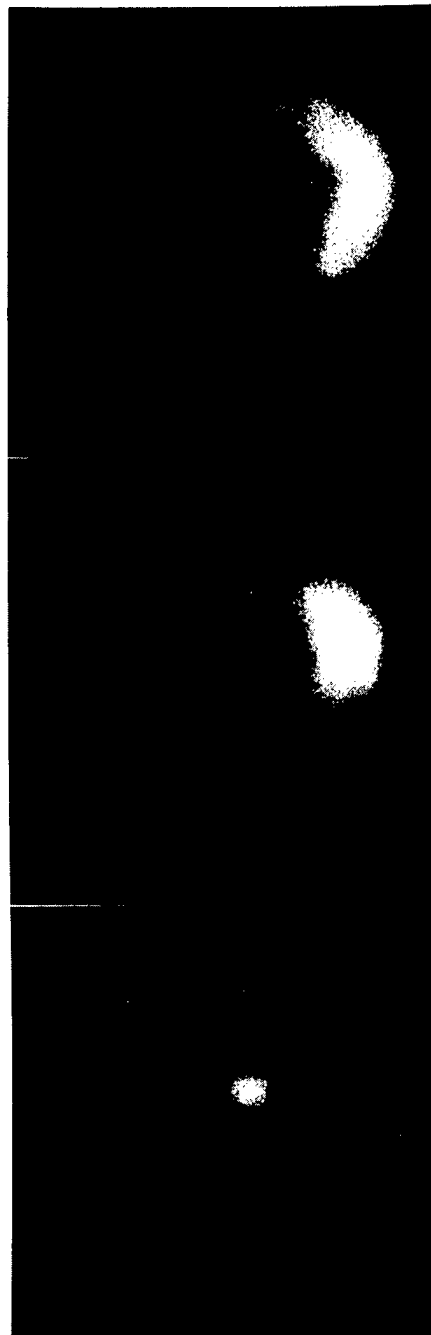


Fig. 5. Actual photographs of the bloomed, corrected, and unbloomed beams in the focal plane. The top two pictures correspond to the pinhole traces of Fig. 4. The slight ellipticity of the unbloomed spot results from insufficient shutter speed to freeze the beam.

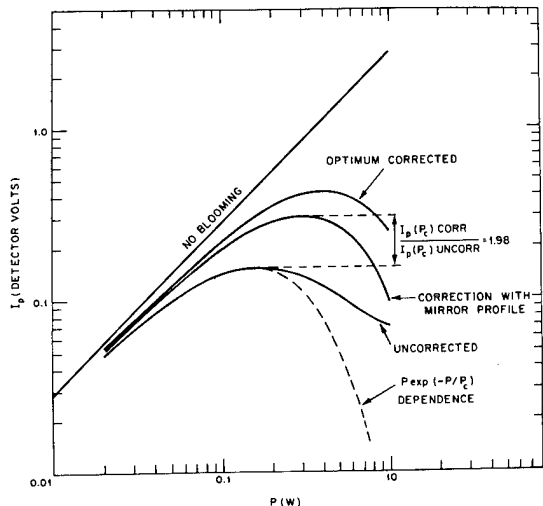


Fig. 6. Propagation-code results of peak focal-plane intensity vs input power with and without correction. The straight line would be the intensity if there were absorption but no blooming. The dotted line represents the suggested dependence  $I_p \propto P \exp(-P/P_c)$ . Input parameters for the code were the experimental conditions of Fig. 3.

picture we see the corrected beam, reduced in size, and with only a slight remaining indication of a crescent shape. For comparison, the bottom photograph shows the low-power unbloomed beam. (The somewhat elliptical shape results from the fact that the shutter speed is not fast enough to freeze the beam.) Note that the corrected and uncorrected bloomed beams are both shifted into the wind with respect to the unbloomed beam, since our deformable mirror does not add a tilt correction. We observe that, consistent with the intensities shown in Fig. 3, the corrected spot size is still larger than the unbloomed spot size.

#### B. Comparison with Propagation-Code Results

To compare our experimental results with theoretical predictions for phase compensation of thermal blooming we have employed the Bradley-Herrmann propagation code. In Fig. 6 we show propagation-code-generated plots of peak focal-plane irradiance against power for no correction and for two different corrections. The upper corrected curve is the opti-

mum correction using the Bradley-Herrmann method; the lower corrected curve is the correction obtained using the Zernike polynomial expansion of the contour actually on the mirror. The input parameters used in the code were the experimentally measured conditions corresponding to the results of Fig. 3. To facilitate comparison of theory and experiment the curves of Figs. 3 and 6 have been normalized to the same unbloomed intensity.

Looking first at the uncorrected curves we note that both theoretical and experimental curves follow roughly the dependence  $I_p \propto P \exp(-P/P_c)$  until  $P \approx 2P_c$ . Beyond this point the curves fall off much more slowly than given by the exponential dependence. At  $P = 3P_c$ , for instance, the theoretical curve has a peak irradiance twice that given by the simple exponential dependence. The theoretical curve peaks at  $P = 0.155$  W; the experimental curve, at  $P = 0.18$  W. Thus, the critical powers agree to within  $\sim 15\%$ —good agreement considering the many possibilities for consistent error. But although the critical powers agree well, the experimental and theoretical maximum intensities are not in such good agreement. Some of the disagreement is attributable to the difference in  $P_c$ . But, as illustrated in Fig. 3, we often find that the experimentally determined intensity at  $P_c$  is about  $1/2$  the unbloomed intensity, while the theoretical prediction is that the intensity at  $P_c$  should be  $1/e$  times the unbloomed intensity. The reason for this disagreement is still unclear.

Comparing the corrected curves we find that the experimental curve falls almost on the optimum theoretical curve; but this agreement is probably a fortuitous coincidence resulting from the consistent shift between theoretical and experimental results. To compare more properly the corrected curves we refer to Table I and compare the increases in irradiance over the uncorrected values. Experimentally we observe that the maximum intensity increases a factor of 1.76 compared to 1.98 for the theoretical increase—an agreement within 15%. The maximum increase at any power is 2.87 experimentally compared to 2.48 theoretically—again an agreement within 15%. The agreement in  $P_c$  is not so close—2.44 experimentally in 1.94 theoretically—but a look at Fig. 3 shows that it is extremely difficult to determine accurately the critical power for the experimental corrected curve.

Table I.

	$P_c$	$I_p(P_c)$	$P_c$ (corrected)	$I_p(P_c)$ corrected	Max	$I_p$ corrected
			$P_c$ (uncorrected)	$I_p(P_c)$ uncorrected		$I_p$ uncorrected
Experimental uncorrected	0.18	0.90	—	—	—	—
Experimental corrected	0.44	1.55	2.44	1.76	2.87	—
Theoretical uncorrected	0.155	0.56	—	—	—	—
Theoretical mirror corrected	0.300	1.11	1.94	1.98	2.48	—
Theoretical optimum corrected	0.415	1.53	2.68	2.73	4.33	—

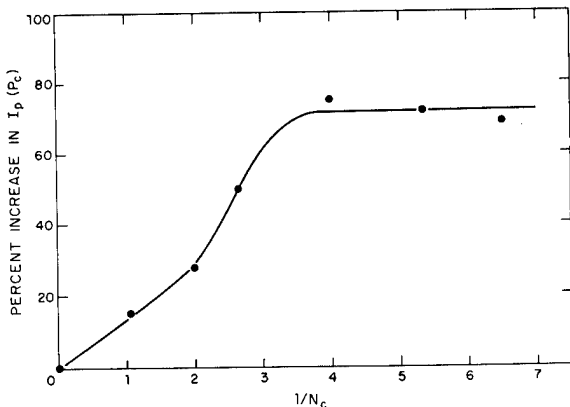


Fig. 7. Percentage increase in maximum intensity vs  $1/N_c$ .  $N_\omega = 10$ . Other parameters are listed in the text.

The experimental correction is still  $\sim 30\%$  below the optimum correction. This difference results primarily not from any deficiency of the mirror but from the fact that only third-order corrections were specified for the mirror surface. Theoretically, adding phase corrections through fifth order results in corrected intensities very close to optimum; so there is reason to believe that if the mirror figure were corrected through the fifth order the experimental curve would also approach the optimum.

The propagation-code results are seen to give quantitative agreement with the experimental results to within about 15%. Considering the many parameters involved in making the comparison—eleven experimental values must be supplied in the propagation code—and the concomitant chances for consistent error we believe this 15% agreement represents very good agreement indeed.

### C. Results of Varying Cross-Wind Velocity

In our experimental arrangement we can vary the effective cross-wind velocity  $v$ , while keeping  $N_\omega$  constant, by varying the slew frequency  $\omega$ . In the absence of conduction the cross-wind velocity and the input power appear only in the distortion number and only in the combination  $N_D \propto P/v$ . Thus, we expect that the critical power  $P_c$  and the maximum intensity  $I_p(P_c)$  should increase linearly with  $v$ . Experimental results verify these expectations. If  $v$  is large enough to make conduction negligible,  $P_c$  and  $I_p(P_c)$  are proportional to  $v$  for both uncorrected and corrected beams.

Since  $N_c \propto 1/v$ , as  $v$  becomes small, conduction becomes important, and this linear behavior is no longer observed. And as  $v \rightarrow 0$ , conduction dominates, and  $P_c$  and  $I_p(P_c)$  approach constant values determined by conduction alone. In addition, as conduction becomes important, our phase corrections become less effective, since the phase profile was derived using a theoretical treatment that neglected conduction. This effect may be seen in Fig. 7, where we plot the percentage increase in  $I_p(P_c)$  against  $1/N_c$ . When  $1/N_c = 0$ , conduction is the only cool-

ing mechanism, and no correction is obtained. As  $1/N_c$  increases, forced-convection cooling becomes more effective, and the percentage improvement rises sharply. Finally, when  $1/N_c$  reaches a value such that conduction is negligible compared to forced convection, the improvement levels off at its maximum value. From these results we conclude that if  $N_c \lesssim 0.3$ , conduction may be ignored compared to forced convection.

### D. Results of Varying Slewing Number

By simultaneously changing the distance from the slewing mirror to the cell entrance and adjusting  $\omega$ , we can change  $N_\omega$  while keeping  $v$  constant. Increasing  $N_\omega$  increases the cooling at the far end of the cell relative to that at the cell entrance; thus, as  $N_\omega$  increases, the region over which significant blooming occurs is compressed toward the cell entrance. This compression of the blooming zone should, in turn, make it easier for adaptive-optics systems to correct for the blooming.

The experimental results are shown in Fig. 8, where we plot percentage increase in maximum intensity against  $N_\omega$ . We observe that, consistent with theoretical predictions, the phase correction is more effective at higher slewing numbers. At first, the percentage improvement increases roughly linearly with  $N_\omega$ , but as  $N_\omega$  is further increased the incremental improvement decreases. Thus, there is some indication that a practical limit may be reached beyond which further reducing the blooming zone does not significantly improve the correction.

### E. Required Accuracy of Phase Correction

In Fig. 3 we showed a corrected curve with the mirror amplitude always adjusted to give maximum intensity. But from a practical point of view, it is also important to know how sensitive this maximum is to changes in the deformation amplitude. In Fig. 9 we

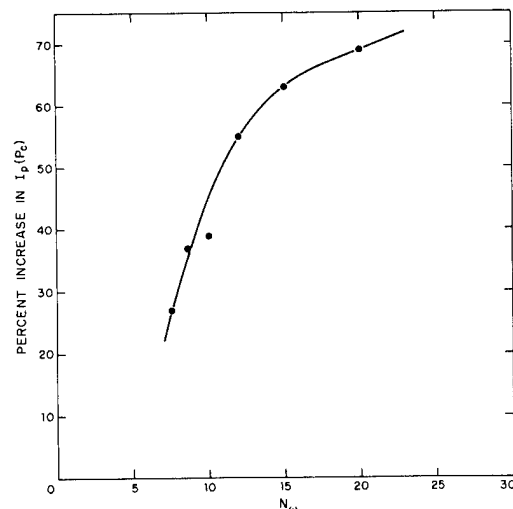


Fig. 8. Percentage increase in maximum intensity vs slewing number.  $v = 1.65 \text{ cm/sec}$ ,  $N_c = 0.19$ . Other parameters are listed in the text.

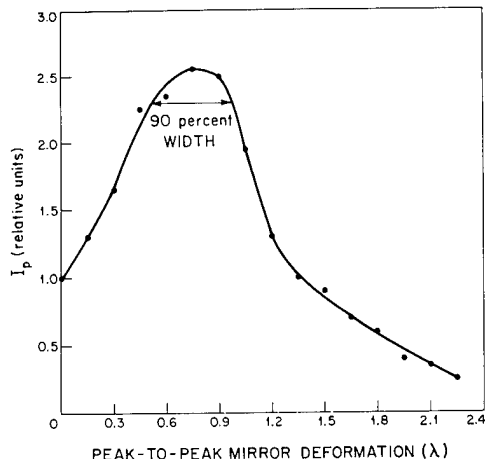


Fig. 9. Peak focal-plane intensity vs peak-to-peak mirror deformation amplitude. The mirror profile is given in Fig. 1.  $v = 1.65$  cm/sec,  $N_C = 0.19$ ,  $N_w = 10$ ,  $P = 0.4$  W. Other parameters are listed in the text.

plot peak irradiance against peak-to-peak mirror deformation for a particular set of experimental conditions.  $I_p$  is normalized so that  $I_p = 1.0$  when the deformation is zero (mirror flat); the shape of the mirror contour is still given by Fig. 1. We note that the peak corrected intensity is a factor of 2.5 greater than uncorrected—a respectable correction. But equally important, we observe that the correction curve is bell-shaped with an extremely broad peak. The width at 90% maximum is marked; we see that the amplitude of the phase correction can vary  $\pm 30\%$ , while the irradiance decreases only 10%. This result is extremely encouraging, for it demonstrates that one does not have to apply phase corrections with great precision for them to be effective.

Our experimental results are uniformly in accord with the case shown. In each case there is a broad maximum in the irradiance vs deformation curve. This pleasant result was unanticipated theoretically, but we have since checked our results using the Bradley-Herrmann propagation code. We found theoretically that varying the deformation amplitude  $\pm 20\%$  from optimum produced only a 5% decrease in peak intensity—a result in good agreement with the experimental results.

## V. Conclusion

In this investigation we have obtained the first experimental evidence for the feasibility of compensating for cw convection-dominated thermal blooming by using a deformable mirror to add phase corrections to the laser beam. We have conclusively demonstrated that this technique can produce significant increases in transmitted intensity. Further work is necessary to determine the limits of the correction method, but its basic applicability has now been experimentally proven.

We thank J. Herrmann and L. A. Popper for help with the propagation code and J. J. Tynan for help with the experimental apparatus.

This work was sponsored by the Advanced Research Projects Agency of the Department of Defense.

## References

1. See, for example, F. G. Gebhardt and D. C. Smith, IEEE J. Quantum Electron. **QE-7**, 63 (1971); A. H. Aitken, J. N. Hayes, and P. B. Ulrich, Appl. Opt. **12**, 193 (1973).
2. L. C. Bradley and J. Herrmann, Appl. Opt. **13**, 331 (1974).
3. J. Feinlieb, S. G. Lipson, and P. F. Cone, Appl. Phys. Lett. **25**, 311 (1974).

## Bandwidth specification for adaptive optics systems\*

Darryl P. Greenwood

*Lincoln Laboratory, Massachusetts Institute of Technology, Lexington, Massachusetts 02173*

(Received 9 July 1976)

A simplified expression for the bandwidth of an adaptive optics system is found to depend on a weighted path integral of the turbulence strength, where the weighting is transverse wind velocity to the 5/3 power. The wave-front corrector is conservatively assumed to match the phase perfectly, at least spatially, if not temporally. For the case of astronomical imaging from a mountaintop observatory, the necessary bandwidth is found to be less than 200 Hz.

In an earlier paper,<sup>1</sup> the power spectra describing corrector motion were considered as necessary elements of a complete servo system design for an adaptive optics system. However, for a preliminary design, a more simplified handbook-type formula for bandwidth is more desirable. This paper presents such a formula for the servo cutoff frequency without making any significantly limiting assumptions. Basically, the result depends on a weighted integral of the turbulence strength  $C_n^2$ , where the weighting is the transverse wind velocity

to the  $\frac{5}{3}$  power. Even that integral may be easily evaluated analytically when  $C_n^2$  is a constant and the wind speed is composed of a constant plus a pseudowind due to slew. The result of this final simplification may be easily programmed on a hand-held scientific calculator.

Rather than investigate the way a wave-front corrector would respond to a phase aberration, we have considered the statistics of the phase itself, so the resultant bandwidth is conservative in that we assume the corrector

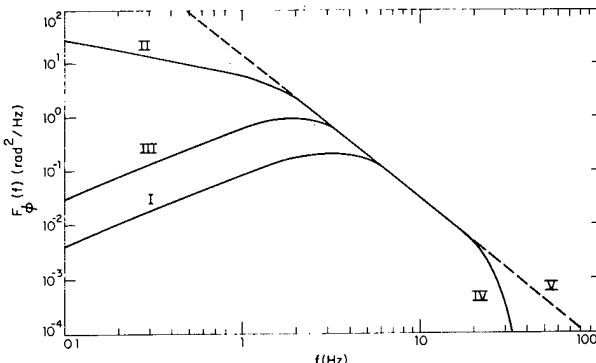


FIG. 1. Representative plots of the power spectra of segments within a phase corrector, for pistons located at the center (I) and at the edge (II and III). Curve II is for a gross piston reference and curve III for a gross tilt reference. The type of reference does not affect curve I. The high-frequency roll-off is determined by the size of the corrector, with IV representing a finite corrector segment  $\frac{1}{10}$  the diameter of the aperture, and V representing a segment of size zero. The entire dashed line is the simple power spectrum given by Eq. (1).

perfectly matches the wave front, at least spatially, if not temporally. This avoids making any assumption on the nature of the corrector, and the corrector may be modal or zonal, segmented or continuous. To amplify the usefulness of the resultant formula, we carry out integrations for two cases: one representing a near-horizontal, moderately short range, and one consistent with astronomical observation.

In the more detailed analysis,<sup>1</sup> we considered a segmented corrector composed of any array of movable pistons which could also be tilted in order to form a least-squares fit to the wave front over the small circular region defined by the pistons. There was an option of referencing the phase at a point in the aperture to either the average phase across the aperture (gross piston reference) or the tilt across the aperture (gross tilt reference). Examples of such spectra are shown in Fig. 1 for pistons at the center and the edge of the aperture. These curves are diagrammatic in that they are not for any specific atmospheric conditions. The low frequencies in these curves are governed by the type of phase reference chosen, whereas the high frequencies are affected by the segment size. If we let the segment size go to zero, then all the curves have a common high-frequency asymptote given by a path integral of Eq. (72) in the earlier paper. The result, which applies to either plane or spherical waves, is

$$\lim_{f \rightarrow \infty} F_\phi(f) = 0.0326 k^2 f^{-8/3} \int_0^L C_n^2(z) v^{5/3}(z) dz , \quad (1)$$

where  $f$  is cyclic frequency,  $k = 2\pi/\lambda$  is the wave number ( $\lambda$  is wavelength),  $L$  is the path length,  $v(z)$  the wind speed transverse to the path,  $C_n^2(z)$  the refractive-index structure parameter, and  $z$  is the incremental position along the path from  $z=0$  at the telescope (or receiver) to  $z=L$  at the source. For astronomical seeing, the upper limit  $L$  is replaced by  $\infty$ .

The asymptote given by Eq. (1) is simply the spectrum of phase for Kolmogorov turbulence, where the phase is

not referenced to either gross piston or gross tilt. The phase spectrum is also given by Tatarskii,<sup>2</sup> but only for the special case where  $v(z)$  and  $C_n^2(z)$  are independent of  $z$ . A tacit assumption in the derivation of Eq. (1) is that the frequencies are small compared with the characteristic frequency of amplitude scintillation, or  $f \ll v/(\lambda L)^{1/2}$ . Admittedly,  $v$  is actually a function of path position  $z$ , and  $L$  may be only a scale height for astronomical seeing; but rather than go into a more rigorous analysis, we note that if the inequality is reversed, such that  $f \gg v/(\lambda L)^{1/2}$ , then Eq. (1) is simply multiplied by  $\frac{1}{2}$ .

Bandwidths are determined by integrating  $F_\phi(f)$  as filtered by a filter rejection response. Suppose the closed-loop servo response, the Fourier transform of the impulse response, is given by the complex function  $H(f, f_c)$ , where  $f_c$  represents a characteristic frequency such as a 3 dB point. The rejection response, in terms of power, is then  $|1 - H(f, f_c)|^2$ . Thus, the rejected, or uncorrected, power is

$$\sigma_\phi^2 = \int_0^\infty |1 - H(f, f_c)|^2 F_\phi(f) df . \quad (2)$$

Typically, it is  $\sigma_\phi^2$  which we will specify in order to determine  $f_c$  for a certain set of atmospheric conditions.

Since there are many types of servo closed-loop responses which might be implemented, we chose two extreme forms for  $H(f, f_c)$  which should represent the range of possibilities. First, to represent a sharp cut-off, we used a binary filter given by

$$H(f, f_c) = \begin{cases} 1 & f \leq f_c \\ 0 & f > f_c \end{cases} \quad (3)$$

Secondly, we chose an  $RC$  filter to represent a slow roll-off, and in fact, many adaptive optics servo systems have such a response in the neighborhood of the 3 dB point. (For higher frequencies, the actual response may drop off more rapidly than 20 dB/decade, but this will have little impact since the spectrum itself has a rather steep  $f^{-8/3}$  dependence.) For the  $RC$  filter we have

$$H(f, f_c) = (1 + if/f_c)^{-1} \quad (4)$$

We will not concern ourselves with the phase lag associated with such a filter.

If we assume the cutoff frequency which will be eventually derived is to the right of the low-frequency breaks indicated in Fig. 1, then it is sufficient to use the asymptotic form of  $F_\phi(f)$  in the integration of Eq. (2). This assumption may be alternatively stated as the rejected power  $\sigma_\phi^2$ . From the parent paper,<sup>1</sup> we find that the aperture-averaged variance of phase referenced to gross tilt is

$$\sigma_\phi^2 = 0.141 (D/r_0)^{5/3} , \quad (5)$$

where  $D$  is the telescope diameter and  $r_0$  is Fried's coherence length.<sup>3</sup> For convenience, we repeat here the definition of  $r_0$  as

$$r_0^{-5/3} = 0.423 k^2 \int_0^L C_n^2(z) Q(z) dz , \quad (6)$$

where  $Q(z)=1$  for plane waves, and  $Q(z)=[(L-z)/L]^{5/3}$  for spherical waves. A typical value of  $\sigma_r$  might be  $0.2\pi$  rad (or  $\frac{1}{10}$  wave), which requires that the integrated turbulence strength be such that  $D/r_0 \gg 0.74$ . Fortunately,  $D/r_0$  should be much greater than 0.74 to warrant the use of an adaptive optic in the first place. So we comfortably proceed with the integration of Eq. (2), using the asymptotic spectrum, Eq. (1). After integrating Eq. (2) with a binary filter, we invert the result to express  $f_c$  in terms of  $\sigma_r$  and find

$$f_c = [0.0196 (k/\sigma_r)^2 \int_0^L C_n^2(z) v^{5/3}(z) dz]^{3/5} . \quad (7)$$

For the  $RC$ -filter function, the constant 0.0196 becomes 0.102, and thus  $f_c$  is 2.70 times larger.

There are two special cases of interest. The first is consistent with many ground-based operations over near-horizontal ranges, and the second is that of astronomical observation. For the first case, we assume  $C_n^2$  is a constant and the transverse wind speed is composed of a constant  $v_a$  plus a pseudowind  $\omega z$  due to slew-ing at an angular rate  $\omega$ . Then we find

$$f_c = \left\{ 7.34 \times 10^{-3} \left( \frac{k}{\sigma_r} \right)^2 C_n^2 \frac{v_a^{8/3}}{\omega} \left[ \left( 1 + \frac{\omega L}{v_a} \right)^{8/3} - 1 \right] \right\}^{3/5} \quad (8)$$

for a binary filter, and  $f_c$  is 2.70 times higher for an  $RC$  filter. As an example, suppose  $\sigma_r = 0.2\pi$  rad,  $\lambda = 10.6 \mu\text{m}$ ,  $C_n^2 = 10^{-13} \text{ m}^{-2/3}$ ,  $v_a = 4 \text{ m/s}$ ,  $\omega = 0.01 \text{ rad/s}$ , and  $L = 2000 \text{ m}$ . For these conditions, we find  $f_c$  would be in the range of 31 Hz for a binary filter to 84 Hz for an  $RC$  filter.

For the astronomical case, the models for  $v$  and  $C_n^2$  become more complicated. We have chosen to calculate  $f_c$  based on recently published data for an astronomical site. Miller, Zieske, and Hanson<sup>4</sup> report profiles of  $C_n^2$  versus altitude for three nights at the ARPA Maui Optical Station (AMOS). Our model of their data is

$$C_n^2(z) = [2.2 \times 10^{-13} (z \sin\theta + 10)^{-1.3} + 4.3 \times 10^{-17}] \times \exp[-(z \sin\theta)/4000] , \quad (9)$$

where  $\theta$  is the elevation angle and the units of  $C_n^2$  and  $z$  are  $\text{m}^{-2/3}$  and  $\text{m}$ , respectively. For a wind velocity model, we averaged rawinsonde data<sup>5</sup> collected at Lihue (island of Kauai), Hawaii, for the years 1950–1970 and at Hilo, Hawaii, for the years 1950–1974. We modeled wind speed as a constant, to represent the lower altitudes, plus a Gaussian to represent the jet stream. The model, consisting of the mean wind speed plus one standard deviation, is

$$v(z) = 8 + 30 \exp \left\{ - \left[ \frac{(z \sin\theta - 9400)^2}{4800} \right] \right\} , \quad (10)$$

where  $v$  and  $z$  are in MKS units. Implicit in Eq. (10) is the knowledge that the site altitude corresponding to  $z=0$  is 3048 m above MSL. We have taken the conservative assumption that the winds are entirely transverse to the path; however, if the wind is blowing predominantly downrange rather than cross-range, there would be an additional  $\sin\theta$  multiplying all of Eq. (10).

For the conditions of turbulence and wind speed given

in Eqs. (9) and (10), as well as for  $\sigma_r = 0.2\pi$  rad,  $\lambda = 0.5 \mu\text{m}$ , and  $\theta = 90^\circ$ , the calculated cutoff frequencies are  $f_c(\text{binary}) = 28 \text{ Hz}$  and  $f_c(\text{RC}) = 75 \text{ Hz}$ . For these same conditions, we may calculate  $r_0$  and verify the assumption that  $D/r_0 \gg 0.74$ . Using Eq. (6) we find  $r_0 = 0.13 \text{ m}$ , and thus  $D \gg 0.1 \text{ m}$ , which is easily satisfied. This value of  $r_0$  compares favorably with the median value of 0.10 m (at  $\lambda = 0.5 \mu\text{m}$ ) reported by Fried<sup>3</sup> for the U.S. Naval Observatory at Flagstaff, Arizona, and the Kitt Peak National Observatory.

These values of  $f_c$  and  $r_0$  can easily be scaled to other elevation angles and wavelengths. The elevation angle scalings are  $f_c \sim (\sin\theta)^{-3/5}$  assuming the winds are entirely cross-range,  $f_c \sim (\sin\theta)^{2/5}$  when the winds are downrange, and  $r_0 \sim (\sin\theta)^{3/5}$  independent of winds. The wavelength (or actually wave number) scalings are  $f_c \sim k^{6/5}$  and  $r_0 \sim k^{-6/5}$ . We also suppose the reader may want to increase or decrease the entire  $C_n^2$  profile, for which we point out that  $f_c \sim (C_n^2)^{3/5}$  and  $r_0 \sim (C_n^2)^{-3/5}$ . Overall wind-speed scaling affects only  $f_c$  in that  $f_c \sim v$ . Let us now consider what may be a near-worst case, or  $\theta = 30^\circ$  (winds cross-range) and a  $C_n^2$  twice the values of the model. We shall not scale  $v$  since the model already consists of the mean plus one standard deviation. Also, at least for the visible wavelengths,  $\lambda = 0.5 \mu\text{m}$  should suffice. For these near-worst-case conditions, the actual cutoff frequency may lie between  $f_c(\text{binary}) = 64 \text{ Hz}$  and  $f_c(\text{RC}) = 172 \text{ Hz}$ .

In summary, we have provided simplified formulas for the bandwidth of the phase corrector and servo control of an adaptive optics system. The formulas should be used as good rules-of-thumb for perhaps all but the very final stages of the servo design. At that point, more precise power spectra<sup>1</sup> should be consulted. If we have used the more precise spectra with the high-frequency roll-off which results from having a finite actuator spacing, the calculated bandwidth would have been slightly lower. The specification derived in this paper is to be taken as a conservative estimate, based on an infinite number of corrector actuators. To apply our result, Eq. (7), requires knowledge of both wind speed and turbulence profiles on the optical path. To demonstrate the utility of the formula, we investigate two cases of interest: one essentially a horizontal path and one consistent with astronomical observation from a mountaintop. In both cases we found the bandwidths to be fairly low, less than 200 Hz, giving encouragement that the control system and corrector mirror need not be extremely complicated for many applications.

\*This work was supported by the Advanced Research Projects Agency of the Department of Defense.

<sup>1</sup>D. P. Greenwood and D. L. Fried, "Power spectra requirements for wave-front-compensative systems," *J. Opt. Soc. Am.* **66**, 193–206 (1976).

<sup>2</sup>V. I. Tatarskii, *The Effects of the Turbulent Atmosphere on Wave Propagation* (U. S. Department of Commerce, Washington, D. C., NTIS T68-50464, 1971), p. 268.

<sup>3</sup>D. L. Fried and G. E. Mevers, "Evaluation of  $r_0$  for Propagation Down Through The Atmosphere," *Appl. Opt.* **13**, 2620–2622 (1974). [Errata: *Appl. Opt.* **14**, 2567 (1975)].

<sup>4</sup>M. Miller, P. Zieske, and D. Hanson, "Characterization of Atmospheric Turbulence," *Proceedings of the SPIE/SPSE Technical Symposium East on Imaging Through The Atmosphere*, Vol. 75, paper 75-05.

<sup>5</sup>D. P. Greenwood and D. L. Fried, "Power Spectra Requirements for Wavefront-Compensative Systems," Technical Report RADC-TR-75-227, Rome Air Development Center, Griffiss AFB, New York, Sept. 1975.

# Properties of phase conjugate adaptive optical systems\*

Jan Herrmann

*Massachusetts Institute of Technology, Lincoln Laboratory, Lexington, Massachusetts 02173*

(Received 12 July 1976)

The phase conjugate COAT (coherent optical adaptive technique) is investigated for thin, nonlinear lenses, simulating thermal blooming. The iteration scheme has convergent and divergent regimes.

## I. INTRODUCTION

The expression phase conjugate coherent optical adaptive technique (COAT) is a term applied to a technique used to compensate for atmospherically induced phase distortions of a laser beam.<sup>1</sup> The signal from a reflecting target is analyzed in the transmitter-receiver aperture and the conjugate of its phase is applied as a correction to the transmitted wave. The phase conjugate COAT scheme has to be distinguished from the multidither COAT,<sup>2</sup> which uses a modulation technique of the phase front to maximize the intensity on a glint in the target plane.

In order to reconstruct images, it is necessary to control the amplitude of the transmitted beam as well as its phase. If, however, one desires to maximize the intensity delivered onto the target, amplitude control is not necessary, and it has been demonstrated that phase conjugate COAT systems can compensate for the phase distortions due to atmospheric turbulence.<sup>1</sup>

Calculations with our propagation codes using a phase conjugate COAT have also been performed to reduce thermal blooming, but we found, as did others,<sup>3</sup> that the presence of strong thermal blooming can lead to divergence of the iteration scheme.

We have investigated convergence properties of the phase conjugate COAT by inserting thin, nonlinear lenses (simulating thermal blooming) between the transmitter and the focus. The phase conjugate correction is performed using the following scheme. The outgoing wave is first focused at the target; it arrives with a certain irradiance level at the lenses, which determines the radius of curvature of each lens. The return wave is assumed to originate from a point source in the tar-

get plane. It passes through the lenses, and its radius of curvature at the transmitter is used as the radius of curvature of the next outgoing wave. The results show that there exist a convergent and a divergent range of parameters, depending on the strength of the nonlinearity. Convergence occurs for cases where an appropriate value of the radius of curvature at the transmitter leads to complete refocusing. For cases where refocusing is not possible, the phase conjugate COAT iteration diverges.

In this paper we study the convergence property of an idealized phase conjugated COAT system. The phase changes appearing in nonlinear propagation calculations are replaced by thin lenses which change only the curvature of the wave front. We perform the calculations in the geometric optics limit as well as with Gaussian beams. The convergence properties of these two cases are qualitatively the same. The program was written with an arbitrary number of equally spaced lenses. The qualitative features of the convergence of the phase conjugate COAT are independent of the number of lenses.

## II. NONLINEAR LENSES

The change in the curvature of the wave front due to a lens at position  $z$  is assumed to be

$$K(z) = S[a_t/a(z)]^Q, \quad (1)$$

where  $S$  is the strength of the nonlinearity,  $a(z)$  is the radius of the beam, and  $a_t$  is the radius at the transmitter. The value of the exponent  $Q$  can be arbitrarily chosen.

The main motivation for introducing such lenses is to simulate cw thermal blooming to a first order. The

index of refraction of the medium due to energy absorbed from a Gaussian beam is

$$\Delta n \approx \frac{\alpha P}{v} \frac{1}{a_x} \left( 1 + \operatorname{erf} \frac{x}{a_x} \right) \exp \left( -\frac{y^2}{a_y^2} \right), \quad (2)$$

where  $\alpha$  is the absorption coefficient,  $P$  the power of the beam,  $v$  the transverse wind velocity, and  $a_x$  and  $a_y$  are the radii in  $x$  and  $y$  directions. In the center of the beam there is no curvature in the  $x$  direction. The curvature in the  $y$  direction is proportional to  $1/a_y^3$ . A thermal-blooming lens is therefore approximately described by the value  $Q = 3$  in the expression for the nonlinear lens, Eq. (1).

### III. GEOMETRICAL BEAMS WITH A SINGLE LENS

We describe in some detail the simplest case, which is the geometrical optics limit with a single lens. We require that the focus of the corrected beam appear in the target plane.

#### A. Linear propagation

The undisturbed beam focuses at the target if  $R_T$  equals the distance to the target  $R$ ; the notation used is described in Fig. 1. Inserting a lens at a distance  $L$  from the focus changes the curvature of the wave front by  $K$  and the focus is displaced by the distance  $D$  determined by the relation

$$\frac{1}{L+D} = \frac{1}{L+R_T - R} - K, \quad (3)$$

valid for any value of the initial radius of curvature  $R_T$ .

The requirement  $D=0$  leads to the condition for the corrected radius of curvature at the transmitter  $R_{TC}$ :

$$R_{TC} = R - L^2/(L+1/K). \quad (4)$$

A glint inserted in the target plane and propagated through the lens arrives at the transmitter with the same radius of curvature  $R_{TC}$ . In this derivation, no limit was imposed on the transmitter size or on the size of the beam at the position of the lens.

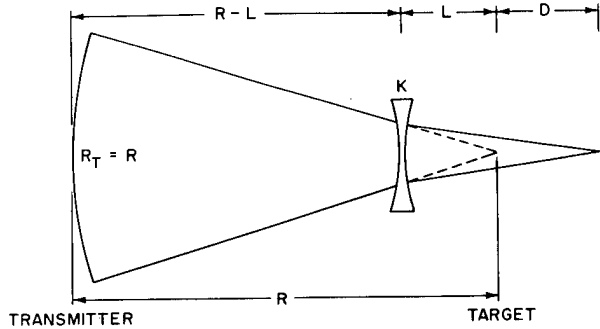
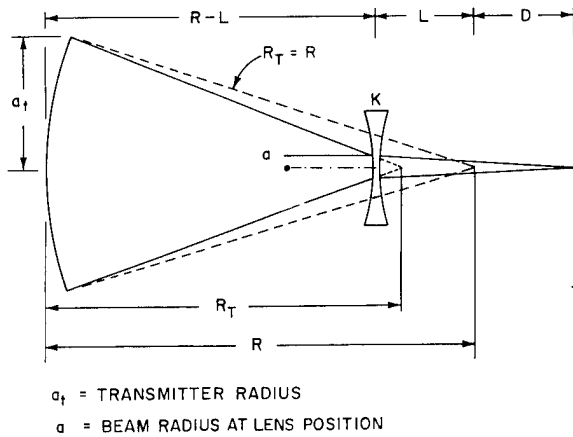


FIG. 1. Notation used in the phase conjugate COAT calculations for geometric beam.



$a_t$  = TRANSMITTER RADIUS

$a$  = BEAM RADIUS AT LENS POSITION

FIG. 2. Beam with corrected radius of curvature at the transmitter.

#### B. Nonlinear propagation

1. *Analytical solutions:* We now keep the transmitter size and the power of the beam constant and assume that the curvature  $K$  is proportional to the irradiance,

$$K = S(a_t/a)^2, \quad (5)$$

where  $a$  is the radius of the beam at the position of the lens. This is a special case of Eq. (1) for  $Q=2$ , permitting simple explicit solutions. The radius  $a$  is given by (see Fig. 2)

$$a_t/a = R_T/(L+R_T - R). \quad (6)$$

The equivalent to Eq. (3) is now

$$\frac{1}{L+D} = \frac{1}{L+R_T - R} - \frac{SR_T^2}{(L+R_T - R)^2}. \quad (7)$$

The requirement  $D=0$  leads to a quadratic equation for the radius of curvature at the transmitter with the condition for the existence of a real root

$$1 - 4SR(R-L)/L \geq 0. \quad (8)$$

If  $S$  and  $L$  do not satisfy the condition, Eq. (8), we ask for the radius of curvature at the transmitter which minimizes the radius of the beam in the target plane, which is given by  $a_f = aD/(L+D)$ . Using Eqs. (6) and (7) and the requirement  $da_f/dR_T = 0$ , we get a quadratic equation for  $R_T$ . The solution of this equation leads to the minimum radius of the beam in the focal plane, which we indicate by a horizontal dashed line in Fig. 3.

2. *Iterative solutions:* The phase conjugate correction is performed using the following interaction scheme. We call  $R_{Tn}$  the radius of curvature at the transmitter and  $K_n$  the curvature of the nonlinear lens at the  $n$ th iteration. We start with  $R_{T0} = R$  and the initial curvature of the lens  $K_0 = S(R/L)^2$  and get a new value for the radius of curvature at the transmitter

$$R_{T(n+1)} = R - L^2/(L+1/K_n), \quad (9)$$

using the value of the curvature of the lens

$$K_n = SR_{Tn}^2/(R_{Tn} + L - R)^2 \quad (10)$$

for each iteration.

The results of the iteration are presented in Fig. 3,

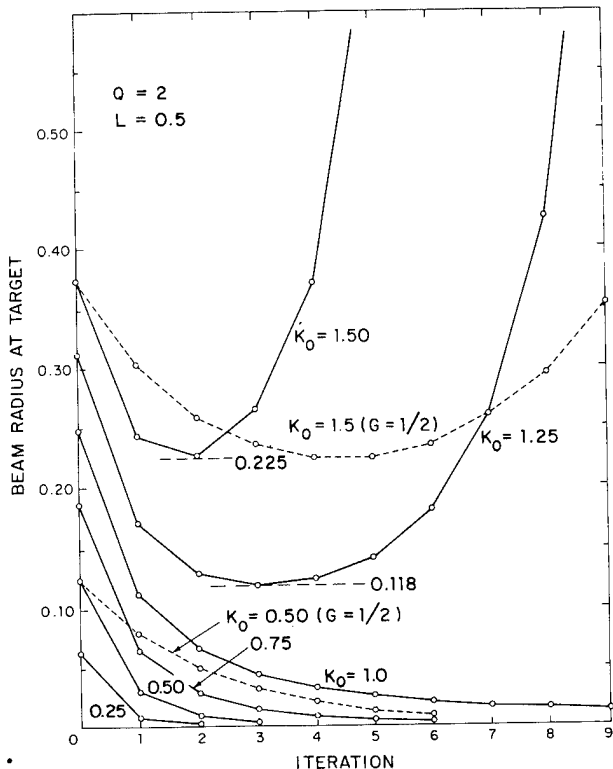


FIG. 3. Beam radius at the target as a function of iteration for different values of the initial curvature  $K_0 = S/L^2$ . The two dashed curves use an iteration with half the gain.

where we plot the radius in the target plane  $a_t$  as a function of the iteration number for the case  $L = R/2$ . Other values of  $L$  behave qualitatively the same. For  $K_0 \leq 1$  a solution  $D = 0$  exists and the iteration seems to converge. For  $K_0 \geq 1$  the iteration approaches the analytical solution but diverges for further iterations.

An attempt was made to affect the divergence by reducing the gain of the iteration, using for the new radius of curvature the average of the value calculated by Eq. (9) and the previous one,

$$R'_{Tn} = 0.5(R_{Tn} + R_{T(n-1)}),$$

for the calculation of the curvature by Eq. (10). The results are indicated in Fig. 3 by  $G = 1/2$  for two values,  $K_0 = 0.5$  and  $K_0 = 1.5$ . Convergence and divergence for these two cases are slower, but not qualitatively changed.

### C. Phase conjugate COAT with time constants

In the previous sections, a study of a simple single lens system was presented in order to simulate the phase-conjugated COAT technique and demonstrate the lack of convergence for strong enough nonlinearities. The iteration performed there corresponds to the condition sketched in Fig. 4, for which the atmospheric time constant  $t_{at}$  is much smaller than the iteration time constant  $t_{it}$ , describing a system which uses a phase correction based on the return from a glint only after the atmosphere reaches steady-state conditions. We generalize the iteration scheme, permitting an arbitrary value of  $t_{it}/t_{at}$ , assuming an exponential ap-

proach of the nonlinear lens to the steady state. This modification leads to the iteration

$$R_{T0} = R, \quad K'_{-1} = 0 \text{ with } n = 0, 1, 2, \dots,$$

$$K_n = S[R_{Tn}/(L - R + R_{Tn})]^Q,$$

$$K'_n = fK'_{n-1} + (1-f)K_n,$$

$$R_{T(n+1)} = R - L^2(L + 1/K'_n)^{-1},$$

where  $R_{Tn}$  is the radius of curvature at the transmitter for the  $n$ th iteration. The strength of the nonlinearity is  $S$  and  $Q$  is its power law. The position of the lens is  $L$ , measured from the target. The steady-state value of the curvature of the lens is  $K_n$ , but the actual curvature is  $K'_n$ , determined at the moment when the glint return senses it. The time constants are included in the coefficient  $f = \exp(-t_{it}/t_{at})$ . This model describes a correction system which itself has a zero time constant. The results of the iteration with atmospheric time constants are shown in Fig. 5 for a particular case. The beam radius at the target is plotted as a function of the iteration for some values of the coefficient  $f$ . The curves with larger atmospheric time constants, corresponding to larger values of  $f$ , are lower than the ones with shorter time constants, but eventually they also diverge.

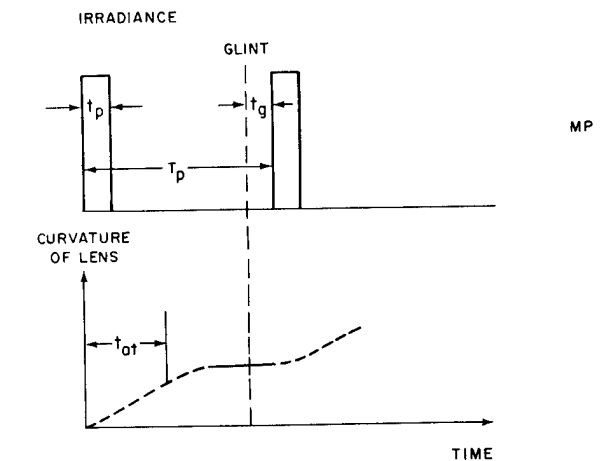
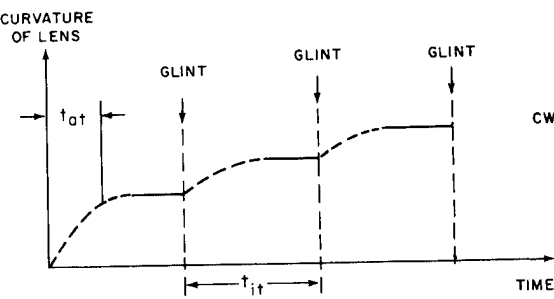


FIG. 4. Schematic representation of phase conjugate COAT systems with an atmospheric time constant  $t_{at}$ . For the cw case, the iteration time is  $t_{it}$ . For the MP case, the pulse length is  $t_p$ , the pulse spacing is  $T_p$ , and the time between the sensing of the atmosphere by a glint return and the next pulse is  $t_g$ . Standard multipulse conditions require  $t_p \ll t_{at} \ll T_p$ .

If we reduce the iteration time constant, we can increase the time before onset of the divergence. Let us assume an atmospheric time constant of 0.1 s and an iteration time of 1 ms giving a value  $f = 0.99$ . The divergence started after about 500 iterations, corresponding in this case to  $\frac{1}{2}$  s. A fast correcting adaptive system can, temporarily at least, overcome the divergence problems of the phase conjugate COAT for cw beams.

In Fig. 4 we also present the situation for a multipulse case. The pulse length is called  $t_p$ , and the pulse spacing  $T_p$ . Standard multipulse cases satisfy  $t_p \ll t_{at} \ll T_p$ , expressing the condition that no self-blooming for each pulse occurs, and that each pulse is subjected to the heat deposit from previous pulses only, assuming validity of the long-time hydrodynamic limit. If the time between the glint sensing and the next pulse  $t_\epsilon$  is much smaller than the atmospheric time constant  $t_{at}$ , the system becomes linear for that particular pulse. The corrections due to such phase-conjugated COAT systems are limited by finite aperture sizes.

#### IV. GAUSSIAN BEAMS AND MULTILENS SYSTEMS

##### A. Limits to the phase compensation for a Gaussian beam for linear distortions

Phase corrections for linear systems (e.g., turbulence) can restore the irradiance in the focal plane only

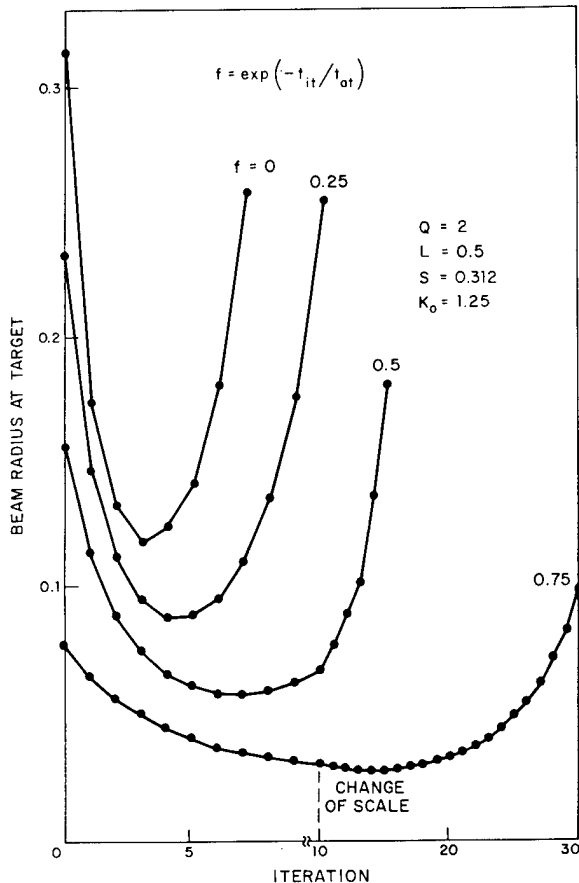
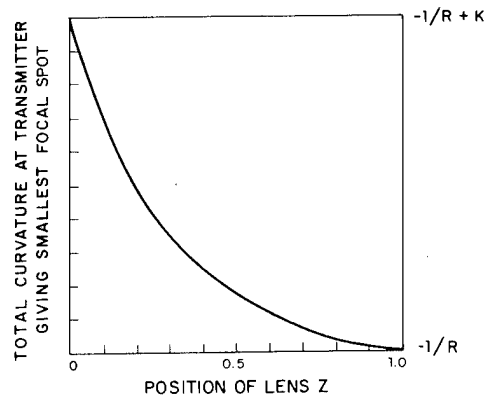
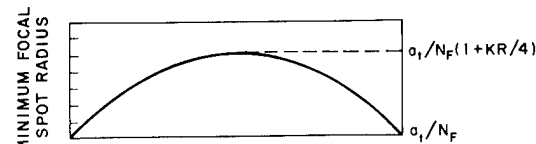


FIG. 5. Radius of beam in the target plane as a function of iteration number for some values of the time constants described by the coefficient  $f = \exp(-t_{it}/t_{at})$ .



LIMITS TO PHASE CORRECTION  
FOR LINEAR SYSTEM

FIG. 6. Limits to phase correction for Gaussian beam for single constant lens inserted at distance  $z$  between transmitter and target.

to a limited degree if a fixed transmitter size is assumed. We show this for the simple case of a constant thin lens with curvature  $K$  inserted in a Gaussian beam<sup>4</sup> at a position between the transmitter and target.

The beam radius in the target plane  $a_t$  is given by

$$a_t^2 = a_t^2 [1 + CR + KR(1 - z) + KRz(1 - z)]^2 + a_t^2 [1 + KRz(1 - z)]^2 / N_F^2,$$

where  $a_t$  is the radius of the beam at the transmitter ( $1/e$  power),  $R$  the range,  $C$  the curvature of the beam

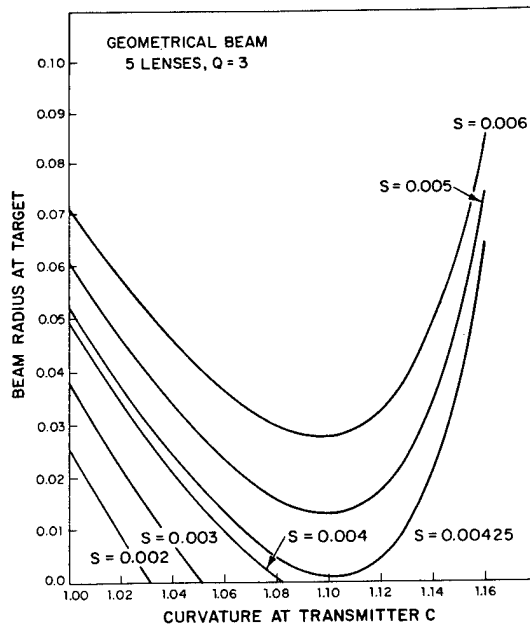


FIG. 7. Beam radius at target vs curvature at transmitter for five-lens system with geometrical beam.

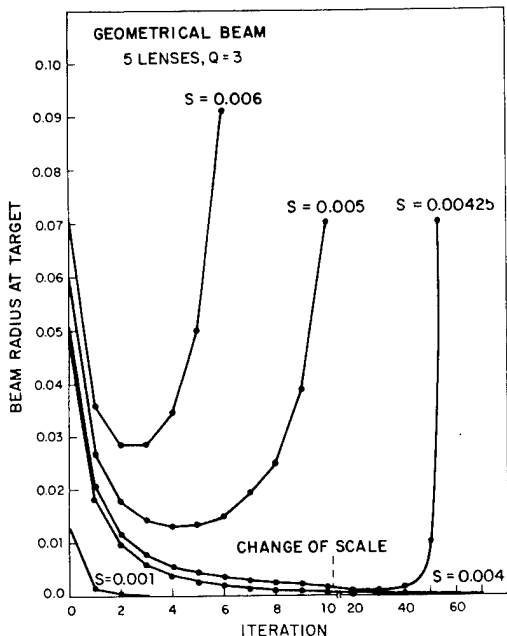


FIG. 8. Beam radius at target vs iteration for cases of Fig. 7.

at the transmitter which is being varied,  $N_F = ka_t^2/R$  the Fresnel number, and  $z$  is the distance to the thin lens measured from the transmitter in units of  $R$ .

The minimum radius of the Gaussian beam  $a_{f, \min}$ , which can be achieved by appropriate choice of the curvature  $C$  at the transmitter, is

$$a_{f, \min} = a_t [1 + KRz(1 - z)]/N_F ;$$

its maximum value as a function of  $z$  is at  $z = \frac{1}{2}$ . The curvature which gives the minimum radius  $C_{\min}$  is

$$C_{\min} R = -[1 + KR(1 - z)]/[1 + KRz(1 - z)] .$$

The minimum radius and the corresponding curvature

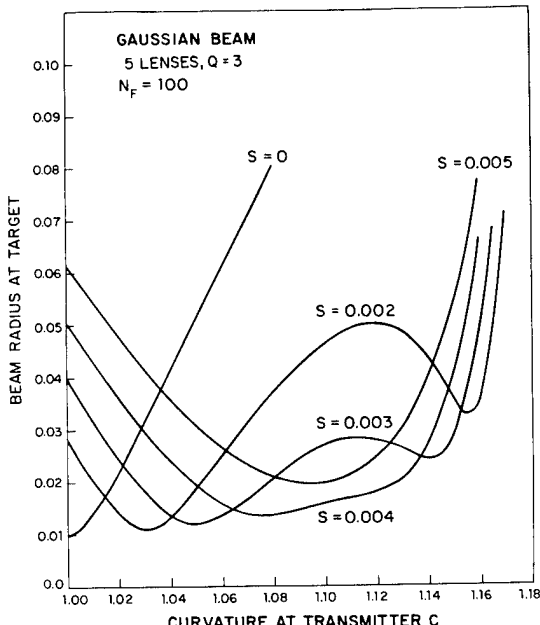


FIG. 9. Beam radius at target vs curvature at transmitter for five-lens system with Gaussian beam.

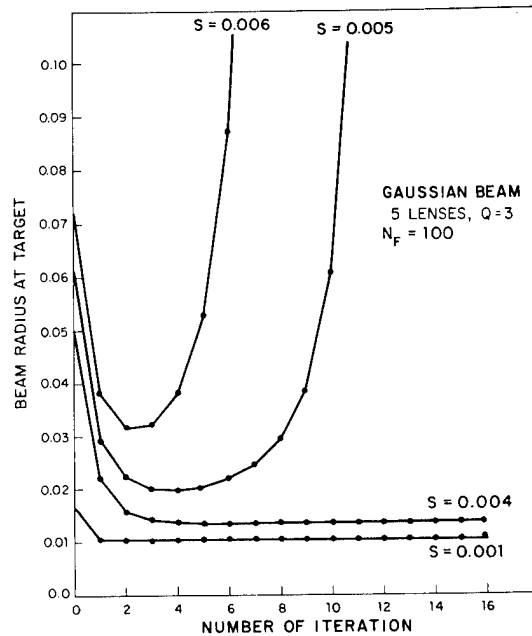


FIG. 10. Beam radius at target vs iteration for the cases of Fig. 9.

are plotted as a function of  $z$  in Fig. 6. At  $z=0$  a complete correction is possible, and at  $z=1$  no correction is required.

#### B. Nonlinear propagation

Our model for a phase conjugate COAT system was extended to permit multiple lenses. A further extension permits us to use Gaussian beams for the beam propagated from the transmitter to the target. A geometrical beam is kept for the glint return.

In Fig. 7 we plot the radius of the geometrical beam in the target plane as a function of curvature at the transmitter  $C$  for some values of the strength of nonlinearity  $S$  for a system of five uniformly spaced lenses. It can be seen that it is not possible to perform an exact compensation for values  $S > 0.004$ . The phase-conjugate iteration for the same five-lens system is shown in Fig. 8. The onset of divergence seems to coincide with the lack of an exact compensation.

In Fig. 9 we plot the radius in the target plane for a five-lens system using a Gaussian beam with a Fresnel number of  $N_F = 100$ . The diffraction-limited radius is now  $1/N_F$ . The onset of divergence is related in some way to the change in the shape of the curves. The phase conjugate COAT iteration is shown in Fig. 10. It exhibits the same qualitative features as the geometrical beam in Fig. 7, but it shows that for Gaussian beams, even for the convergent cases, the radius cannot be reduced to the diffraction-limited value.

#### V. CONCLUSION

In conclusion, the phase conjugate COAT method leads to nearly complete compensation of atmospheric turbulence and partial compensation for cases with moderate thermal blooming, with and without turbulence, so long as the effective thermal lens is thin and near the transmitter, as for slewed beams. For cases

with substantial thermal blooming, the phase conjugate method gives some initial improvement but does not converge. A sufficiently fast correction system may overcome this problem for a limited time.

All calculations presented here refer to idealized cases; questions relating to an experimental realization (like phase measurements, signal to noise) have not been included in our study.

#### ACKNOWLEDGMENTS

The author wishes to acknowledge stimulating discussions with L. C. Bradley of M. I. T. Lincoln

Laboratory and D. L. Fried, Optical Science Consultants.

\*This work was sponsored by the Advanced Research Projects Agency of the Department of Defense.

<sup>1</sup>W. T. Cathey, C. L. Hayes, W. C. Davis, and V. F. Piz-zuro, *Appl. Opt.* **9**, 701 (1970).

<sup>2</sup>W. B. Bridges, P. T. Brunner, S. P. Lazzara, T. A. Nussmeier, T. R. O'Meara, J. A. Sanguinet, and W. P. Brown, Jr., *Appl. Opt.* **13**, 291 (1974).

<sup>3</sup>W. P. Brown, Jr., Hughes Aircraft Co. Technical Report N00014-73-C-0460 (August 1973); J. Winocur, Rockwell International (private communication).

<sup>4</sup>H. Kogelnik and T. Li, *Appl. Opt.* **5**, 1550 (1966).

# Tracking turbulence-induced tilt errors with shared and adjacent apertures\*†

Darryl P. Greenwood

Lincoln Laboratory, Massachusetts Institute of Technology, Lexington, Massachusetts 02173

(Received 29 July 1976)

Tracking apertures which are on axis, off axis, and annular with respect to the pointer optics are considered in terms of their effectiveness in canceling atmospheric turbulence-induced wave-front tilt errors. The off-axis tracker is found to be the least effective, whereas the annular configuration is least sensitive to the wind profile and slewing conditions. The key to minimizing the centroid wander in the focal plane is the proper setting of the low-pass cutoff frequency of the tracking servo. That setting is based on wind velocity, slew rate, and aperture diameters. A too-high setting of the cutoff frequency can actually degrade tracker performance when the tracking aperture is small.

## I. INTRODUCTION

In many optical pointing and tracking systems it is not practical to beam split the incoming wave front in order to derive a tracking signal. Often the tracking optics are placed outside the aperture of the pointer. Such a configuration is acceptable for the gross tracking of the target, but there are serious reservations as to whether turbulence errors can be effectively canceled in this configuration. The problem is that the scale sizes of the phase aberrations due to turbulence may be smaller than either the pointer or tracker optics and hence the two fields of view may not see the same phase variations. We will investigate the theoretical effectiveness of tracking in an off-axis configuration by considering the correlation of wave-front tilts on two apertures of different diameters.

We can state in advance that the prognosis for off-axis tracking of turbulence is poor, but we will not leave the situation there. Two other configurations are considered which offer much greater advantages to canceling turbulence-induced centroid motion. Both place the tracker concentric with the pointer. The first is to place the tracker within the pointer central obscuration, and the second is to place the tracker in an annulus surrounding the pointer.

Our method of specifying tracker effectiveness is to calculate the statistical variance of the difference between where you would like to point and where the tracker tells you to point. It is important in this analysis and in the real system to include a variable cutoff frequency of the tracker servo response. High temporal frequencies must be carefully rejected because they correspond to those small scale sizes which are not seen the same by both pointer and tracker. The setting of the cutoff frequency will be determined from the natural wind velocity, slew rate, and aperture dimensions. We will provide sets of 15 error curves in normalized coordinates to serve as a reference gallery of conditions from which the user may select the one most appropriate to his tracking scenario.

To evaluate the effectiveness of the various tracker-pointer configurations, we established three geometries as shown in Figs. 1-3. In the first is a pair of filled apertures (i.e., no central obscuration) of diameters  $D$  for the pointer and  $d$  for the tracker. The axial separation is  $r_1$ , and  $r_1$  may be varied from 0 to  $\infty$  essentially. This allows for placement of the tracker on axis or off axis, but when the tracker is within the

field of view of the pointer, a portion of the optical signal must be diverted by means of a beam splitter from the pointer to the tracker. Note the presence of the low-pass filter impulse response  $h(t)$ , which may be inherent in the servo, but which must have a variable cutoff frequency. In Fig. 2 is the second configuration, termed "annular," where again the tracker signal is low-pass filtered before being fed to the pointer. We choose, for the annular configuration, to retain the symbol  $D$  for the larger diameter and  $d$  for the smaller. Hence the pointer is now of diameter  $d$ , whereas for the filled configuration it was of diameter  $D$ . Finally, in Fig. 3 we return to the on-axis case and allow the tracker to obscure a region of the pointer. We will find that the results of this configuration, termed "interior," are almost identical to the filled configuration with  $r_1 = 0$ , so long as  $d \gtrsim \frac{1}{2}D$ .

## II. THEORY

For each configuration we wish to minimize the error signal  $\epsilon(t)$  between the desired pointer angle  $\alpha_p(t)$  and the indicated tracker angle  $\alpha_t(t)$  as filtered by  $h(t)$ . This is represented by the convolution relation

$$\epsilon(t) = \alpha_p(t) - \alpha_t(t) * h(t) . \quad (1)$$

More physically,  $\epsilon(t)$  is the angular wander of the centroid in the target plane, if we follow reciprocity arguments. The error variance is readily found to be

$$\sigma_\epsilon^2(f_{co}) = \int_0^\infty W_p(f) df + \int_0^\infty H(f, f_{co}) W_t(f) df - 2 \int_0^\infty H^{1/2}(f, f_{co}) W_{tp}(f) df , \quad (2)$$

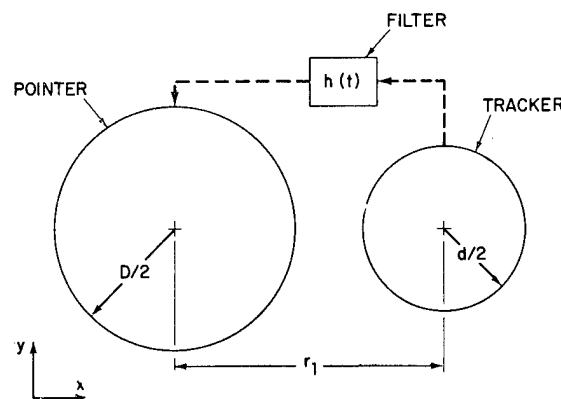


FIG. 1. Geometry: filled configuration.

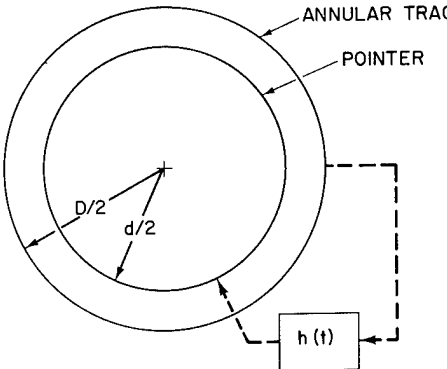


FIG. 2. Geometry: annular configuration.

where  $H(f, f_{co})$  is the modulus-squared Fourier transform of  $h(t)$  and is assumed to have a well-defined cut-off frequency  $f_{co}$ . The power spectral densities  $W_p$  and  $W_i$  are the auto-spectra of  $\alpha_d$  and  $\alpha_i$ , and  $W_{tp}$  is the cross spectrum of  $\alpha_i$  with  $\alpha_p$ .

Spectra for the filled configuration may be obtained from the work by Greenwood and Fried<sup>1</sup> on wave-front compensative systems. In turn, spectra for the annular and interior configurations may be derived from those of the filled configuration by some geometrical considerations. Note that we will be considering wave-front tilts rather than intensity centroids for mathematical convenience. These quantities are not precisely the same but are very similar.<sup>2</sup> For an aperture of diameter  $D$ , the tilt angle  $\alpha_D$  is defined

$$\alpha_D(t) = 2\lambda A_D^{-2} \int d\tilde{x} W_D(\tilde{x}) \phi(\tilde{x}, t) x, \quad (3)$$

where  $\phi(\tilde{x}, t)$  = the spatio-temporal phase incident on the aperture,

$$W_D(\tilde{x}) = \begin{cases} 1, & |\tilde{x}| \leq \frac{1}{2}D \\ 0, & |\tilde{x}| > \frac{1}{2}D \end{cases}$$

$\tilde{x}$  is the vector  $(x, y)$ ,  $d\tilde{x}$  the incremental area  $dx dy$ ,  $A_D$  the aperture area  $\frac{1}{4}\pi D^2$ , and  $\lambda$  is the wavelength. For an aperture of diameter  $d$ , displaced a vector distance  $r_1$  from the aperture of diameter  $D$ , the tilt angle  $\alpha_d$  is

$$\alpha_d(t; \tilde{r}_1) = 2\lambda A_d^{-2} \int d\tilde{x} W_d(\tilde{x}, \tilde{r}_1) \phi(\tilde{x}, t) (x - r_{1x}), \quad (4)$$

where

$$W_d(\tilde{x}, \tilde{r}_1) = \begin{cases} 1, & |\tilde{x} - \tilde{r}_1| \leq \frac{1}{2}d \\ 0, & |\tilde{x} - \tilde{r}_1| > \frac{1}{2}d \end{cases}$$

$A_d$  is the aperture area  $\frac{1}{4}\pi d^2$ , and  $r_1 = (r_{1x}, r_{1y}) = (r_1 \cos \delta, r_1 \sin \delta)$ . Note the angular dependence  $\delta$ , which stems from a geometrical asymmetry, will lead to the off-axis results being a function of the orientation of tilt. Two values of  $\delta$ , namely 0 and  $\frac{1}{2}\pi$ , will be sufficient to describe the off-axis angular dependence, and these angles will correspond to tilts in the  $x$  and  $y$  directions, respectively, as indicated in Fig. 1.

The next step is to define the auto and cross covariances of  $\alpha_d$  and  $\alpha_D$  as

$$\begin{aligned} C_d(\tau) &= \langle \alpha_d(t) \alpha_d(t + \tau) \rangle, \\ C_D(\tau) &= \langle \alpha_D(t) \alpha_D(t + \tau) \rangle, \\ C_{dD}(\tau) &= \langle \alpha_d(t) \alpha_D(t + \tau) \rangle, \end{aligned} \quad (5)$$

and we know  $\langle \alpha_d \rangle = \langle \alpha_D \rangle = 0$ . For the moment, let the subscript  $i$  represent  $D$ ,  $d$ , or  $dd$ . The Fourier transforms of  $C_i(\tau)$  are

$$W_i(f) = 4 \int_0^\infty d\tau \cos(2\pi f\tau) C_i(\tau). \quad (6)$$

Note that this is a one-sided transform, such that

$$\sigma_i^2 = \int_0^\infty df W_i(f). \quad (7)$$

From the earlier paper,<sup>1</sup> we find a general expression for the spectra to be

$$W_i(f) = -\frac{1}{2} \int d\tilde{r} T_i(\tilde{r}) W_{\delta\phi}(\tilde{r}; f), \quad (8)$$

where  $T_i$  is a transfer function associated with the aperture size and separation, and  $W_{\delta\phi}$  is the atmospheric phase-difference power spectrum. To eliminate possible confusion as to which  $T_i$  to use in the earlier paper,<sup>1</sup> we feel that it is worthwhile to repeat the transfer functions. They are

$$T_d(r, \theta) = 2 \left( \frac{\lambda}{A_d \pi} \right)^2 \begin{cases} \cos^{-1} \left( \frac{r}{d} \right) - \left( \frac{r}{d} \right) \left[ 1 - \left( \frac{r}{d} \right)^2 \right]^{1/2} - \frac{2}{3} \frac{r}{d} \left[ 1 - \left( \frac{r}{d} \right)^2 \right]^{3/2} (1 + 4 \cos^2 \theta), & 0 \leq r \leq d \\ 0, & d \leq r, \end{cases} \quad (9a)$$

$$T_D(r, \theta) = T_d(r, \theta) \text{ with } d = D, \quad (9b)$$

$$T_{dd}(r, \theta) = \left( \frac{\lambda}{A_d \pi} \right)^2 \begin{cases} \pi, & 0 \leq r_2 \leq \frac{D-d}{2} \\ \left( \frac{D}{d} \right)^4 \cos^{-1} \gamma_1 + \cos^{-1} \gamma_2 - \left[ \gamma_2 + \gamma_1 \left( \frac{D}{d} \right)^3 \right] (1 - \gamma_2^2)^{1/2} \\ - \frac{4r_2}{3d} (1 - \gamma_2^2)^{3/2} \left[ 1 + \frac{4}{r_2^2} (r \cos \theta + r_1 \cos \delta)^2 \right], & \frac{D-d}{2} \leq r_2 \leq \frac{D+d}{2} \\ 0, & \frac{D+d}{2} \leq r_2 \end{cases} \quad (10)$$

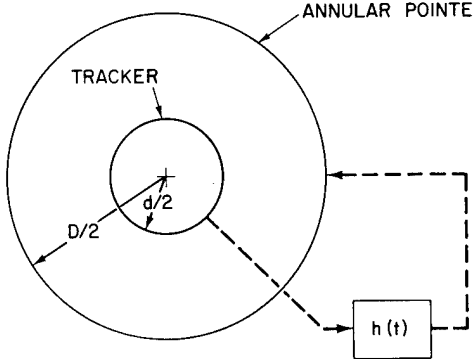


FIG. 3. Geometry: interior configuration.

where

$$\begin{aligned} r_2 &= [r^2 + r_1^2 + 2rr_1 \cos(\delta - \theta)]^{1/2}, \\ r_1 &= [r_2^2 + (\frac{1}{2}D)^2 - (\frac{1}{2}d)^2]/r_2 D, \\ r_2 &= [r_2^2 + (\frac{1}{2}d)^2 - (\frac{1}{2}D)^2]/r_2 d. \end{aligned}$$

It should already be apparent that in the filled configuration

$$\begin{aligned} W_p &= W_D, \\ W_t &= W_d, \\ W_{tp} &= W_{dD}. \end{aligned} \quad (11)$$

However, for the spectra of an annular aperture of outer diameter  $D$  and inner diameter  $d$ , and a filled aperture of diameter  $d$  located concentric with the annulus, we must return to the aperture integrals which define tilt. The least-squares definition of tilt on an annulus is

$$\begin{aligned} \alpha_A(t) &= \frac{2\lambda}{A_D^2 - A_d^2} \left( \int d\tilde{x} W_D(\tilde{x}) \phi(\tilde{x}, t) x \right. \\ &\quad \left. - \int d\tilde{x} W_d(\tilde{x}, 0) \phi(\tilde{x}, t) x \right), \end{aligned} \quad (12)$$

which can be easily rewritten in terms of  $\alpha_D$  and  $\alpha_d$  as

$$\alpha_A(t) = \frac{1}{A_D^2 - A_d^2} [A_D^2 \alpha_D(t) - A_d^2 \alpha_d(t; 0)]. \quad (13)$$

Because of the simple relation that  $\alpha_A$  has with  $\alpha_D$  and  $\alpha_d$ , we may write the pointer and tracker spectra for the annular configuration as

$$\begin{aligned} W_p &= W_d, \\ W_t &= b_2^2 W_D + b_1^2 W_d - 2b_1 b_2 W_{dD}, \\ W_{tp} &= b_2 W_{dD} - b_1 W_d, \end{aligned}$$

where

$$\begin{aligned} b_1 &= [(D/d)^4 - 1]^{-1}, \\ b_2 &= [1 - (d/D)^4]^{-1}. \end{aligned} \quad (14)$$

For the interior configuration, we merely interchange  $W_p$  and  $W_t$  in Eq. (14).

We do not yet need relations for  $W_{\delta\phi}$  in order to determine the low and high  $f_{co}$  asymptotes of  $\sigma_e^2$ . To derive these limits, we will need the variance and covariances of  $\alpha_d$  and  $\alpha_D$ , given by Eq. (7), and the variance of the difference  $\alpha_d - \alpha_D$ , given by

$$\sigma_{D-d}^2 = \sigma_d^2 + \sigma_D^2 - 2\sigma_{dD}^2. \quad (15)$$

Referring to Eq. (2), we may calculate the asymptotes for the filled configuration as

$$\begin{aligned} \sigma_e^2(0) &= \sigma_D^2, \\ \sigma_e^2(\infty) &= \sigma_{D-d}^2. \end{aligned} \quad (16)$$

Note that, via Eq. (15),  $\sigma_{D-d}^2$  may be greater than or less than  $\sigma_D^2$  depending on the value of  $\sigma_{dD}^2$ . Consider the limit when  $\sigma_{dD}^2 \rightarrow 0$ , corresponding to a large separation  $r_1$ . In this case,  $\sigma_e^2(0) < \sigma_e^2(\infty)$ , which says that if we track with the widest possible bandwidth in the off-axis situation, we may actually have higher tracking errors than if we had not attempted to track turbulence at all. In the annular configuration, the asymptotes are

$$\begin{aligned} \sigma_e^2(0) &= \sigma_d^2, \\ \sigma_e^2(\infty) &= b_2^2 \sigma_{D-d}^2. \end{aligned} \quad (17)$$

For small values of  $d/D$  it is possible for  $\sigma_e^2(\infty)$  to exceed  $\sigma_e^2(0)$ ; however, for the more interesting case of a narrow annulus, or  $d/D \rightarrow 1$ ,  $\sigma_e^2(\infty)$  is invariably much smaller than  $\sigma_e^2(0)$ , and the tracking is quite effective. For the interior configuration, the asymptotes are

$$\begin{aligned} \sigma_e^2(0) &= b_2^2 \sigma_D^2 + b_1^2 \sigma_d^2 - 2b_1 b_2 \sigma_{dD}^2, \\ \sigma_e^2(\infty) &= b_2^2 \sigma_{D-d}^2. \end{aligned} \quad (18)$$

Again, we cannot state that  $\sigma_e^2(\infty)$  is definitely less than  $\sigma_e^2(0)$ . Also, the asymptotes do not define the behavior of the curves for intermediate values of  $f_{co}$ . We will see in the graphs to be shown later that in the filled and interior configurations there are substantial dips in the  $\sigma_e^2(f_{co})$  curves which identify optimum cutoff frequencies.

In deriving the phase-difference spectra, we chose to ignore wind direction in order to simplify inordinate and expensive computer intergrations which change the precision little. In fact, turbulence and wind conditions in a field situation are generally known so poorly that the added precision is wasted. Conceivably, one could take advantage of the transport of turbulence from one aperture to another, but we will take a conservative approach of looking at the correlation of tilts with no time lag. Assuming the angle  $\theta = 0$ , we find for spherical waves emanating from a point source on the target that

$$\begin{aligned} W_{\delta\phi}(r; f) &= 0.1305 k^2 L f^{-8/3} \\ &\times \int_0^1 ds v^{5/3}(s) \sin^2[\pi r fs/v(s)] C_n^2(s), \end{aligned} \quad (19)$$

obtained from expressions in Lee and Harp<sup>3</sup> or Clifford.<sup>4</sup> In Eq. (19) we have  $L$  as the range,  $v(s)$  the wind speed normal to the path, possibly including a pseudo-wind due to slewing,  $C_n^2(s)$  the refractive-index structure parameter, and  $s$  the incremental path length ranging from 0 at the point source to 1 at the tracker.

The analysis is now at a point where we may specify  $v(s)$  and  $C_n^2(s)$  and integrate over the path to determine  $W_{\delta\phi}$ . We will use simplified forms for velocity and turbulence which we believe represent most cases of interest. First, we say  $C_n^2$  is a constant along the path, since generally the paths are of low elevation angle,

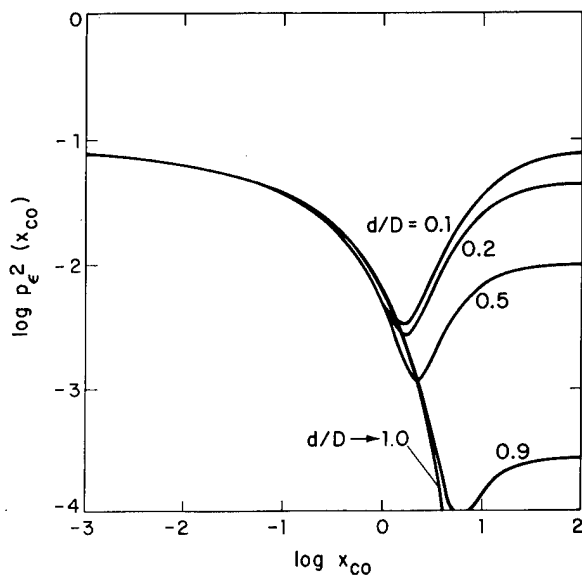


FIG. 4. Error variance vs cutoff frequency: filled on-axis configuration, wind case 1.

and thus  $C_n^2$  is known very poorly. Fortunately, we have found that the results, in the form of  $\sigma_e^2(f_{co})$ , are not very sensitive to the  $C_n^2$  profile. Secondly, we chose three possible forms for  $v(s)$ . Wind case 1 will represent a constant transverse wind velocity given by

$$v(s) = v_a . \quad (20)$$

This case represents targets and tracker platforms which have a low relative motion. Wind case 2 is to represent a slew-dominated situation where the tracker platform is essentially stationary relative to the target motion, or

$$v(s) = \omega L(1 - s) , \quad (21)$$

where  $\omega$  is the slew rate. Wind case 3 reverses this situation by having the target essentially stationary,

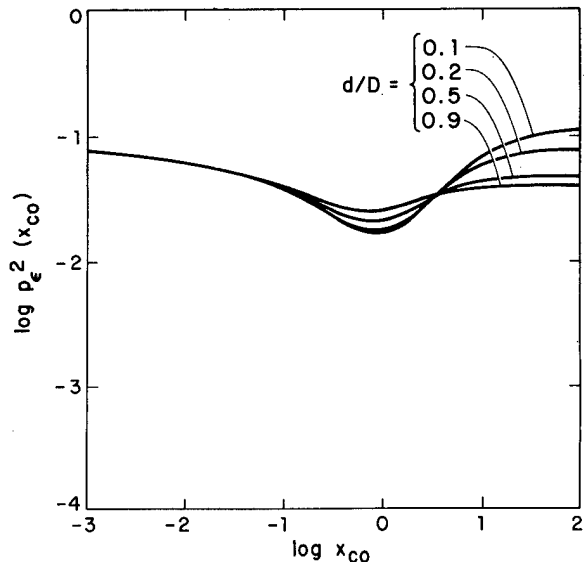


FIG. 6. Error variance vs cutoff frequency: filled contiguous off-axis configuration, tilt y, wind case 1.

and having the tracker platform moving at a high rate, or

$$v(s) = \omega L_s . \quad (22)$$

For the above assumptions, we may write the phase-difference spectrum in a convenient normalized format. The general form involves  $D$ , the larger aperture diameter, because of later aperture integrals which will be relative to  $D$ :

$$W_{\delta\phi}(r; f) = 0.330 k^2 L C_n^2 D^{5/3} (f/f_0)^{-8/3} f_0^{-1} K(f r/f_0 D) , \quad (23)$$

where  $f_0$  is a characteristic frequency having a different expression depending upon which wind case is of interest. For wind case 1 we have

$$f_0 = v_a / \pi D \quad (24)$$

$$K(u) = \frac{4}{3} \left( 1 - \frac{\sin(2u)}{2u} \right) .$$

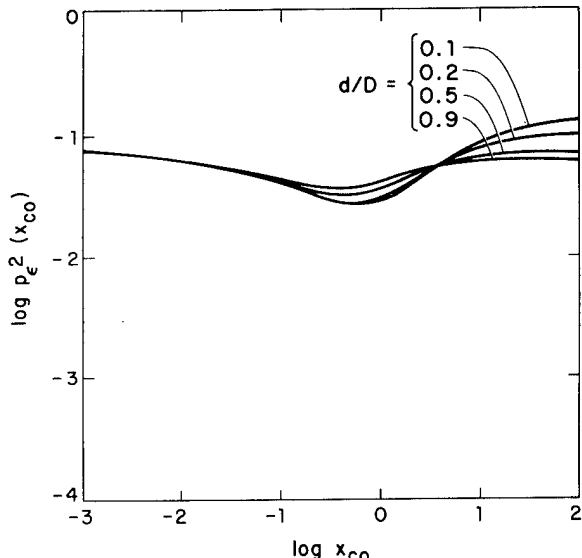


FIG. 5. Error variance vs cutoff frequency: filled contiguous off-axis configuration, tilt x, wind case 1.

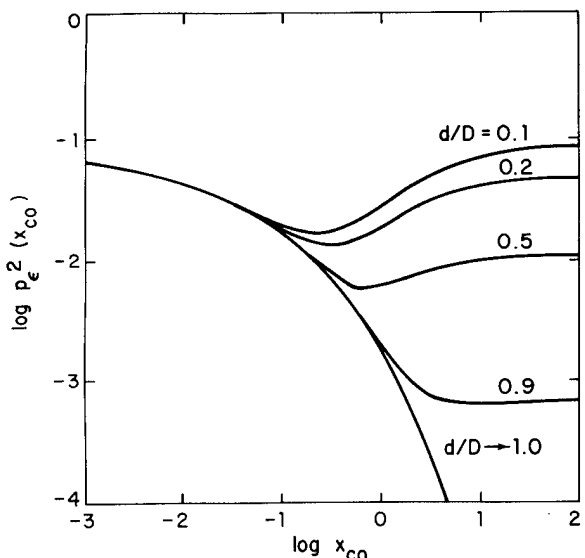


FIG. 7. Error variance vs cutoff frequency: filled on-axis configuration, wind case 2.

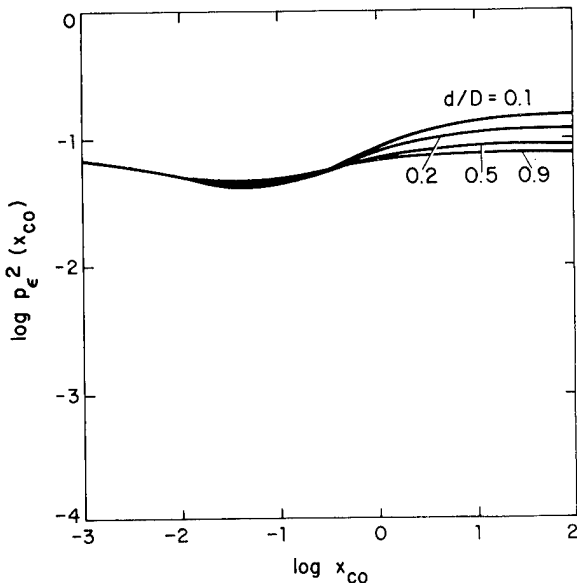


FIG. 8. Error variance vs cutoff frequency: filled contiguous off-axis configuration, tilt  $x$ , wind case 2.

In wind case 2 we have

$$f_0 = \omega L / \pi D \quad (25)$$

$$K(u) = \frac{8}{3} \int_0^1 ds (1-s)^{5/3} \sin^2 \left( \frac{su}{1-s} \right) .$$

Finally, in wind case 3 we have

$$f_0 = \omega L / \pi D \quad (26)$$

$$K(u) = \sin^2 u$$

To further minimize the number of parameters which will appear in the results, we chose to normalize  $\sigma_e^2$  and  $f_{co}$  as follows:

$$p_e^2 = \sigma_e^2 / (13.0 D^{-1/3} L C_n^2), \text{ and } x_{co} = f_{co} / f_0 . \quad (27)$$

Now  $p_e^2(x_{co})$  depends on  $d/D$  for all configurations, and

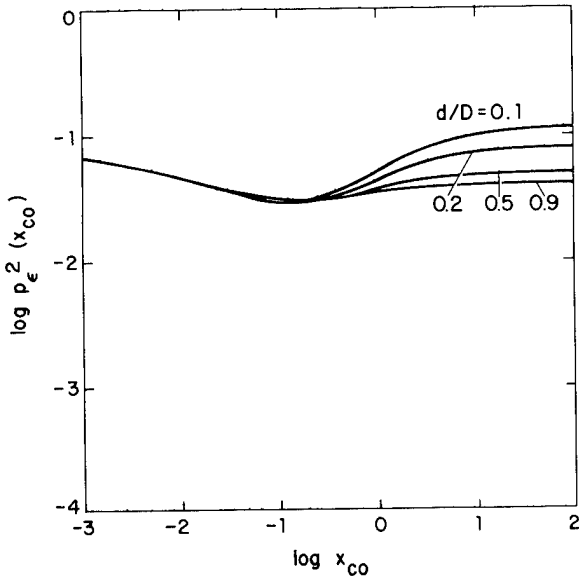


FIG. 9. Error variance vs cutoff frequency: filled contiguous off-axis configuration, tilt  $y$ , wind case 2.

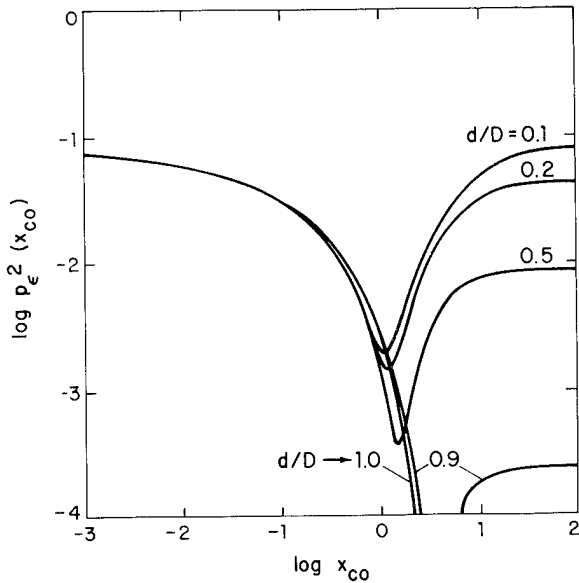


FIG. 10. Error variance vs cutoff frequency: filled on-axis configuration, wind case 3.

on  $r_1/D$  and  $\delta$  in the filled configuration when  $r_1 > 0$ . Furthermore,  $p_e^2$  depends on the choice of a type of low-pass filter. We tried two types of filter, a binary one that is unity up to the cutoff frequency and zero above, and an RC filter given by

$$H(f, f_{co}) = [1 + (f/f_{co})^2]^{-1} . \quad (28)$$

Since the results were not substantially different, we will present curves only for the RC filter. Many realistic closed-loop servo responses have a character similar to Eq. (28) in the neighborhood of the 3 dB point. Although realistic responses roll off faster than Eq. (28) for  $f > f_{co}$ , that will not affect the results since the tilt spectra themselves roll off at a high rate (typically at  $f^{-11/3}$ ).

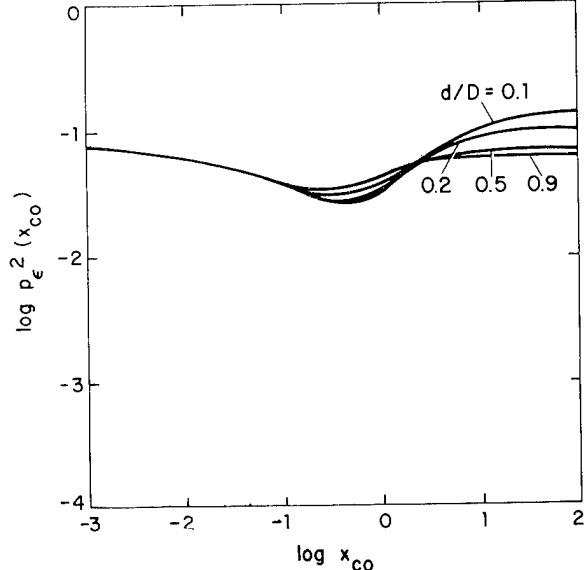


FIG. 11. Error variance vs cutoff frequency: filled contiguous off-axis configuration, tilt  $x$ , wind case 3.

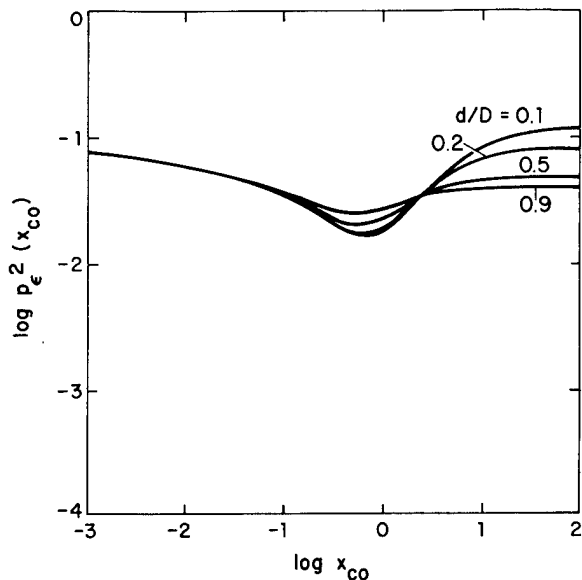


FIG. 12. Error variance vs cutoff frequency: filled contiguous off-axis configuration, tilt  $y$ , wind case 3.

### III. RESULTS

As stated previously, our goal, in the presentation of results, is to present a sufficient number of curves to serve as standards for most tracking cases of interest. There are fifteen figures (4-18) which represent the three wind cases and these configurations: filled on-axis (Figs. 4, 7, 10), filled off-axis tilt  $x$  (Figs. 5, 8, 11), filled off-axis tilt  $y$  (Figs. 6, 9, 12), annular (Figs. 13-15), and interior (Figs. 16-18). A representative range of values for  $d/D$  was chosen as 0.1, 0.2, 0.5, and 0.9, and where meaningful,  $d/D \rightarrow 1.0$ . For off-axis trackers, we assumed the tracker and pointer optics were contiguous; hence, for the stated values of  $d/D$ , we have  $r_1/D = 0.55, 0.6, 0.75$ , and  $0.95$ , where generally  $r_1/D = \frac{1}{2}(1+d/D)$ .

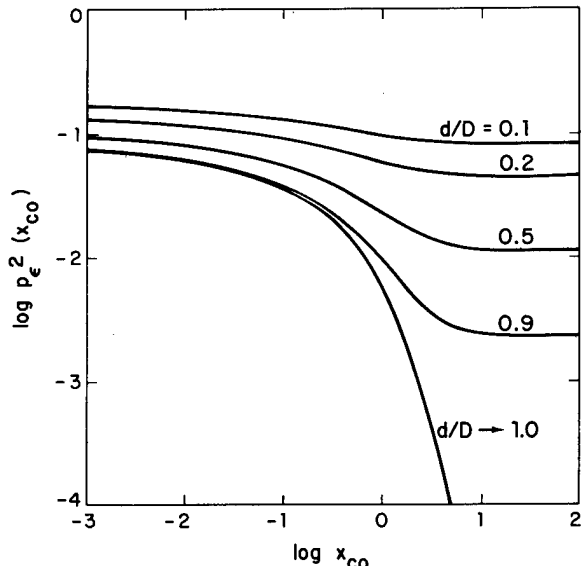


FIG. 13. Error variance vs cutoff frequency: annular configuration, wind case 1.

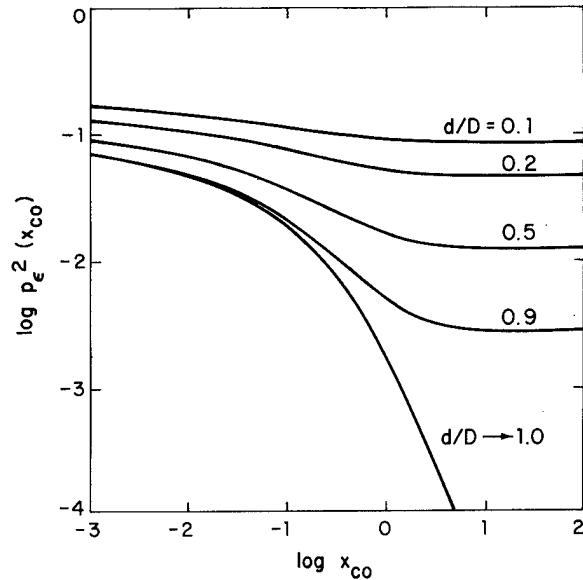


FIG. 14. Error variance vs cutoff frequency: annular configuration, wind case 2.

For a quality measure, we define a reduction factor  $R$  as

$$R = \min[p_e^2(x_{co})]/p_e^2(0), \quad (29)$$

since we are minimizing  $p_e^2$  with respect to the tracking error when no turbulence tracking is attempted. The significance of a particular value of  $R$  may be evaluated on an absolute basis, by comparing the residual tracking error  $R\sigma_e^2(0)$  with the diffraction-limited beam size  $(1.22\lambda/D)^2$ , and we will demonstrate this with particular system and turbulence parameters. However, we may also categorize  $R$  on a relative basis. If the rms tracking error cannot be reduced by better than a factor of  $\sqrt{2}$  (i.e.,  $R = 0.5$ ), the tracking improvement will hardly be measurable. In contrast, an rms error

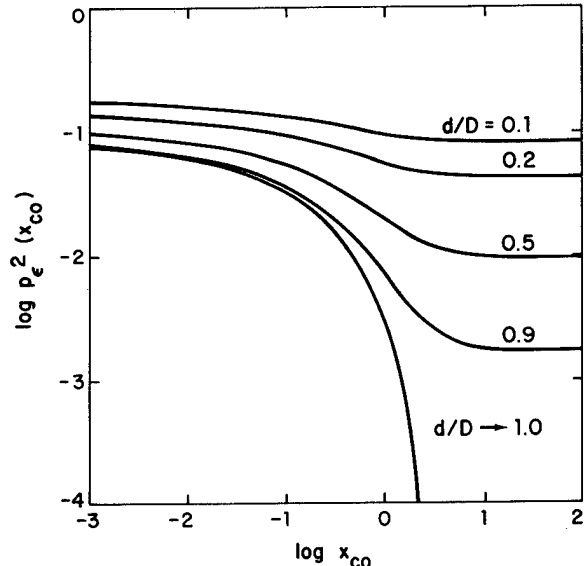


FIG. 15. Error variance vs cutoff frequency: annular configuration, wind case 3.

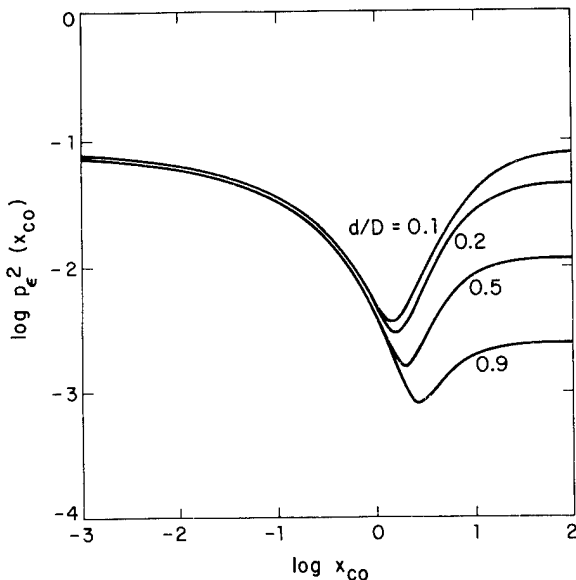


FIG. 16. Error variance vs cutoff frequency: interior configuration, wind case 1.

correction of at least a factor of 5 (i.e.,  $R = 0.04$ ) will significantly enhance system performance.

Consider first Fig. 4, which is for the on-axis filled configuration and wind case 1 (constant winds). There is obviously a substantial tracking improvement, as noted by the dips in the curves, provided  $x_{co}$  is set properly. For  $d/D = 0.1$ , the improvement factor  $R = 0.039$ , and this occurs at  $x_{co} = 1.45$ . To make these numbers more meaningful, consider the following rather arbitrary set of conditions:  $D = 1$  m,  $v_a = 4$  m/s,  $L = 5000$  m, and  $C_n^2 = 10^{-13}$  m<sup>-2/3</sup>. We will need the asymptotic value of  $p_e^2$  which applies independent of wind profile or value of  $v_1$ :

$$p_e^2(0) = 0.0885 . \quad (30)$$

To obtain the asymptote in unnormalized units we apply

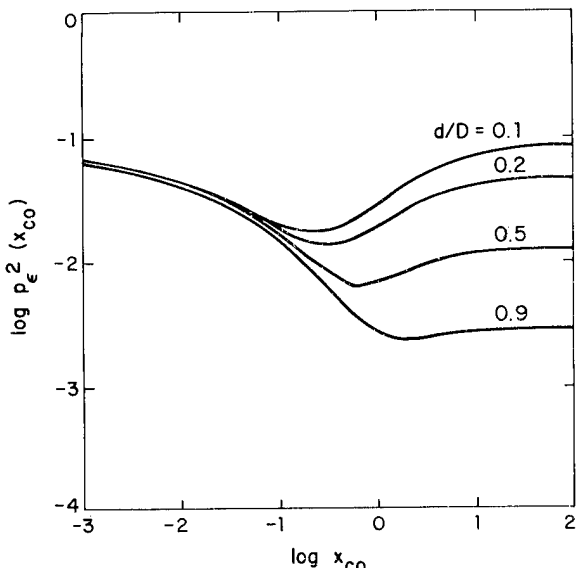


FIG. 17. Error variance vs cutoff frequency: interior configuration, wind case 2.

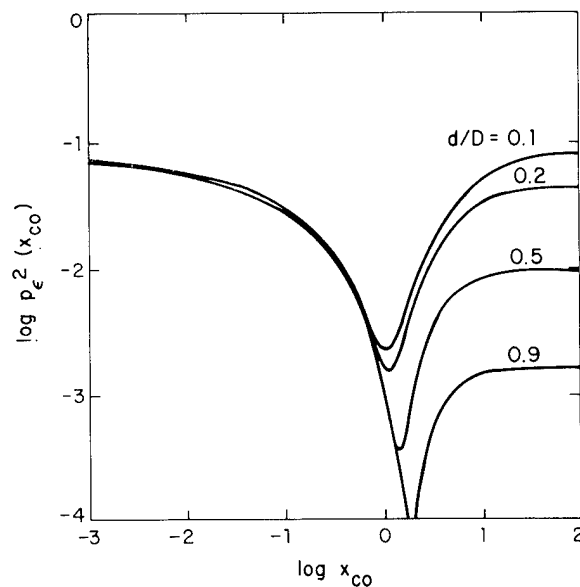


FIG. 18. Error variance vs cutoff frequency: interior configuration, wind case 3.

Eq. (30) to Eq. (27), which for the stated conditions gives us  $\sigma_e^2(0) = 5.75 \times 10^{-10}$  rad<sup>2</sup>. According to the calculated value of  $R$  we may reduce this error to  $\sigma_e^2 = 2.24 \times 10^{-11}$  rad<sup>2</sup>. Note the residual error is equivalent to the diffraction-limited spread  $2.15 \times 10^{-11}$  rad<sup>2</sup>, calculated as  $(1.22 \lambda/D)^2$  at  $\lambda = 3.8 \mu\text{m}$ . The optimum cutoff frequency to achieve this reduction is  $f_{co} = v_a x_{co} / \pi D$ , such that  $f_{co} = 1.8$  Hz. This cutoff should be easily attainable for a tracking servo driving a 1 m system.

It is perhaps surprising that a substantial tracking improvement occurs for a  $d/D$  as small as 0.1, since the tracker is observing only  $\frac{1}{100}$ th the area of the pointer in estimating the pointer angle. The key is in the proper rejection of small turbulence scale sizes by filtering out the high frequencies. Alternatively, we may think of averaging an ensemble to wave fronts for a period of time based on the pointer diameter and the wind velocity. That averaging time is approximately  $(2\pi f_{co})^{-1}$ .

Also in Fig. 4 we have shown the asymptotic curve as  $d/D \rightarrow 1$ , to demonstrate the use of beam-splitting optics such that the pointer and tracker have the same aperture. Now, as expected, the optimum tracking occurs for the highest possible cutoff frequency, but that frequency need not exceed  $x_{co} \approx 3$ .

Now let us compare the curves in Fig. 4 for an on-axis tracker with those of Figs. 5 and 6 for a contiguous off-axis tracker. The dips in the off-axis curves are no longer substantial. Tracking improvement for  $d/D = 0.1$  is a mediocre  $R = 0.31$  for tilt  $x$  (at  $x_{co} = 0.5$ ) and is slightly better for tilt  $y$  with  $R = 0.19$  ( $x_{co} = 0.9$ ). For larger  $d/D$ , the tracker improvement becomes even poorer, suggesting we are intercepting more and more incorrect turbulence information. Thus if the tracker must be off axis, it should be small and as close as possible to the pointer.

Figures 5 and 6 are good examples of the tracking degradation which could result from setting the cutoff

frequency too high. In particular, for the smaller values of  $d/D$ , the asymptote  $p_\epsilon^2(\infty)$  exceeds  $p_\epsilon^2(0)$ .

In comparing Fig. 5 with Fig. 6, we note that tilt  $y$  has lower values of  $R$  than tilt  $x$ . This is a result of a higher correlation between tilts on a common axis (the  $x$  axis, about which we have tilt  $y$ ) than between tilts on parallel but not common axes (namely,  $y$  axes, about which we have tilt  $x$ ). The axes are depicted in Fig. 1.

In Figs. 7–9 we have similar results for the second wind case, that of slew-dominated winds and a moving target. In comparing these results with Figs. 4–6, we note the improvement is not so great as in the first wind case. For example, the on-axis  $d/D = 0.1$  curve has an  $R = 0.20$  at  $x_{co} = 0.18$ . For a more accurate track, a larger  $d/D$  would be required. To evaluate the dependence on wind profile, let us consider the other extreme in winds given by case 3, which is still slew dominated, but now the tracker platform is in motion relative to the target. The results in Figs. 10–12 demonstrate the best improvement so far, with  $R = 0.023$  at  $x_{co} = 1.14$  for  $d/D = 0.1$  and  $r_1 = 0$ .

We may explain the wind profile dependence by considering a hypothetical point frozen in the turbulence field, where that point is transported by the wind transverse to the path. The transport time necessary for the hypothetical point to traverse the beam is  $T(s) = Ls/v(s)$ . If the wind increases linearly from zero at the point source, then the transport time is independent of position along the path, since  $v(s) \sim s$ . This leads to a resonance between the winds and the wave front, and in essence, the tracker and pointer see aberrations moving at a constant transport rate, independent of path position. This is of course wind case 3, where we saw the best tracking improvement. Whenever the winds have a profile which deviates from this ideal, the phase aberrations move into and out of the field of view at varying rates along the path, and the tracking improvement increasingly degrades as  $Ls/v(s)$  departs from a constant. The next best case which we considered is wind case 1, where  $v(s) \sim \text{const}$  and  $T(s) \sim s$ . Even here, the graphs indicate substantial tracking improvement. The worst case is then wind case 2, where  $v(s) \sim (1-s)$  and  $T(s) \sim s/(1-s)$ , which even goes to infinity at the tracker/pointer.

The results for the annular configuration and the three wind cases given in Figs. 13–15 do not exhibit the same strong dependence on wind profile as we saw in the filled configuration. Now the optimum track occurs for the highest cutoff frequency possible; however, it is generally not necessary to exceed  $x_{co} \approx 4$  for any wind profile or annular width. This also suggests if the tracking situation, including slew rates and ambient winds, is unknown to some extent at the time of system design, that the annular configuration should be used.

Our method of normalization caused the annular curves to asymptote to different low-frequency values. We kept the outer diameter  $D$  fixed and varied the pointer diameter  $d$ . There certainly is no loss of generality since actual numbers can be extracted by re-

versing the normalization procedure; however, this situation conforms to having a particular size optic shared between the pointer and tracker. For further reference, the low-frequency asymptote for the annular configuration is

$$p_\epsilon^2(0) = 0.0885(d/D)^{-1/3}. \quad (31)$$

In the annular configuration, the optimum tracking occurs for the thinnest annulus. This may be at first surprising, but in fact a measurement of phase around the periphery of an aperture is sufficient to define the centroid position, provided amplitude effects are negligible, and we have tacitly made that assumption. This was previously pointed out in Sec. IIIA of Hogge and Butts<sup>2</sup>. Physically, we do not want an annular tracker to extend out and sense improper turbulence information, since temporal filtering will not be of use in rejecting such information. In practice, the annular width will probably be set by signal-to-noise considerations; however, a sufficient amount of energy should be collected in an annulus of width  $0.05D$  (corresponding to  $d/D = 0.9$ ). In this case, a substantial improvement is evidenced by an  $R$  of 0.026.

Finally, Figs. 16–18 represent the interior configuration and are to be compared with the on-axis filled configuration, Figs. 4, 7, and 10. Recall that the physical difference between these configurations is that in the interior configuration the entire pointer aperture must be beam split, even if the tracker only observes a portion of it. The interior configuration is thus the one which we might implement; however, for the sake of analysis, we would prefer to concentrate on the filled. The excellent agreement between the figures for  $d/D \gtrsim 0.5$  supports our desires. We may further conclude that we can fairly accurately estimate the tilt in an annulus by measuring the tilt in the region interior to the annulus, provided we properly low-pass filter (or time average, as noted previously).

As a final remark, it is worthwhile to note that the dips in the error curves are fairly broad, so that the servo cutoff frequency need not be set precisely for the tracking to be effective. Furthermore, this indicates that the dips are not a result of some mathematical artifact and can be achieved in practice. By varying the wind profile through extremes, we further verified that the dips are not simply isolated mathematical peculiarities.

#### IV. CONCLUSION

We have considered tracking apertures which share the area of the pointing optics or which are placed adjacent to the pointer. The off-axis configuration was found to be ineffective in tracking turbulence-induced tilt errors, since the turbulence is not seen in the same manner by both pointer and tracker fields of view. When the tracker is placed concentric with the pointer, in either the region of the central obscuration or in an annulus, the tracking accuracy improves. In all cases it is important to properly low-pass filter the signal fed from the tracker to the pointer. Such a capability exists in the servo closed-loop response. The setting

of the cutoff frequency is determined by the aperture diameters, wind velocity, and slew rate. These parameters are applied to a gallery of graphs (Figs. 4-18), which are for varied wind and slew conditions as well as for the varied tracker/pointer configurations. We feel these curves cover the cases of interest; however, formulas provided in the preceding text may be used to calculate error curves for particular slew rates, and wind velocity and turbulence profiles.

\*This work was sponsored by the High Energy Laser Project Office, PMS-405, Naval Sea Systems Command, Washington, D.C.

†A portion of this material was presented at the OSA/IEEE

Conference on Laser and Electro-Optical Systems, May 25-27, 1976, San Diego, Calif., paper THF10; see J. Opt. Soc. Am. 66, 392A (1976).

<sup>1</sup>D. P. Greenwood and D. L. Fried, "Power spectra requirements for wave-front-compensative systems," J. Opt. Soc. Am. 66, 193-206 (1976).

<sup>2</sup>C. B. Hodge and R. R. Butts, "Frequency Spectra for the Geometric Representation of Wavefront Distortions Due to Atmospheric Turbulence," IEEE Trans. Ant. Prop. AP-24, 144-154 (1976).

<sup>3</sup>R. W. Lee and J. C. Harp, "Weak Scattering in Random Media, with Applications to Remote Probing," Proc. IEEE 57, 375-406 (1969).

<sup>4</sup>S. F. Clifford, "Temporal-frequency spectra for a spherical wave propagating through atmospheric turbulence," J. Opt. Soc. Am. 61, 1285-1292 (1971).

## Simultaneous optical and x-ray imaging telescopes

R. C. Harney

MIT Lincoln Laboratory, Lexington, Massachusetts 02173.

Received 15 March 1977.

Of major importance in modern x-ray astronomy is the optical and radio identification of x-ray sources and the correlation of x-ray structure with optical and radio structure in extended sources. X-ray imaging telescopes operated on satellite observatories will be an invaluable tool in this task. Studies indicate that grazing-incidence paraboloid-hyperboloid telescopes can produce high-quality (coma-free) images with angular resolution approaching 1 sec of arc and high sensitivity in the 1-4-keV energy region.<sup>1,2</sup> In this Letter we discuss a simple addition to these systems which should greatly enhance their utility.

A typical paraboloid-hyperboloid x-ray telescope is shown in Fig. 1. X radiation, which is incident axially on the paraboloid of revolution, is reflected onto the hyperboloid of revolution and then reflected again onto an imaging detector. Reflection from the hyperboloid corrects for coma, producing a high-quality image. A diaphragm shields the x-ray detector from radiation, which does not strike the collimating paraboloid.

If the paraboloid-hyperboloid objective is of sufficient optical quality to produce a good x-ray image it will produce a good optical image as well. Because the optical system is totally reflecting in character, the x-ray and optical images will be perfectly superimposed with identical scale factors and aberrations, though the resolutions of the two images will undoubtedly be different. Thin plastic film can reflect a significant fraction (8-10%) of visible light without drastically attenuating the x radiation passing through it. Thin beryllium foils will reflect substantially more optical radiation, although with somewhat higher x-ray attenuation. If such a film or foil is placed before the focus of the objective, a separate optical image will be formed from the reflected radiation. If the plastic film is flat, the new optical image will also have the same scale factors and aberrations as the x-ray image. By placing an optical imaging detector at the plane of this optical image, an astronomical object can be simultaneously imaged and detected in both x rays and visible light. Problems associated with correlating x-ray information with star charts and atlas photographs taken on different scales at different instruments can thus be eliminated.

Assuming the x-ray and optical detectors have equal quantum efficiencies, the optical detection limit of a simultaneous optical and x-ray imaging telescope can be estimated. Consider a telescope with a 1000-cm<sup>2</sup> collecting area and an x-ray sensitivity (1-4 keV) of 10<sup>-4</sup> photons-cm<sup>-2</sup>-sec<sup>-1</sup> for a 10<sup>4</sup>-sec integration time. Including the reflection losses from the plastic film, the optical sensitivity should be within a factor of five (<2 mag) of the x-ray value. An optical sensitivity of 10<sup>-4</sup> photons-cm<sup>-2</sup>-sec<sup>-1</sup> corresponds to a detection limit of magnitude 22. As this is comparable with the photographic detection limit of a large ground-based telescope, it should be sufficient to permit optical identification of almost

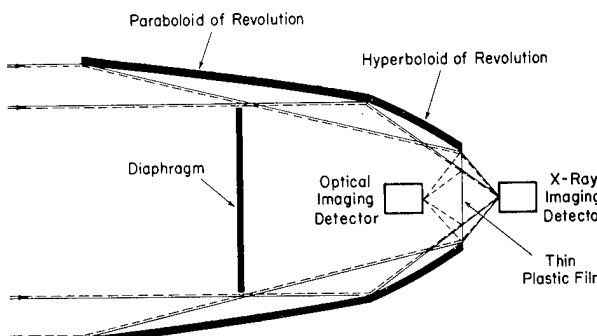


Fig. 1. Schematic of a paraboloid-hyperboloid telescope capable of simultaneous x-ray and optical imaging and detection. Solid rays depict the paths followed by x radiation; dotted rays depict the paths followed by optical radiation.

any x-ray source.

Many new x-ray telescopes employ nested reflecting elements to increase the collecting area while maintaining a fixed over-all size. This will reduce the size of the obscured region behind the diaphragm. If the remaining space is too small to accommodate the optical detector, the plastic film can be oriented at 45° to the telescope axis with the optical detector placed off to the side of the telescope. The scale factors will remain unchanged by this modification.

Compared with the conventional approach of using optical and x-ray detectors, which can be alternately rotated into the image plane of the telescope, the proposed simultaneous detection system offers both advantages and disadvantages. Possible disadvantages are somewhat reduced x-ray and optical sensitivities. Despite the <50% duty cycle inherent in the conventional approach, losses in x-ray transmissions and optical reflection from the plastic film may cause an even larger reduction in the sensitivities for the simultaneous imaging approach. Fortunately, the reduction relative to the conventional approach should not exceed a factor of five in the worst case. One of the advantages of the simultaneous imaging approach is the ability to eliminate the mechanism for alternating the detectors (which necessarily entails using moving parts). In addition, for the study of x-ray sources of a variable or transient nature, the simultaneous imaging approach is clearly superior.

In conclusion, a simple modification to the design of x-ray imaging telescopes will allow for simultaneous optical imaging as well. This modification is expected to have minimal deleterious effects on telescope performance and should be of tremendous benefit to x-ray astronomy.

The work was sponsored by the Department of the Air Force.

### References

1. I. L. Beigman, L. A. Vainshtein, Yu. P. Voinov, and V. P. Shevelko in *Radio, Submillimeter, and X-Ray Telescopes*, Trudy Vol. 77, N. G. Basov, Ed. (Consultants Bureau, New York, 1976).
2. R. Giacconi, W. P. Reidy, G. S. Vaiana, L. P. Van Speybroeck, and T. F. Zehnpfennig, *Space Sci. Rev.* 9, 3 (1969).

## PROPAGATION OF ULTRASHORT LIGHT PULSES IN A RESONANT MEDIUM\*

R.C. HARNEY

Massachusetts Institute of Technology, Lincoln Laboratory, P.O. Box 73  
Lexington, Massachusetts 02173, USA

Received 17 May 1977  
Received in final form 20 September 1977

Mishkin's analytical treatment of ultrashort light pulse propagation in a resonant two-level medium is extended to discuss quantitatively the behavior of the pulse area, pulse energy, pulse shape, and initial population inversion density. The relationship of these properties to physically measurable parameters indicates that the  $nd\ u$  and  $sd\ u$  solutions are experimentally indistinguishable from the  $dn\ u$  and  $cn\ u$  solutions, respectively. The initial population inversion densities required for the  $dn\ u$  and  $nd\ u$  solutions to be stable are less than  $-1$  for values  $k < 1$  and therefore not physically realizable. We conclude that  $cn\ u$  is the only physically significant solution to the Maxwell-Schroedinger equations.

### 1. Introduction

In an earlier paper in this journal<sup>1</sup>), Mishkin presented an analytical investigation of the propagation of ultrashort light pulses through a resonant two-level medium. Such propagation is governed by the coupled Maxwell-Schroedinger equations,

$$\frac{d\epsilon}{dt} = \alpha \langle S \rangle_{\Delta\omega}, \quad (1.1)$$

$$\frac{\partial C}{\partial t} = -\Delta\omega S, \quad (1.2)$$

$$\frac{\partial S}{\partial t} = \Delta\omega C + \epsilon\eta, \quad (1.3)$$

$$\frac{\partial\eta}{\partial t} = -S\epsilon, \quad (1.4)$$

where  $\epsilon$  is the envelope of the incident electric field,  $C$  and  $S$  are the in-phase and out-of-phase components of the macroscopic polarization induced in the medium,  $\eta$  is the population inversion density,  $\Delta\omega$  is the difference between the resonant frequency of the medium  $\omega$  and the frequency of the electric field  $\omega_0$ . The resonant medium is described by a symmetric inhomogeneously-

\* This work was sponsored by the Department of the Air Force.

broadened lineshape function  $g(\Delta\omega)$  and an inverse Beers length  $\alpha$  given by

$$\alpha = 2\pi n_0 \omega_0 p^2 / h, \quad (1.5)$$

where  $n_0$  is the number density of active atoms and  $p$  is the dipole matrix element of the resonant transition.

Mishkin found that the steady-state solutions to eqs. (1.1)–(1.4) have the form

$$\epsilon = \epsilon_0 e(u), \quad (1.6)$$

$$C = \tau \Delta\omega A(\Delta\omega) e(u), \quad (1.7)$$

$$S = -A(\Delta\omega) \partial e(u) / \partial t, \quad (1.8)$$

$$\eta = \eta_0 + \frac{1}{2} \epsilon_0 \tau A(\Delta\omega) e^2(u), \quad (1.9)$$

where  $u = (t - z/V)/\tau$  is the retarded time measured in units of a characteristic time  $\tau$ ,  $A(\Delta\omega)$  is a frequency response function,  $\eta_0$  is the population inversion density that would exist in the absence of the applied electric field, and the  $e(u)$  are the Jacobi elliptic functions<sup>2)</sup>:  $\text{cn } u$ ,  $\text{dn } u$ ,  $\text{sd } u$ , and  $\text{nd } u$ . Table I summarized the properties of these solutions as obtained by Mishkin<sup>1)</sup> and from derivations to follow in this paper.

There has been significant (though unpublished) controversy concerning the validity of these results<sup>3)</sup>. Some people contend that since the  $\text{nd } u$  and  $\text{sd } u$  solutions can be obtained by transforming the arguments of the  $\text{cn } u$  and  $\text{dn } u$  solutions,

$$\text{sd } u = (1 - k^2)^{-1/2} \text{cn}(u - K) \quad (1.10)$$

and

$$\text{nd } u = (1 - k^2)^{-1/2} \text{dn}(u - K), \quad (1.11)$$

there are only two physically significant solutions.  $K$  is the complete elliptic integral of the first kind with modulus  $k$ . Mishkin argues that such a transformation is equivalent to an alteration of the physical situation, and consequently, there are two different classes of significant solutions. The purpose of the present work is to extend and analyze Mishkin's work and use the new results to determine which of the Jacobi elliptic function solutions have physical significance.

The pulse energy, pulse area, pulse shape, and initial population inversion density are discussed with special attention to their dependence on physically measurable quantities. It is found that the properties of the  $\text{nd } u$  and  $\text{sd } u$  solutions have identical dependences on physically measurable quantities as the properties of the  $\text{dn } u$  and  $\text{cn } u$  solutions, respectively. Furthermore, the initial population inversion density required for the  $\text{dn } u$  and  $\text{nd } u$  solutions to be stable is not physically realizable (being less than  $-1$  for values of  $k < 1$ ). On the basis of these results we conclude that  $\text{cn } u$  is the only physically significant solution for  $k < 1$  with  $\text{sech } u$  being the only significant solution in the limit  $k = 1$ .

## 2. Pulse energy

The energy per period,  $W$ , of the Jacobi elliptic solutions can be determined from integrals of the form

$$W = \epsilon_0^2 \int_0^T e^2(u) dt = \epsilon_0^2 \tau \int_0^{T/\tau} e^2(u) du. \quad (2.1)$$

The results of these integrations are given in terms of the elliptic integrals of the first and second kind,  $K(k)$  and  $E(k)$ , respectively:

$$W(\text{dn } u) = 4\epsilon_0 E(k), \quad (2.2)$$

$$W(\text{cn } u) = 8\epsilon_0 k^{-1} [E(k) - (1 - k^2)K(k)], \quad (2.3)$$

$$W(\text{nd } u) = 4\epsilon_0 [1 - k^2]^{-1/2} E(k), \quad (2.4)$$

$$W(\text{sd } u) = 8\epsilon_0 [k^2(1 - k^2)]^{-1/2} [E(k) - (1 - k^2)K(k)]. \quad (2.5)$$

The explicit behavior of eqs. (2.2)–(2.5) as a function of  $k^2$  is shown in fig. 1. That the sd  $u$  and nd  $u$  solutions tend to infinite energy per period in the

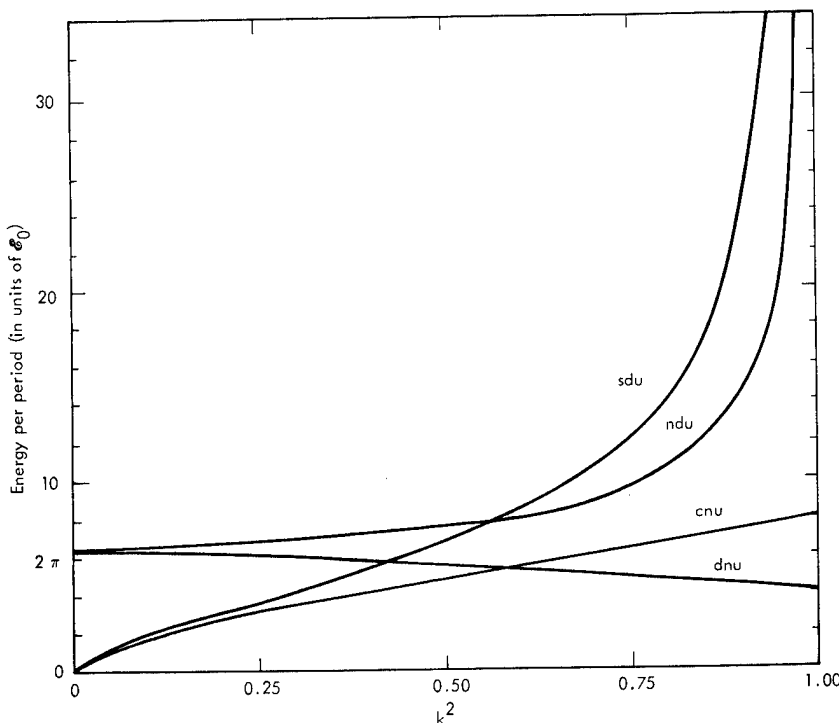


Fig. 1. Behavior of the energy per period as a function of the modulus  $k$  squared for the four Jacobi elliptic function solutions to the Maxwell-Schroedinger equations.

TABLE I.  
Summary of results from Mishkin's work and the present work for the four real Jacobi elliptic function solutions to the Maxwell-Schroedinger equations.

QUANTITY	cnu SOLUTION	dnu SOLUTION
Envelope of electric field ( $E$ )	$E_0 \text{cnu}$	$E_0 \text{dnu}$
In-phase macroscopic polarization ( $C$ )	$\tau \Delta \omega A(\Delta \omega) \text{cnu}$	$\tau \Delta \omega A(\Delta \omega) \text{dnu}$
Out-of-phase macroscopic polarization ( $S$ )	$A(\Delta \omega) \text{snu dnu}$	$k^2 A(\Delta \omega) \text{snu cnu}$
Population inversion density ( $n$ )	$\frac{A}{E_0 \tau} \left[ 2 \text{dn}^2 u - 1 - (\tau \Delta \omega)^2 \right]$	$\frac{A}{E_0 \tau} \left[ 2 \text{dn}^2 u - 2 + k^2 - (\tau \Delta \omega)^2 \right]$
Characteristic time relation ( $E_0 \tau$ )	$2k$	$2$
Frequency response function ( $A(\Delta \omega)$ )	$\frac{2k}{\left[ (1 - (\tau \Delta \omega)^2)^2 + 4k^2 (\tau \Delta \omega)^2 \right]^{1/2}}$	$\frac{2}{\left[ 4 (\tau \Delta \omega)^2 + (k^2 - (\tau \Delta \omega)^2)^2 \right]^{1/2}}$
Period of oscillation ( $T$ )	$4 \tau K(k)$	$2 \tau K(k)$
Integration constant ( $n_0$ )	$\frac{1 - (\tau \Delta \omega)^2 - 2k^2}{\left[ (1 - (\tau \Delta \omega)^2)^2 + 4k^2 (\tau \Delta \omega)^2 \right]^{1/2}}$	$\frac{k^2 - 2 - (\tau \Delta \omega)^2}{\left[ 4 (\tau \Delta \omega)^2 + (k^2 - (\tau \Delta \omega)^2)^2 \right]^{1/2}}$
Ratio of light velocity to pulse velocity ( $\frac{c}{V}$ )	$1 + \alpha \tau^2 \int_{-\infty}^{\infty} g(\Delta \omega) \left[ (1 - (\tau \Delta \omega)^2)^2 + 4k^2 (\tau \Delta \omega)^2 \right]^{-1/2} d\Delta \omega$	$1 + \alpha \tau^2 \int_{-\infty}^{\infty} g(\Delta \omega) \left[ 4 (\tau \Delta \omega)^2 + (k^2 - (\tau \Delta \omega)^2)^2 \right]^{-1/2} d\Delta \omega$
Area per period	$0 \pi$	$2 \pi$
Area per half-period	$4 \sin^{-1}(k)$	$\pi$
Energy per period	$\frac{8 E_0}{k} \left[ E(k) - (1 - k^2) K(k) \right]$	$4 E_0 E(k)$

TABLE I (cont.)

QUANTITY	ndu SOLUTION	sdu SOLUTION
Envelope of electric field ( $E$ )	$E_0 \text{ndu}$	$E_0 \text{sdu}$
In-phase macroscopic polarization ( $C$ )	$\tau \Delta \omega A(\Delta \omega) \text{ndu}$	$\tau \Delta \omega A(\Delta \omega) \text{sdu}$
Out-of-phase macroscopic polarization ( $S$ )	$-k^2 A(\Delta \omega) \text{sdu cdu}$	$-A(\Delta \omega) \text{cdu ndu}$
Population inversion density ( $n$ )	$\frac{A}{E_0 \tau} \left[ k^2 (1 - c^2 u) - (\tau \Delta \omega)^2 \right]$	$\frac{A}{E_0 \tau} \left[ 1 - 2 k^2 c^2 u - (\tau \Delta \omega)^2 \right]$
Characteristic time relation ( $E_0 \tau$ )	$2 (1 - k^2)^{1/2}$	$2 k (1 - k^2)^{1/2}$
Frequency response function ( $A(\Delta \omega)$ )	$\frac{2 (1 - k^2)^{1/2}}{\left[ (k^2 - (\tau \Delta \omega)^2)^2 + 4 (\tau \Delta \omega)^2 \right]^{1/2}}$	$\frac{2 k (1 - k^2)^{1/2}}{\left[ 4 k^2 (\tau \Delta \omega)^2 + (1 - (\tau \Delta \omega)^2)^2 \right]^{1/2}}$
Period of oscillation ( $T$ )	$2 \tau K(k)$	$4 \tau K(k)$
Integration constant ( $n_0$ )	$\frac{k^2 - 2 - (\tau \Delta \omega)^2}{\left[ (k^2 - (\tau \Delta \omega)^2)^2 + 4 (\tau \Delta \omega)^2 \right]^{1/2}}$	$\frac{1 - (\tau \Delta \omega)^2 - 2 k^2}{\left[ 4 k^2 (\tau \Delta \omega)^2 + (1 - (\tau \Delta \omega)^2)^2 \right]^{1/2}}$
Ratio of light velocity to pulse velocity ( $\frac{C}{V}$ )	$1 + \alpha \tau^2 \int_{-\infty}^{\infty} g(\Delta \omega) \left[ (k^2 - (\tau \Delta \omega)^2)^2 + 4 (\tau \Delta \omega)^2 \right]^{-1/2} d\Delta \omega$	$1 + \alpha \tau^2 \int_{-\infty}^{\infty} g(\Delta \omega) \left[ 4 k^2 (\tau \Delta \omega)^2 + (1 - (\tau \Delta \omega)^2)^2 \right]^{-1/2} d\Delta \omega$
Area per period	$2 \pi$	$0 \pi$
Area per half-period	$\pi$	$4 \sin^{-1}(k)$
Energy per period	$\frac{4 E_0}{(1 - k^2)^{1/2}} E(k)$	$\frac{8 E_0}{k (1 - k^2)^{1/2}} \left[ E(k) - (1 - k^2) K(k) \right]$

asymptotic limit ( $k \rightarrow 1$ ) is used as an argument against the validity of these solutions. However, since the asymptotic limit is itself not physically realizable (see section 5) and the pulse energy per period remains finite for all  $k \neq 1$ , arguments of this type are not conclusive grounds for rejection of the nd  $u$  and sd  $u$  solutions.

### 3. Pulse area

The area  $\theta$  contained in any fraction of a period of a Jacobi elliptic function is given by

$$\theta_u = \epsilon_0 \int_0^t e(u) dt = \epsilon_0 \tau \int_0^u e(u) du. \quad (3.1)$$

The results of eq. (3.1) for Mishkin's four solutions are

$$\theta_u(\text{dn } u) = 2 \sin^{-1}(\text{sn } u), \quad (3.2)$$

$$\theta_u(\text{cn } u) = 2 \cos^{-1}(\text{dn } u), \quad (3.3)$$

$$\theta_u(\text{nd } u) = 2 \cos^{-1}(\text{cd } u), \quad (3.4)$$

$$\theta_u(\text{sd } u) = 2 \sin^{-1}(-k \text{ cd } u). \quad (3.5)$$

The total areas per period are found to be either  $0\pi$  or  $2\pi$  as Mishkin determined. From eqs. (3.2)–(3.5) we find that the areas per positive half-period are  $\pi$  for the nd  $u$  and dn  $u$  solutions and  $4 \sin^{-1} k$  for the cn  $u$  and sd  $u$  solutions.

### 4. Experimental comparisons of the cn $u$ , sd $u$ , dn $u$ , and nd $u$ solutions

The solutions cn  $u$  and dn  $u$  are related to the solutions sd  $u$  and nd  $u$  by a transformation of the argument [eqs. (1.10) and (1.11)]. However, this is not in itself a valid argument against the existence of these solutions as physically different entities. If the sd  $u$  and nd  $u$  solutions can be experimentally distinguished from the cn  $u$  and dn  $u$  solutions, then all four are physically significant.

The question immediately arises as to which of the quantities defined in the preceding work are in principle experimentally measurable. The period of oscillation  $T$  may be readily obtained from a time-resolved intensity measurement. However, as is evident from table I, the cn  $u$  and sd  $u$  solutions have identical dependences on  $\tau$  and  $k$ , as do the dn  $u$  and nd  $u$  solutions. Consequently, measurement of the period cannot distinguish between cn  $u$  and sd  $u$  or dn  $u$  and nd  $u$ , although it can be used to determine between cn  $u$  and dn  $u$  (if  $\tau$  and  $k$  are known). The pulse velocity  $V$  is also in principle a

measurable quantity. However, it too cannot be used to distinguish between the  $\text{cn } u$  and  $\text{sd } u$  solutions or the  $\text{dn } u$  and  $\text{nd } u$  solutions.

The initial population inversion density  $\eta_0(\Delta\omega)$  can be determined by measuring the gain or attenuation of a weak, frequency-tunable probe beam. This quantity cannot be used to distinguish between the solutions (except between  $\text{cn } u$  and  $\text{dn } u$ ) for the same reasons as before. However, it can be used to obtain the modulus  $k$ . Coupling the value of  $k$  with a measurement of the period  $T$  yields a value for the characteristic time  $\tau$ . From the values of  $\tau$  and  $k$  a different value of  $\epsilon_0$  is calculated for each solution. Consequently, if  $\epsilon_0$  can be experimentally measured and compared with the predicted values, the different solutions can be distinguished.

The absolute value of the electric field envelope as a function of time can be determined from intensity measurements. However, to determine  $\epsilon_0$  from a measurement of  $\epsilon(t)$ , both the transformation of  $\epsilon(t)$  to  $\epsilon(u)$  and where to place  $u = 0$  must be known (a displacement in  $u$  such that  $u \rightarrow u + K(k)$  is the essence of the transformations between the members of each pair of solutions). The transformation of  $\epsilon(t)$  to  $\epsilon(u + \phi)$  where  $\phi$  is a phase factor is readily performed given a knowledge of the characteristic time  $\tau$ . The phase  $\phi$  on the other hand cannot be determined from any measurement. A precise determination of  $\phi$  would correspond to a knowledge of one's absolute position in space-time as the assumptions of a steady-state solution require that the pulse train has propagated through an infinite distance of absorber for an infinite length of time. The net result is that  $\epsilon_0$  cannot be measured. The maximum value of the electric field envelope, denoted  $\epsilon_{\max}$  can be readily obtained from  $\epsilon(t)$ . Using the definitions of the elliptic solutions<sup>2)</sup> and eqs. (1.10) and (1.11) we find that if

$$\epsilon_{\max}(\text{cn } u) = \epsilon_{\max}(\text{dn } u) = \epsilon_0 \quad (4.1)$$

then

$$\epsilon_{\max}(\text{sd } u) = \epsilon_{\max}(\text{nd } u) = \epsilon_0/(1 - k^2)^{1/2}. \quad (4.2)$$

Substituting this result into the expressions for  $\epsilon_0\tau$  from table I we obtain

$$\epsilon_{\max}\tau(\text{sd } u \text{ or } \text{cn } u) = 2k, \quad (4.3)$$

$$\epsilon_{\max}\tau(\text{nd } u \text{ or } \text{dn } u) = 2. \quad (4.4)$$

Consequently, measurements of the electric field envelope cannot distinguish between  $\text{cn } u$  and  $\text{sd } u$  or between  $\text{dn } u$  and  $\text{nd } u$ . The ambiguity in  $\epsilon_0$  also means that measurements of the pulse energy per period cannot be used to distinguish between the solutions.

Similar problems with the arbitrariness of  $\phi$  plague attempts to distinguish between the solutions by measuring the population inversion density as a function of reduced time or by determining the area as a function of the interval between  $u = 0$  and  $u = u'$  ( $u'$  arbitrary). In both cases if  $u + \phi$  is

chosen to be zero when  $\epsilon = \epsilon_{\max}$ , the appropriate expressions turn out to be identical for  $\text{cn } u$  and  $\text{sd } u$  and for  $\text{dn } u$  and  $\text{nd } u$ .

In summary, no experiment or set of experiments can be formulated which can distinguish between the  $\text{cn } u$  and  $\text{sd } u$  solutions or between the  $\text{dn } u$  and  $\text{nd } u$  solutions, while the  $\text{cn } u$  and  $\text{dn } u$  solutions are easily distinguished. Consequently, Mishkin's  $\text{sd } u$  and  $\text{nd } u$  solutions have no new physical significance as they are indistinguishable from the  $\text{cn } u$  and  $\text{dn } u$  solutions.

### 5. Pulse shape; comparison of $\text{cn } u$ , $\text{dn } u$ , and $\text{sech } u$

The only stable  $2n\pi$  ( $n > 0$ ) pulse shapes observed in propagation experiments and computer simulations resemble hyperbolic secants or superpositions of hyperbolic secants. As a result some people have suggested that only the  $\text{sech } u$  solution is physically realizable<sup>3</sup>). However, the computer simulations have been performed for  $\eta_0 = -1$  (corresponding to the asymptotic limit,  $k = 1$ ). Since both  $\text{cn } u$  and  $\text{dn } u$  reduce to  $\text{sech } u$  in the asymptotic limit, only  $\text{sech } u$  solutions are expected. The experiments obviously could not have  $\eta_0 = -1$  since the temperature was above absolute zero. In fig. 2 the functions  $\text{cn}(u \mid k = 0.999)$ ,  $\text{dn}(u \mid k = 0.999)$ , and  $\text{sech } u$  are compared. At  $\Delta\omega = 0$ , simple calculations (see section 6) indicate that  $k = 0.999$  corresponds to the  $\eta_0(0)$  that would exist in thermal equilibrium at 3860 K if  $\hbar\omega_0 = 2$  eV (visible light). The differences between the three solutions shown in the figure are so small except in the low-intensity region near the minimum (inflection point) of the  $\text{dn } u$  ( $\text{cn } u$ ) solution that it would be exceedingly difficult to distinguish experimentally between a  $\text{sech } u$  pulse and a  $\text{cn } u$  or  $\text{dn } u$  solution truncated by

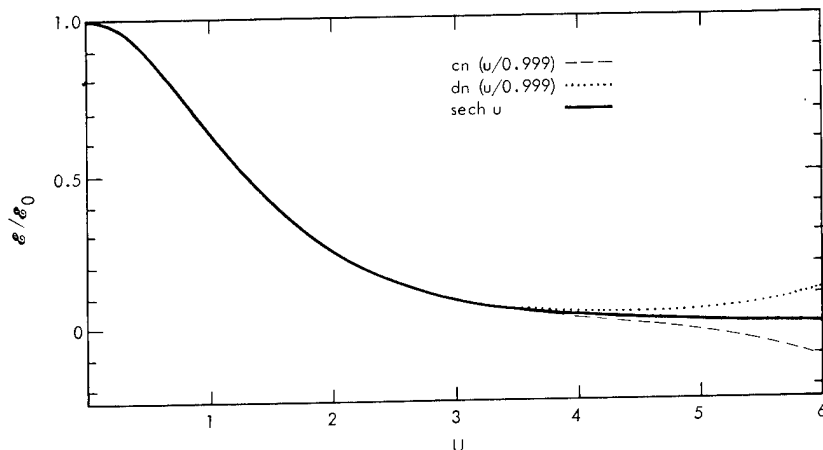


Fig. 2. Comparison of the electric field strength as a function of the reduced time for three different solutions to the Maxwell-Schroedinger equations:  $\text{sech } u$ ,  $\text{cn}(u \mid k = 0.999)$ , and  $\text{dn}(u \mid k = 0.999)$ .

the lack of sufficient energy to form a periodic pulse train. At room temperature, the effective value of  $k$  is  $1 - (9 \times 10^{-36})$  for  $h\omega_0 = 2$  eV. Here the differences in intensity between the three solutions could not be detected by any means. Consequently, these "experimental" arguments against the Jacobi elliptic function solutions have no substantial basis.

### 6. Initial population inversion density

In the preceding sections it was shown that  $\text{cn } u$  and  $\text{dn } u$  (or equivalently  $\text{sd } u$  and  $\text{nd } u$ ) are the only experimentally distinguishable solutions to the Maxwell-Schroedinger equations. It is of equal importance to determine if both of these solutions are physically realizable. The answer can be obtained by considering the initial population inversion density,  $\eta_0$ . In figs. 3 and 4,  $\eta_0$  is plotted as a function of  $\tau\Delta\omega$  for several values of the modulus  $k$  for both the  $\text{cn } u$  (and  $\text{sd } u$ ) and  $\text{dn } u$  (and  $\text{nd } u$ ) solutions. The initial population inversion density required by the  $\text{cn } u$  solutions remains between the limits of +1 and -1 for all values of  $k$  and  $\Delta\omega$ , as it must to be physically viable. However, the initial population inversion density for the  $\text{dn } u$  solution is less

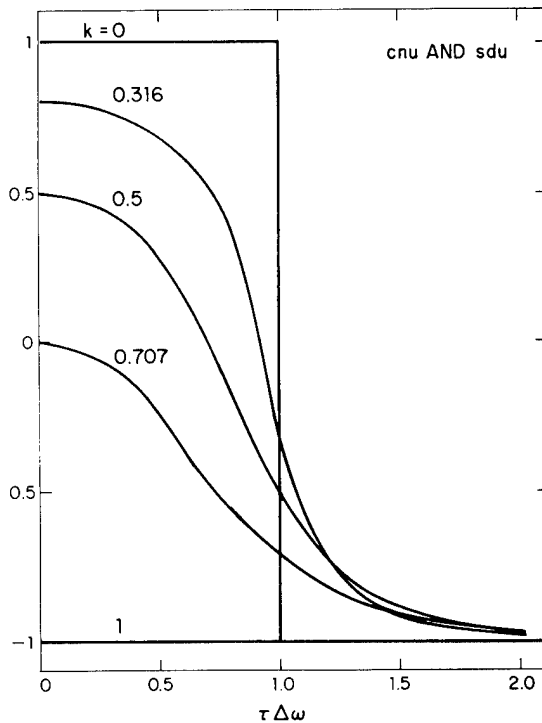


Fig. 3. The initial population inversion density  $\eta_0$  as a function of  $\tau\Delta\omega$  for the  $\text{cn } u$  and  $\text{sd } u$  solutions. The curves correspond to values of  $k = 1.0, 0.707, 0.5, 0.316$ , and 0.

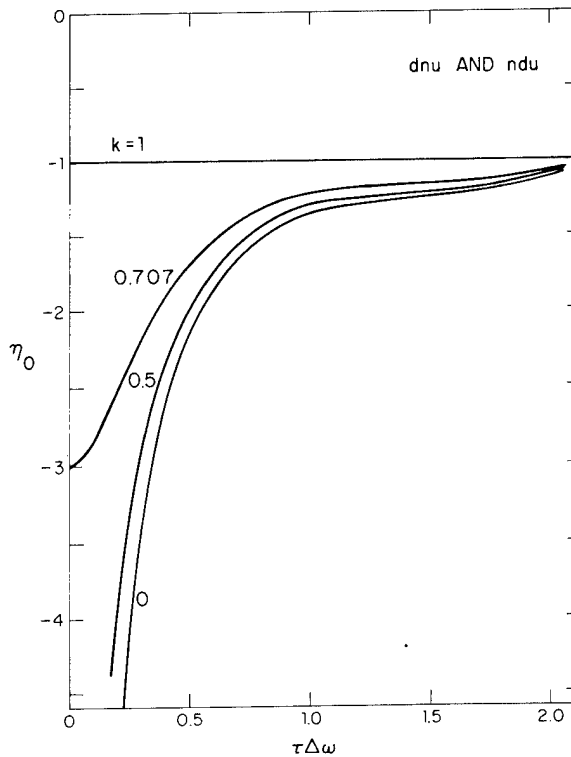


Fig. 4. The initial population inversion density  $\eta_0$  as a function of  $\tau\Delta\omega$  for the  $\text{dn } u$  and  $\text{nd } u$  solutions. The curves correspond to values of  $k = 1.0, 0.707, 0.5$ , and  $0$ .

than  $-1$  for all values of  $\Delta\omega$  and  $k$  (except  $k = 1$ ). Thus, the  $\text{dn } u$  solution requires an initial population inversion density which cannot be produced by any physical means except in the asymptotic limit ( $k = 1$ ) which is itself not physically attainable. Consequently, we must conclude that  $\text{cn } u$  is the only physically significant solution to the Maxwell-Schroedinger equations.

Further insight into the behavior of the  $\text{cn } u$  solution can be obtained by studying the frequency dependence of  $\eta_0$  in the regime where  $k \sim 1$ . Let  $k^2 = 1 - \delta$  with  $\delta$  being a small number. Substituting this value into the expression for  $\eta_0(\text{cn } u)$  yields

$$\eta_0 = \frac{-[1 + (\tau\Delta\omega)^2] + 2\delta}{[((1 + (\tau\Delta\omega)^2)^2 - 4\delta(\tau\Delta\omega)^2)^{1/2}}. \quad (6.1)$$

Appropriate expansion of the denominator yields

$$\eta_0 \approx -1 + \frac{2\delta}{(1 + (\tau\Delta\omega)^2)^2} \quad (6.2)$$

or

$$\eta_0 + 1 \approx \frac{2(1 - k^2)}{(1 + (\tau\Delta\omega)^2)^2}, \quad (6.3)$$

where we have neglected terms in  $\delta^2$  or larger. On resonance we find

$$\eta_0 \approx 1 - 2k^2 \approx e^{-\hbar\omega/kT} \quad (6.4)$$

Eq. (6.4) was utilized in the determination of  $k$  in section 5.

The frequency dependence of eq. (6.3) bears a similarity to the lineshape governing the energy stored in a forced, damped harmonic oscillator. Since the harmonic oscillator is a small displacement approximation to the pendulum oscillator (of which the coherently-driven two-level system is a good example) this is not surprising. It is not a lineshape which is encountered in equilibrium atomic systems. However, it could be produced by an appropriately frequency-tailored optical pump. In a similar  $k \sim 1$  expansion for the frequency response function  $A(\Delta\omega)$  of the  $\text{cn } u$  solution we find

$$A(\Delta\omega) \approx \frac{2}{1 + (\tau\Delta\omega)^2} \quad (6.5)$$

which is the familiar Lorentzian lineshape function.

## 7. Conclusions

In this work we analyzed the behavior of the four real Jacobi elliptic function solutions to the Maxwell-Schroedinger equations. Determination of the experimentally measurable quantities for each solution indicates that the  $\text{sd } u$  solution cannot be distinguished experimentally from the  $\text{cn } u$  solution and that the  $\text{nd } u$  solution cannot be distinguished experimentally from the  $\text{dn } u$  solution. In addition, it was discovered that the  $\text{dn } u$  solution requires an initial population inversion density which cannot be physically realized. Therefore we conclude that  $\text{cn } u$  is the only physically significant steady-state solution to the Maxwell-Schroedinger equations.

## Acknowledgements

The author wishes to acknowledge many informative discussions with E.A. Mishkin concerning his work and possible interpretations of his results.

## References

- 1) E.A. Mishkin, *Physica* 73 (1974) 459.
- 2) M. Abramowitz and I.A. Stegun, *Handbook of Mathematical Functions*, Chs. 16 and 17 (Dover, New York, 1964).
- 3) E.A. Mishkin, private communication.

# Active laser resonator control techniques

R. C. Harney

MIT Lincoln Laboratory, Lexington, Massachusetts 02173.

Received 23 November 1977.

0003-6935/78/0601-1671\$0.50/0.

© 1978 Optical Society of America.

The output beams from transverse-flow lasers using unstable resonators are usually severely aberrated due to refractive-index inhomogeneities in the gain medium. The resulting phase distortions in the output beam may be significantly reduced by using an externally placed adaptive mirror system.<sup>1</sup> However, the intensity inhomogeneities in the output beam caused by the intracavity phase distortions will remain. Intuitively, a more uniform intensity distribution will result if the phase profile is kept uniform throughout the laser cavity than if the phase profile is allowed to vary randomly. Consequently, it is suggested that the phase distortions and the intensity inhomogeneities may be simultaneously minimized by placing the adaptive mirror inside the laser resonator. In this Letter we examine some advantages and disadvantages of four candidate techniques for active resonator phase control. No discussion is given of the spatial and temporal bandwidths required for effective correction of typical phase aberrations encountered in real systems. Preliminary work on this aspect of the problem is described in Ref. 2. All four techniques will be assumed to possess unlimited bandwidth, and all will be discussed in the context of ring resonators with folded gain media (Fig. 1), although the discussions may be generalized to apply to almost any resonator-gain medium configuration.

Before proceeding to describe the different techniques for resonator control let us discuss the placement of the deformable mirror. In principle, the deformable mirror may be located anywhere inside the cavity. However, it is probably superior to place it between the two gain regions (or, if one is considering a conventional resonator-single gain region system, on the opposite side of the gain region from the scraper mirror). This choice is based on the hypothesis that a more uniform intensity profile will result if the maximum excursion from zero of the rms optical phase distortion (OPD) is kept as small as possible. This hypothesis is based on the fact that the degradation of an intensity profile is a nonlinear function of the OPD. The rms OPD as a function of distance along the cavity axis is illustrated in Fig. 2 for two different choices of mirror position. In case A the deformable mirror is placed just before the scraper mirror. After propagating through the gain regions, an initially flat wavefront acquires an OPD of amplitude 2 (arbitrary units). Placing the phase conjugate of this aberrated wavefront on the deformable mirror results in a flat wavefront immediately upon reflection. In case B the deformable mirror is placed between the two gain regions. After propagating through the first gain region, an initially flat wavefront acquires an OPD of unit amplitude. Twice the phase conjugate of the aberrated wavefront applied to the deformable mirror will upon reflection yield a phase conjugate aberrated wavefront. Assuming the rms OPD resulting from each gain region is identical (a valid assumption for most large-scale aberrations, the aberrations least affected by bandwidth limitations, in such folded systems), the phase conjugate wavefront will yield a flat wavefront after propagation through the second gain region. Since the maximum rms OPD for case B is half that for case A, case B should result in superior intensity profile correction.

The first active resonator control scheme to be discussed

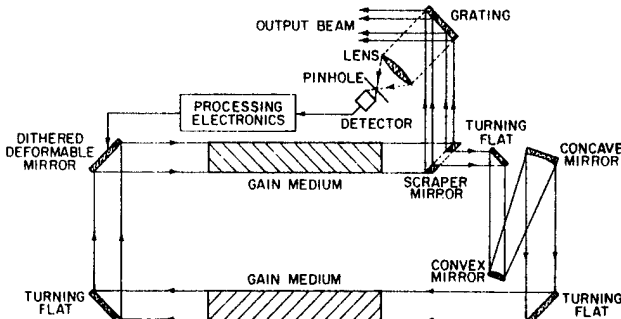


Fig. 1. Schematic of an active resonator employing the intensity-maximizing multidither technique.

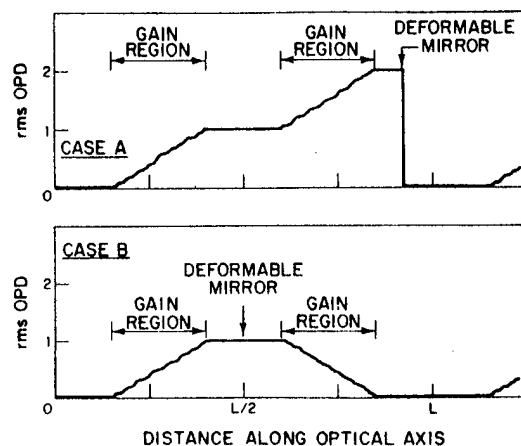


Fig. 2. The rms OPD as a function of distance along the optical axis for two active resonator configurations. In case A the deformable mirror is located just before the scraper mirror. In case B the deformable mirror is located between the two gain regions. In both cases the scraper mirror is located at  $O, L, 2L, \dots$

may be described as an intensity-maximizing multidither (IMMD) technique and is illustrated in Fig. 1. The actuators of the deformable mirror are oscillated (dithered) either in a zonal fashion with a different dither frequency for each actuator or in a modal fashion with a different dither frequency for each mode or preset pattern of actuator deformations. The choice of zonal or modal operation is determined by bandwidth considerations. Dithering will result either in a true oscillation of total output power at each dither frequency or in an oscillating phase aberration (which will result in an oscillating on-axis intensity in a focused beam) at each dither frequency or both. If a small fraction of the output intensity is sampled by a grating and focused onto a pinhole placed in front of a photodetector, the time-dependent detector signal will contain components at each dither frequency. The intensity in each frequency component can be nulled by adjusting the dc offset of the appropriate actuator (or actuator mode). This process maximizes the focused intensity, which frequently implies the most uniform phase and intensity profile (which can be obtained from the deformable mirror being used) has been achieved.

The second scheme may be described as a phase-uniformizing multidither (PUMD) technique and is illustrated in

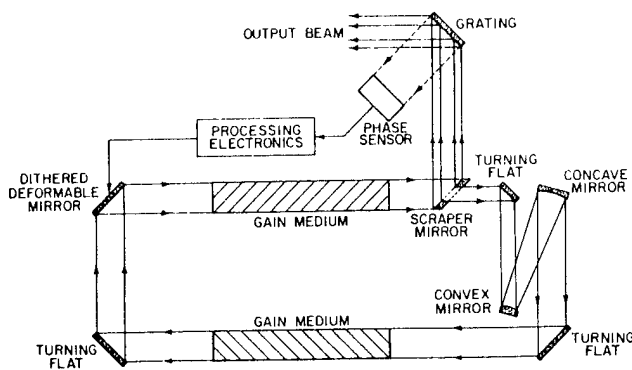


Fig. 3. Schematic of an active resonator employing the phase-uniformizing multidither technique. In the intensity-uniformizing multidither technique the phase sensor is replaced by an intensity profile sensor.

Fig. 3. As in the first technique the actuators of the deformable mirror are dithered either modally or zonally, but in contrast to IMMD, in the PUMD technique the phase profile of the output beam is measured. This may be accomplished by a shearing interferometer<sup>3</sup> or similar device. Appropriate processing of the phase sensor data yields signals proportional to the rms OPD component at each dither frequency. By varying the dc offset of each dithered element, the rms OPD signals can be minimized, thus producing a uniform output phase. A modification of the PUMD technique detects the output intensity profile (e.g., with a detector array). Processing of these data can yield signals proportional to an rms intensity nonuniformity component at each dither frequency. It should then be possible to process these signals with an appropriate algorithm to yield a uniform output intensity. Such an intensity-uniformizing multidither (IUMD) system could also be used to generate particular nonuniform intensity profiles while a PUMD system could generate particular phase profiles. These abilities might be useful in some applications.

The fourth technique is best described as phase conjugate (PC) active resonator control and is illustrated in Fig. 4. In the PC technique, the phase of the radiation in the propagation region between the two gain regions, but before reflection from the deformable mirror, is measured by a phase sensor. Appropriate processing electronics generate twice the phase conjugate of the aberrated wavefront on the deformable mirror. After reflection the wavefront is the phase conjugate of the initial aberrated wavefront. Continued propagation

through the second gain region then results in a flat wavefront at the scraper mirror.

Each of these techniques has advantages and disadvantages. IMMD maximizes the focusable intensity in the output. Usually this maximized intensity results from a uniform phase and intensity profile. However, in a laser oscillator a distorted phase may lead to more effective utilization of the gain medium with a resulting increase in output power and a possible increase in focusable intensity. Thus IMMD may not always result in a uniform output phase. PUMD, on the other hand, produces a uniform phase but may not utilize the gain medium effectively. Thus it may not maximize the focusable intensity. Similar statements apply to the PC technique. IUMD produces a uniform intensity profile but does not necessarily produce either a uniform phase or the maximum focusable intensity. It may, of course, be possible to correct any remaining IUMD phase distortion with an extracavity deformable mirror. Since the different techniques do not necessarily yield the same output beam characteristics, the choice of technique depends to some extent on the properties required of the output beam. If uniform phase output is of utmost importance, PUMD or PC is the *a priori* choice (if little is known about the gain medium with which the active resonator is to be used); if maximum focused intensity is important, IMMD is the *a priori* choice; if a uniform intensity profile is important, IUMD is the *a priori* choice. The *a priori* choice, of course, may not be the optimum technique when bandwidth limitations, the detailed aberration qualities of the gain medium, and other systems considerations are fully analyzed.

PC has the disadvantages that it is a predictor-corrector technique. Thus, if the two gain media are not identical or if there are aberrations in the beam expander portion of the resonator, the PC technique will not function perfectly. PUMD is a closed-loop system and does not suffer from this drawback of PC. However, the processing electronics are exceedingly complex (possibly involving a large on-line computer) and could be too costly to implement effectively. The same is true of IUMD. IMMD is the simplest and least expensive technique, but as mentioned earlier it may not provide the desired output beam characteristics.

In conclusion we have described four conceptually different techniques for active resonator control. No one technique is free from disadvantages, yet all are viable and have some desirable characteristics. The proper choice of technique depends on the constraints placed upon the total system, the specific gain medium employed, and the desired output beam characteristics. Consequently, a detailed investigation (including consideration of practical bandwidth constraints) is warranted for each new laser system where active resonator control is proposed.

This work was sponsored by the Department of the Navy.

## References

1. J. E. Pearson, Opt. Eng. 15, 151 (1976).
2. R. H. Freeman, R. J. Freiberg, H. R. Garcia, and G. M. Callahan, Opt. Letts. 2, 61 (1978).
3. J. C. Wyant, Appl. Opt. 14, 2622 (1975).

Fig. 4. Schematic of an active resonator employing the phase conjugate technique.

## A COMPACT 10.6 $\mu$ m IMAGING RADAR\*

P. J. Berger, S. Marcus, and J. Martin  
Massachusetts Institute of Technology  
Lincoln Laboratory  
Lexington, Massachusetts 02173

### ABSTRACT

A 10.6 $\mu$ m imaging radar is being developed as a candidate all-weather gunsight for tactical air-to-ground aircraft. A testbed laser radar has been constructed to evaluate the relevant system parameters. The basic optical elements of the system are a high-PRF passively Q-switched CO<sub>2</sub> laser, a two-dimensional scanner, a 10X-refractive telescope, and a HgCdTe reverse-biased photodiode heterodyne detector. The raster scan has 128 x 128 resolution elements and dual memory signal processing provides a real time display of the scene. Objects of tactical interest have been imaged against terrain at ranges out to 5 km. Frame averaging and log-amplification were found to be effective in shape definition. Images have been obtained in haze, light fog and heavy rain. The images obtained to date give only a qualitative indication of the system performance; quantitative assessment will be performed with the addition of a digital tape recording and processing system.

### 1. INTRODUCTION

A radar operating at a wavelength of 10.6 $\mu$ m combines several important features which make it an attractive candidate as an all-weather gunsight for tactical air-to-ground aircraft. These include a beam spread narrow enough for target resolution and imaging<sup>1,2</sup>, Doppler shifts large enough for MTI processing<sup>3,4</sup>, the ability to measure range<sup>2,5</sup>, and a modest degree of weather penetration<sup>2,4</sup>. Furthermore, CO<sub>2</sub> lasers and coherent detection techniques combine to give a highly efficient system. During the past few years several different types of 10.6 $\mu$ m radars have been

\*This work was sponsored by the Department of the Air Force under Contract F19628-76-C-0002.

1. T. J. Gilmartin, H. A. Bostick, and L. J. Sullivan, "10.6 $\mu$ m CO<sub>2</sub> Laser Radar" (U), NEREM Record, 168-169 (1970).
2. C. J. Buczak, "10-Micron Laser Radar for Low-Level Flight" (U), Triservice Conference, Colorado Springs (July 1975).
3. H. A. Bostick, "A Carbon Dioxide Laser Radar System" (U), IEEE J. Quantum Electron. QE-5, 232 (1967).
4. R. A. Brandewie and W. C. Davis, "Parametric Study of a 10.6 $\mu$  Laser Radar" (U), Appl. Opt. 11, 1526-1533 (1972).
5. W. E. Bicknell, L. R. Tomasetta, and R. H. Kingston, "10.6 $\mu$ m FM-Chirp Radar Using Narrow-Band Correlation Detection" (U), IEEE J. Quantum Electron. (Corresp.) QE-11, 308-311 (1975).

constructed and applied to various problems, such as wire detection<sup>6</sup>, surveillance<sup>7,8</sup>, and ground mapping .

We are concerned with developing an imaging radar for the tactical air-to-ground scenario which is illustrated in Figure 1. In this application objects of tactical size and texture are

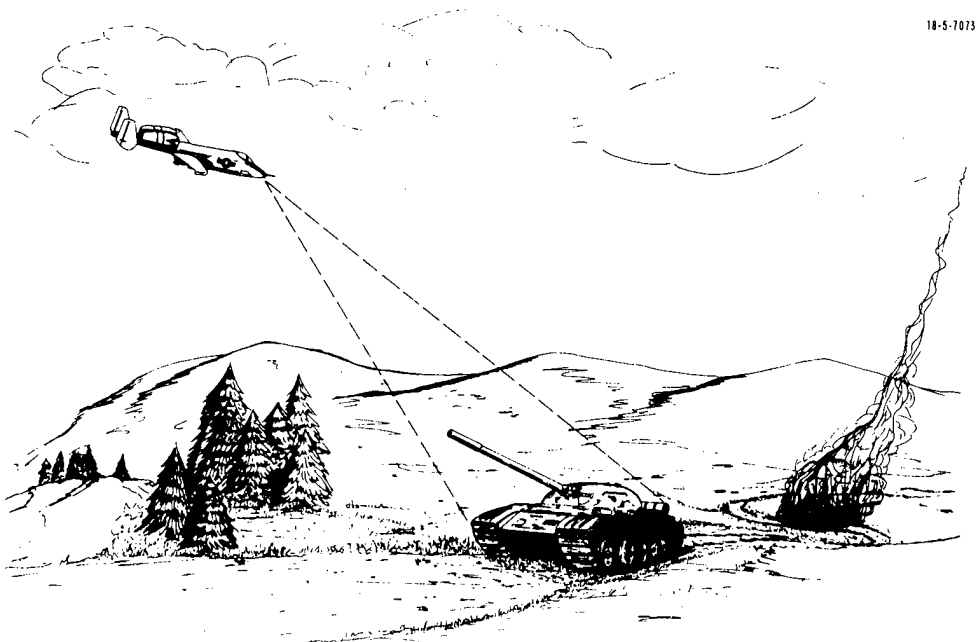


FIGURE 1. TACTICAL AIR-TO-GROUND SCENARIO

6. M. L. Skolnick, G. F. Gurski, A. A. Vuylsteke, and C. J. Buczek, "Laser Obstacle Terrain Avoidance Warning System" (U), Contract DAAB07-72-0145, United Technologies Corp., Research Center (February 1975).
7. C. L. Hayes and R. A. Brandewie "10.6 $\mu$ m Target Imagery Studies" (U), Contract DAAB07-70-C-0003, Rockwell International Corp., Electronic Research Division.
8. C. L. Hayes, "CO<sub>2</sub> MTI Laser Radar for Personnel and Vehicular Detection" (U), Contract DAAB07-74-C-0063, Rockwell International Corp., Electronic Research Division (December 1975).

located against a terrain background; that is, the image may be degraded by ground clutter. Furthermore, in order for the pilot to align his gunsight, images must be obtained in real time at reasonably high frame rates. For this application we believe that a pulsed, range-gated imaging radar will be most effective. The use of a pulse permits a direct, accurate measurement of the range for fire control and the receiver can be gated to reduce atmospheric backscatter and improve the contrast of images against terrain.

During the past year we initiated a program to develop a compact imaging radar at  $10.6\mu\text{m}$  tailored to the air-to-ground mission. The objectives of the program are listed in Table I.

TABLE I. PROGRAM OBJECTIVES

- (1) IMAGE TACTICAL TARGETS AGAINST TERRAIN BACKGROUND  
AT 1 TO 5-km RANGE
- (2) DETERMINE WEATHER PENETRATION CAPABILITY IN HAZE,  
FOG AND RAIN
- (3) EVALUATE FACTORS AFFECTING IMAGE QUALITY SUCH AS  
SPECKLE, GLINT AND SCATTERING
- (4) DETERMINE CRITERIA FOR DETECTION, RECOGNITION  
AND IDENTIFICATION

The first goal is to demonstrate that high quality images of tactical targets located against a terrain background can be obtained in real time with a pulsed, range-gated laser radar. The next two goals are to ascertain to what degree the laser radar can penetrate bad weather and to examine the factors which influence the quality of real time imagery. In particular, target speckle is recognized to be a problem with laser imagery at  $10.6\mu\text{m}$ <sup>2,9,10</sup>. The final goal is to develop processing criteria for the detection, recognition, and identification of targets with the airborne  $10.6\mu\text{m}$  imaging radar.

---

9. C. J. Buczek, "Speckle Heterodyne Detection and Object Rotation" (U), Topical Meeting on Speckle Phenomena in Optics, Microwaves, and Acoustics, Asilomar (February 24-26, 1976).
10. S. P. Tomczak, "Diffuse Target Scintillation in  $10.6\mu\text{m}$  Laser Radar" (U), Report No. TT-9, MIT/Lincoln Laboratory (March 1976).

## 2. TESTBED LASER RADAR

The block diagram of the testbed laser radar is shown in Figure 2. The basic components are a high PRF transmitter, a scanner and beam expanding telescope which give a raster scan of the scene, a heterodyne detector and signal processing electronics. Also identified are electronics for controlling the PRF of the transmitter and frequency offset of the laser local oscillator. In addition, the transmitted pulse is monitored for gating the return signal.

18-5-7075

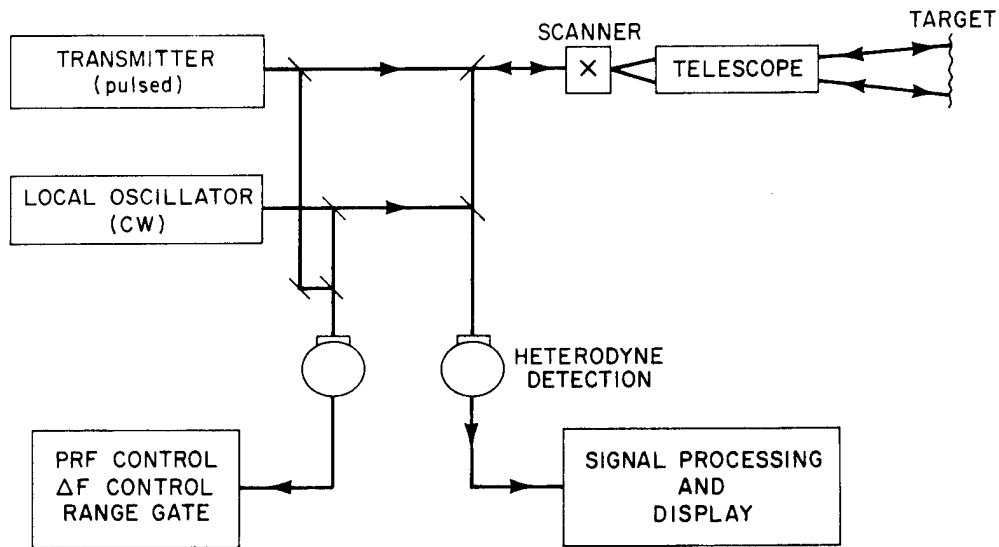


FIGURE 2. TESTBED LASER RADAR

Two of the design considerations should be reviewed here before proceeding with a description of the components. First, the diameter of the transmit/receive aperture was chosen to be 10 cm. This diameter is adequate from signal-to-noise considerations and allows for a compact design. In addition, there should be little loss of coherence over this aperture with a 10-km round trip under average turbulence conditions. It remains to be seen whether the resolution obtained with this aperture is adequate for the identification of tactical targets at the ranges of interest. Second, with a transmit aperture of 10 cm it is necessary to employ image plane scanning in order to generate a raster scan at high frame rates. This eases the scanner requirement but places a burden on the telescope, namely that it must maintain beam quality over a range of off-axis angles.

A description of the major components follows:

a) Pulsed Laser Transmitter.

A picture of the transmitter is shown in Figure 3. The laser is a low pressure CO<sub>2</sub> laser of the Freed design<sup>11</sup>, modified to include a stainless steel absorption cell for passive Q-switching. A grating is used for line selection and the output mirror is attached to a PZT stack for fine tuning. This laser gives a cw power of 10 watts and an output beam having a (1/e<sup>2</sup>)-diameter of 1 cm. (The laser shown here is the testbed which was used to study various types of Q-switching and to obtain the images shown in this paper. A compact version is being developed for the airborne mission).

The laser is passively Q-switched with a mixture of SF<sub>6</sub> and He. Stable Q-switching was observed at rates from a few kilohertz to 130 kHz. The pulse-width was slightly less than 0.4 $\mu$ sec at 20 kHz and increased to 0.7 $\mu$ sec at 130 kHz; the average power over this interval held nearly constant at 5-6 watts. The PRF is a function of the length of the cavity, which provides the basis for electronic control and stabilization of the PRF<sup>12</sup>.

Active Q-switching with a rotating wheel<sup>13</sup> was also studied. Stable Q-switching was obtained at rates up to 50 kHz. The pulse-widths were narrower than those obtained by passive Q-switching. The average powers were comparable.

11. C. Freed, "Design and Short-Term Stability of Single-Frequency CO<sub>2</sub> Lasers" (U), IEEE J. Quantum Electron. QE-4, 404-408 (1968).

12. C. J. Buczek, R. J. Freiberg, and M. L. Skolnick, "Laser Injection Locking" (U), Proc. IEEE 61, 1411-1431 (1973).

13. D. Meyerhoffer, "Q-switching of the CO<sub>2</sub> Laser" (U), IEEE J. Quantum Electron. QE-4, 762-769 (1968).

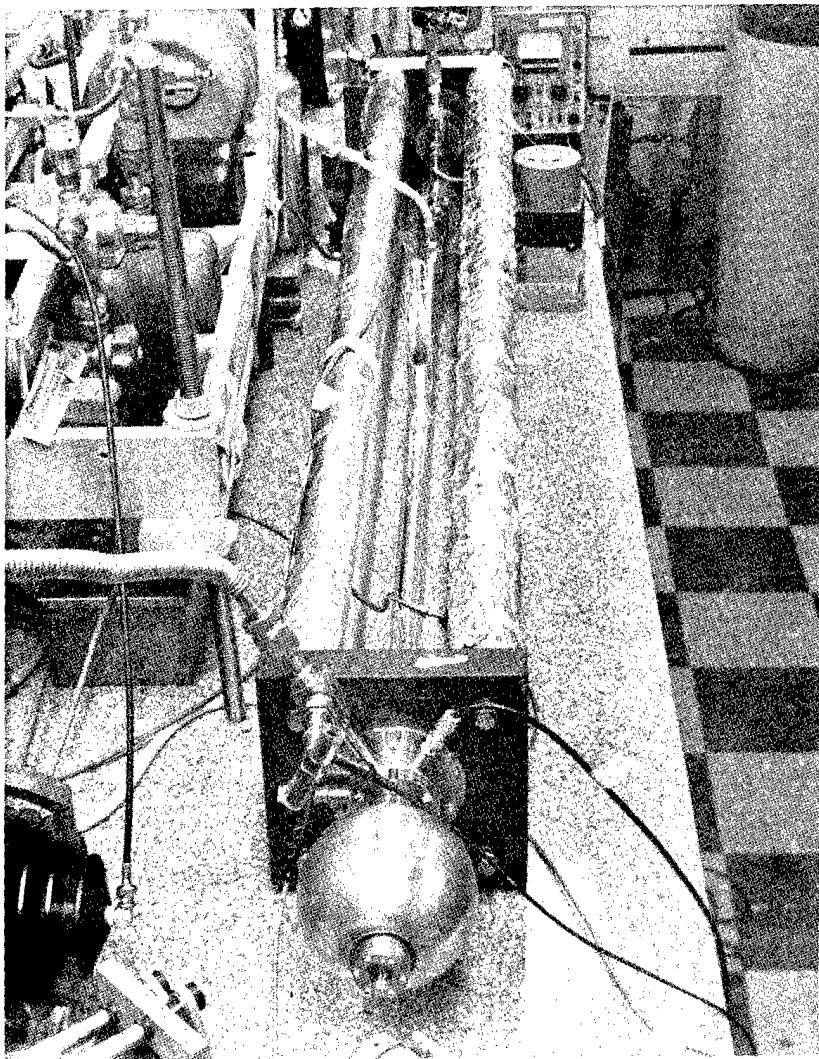


FIGURE 3. PASSIVELY Q-SWITCHED CO<sub>2</sub> LASER

b) Scanner

A pair of General Scanning Model G-100 PD galvanometer-type scanners are used to give a raster scan of the scene. The fast scanner is driven at 140 Hz and the slow scanner at 1 Hz. The drive voltages are feedback controlled to give a nearly sawtooth scan. For the scanners used in this work, 4 msec of the 7 msec fast scan and 0.9 sec of the 1 sec slow scan were found to be highly linear and reproducible from scan to scan. This results in an overall scan efficiency of slightly greater than 50%.

c) Transmit and Receive Telescope

The common transmit and receive telescope, manufactured by Space Optics Research Laboratories, is a 10X - astronomical telescope with germanium refracting elements. The  $(1/e^2)$ -diameter of the transmitted beam is 10 cm, giving a theoretical half-intensity divergence of 0.12 mrad. By scanning the input 1-cm diameter beam over 8.6 degree the transmitted beam is scanned over 0.86 degree or 15 mrad. Thus, ideally there would be 125 x 125 resolved elements in the scan. In practice, the size of a resolution cell is found to be approximately 1.5-times the theoretical value.

d) Local Oscillator

The local oscillator is a Sylvania Model 941S CO<sub>2</sub> laser equipped with PZT tuning for line selection and frequency control. Of the 3 watts of output power 1 mW is focussed onto the heterodyne detector where it is mixed with the return signal. A portion of the local oscillator power is mixed with the output of the pulsed laser and the beat monitored to maintain the offset frequency at 13 MHz.

e) Heterodyne Detector

The heterodyne detector is a reverse-biased HgCdTe photodiode fabricated at Lincoln Laboratory. The measured quantum efficiency is 0.5 at 10.6 $\mu$ m giving a minimum detectable power of 10<sup>-19</sup>W/Hz. The diameter of the detector element is 120 $\mu$ m and is nearly completely filled by using a 6.35-cm focal length lens to focus the return signal and local oscillator beams. A heterodyne mixing efficiency of 0.5 was observed, the departure from theoretical being caused by thermal loading of the detector by the local oscillator beam.

f) Signal Amplification

The signal levels at the output of the heterodyne detector range from 10 $\mu$ V for a diffuse reflection at long ranges to 100 mV for a strong glint. As the brightest shade of the display corresponds to 2V, the amplifier is required to have a maximum gain of 105 dB with 80 dB of gain control. Both linear and log-IF amplifiers were used. The linear amplifier chain is a super-heterodyne receiver with a r-f local oscillator used to raise the carrier frequency to 60 MHz where efficient narrow band filtering and video detection can be achieved. Gain control is exercised in the preamp stages with a voltage controlled attenuator. The log-IF also employs a

60 MHz carrier frequency and obviates the need for gain control since it has an 80 dB dynamic range.

g) Signal Processing

The signal processing scheme is illustrated in Figure 4. The voltage from the output of the amplifier chain is fed into a 4-bit A/D converter. Signals falling within the range gate are digitized in 50 nsec increments and an auction procedure is used to determine the peak value falling within the gate. This word is assigned a serial position in a 128 x 128 array, the scanner being synchronized by the array addressing system. With the laser PRF of 32 kHz, a 128 x 128 array of resolution cells, and a scanner efficiency of 50%, the frame rate is  $1 \text{ sec}^{-1}$ . The dual memory approach, illustrated in Figure 4, was utilized to obtain a flicker-free display at this low frame

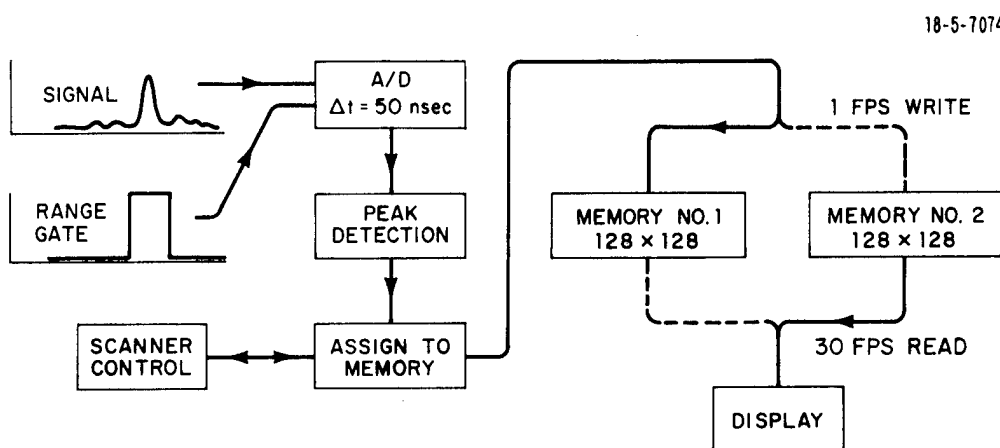


FIGURE 4. SIGNAL PROCESSING

rate in near real time. While a new frame is being written onto one memory, the other is being read out onto the CRT display at a 30 Hz refresh rate. The Z-axis control on the CRT was adjusted to permit the display of 10 gray shades.

The signal processing system is compatible with other digital equipment and plans have been made to extend the capability of the system. First, a digital tape recording system is being added to record data for subsequent processing with a digital computer. This will permit a quantitative analysis of weather effects and the factors influencing image quality. One of the goals of this phase of the work will be to develop techniques for real time processing of the images. If these techniques are successful, they will be implemented in real time with a dedicated processor which can be integrated with the system described above.

The power signal-to-noise equation for a heterodyne receiver employing a matched bandwidth is

$$\frac{S}{N} = \frac{E_T}{h\nu} \cdot \frac{A_R}{\pi R^2} \cdot \bar{\rho} \cdot \eta \cdot \epsilon \cdot e^{-2\alpha R}$$

The factors appearing in this equation are identified in Table II. Inserting the values appropriate to this work, we find that a power signal-to-noise ratio of 50 obtains for a range of 4.5 km with an atmospheric attenuation of 2 dB/km. The implications of the 2 dB/km attenuation design goal are discussed later. We note that the laser PRF of 32 kHz is compatible with imagery out to 4.5 km without range ambiguity.

TABLE II. 10.6- $\mu$ m LASER RADAR PERFORMANCE FACTORS

AVERAGE LASER POWER	5 W
PULSE WIDTH	$0.5 \times 10^{-6}$ s
REPETITION RATE	32 kHz
TRANSMITTED PULSE ENERGY	$E_T = 1.56 \times 10^{-4}$ J
ENERGY PER PHOTON	$h\nu = 1.87 \times 10^{-20}$ J
AVERAGE TARGET REFLECTIVITY	$\bar{\rho} = 0.1$
APERTURE DIAMETER	$D_R = 10$ cm
DETECTOR QUANTUM EFFICIENCY	$\eta = 0.5$
OPTICAL EFFICIENCY	$\epsilon = 0.06$

### 3. IMAGES

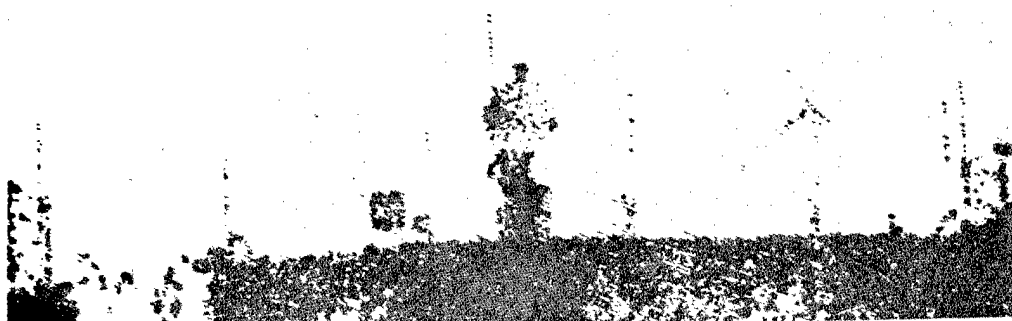
The testbed laser radar is housed in a small building on the roof of the laboratory. Targets which can be imaged from this location include a radar tower on the top of a hill at a distance of 0.5 km and various objects which can be placed on a field extending from 2 to 3 km. The test conditions are similar to those which would be experienced in a field test; for instance, the temperature and humidity of the building are not controlled, the system is not attached to a stable platform, and the atmosphere is rich in RFI generated by nearby microwave radars. In addition, the slant path down to the field passes over steel roofs and pavement. Strong turbulence is evident on sunny days.

a) Radar Towers at 0.5 km

A picture of the radar tower at 0.5 km and the laser image are shown in Figure 5. The laser



(a) TELESCOPE PHOTOGRAPH



(b)  $\text{CO}_2$  LASER IMAGE

FIGURE 5. RADAR TOWER AT 0.5 KM

image is a composite of several overlapping images, each one being a single frame or realization of the scene. The diameter of the mast behind the central dish is 7.5 cm and the square plate to the left of center is 72 cm on edge. The diameter of the laser beam at this range is 7.5 cm and we see that the laser is picking up details of this magnitude. In particular we note that the FM antenna on the right side stands out stronger in the laser images than in the visible photograph. The tall pine on the left and the top branches of the deciduous trees on the right mask portions of the tower in both the visible and laser images (The laser image was taken in March before the deciduous trees had filled out).

b) Tank Against Terrain at 2 and 3 km

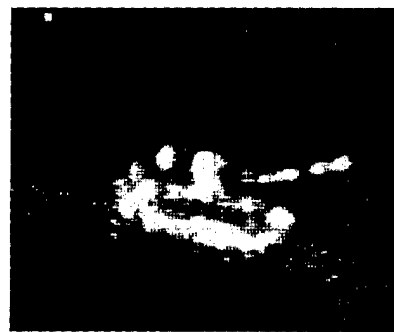
To test the ability of the laser radar to image a tactical target against terrain background a M-60 tank was positioned on the field at 2 and 3 km. Figure 6 and 7 show the visible photographs



(a) TELESCOPE PHOTOGRAPH



(b) LASER IMAGE - SINGLE FRAME



(c) LASER IMAGE - 32 FRAME AVERAGE

FIGURE 6. TANK AT 2 KM

taken with a Celestron 5 telescope and the corresponding laser images. The slant angles for these ranges are 1.5 and 1 degree, respectively and the scan includes a wide terrain coverage. The lines marking the border between grass and pavement are wavy, particularly those in Figure 6, an indication of the strong turbulence experienced on this particular day..

Two laser images of the tank are shown in Figure 6. The one to the left, Figure 6(b) is a photograph of a single frame of data and shows the main body and some of the detail of the tank, including the gun and the antenna. The image to the right, Figure 6(c) was taken by reducing the gain slightly and integrating 32 frames on Polaroid film. Better definition of the subject results from this frame averaging. Since the aspect angle does not change from frame-to-frame, except for vibration of the laser platform and path deviations caused by turbulence, the speckle pattern at the receiver is approximately frozen and a large number of frames are required to effect the improvement shown in Figure 6(c). In the airborne application both the aspect angle and the range will change from frame-to-frame and fewer frames should be required to average target speckle.

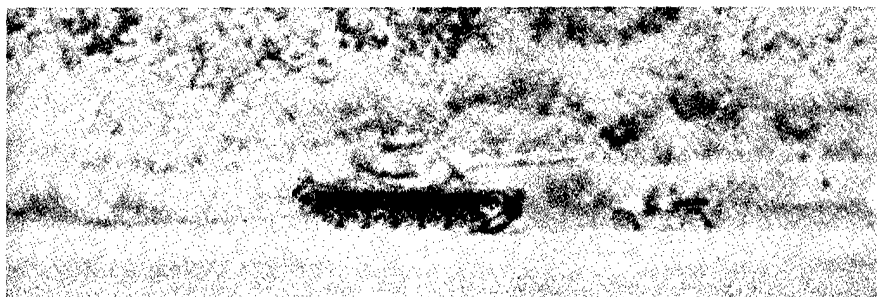
At 2 km the laser beam diameter is 36 cm, indicated by the box in the upper left hand corner of the images. The body of the tank is 3.2 m high by 8 m long, that is, it subtends 9 x 22 resolution elements. This number of resolution cells appears to be adequate for recognizing the tank with a single frame.

The scene at 3 km, Figure 7, includes the tank, a jeep, and personnel. The flat green coloring of the jeep blends into the foliage background in the visible photograph. The civilian with a light colored shirt stands out more prominently on the right. The laser image of the full scene, Figure 7(b), clearly picks out the tank, jeep, and personnel (extreme right and left of image). The frame averaging procedure, described above, was used to improve the definition of the scene.

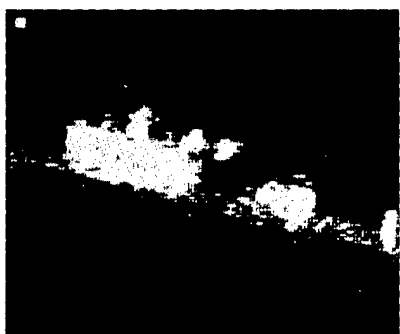
The laser beam diameter at 3 km is 54 cm indicated by the box at the upper left. The tank subtends 6 by 14 resolution cells and as shown in Figure 7(c) it is just possible to recognize the tank with this number of cells. This recognition is, of course, assisted by the well defined shape of the tank and the prominent gun barrel. The jeep and man occupy 3 by 6 and 3 by 1 resolution cells, respectively, and recognition is not possible with the still image. However, by viewing the real time display, men can be recognized by their motion which is characteristically different than mechanical objects.

The high contrast images shown in Figure 6 and 7 were obtained with a 0.4 $\mu$ sec range gate. To understand why this narrow range gate is required, we note that the return from a resolution cell of area A on the desired target must compete with the return from an adjacent ground patch of area  $A/\sin\phi$ , where  $\phi$  is the slant angle. Thus, the ground return can compete with the diffuse reflection from a painted surface when the slant angle is small. The narrow range gate either

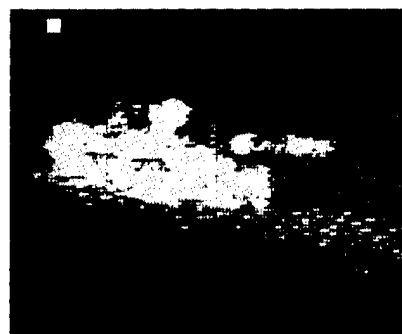
eliminates the ground return or shortens the length of the ground path from which returns are expected.



(a) TELESCOPE PHOTOGRAPH



(b) FULL SCENE - FRAME AVERAGE

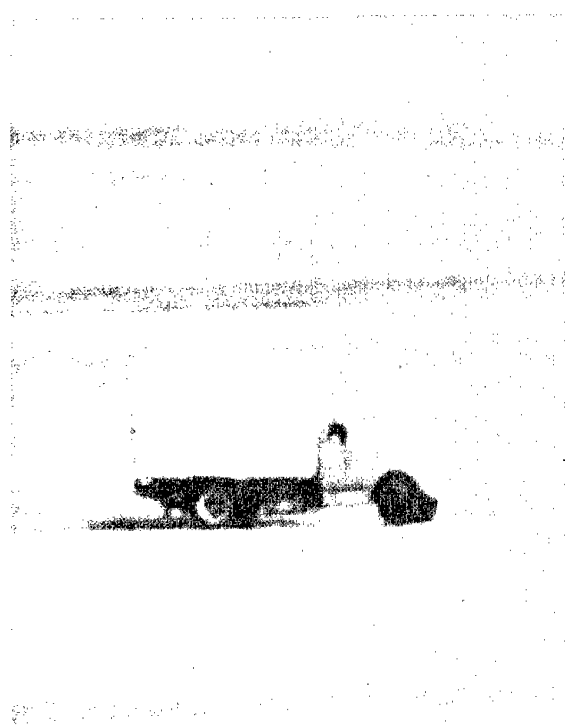


(c) CONTRACTED SCAN -16 FRAME AVERAGE

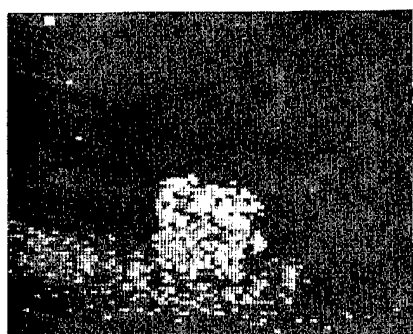
FIGURE 7. TANK, JEEP AND PERSONNEL AT 3 KM

c) Truck at 2 km

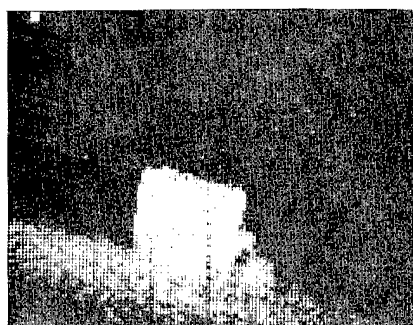
Figure 8 shows a photograph and laser images of a truck located at 2 km. The body of the truck is aluminum and the cab is painted metal and the returns from the body are approximately an order of magnitude stronger than the cab. When a linear amplifier chain is used, the gain required to display the details of the cab is so high that the body display is saturated. This problem is ameliorated by using a logarithmic amplifier to compress the signal. Figure 8(b) shows that good definition of the body and cab are obtained with a single frame. Increased definition is realized by frame averaging, as evidenced by Figure 8(c).



(a) TELESCOPE PHOTOGRAPH



(b) LASER IMAGE - SINGLE FRAME



(c) LASER IMAGE - 16 FRAME AVERAGE

FIGURE 8. TRUCK AT 2 KM

The truck is 3.5 m high by 6.1 m long and subtends 10 by 17 resolution elements. As with the tank this number of resolution cells appears to be adequate for recognizing a familiar shape. A 0.1μsec range gate was used to obtain the laser images shown in Figure 8. In general a narrower range gate will be necessary with a logarithmic amplifier because it compresses the difference between the target return and ground clutter.

#### 4. WEATHER EFFECTS

During the time that the testbed laser radar has been operating, light fog and heavy rain were experienced while imaging the radar tower, and haze and heavy rain were experienced while imaging the truck at 2 km. In all cases, a satisfactory image was obtained by increasing the gain of the system and no image degradation was observed. The effects of weather on the performance of the laser radar will be studied quantitatively with the digital tape recording and processing system; however, the preliminary results indicate that the sizing of the system is correct.

The signal-to-noise equation, presented earlier, includes an allowance of 2 dB/km for atmospheric attenuation. The implications of the 2 dB/km attenuation value are shown in Figure 9, the weather pattern for North Central Europe during January<sup>14</sup>. January is typically one of the worst months for bad weather in North Central Europe as cold damp air from the North Sea is swept over land and the cloud ceiling is often low. The infrared attenuation is predominantly due to water vapor absorption and approximately follows the pattern of the cloud ceiling height. The 5-km slant path is measured from the base of the clouds, similar to the view line of a tactical air-to-ground aircraft seeking ground based targets. We note from this chart that a CO<sub>2</sub> laser radar of the size described in this work would be operational 90% of the time out to the full range of 4.5 km. The

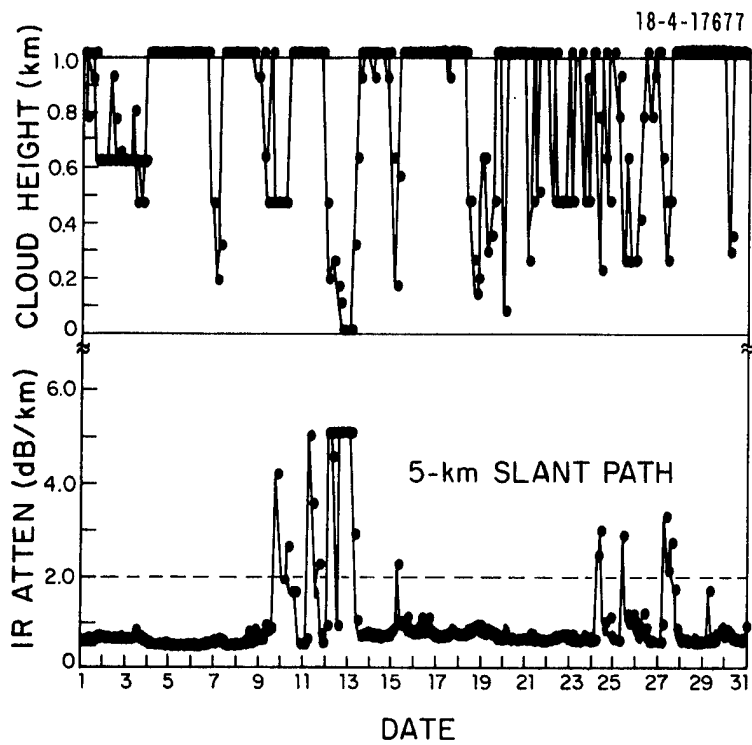


FIGURE 9. JANUARY WEATHER PATTERN-NORTH CENTRAL EUROPE

14. A. P. Modica and H. Kleiman, "Statistics of Global IR Atmospheric Transmission" (1), Report No. TT-7, MIT/Lincoln Laboratory (March 1976).

system is not incapacitated the remaining 10% of the time; it just does not perform out to the maximum desired range. Equally as important as this total percentage is the fact that there are only two intervals during this month when the laser radar is restricted for more than 12 hours. As an indication of the degree of weather penetration, we note that a 3 dB/km design level would increase the fully operational percentage to 95% and reduce the 12 hour restricted performance interval to one per month. This goal could be met by doubling both the average power of the laser and the diameter of the transmit/receive aperture.

##### 5. SUMMARY AND CONCLUSIONS

Tactical targets were imaged against terrain background at ranges out to 3 km, the farthest point accessible from our present location. From the available signal-to-noise at 3 km we would expect satisfactory imaging out to 5 km. The key to obtaining good imagery against terrain was the use of a narrow range-gate, 0.4 $\mu$ sec for the linear amplifier and 0.1 $\mu$ sec for the log-amplifier. It should be noted that the shallow slant angle of 1-1.5 degrees at which we view the objects, aggravates the ground return problem. In the tactical air-to-ground mission the viewing angle will be 10-40 degrees and some relaxation of the gate width would be expected. The use of a narrow range gate should not be an undue burden on the system, as accurate angle and range track are implied in the narrow field-of-view, high-frame-rate mode of operation.

Images were displayed in real time. The frame rate was 1 per second. It is recognized that faster frame rates will be required in the airborne system and techniques are being developed to increase the frame rate.

Preliminary data on weather penetration were obtained and initial design study assumptions were confirmed concerning the required power of the laser and aperture size. Visual observations of the imagery show no degradation due to atmospheric turbulence or scattering. Scintillation was not expected to be a problem with the 10 cm aperture out to ranges of 5 km under average conditions.

Based on the images shown in Figure 5-8 it appears that when the target spans a large number of resolution cells, a good image can be obtained with a single frame. When the resolution approaches some minimum value required for target recognition, image definition can be improved by frame averaging. A large number of frames are required when the transmitter and target are stationary. In the airborne application the aspect angle and range will change between frames and fewer frames should be needed to effect the desired improvement.

When the reflectivity varies greatly from one portion of the target to another, a log amplifier is useful in obtaining a well-defined image. Imaging with a log amplifier suffers from the fact that noise and ground clutter become competitive with the desired signal return. Limiting amplifiers or processing techniques which suppress high and low signal returns may be more effective.

Quantitative criteria for the detection, recognition, and identification of targets have not yet been established. This will involve imaging a large variety of targets against terrain under a variety of weather conditions. From the work performed to date, some qualitative assessments can be made. First, it appears that targets can be detected if they span more than 3-4 resolution elements, e.g. the man and jeep at 3 km. Familiar objects such as radar towers, trucks, and tanks can be recognized if they subtend about 10 x 20 resolution cells. These criteria apply to a single frame realization. By viewing a real time display recognition is often possible to recognize objects with substantially fewer resolution cells.

The effects of weather, factors affecting the image quality, and the criteria for detection, recognition, and identification of targets will be addressed quantitatively with digital tape recording and processing. Processing techniques will then be developed for a dedicated system which will allow real time processing in the airborne system.

Thermal-Blooming Compensation Using the CLASP System\*

By

C.A. Primmerman, F.B. Johnson, and I. Wigdor

Massachusetts Institute of Technology

Lincoln Laboratory

P.O. Box 73

Lexington, Massachusetts 02173

28 October 1977

ABSTRACT

A closed-loop system for phase compensation of thermal blooming has been designed and tested. This system — called CLASP for closed-loop adaptive single parameter — is a single-mode, outgoing-wave dither system. CLASP has demonstrated stable convergence to the optimum thermal-blooming-correction amplitude in a laboratory experiment.

---

\*This work was sponsored by the Advanced Research Projects Agency of the Department of Defense.

## INTRODUCTION

It has been demonstrated both theoretically<sup>1</sup> and experimentally<sup>2</sup> that phase compensation can reduce the effects of thermal blooming for CW, forced-convection-dominated laser beams. This work was done in an open-loop mode, in which the blooming conditions were measured or specified and the appropriate phase correction calculated. In this article we report on a closed-loop system for thermal-blooming compensation.

CLASP (Closed-Loop Adaptive Single Parameter) is a closed-loop system that compensates for thermal blooming by optimizing only one parameter – the amplitude of the phase correction.

CLASP is based on analysis<sup>1</sup> showing that the phase correction for thermal blooming may be separated into two distinct components. One, the shape of the correction profile, depends only on the near-field irradiance distribution. The other, the amplitude of the phase correction, depends on many variables – laser power, cross-wind velocity, slew velocity, absorption. If the near-field irradiance distribution of the laser is measured in advance, the proper correction profile can be calculated and specified for a deformable-mirror system. With the relative profile specified, the far-field irradiance can be maximized by using a CLASP system to optimize the correction as the external variables change.

## EXPERIMENTAL ARRANGEMENT

The experimental arrangement for the CLASP tests is shown in Fig. 1. We use a CW argon-ion laser that produces a Gaussian beam with up to 2 watts at 5145 Å. The beam is expanded to make the  $1/e^2$  diameter 3.8 cm, is truncated at that diameter, and is reflected from the deformable mirror. The deformable mirror is a monolithic piezoelectric mirror<sup>3</sup> having 57 actuators over a 3.8 cm diameter active area. Its relative phase profile is fixed at the optimum profile for thermal-blooming compensation of a truncated Gaussian beam; its magnitude may be adjusted from flat to  $2\lambda$  peak-to-peak on the mirror. After the deformable mirror the beam is contracted to .5 cm by a second collimator, is reflected from the DRAT tracker mirrors, passes through an absorption cell, and is brought to a focus on a single 50-micron pinhole in front of a detector.

The absorption cell is a rotating cylinder 20 cm in diameter by 1 meter long, mounted vertically. It is filled with ethyl alcohol and enough iodine to absorb about half of the incident radiation. The rotation speed can be varied to change the cross-wind velocity, and by having the beam enter the cell close to the axis and exit near the outer edge, slewing can be simulated. Computer calculations show that this rotating cell adequately models the case of a laser beam slewing through the atmosphere.

In order to test the CLASP system it was necessary to design and build another closed-loop system, the DRAT (Dither-Reduced Acquisition and Tracking) tracking system.<sup>4</sup> This system compensates for the thermal blooming shift into the wind and also for any irregularities in the windows of the rotating cell to always keep the peak intensity of the beam on the pin-

hole. The tracker is a type of dither system; it dithers the beam across the pinhole by using two galvenometer scanners operating at non-commensurate frequencies in the range 2-4 kHz. The resulting tracking bandwidth is  $>100$  Hz. The unique feature of this system is that for initial acquisition the system employs a wide-amplitude acquisition dither, but as the tracker converges, the dither amplitude is automatically reduced to maintain the peak very precisely on target.

#### OPEN-LOOP RESULTS

In order to understand the CLASP system performance it is necessary to know the features of the thermal-blooming correction in the absence of CLASP. In Fig. 2 we plot the measured focal-plane peak irradiance against input power for the uncorrected beam, the corrected beam, and the hypothetical case of absorption but no blooming. These results are typical blooming-compensation results and are similar to those previously reported.<sup>2</sup>

The corrected curve in Fig. 2 was obtained by manually adjusting the correction amplitude to get the maximum far-field peak irradiance at each power. As the power increases, larger amplitude corrections are needed. The object of the CLASP system is to automatically optimize the correction amplitude so that no matter where the system starts on the uncorrected curve, it will always converge to a point on the corrected curve.

Note that for severely bloomed conditions ( $P \approx .4W$ ) phase compensation can improve the peak irradiance by more than a factor of three. Figure 3 shows a plot of peak irradiance versus correction amplitude for a severely bloomed case. We see that a maximum improvement of 3.5 is obtained and that the curve is smooth and bell-shaped with a broad maximum. It is this curve on which the CLASP hill-climbing servo works.

### CONTROL SYSTEM

The CLASP system is an example of an outgoing-wave dither system. It is, in fact, the limiting case of a multi-dither system, in which only one mode is dithered. A block diagram of the CLASP system is shown in Fig. 4. The deformable-mirror is dithered by applying the voltage  $V_1 \sin \omega t$ . The peak intensity at the detector is then  $I_p(V) = I_p(V_o + V_1 \sin \omega t)$  where  $V_o$  is the constant correction voltage.  $I_p(V)$  is given by a curve like that shown in Fig. 3, since the peak-to-peak mirror deformation is proportional to the applied voltage,  $V$ . The peak irradiance is bandpass filtered at  $\omega$  and is synchronously demodulated. This synchronous demodulation produces an error signal proportional to the slope of the correction curve, Fig. 3. This fact may be simply shown by expanding  $I_p(V)$  around  $V = V_o$ :

$$I_p(V) = I_p(V_o + V_1 \sin \omega t) = I_p(V_o) + \frac{dI_p}{dV} \Big|_{V_o} V_1 \sin \omega t + \frac{1}{2} \frac{d^2 I_p}{dV^2} \Big|_{V_o} V_1^2 \sin^2 \omega t + \dots$$

By bandpass filtering and synchronously demodulating we eliminate all terms but the second, leaving an error signal proportional to  $\frac{dI_p}{dV} V_1$ . This error signal is amplified and passed through a single intergrator. The resulting correction voltage is then summed with the dither voltage and applied to the deformable mirror.

The control system attempts to null the error signal, which it does by adjusting  $V_o$  to make  $dI_p/dV = 0$ . This condition, of course, is simply the condition for  $I_p$  to be a maximum. Thus, CLASP drives the correction to the optimum  $V_o$  and dithers it about this point.

In actual practice we typically used a square wave dither with a frequency of 10 Hz and an amplitude of  $\lambda/10$  peak-to peak. Using a square-wave dither only changes the synchronously demodulated signal by the constant factor  $4/\pi$  (the first harmonic content of a square wave) compared to sinusoidal dither. The 10 Hz dither gave a control bandwidth of about 1 Hz. This bandwidth is acceptable for thermal-blooming compensation, since thermal blooming is a relatively slow phenomenon. The  $\lambda/10$  peak-to-peak dither is illustrated in Fig. 3. This dither magnitude is large enough to develop the required error signal when the system is not at the optimum correction amplitude, but small enough relative to the broad maximum of the correction curve that the peak irradiance does not change significantly as the correction amplitude is dithered about the optimum.

#### CLOSED-LOOP RESULTS

Figure 5 shows the time response of a typical CLASP shot. The upper trace gives the peak irradiance through the pinhole; the lower trace gives the CLASP correction amplitude. The beam is turned-on at  $t = 0$ , and at the beginning of the irradiance trace we just catch the end of the decay to steady-state blooming. The entire transient is not observed because the tracker is in the acquisition mode during this period. The blooming reaches a steady-state at an intensity about  $1/10$  unbloomed after 0.2 sec and remains constant while the deformable mirror remains flat. At  $t = 1.3$  sec CLASP is activated, the mirror begins to dither, and the correction amplitude increases to maximize the peak irradiance. The system converges smoothly to the optimum correction amplitude of  $0.7\lambda$  peak-to-peak in about 0.4 sec. The peak irradiance increases by a factor of 3 and remains stably at that value as the CLASP system dithers the correction amplitude slightly about the optimum.

For the case illustrated in Fig. 5 CLASP was initiated with the deformable mirror flat. This starting point is the normal one for a closed-loop adaptive optics system. But it is also interesting to see how such a system responds when started from some other point.

In Fig. 6 we show a case in which CLASP was started with too much phase correction initially added. Again the upper trace is peak irradiance, the lower trace is correction amplitude. When the beam is first turned on, the correction amplitude is  $1.6\lambda$  peak-to-peak and the far-field peak irradiance stabilizes at the steady-state value for that phase correction. CLASP is activated at  $t = 3.4$  sec and the correction amplitude drives back to a lower value to optimize the peak irradiance. The correction amplitude converges to

$0.4\lambda$  peak-to-peak indicating that the blooming was less severe than for the case shown in Fig. 5 where the correction amplitude converged to  $0.7\lambda$  peak-to-peak. The peak irradiance increases by a factor of 5, showing that the over-correction was severely degrading the beam.

CLASP converges to the optimum phase-correction amplitude regardless of the starting point. Note, however, that the rise-time is about 1 sec in Fig. 6 compared to .4 sec in Fig. 5. This difference comes from the fact that the shape of the correction curve (Fig. 3) renders the servo-control loop non-linear. Thus, the convergence time is dependent on precisely where one starts on the correction curve.

#### COMPUTER SIMULATION

In order to optimize the design of the CLASP control loop the CLASP system was modeled, mathematically, and a time-domain, step-response simulation done on a digital computer. Figure 7 shows the results from a computer-simulation run. The upper curve is the far-field peak irradiance; the lower curve is the correction amplitude. We observe, in agreement with the experimental results shown in Fig. 5, that the CLASP system converges in about .5 sec and maintains itself stably at the optimum amplitude. The correction curve is broad enough that no discernable change is observed in the peak irradiance as the correction dithers across the optimum.

The simulation illustrated was done with no noise. We have also considered the effect of noise on the CLASP system. When white noise with a bandwidth out to 100 Hz was added in the computer simulation, it was found that CLASP could converge with signal-to-noise ratios as low as 1:5.

## CONCLUSIONS

The CLASP system has shown stable convergence to the optimum thermal-blooming-correction amplitude in a laboratory experiment. The experimental results are in good agreement with computer simulations, demonstrating that the CLASP system is well characterized and working according to its original design. Thus, the CLASP concept of a single-mode, outgoing wave dither system has shown itself to be a viable concept for thermal-blooming correction.

REFERENCES

1. L.C. Bradley and J. Herrmann, *Appl. Opt.* 13, 331 (1974).
2. C.A. Primmerman, and D.G. Fouche, *Appl. Opt.* 15, 990 (1976).
3. J. Feinlieb, S.G. Lipson, and P.F. Cone, *Appl. Phys. Litt.* 25, 311 (1974).
4. F.B. Johnson, I. Wigdor, and C.A. Primmerman (to be published).

FIGURE CAPTIONS

Fig. 1. CLASP experimental arrangement.

Fig. 2. Peak focal-plane irradiance versus input power for corrected and uncorrected beams. The straight line would be the irradiance if there were absorption but no blooming.

Fig. 3. Peak focal-plane irradiance versus peak-to-peak mirror deformation for a severely bloomed case. The arrow indicates the CLASP dither magnitude.

Fig. 4. Block diagram of CLASP control system.

Fig. 5. CLASP time response starting with the deformable mirror flat. Upper trace: Peak focal-plane irradiance. Lower trace: Peak-to-peak mirror amplitude.

Fig. 6. CLASP time response starting with the deformable mirror over correcting. Upper trace: Peak focal-plane irradiance. Lower trace: Peak-to-peak mirror amplitude.

Fig. 7. Computer simulation of CLASP system response. Upper curve: Peak focal-plane irradiance. Lower curve: Peak-to-peak mirror amplitude.

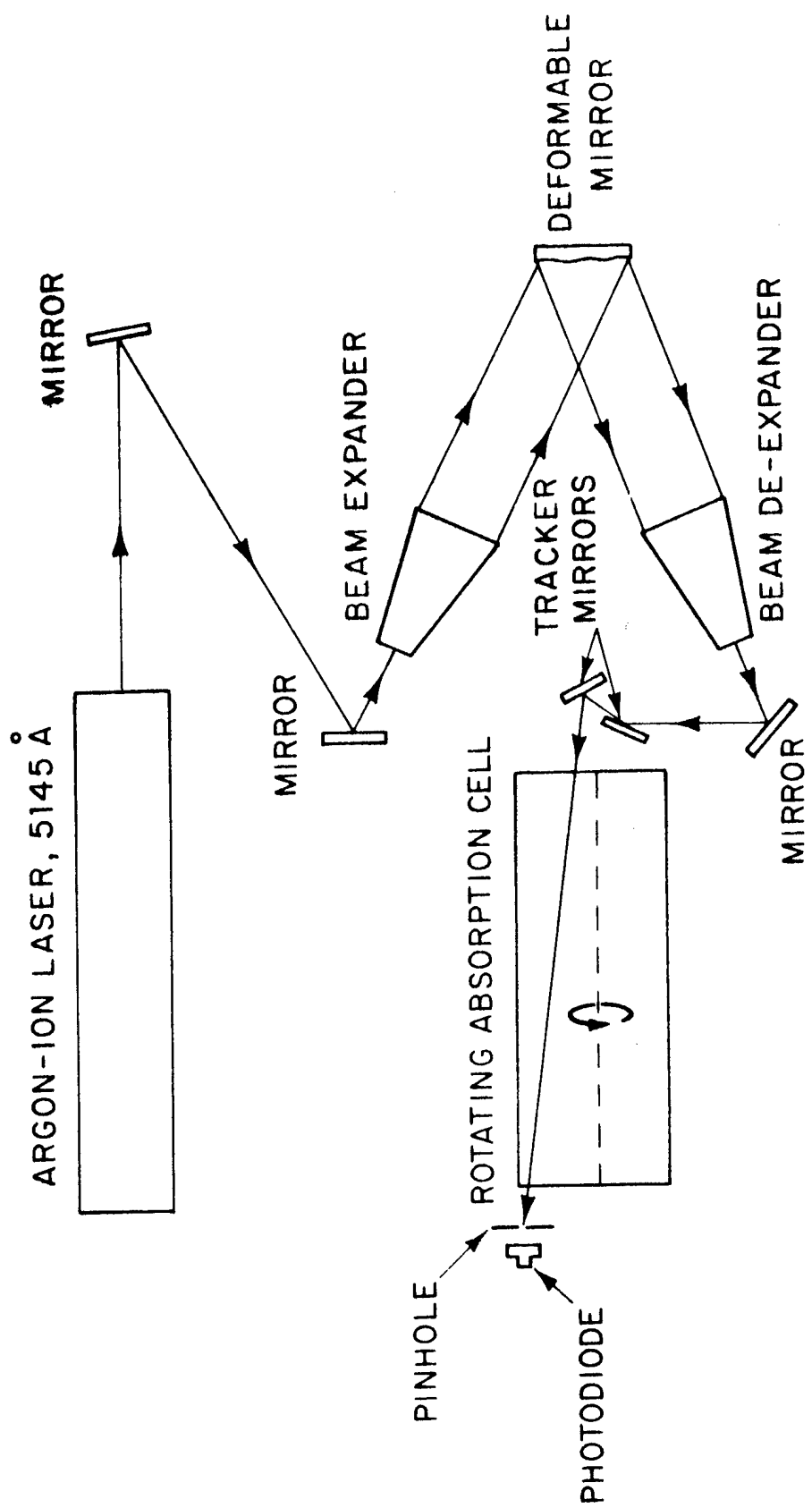


Fig. 4.

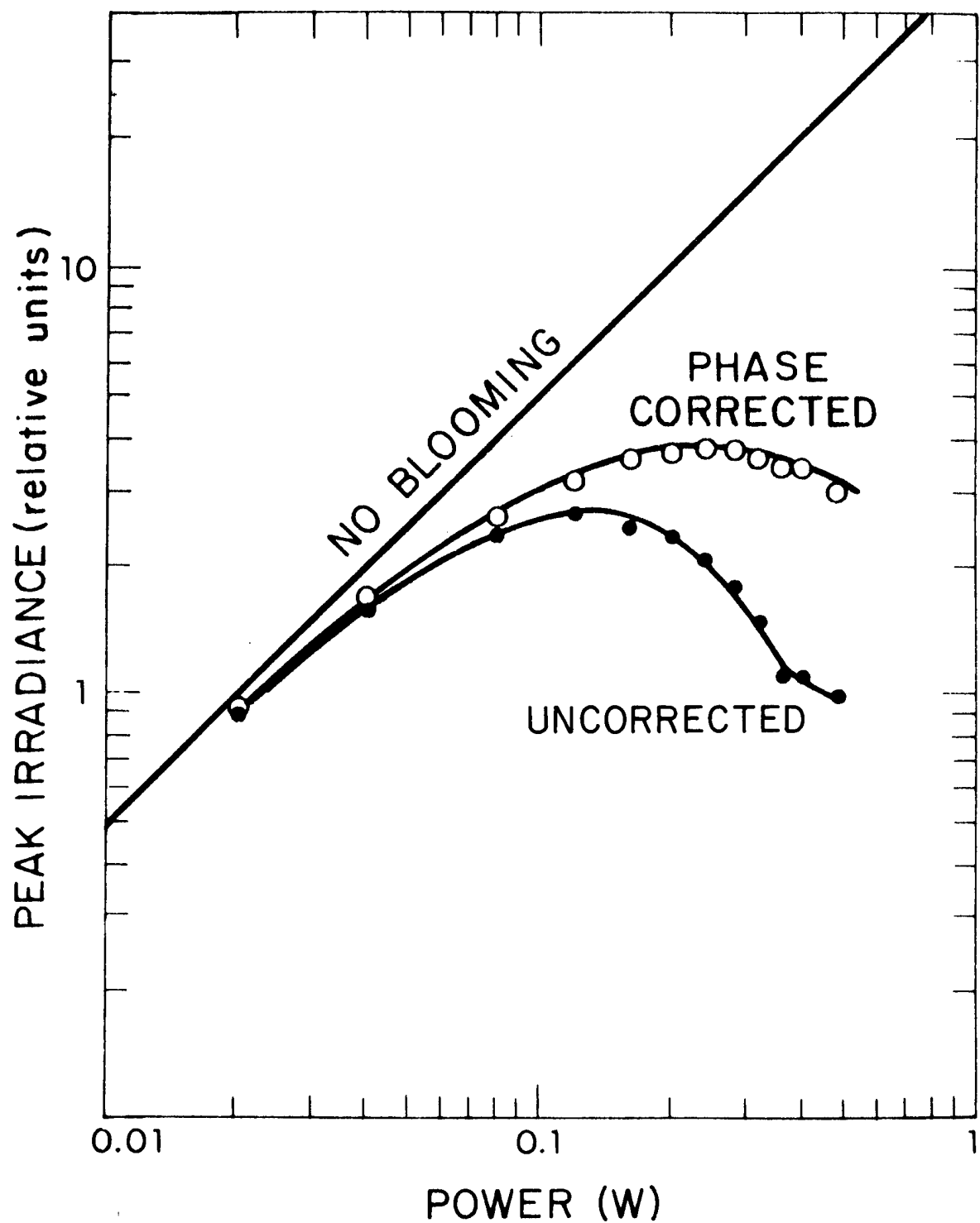


Fig. 2.

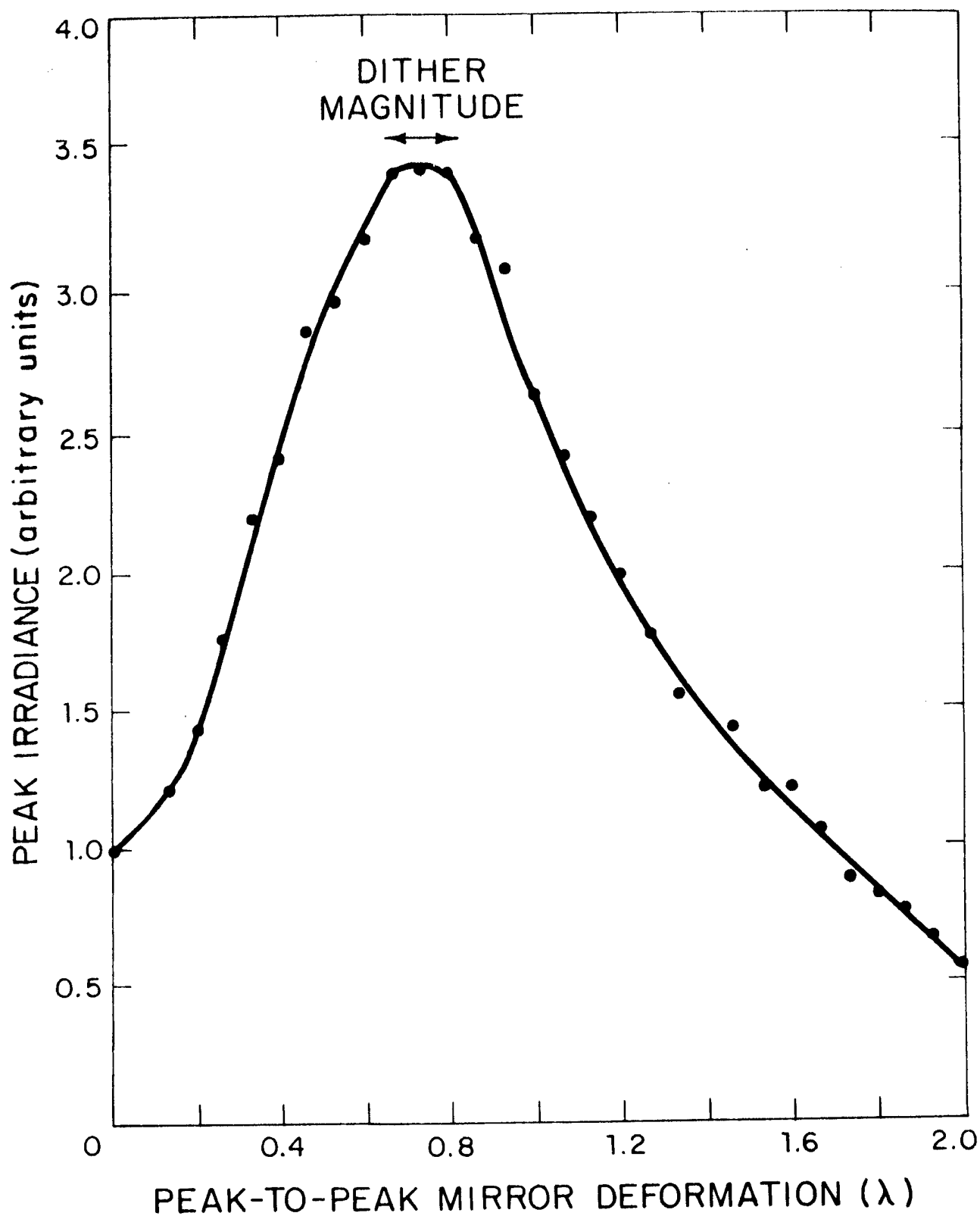


Fig. 3.

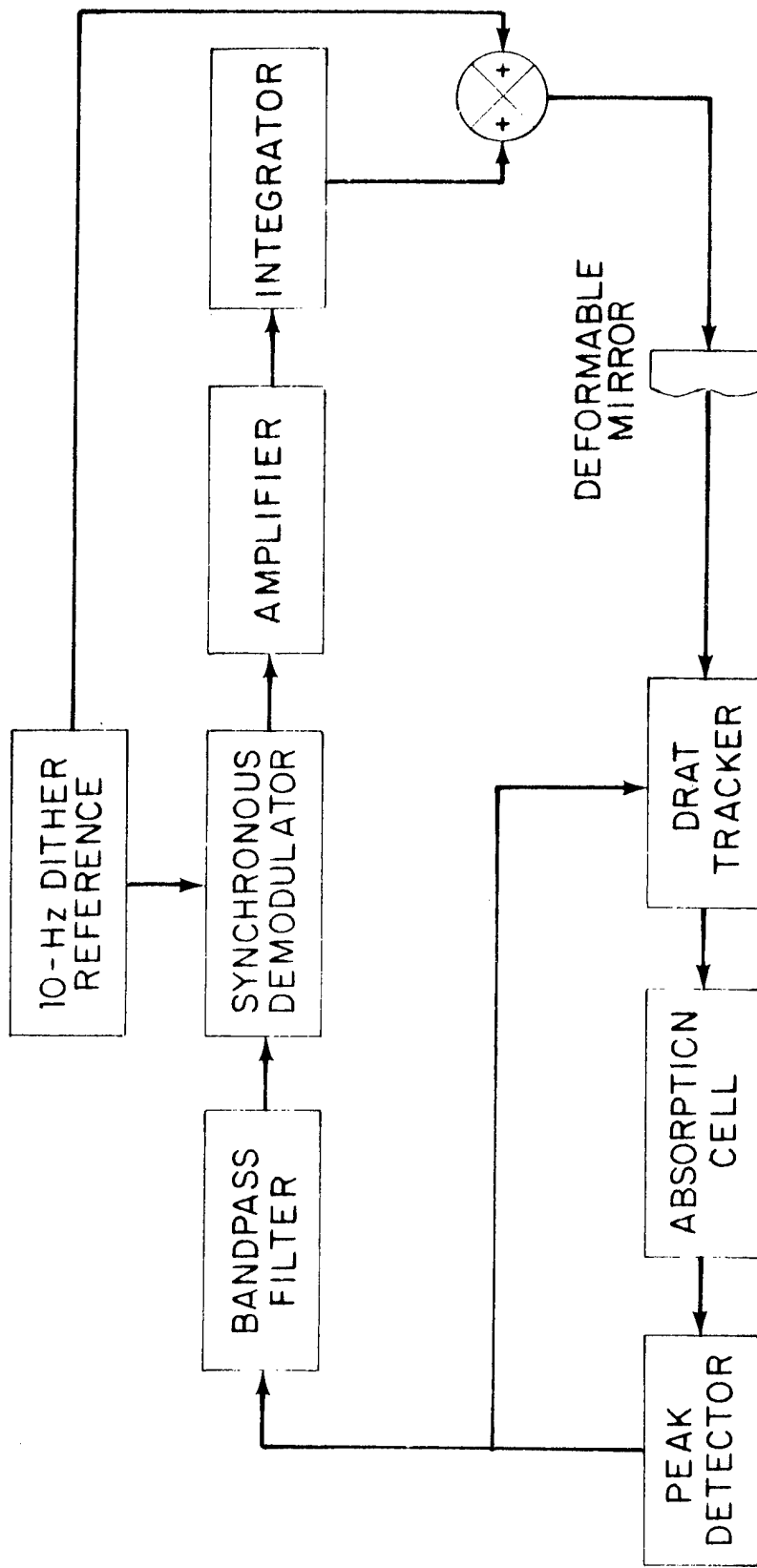


Fig. 4.

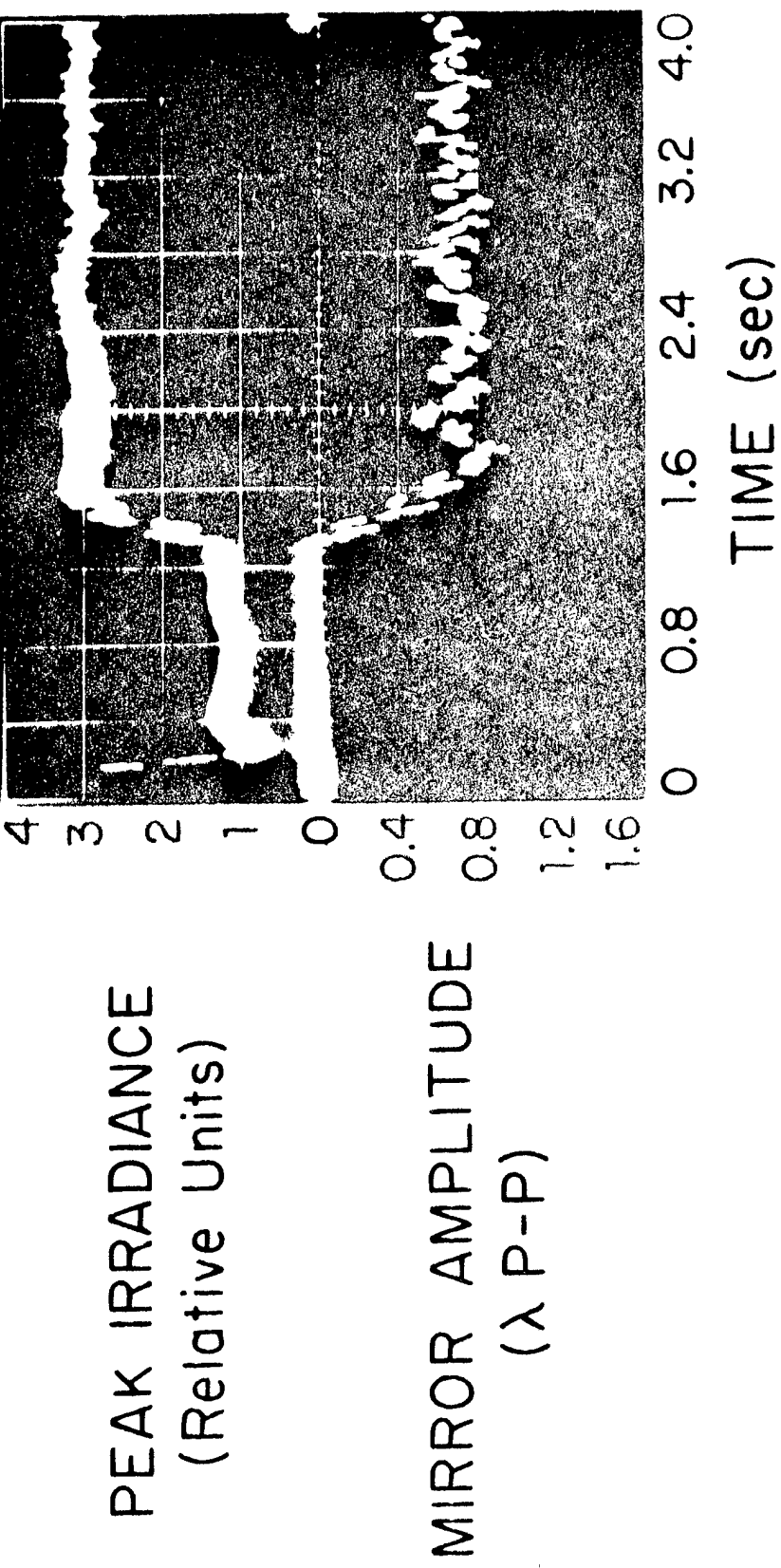


Fig. 5.

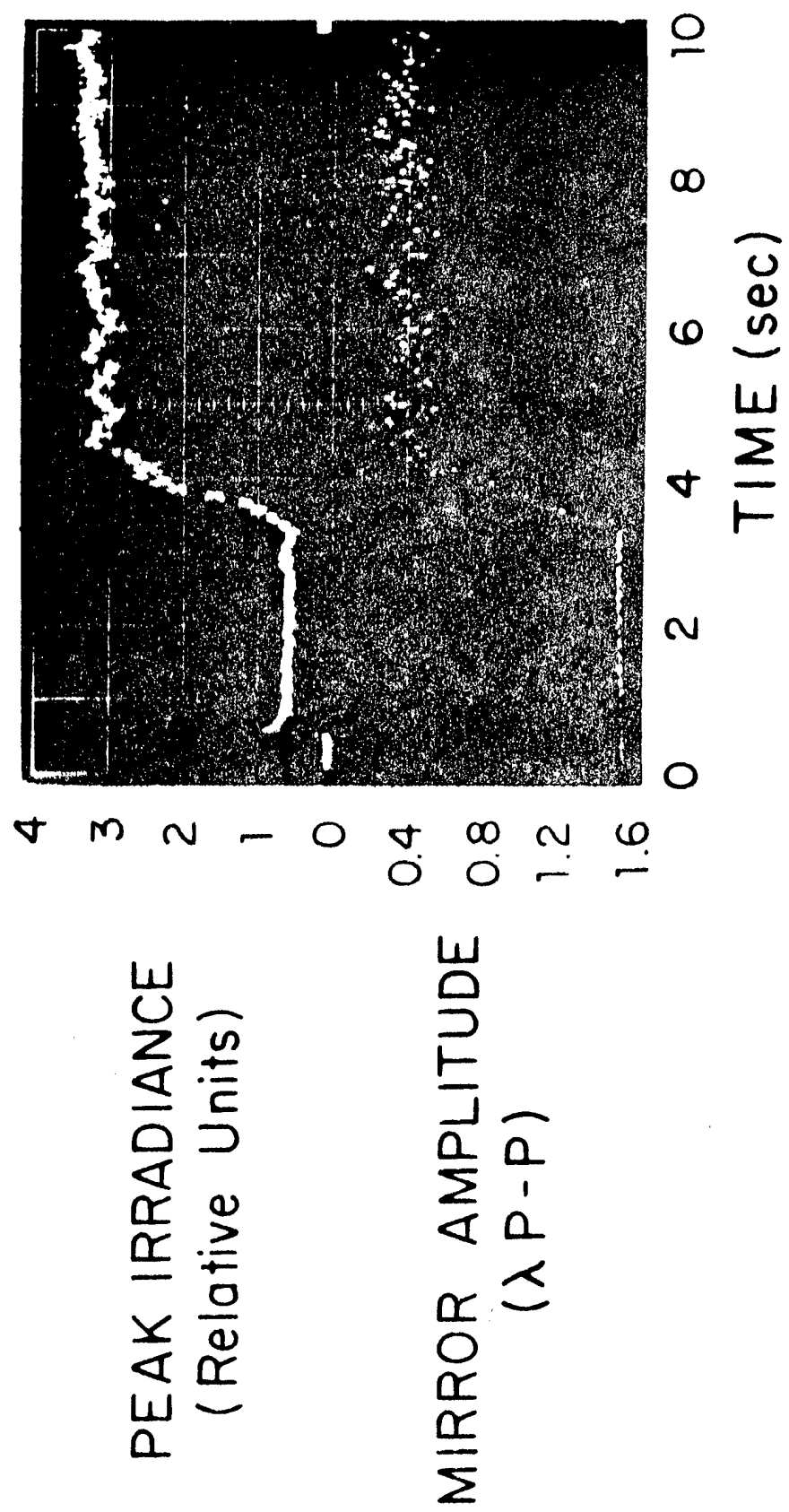
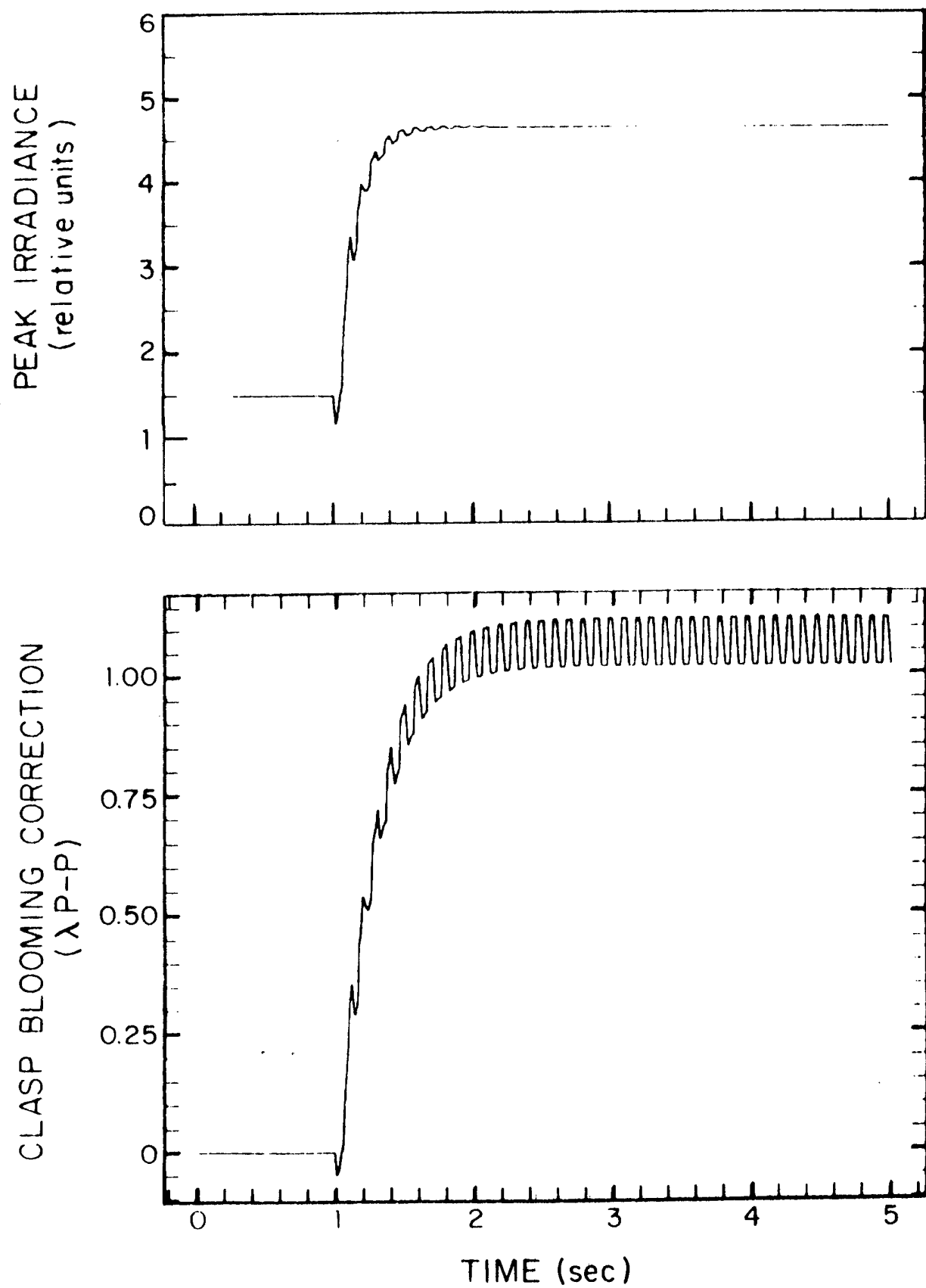


Fig. 6.



HOW MANY PHYSICALLY SIGNIFICANT SOLUTIONS ARE THERE TO THE SELF-  
INDUCED TRANSPARENCY EQUATIONS?\*

R.C. Harney

*M.I.T. Lincoln Laboratory, Lexington, Massachusetts*

The interaction of a coherent electromagnetic wave with a collection of two-level atoms is of major theoretical importance in the study of the interaction of light with matter, not only because analytical solutions can be obtained but also because experiments can be devised which closely approximate this ideal case. In the past there has been some controversy concerning the interpretation of the analytical solutions to this problem [1]. Although previously unpublished, the controversy is real and the problem is of sufficient fundamental importance to demand its resolution. Such is the purpose of the work described here.

In an inhomogeneously broadened two-level medium described by a particle density  $n_0$  and electric dipole matrix element  $p$ , an incident electric field of the form

$$E(z,t) = (\hbar/p) \mathcal{E}(z,t) \cos(kz-\omega t)$$

will induce a macroscopic polarization of the form

$$P(z,t) = n_0 p [\langle C(\Delta\omega, z, t) \rangle_{\Delta\omega} \cos(kz-\omega t) + \langle S(\Delta\omega, z, t) \rangle_{\Delta\omega} \sin(kz-\omega t)]$$

where  $\Delta\omega = \omega - \omega_0$  is the difference between the incident electric field frequency and the resonant frequency of the two-level system and  $\langle \rangle_{\Delta\omega}$  denotes an average over the inhomogeneous line profile.

The mutual interaction of the electric field and the induced polarization can be exactly described using Maxwell's equations and the Schrödinger equation for the medium. In the rotating wave approximation, we obtain the following coupled nonlinear differential equations

$$\frac{d\mathcal{E}}{dt} = \alpha \langle S \rangle_{\Delta\omega} ,$$

$$\frac{\partial C}{\partial t} = -\Delta\omega S ,$$

$$\frac{\partial S}{\partial t} = \Delta\omega C + \eta \mathcal{E} ,$$

$$\frac{\partial \eta}{\partial t} = -S \mathcal{E} ,$$

where  $\alpha = n_0 \omega_{op}^2 / \hbar$  is the inverse Beer's length of the medium,  $\eta$  is the population inversion density, and  $C$ ,  $S$ , and  $\eta$  obey the normalization condition  $C^2 + S^2 + \eta^2 = 1$ . These four equations are commonly referred to as the self-induced transparency equations.

Mishkin assumed that the steady state solutions to these equations would depend only on the retarded time [2]

$$u = \frac{1}{\tau} (t - \frac{z}{V}) ,$$

where  $\tau$  is a characteristic time and  $V$  is the pulse propagation velocity in the medium. With this assumption

$$\mathcal{E} = \mathcal{E}_0 e(u) ,$$

$$C = \tau \Delta\omega \Lambda(\Delta\omega) e(u) ,$$

$$S = -\Lambda(\Delta\omega) \frac{de(u)}{du} ,$$

$$\eta - \eta_0 = (1/2) \mathcal{E}_0 \Lambda(\Delta\omega) e^2(u) ,$$

where  $\Lambda(\Delta\omega)$  is a frequency response function and  $\eta_0$  is the population inversion which would exist in the medium in the absence of the electric field. Substituting these results into the normalization condition yields

$$\left[ \frac{de}{du} \right] = \left[ \left( \frac{\mathcal{E}_0 \tau}{2} \right)^2 e^4 - \left( (\tau \Delta\omega)^2 + \frac{\eta_0 \mathcal{E}_0 \tau}{\Lambda(\Delta\omega)} \right) e^2 + \frac{1 - \eta_0^2}{\Lambda^2(\Delta\omega)} \right]^{1/2}$$

The Jacobi elliptic functions [3] are solutions to this nonlinear differential equation.

## SELF-INDUCED TRANSPARENCY EQUATIONS

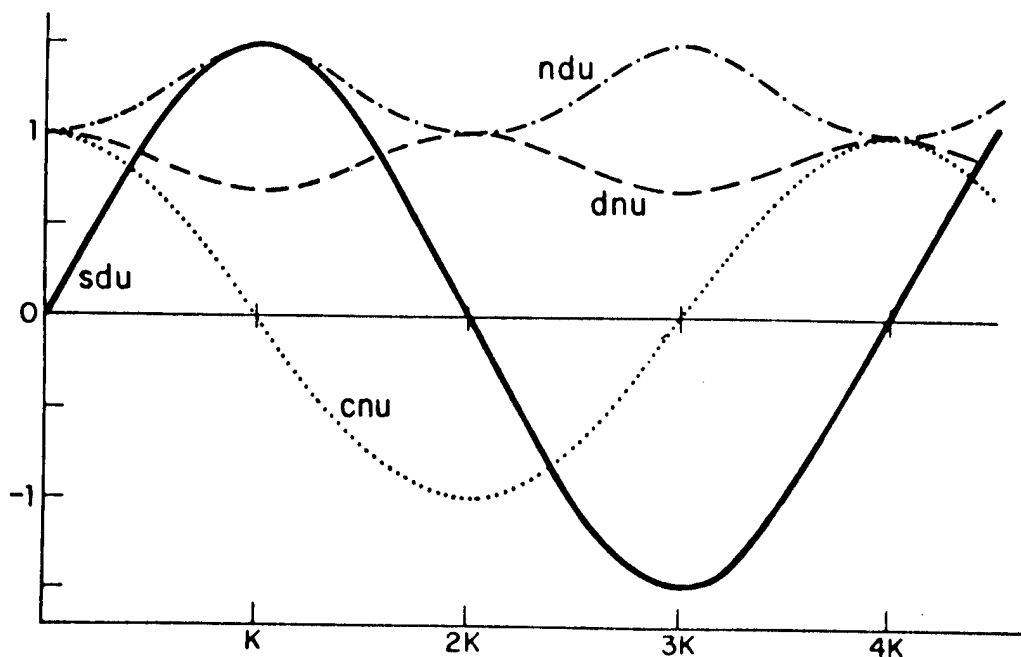


Fig. 1. The four real Jacobi elliptic function solutions to the self-induced transparency equations.

Closer examination indicates that only four of the twelve Jacobi elliptic functions have real values of  $\epsilon_0$  and  $\tau$  and are therefore physically acceptable. The four acceptable solutions (cnu, dnu, sdu, ndu) are shown in Fig. 1. The important physical properties of these solutions have been derived by Mishkin [2] and by the author [4] and are summarized in Table I.

The controversy concerning these solutions arises from the fact that two of the solutions are related to the other two solutions by a change of argument transformation

$$sd(u + K) = (1 - k^2)^{-1/2} cnu, \\ nd(u + K) = (1 - k^2)^{-1/2} dnu,$$

where  $k$  is the modulus of the solution (dependent on the physical parameters of the system) and  $K$  is the elliptic integral of the first kind. One contingent contends that the existence of this transformation means that sdu is equivalent to cnu and that ndu is equivalent to dnu [1]. Mishkin argues that the change of argument is equivalent to a change of the physical situation and that all four solutions are physically significant. Given this situation we should fall back to the only true test of a scientific hypothesis', experiment (or in this case, gedanken experiment). If an experiment can be devised which can distinguish between two solutions, then they are physically distinct. If no experiment can distinguish between them, they are physically equivalent.

QUANTITY	cmw SOLUTION	dmw SOLUTION	dmw SOLUTION	dmw SOLUTION
Envelope of electric field ( $E$ )	$E_0 \text{ cmw}$	$E_0 \text{ dmw}$	$E_0 \text{ dmw}$	$E_0 \text{ dmw}$
In-phase macroscopic polarization ( $C$ )	$\tau \Delta \omega \mathbf{A}(\Delta\omega) \text{ cmw}$	$\tau \Delta \omega \mathbf{A}(\Delta\omega) \text{ dmw}$	$\tau \Delta \omega \mathbf{A}(\Delta\omega) \text{ dmw}$	$\tau \Delta \omega \mathbf{A}(\Delta\omega) \text{ dmw}$
Out-of-phase macroscopic polarization ( $S$ )	$\mathbf{A}(\Delta\omega) \text{ mw dmw}$	$k^2 \mathbf{A}(\Delta\omega) \text{ mw dmw}$	$-k^2 \mathbf{A}(\Delta\omega) \text{ dmw dmw}$	$-\mathbf{A}(\Delta\omega) \text{ dmw dmw}$
Population inversion ( $\alpha$ )	$\frac{\Delta}{E_0} \left[ 2 \delta \omega_u - 1 - (\tau \Delta \omega)^2 \right]$	$\frac{\Delta}{E_0} \left[ 2 \delta \omega_u - 2 + k^2 - (\tau \Delta \omega)^2 \right]$	$\frac{\Delta}{E_0} \left[ k^2 (1 - 2 \alpha^2 \omega_u) - (\tau \Delta \omega)^2 \right]$	$\frac{\Delta}{E_0} \left[ -2 k^2 \alpha^2 \omega_u - (\tau \Delta \omega)^2 \right]$
Characteristic time relation ( $E_0 \tau$ )	$2k$	$2$	$2 (1 - k^2)^{1/2}$	$2 k (1 - k^2)^{1/2}$
Frequency response function ( $\mathbf{A}(\Delta\omega)$ )	$\frac{2\pi}{\left[ (1 - (\tau \Delta \omega)^2)^2 + 4(\tau \Delta \omega)^2 \right]^{1/2}}$	$\frac{2}{\left[ (\tau \Delta \omega)^2 + 4(\tau \Delta \omega)^2 \right]^{1/2}}$	$\frac{2 (1 - k^2)^{1/2}}{\left[ 4 k^2 (\tau \Delta \omega)^2 + (1 - (\tau \Delta \omega)^2)^2 \right]^{1/2}}$	$\frac{2 k (1 - k^2)^{1/2}}{\left[ 4 k^2 (\tau \Delta \omega)^2 + (1 - (\tau \Delta \omega)^2)^2 \right]^{1/2}}$
Period of oscillation ( $T$ )	$4\pi \text{ K}(k)$	$2\pi \text{ K}(k)$	$2\pi \text{ K}(k)$	$4\pi \text{ K}(k)$
Integration constant ( $\gamma_0$ )	$\left[ \frac{1 - (\tau \Delta \omega)^2 - 2k^2}{4(\tau \Delta \omega)^2 + (k^2 - (\tau \Delta \omega)^2)^2} \right]^{1/2}$	$\left[ \frac{k^2 - 2 - (\tau \Delta \omega)^2}{4(\tau \Delta \omega)^2 + (k^2 - (\tau \Delta \omega)^2)^2} \right]^{1/2}$	$\left[ \frac{k^2 - 2 - (\tau \Delta \omega)^2}{4 k^2 (\tau \Delta \omega)^2 + (1 - (\tau \Delta \omega)^2)^2} \right]^{1/2}$	$\left[ \frac{1 - (\tau \Delta \omega)^2 - 2k^2}{4 k^2 (\tau \Delta \omega)^2 + (1 - (\tau \Delta \omega)^2)^2} \right]^{1/2}$
Ratio of light velocity to pulse velocity	$\left( \frac{c}{V} \right) \frac{1 + \alpha^2 \int_0^{\infty} g(\Delta\omega) \left[ (1 - (\tau \Delta \omega)^2)^2 + 4k^2 (\tau \Delta \omega)^2 \right]^{-1/2} d\Delta\omega}{1 + \alpha^2 \int_0^{\infty} g(\Delta\omega) \left[ (1 + \alpha^2 \omega^2 + (k^2 - (\tau \Delta \omega)^2)^2)^{-1/2} d\Delta\omega \right.}$	$\left[ \frac{1 + \alpha^2 \int_0^{\infty} g(\Delta\omega) \left[ (1 - (\tau \Delta \omega)^2)^2 + 4k^2 (\tau \Delta \omega)^2 \right]^{-1/2} d\Delta\omega}{1 + \alpha^2 \int_0^{\infty} g(\Delta\omega) \left[ (1 + \alpha^2 \omega^2 + (k^2 - (\tau \Delta \omega)^2)^2)^{-1/2} d\Delta\omega \right.} \right]^{-1/2}$	$\left[ \frac{1 + \alpha^2 \int_0^{\infty} g(\Delta\omega) \left[ (1 - (\tau \Delta \omega)^2)^2 + 4(\tau \Delta \omega)^2 \right]^{-1/2} d\Delta\omega}{1 + \alpha^2 \int_0^{\infty} g(\Delta\omega) \left[ (1 + \alpha^2 \omega^2 + (k^2 - (\tau \Delta \omega)^2)^2)^{-1/2} d\Delta\omega \right.} \right]^{-1/2}$	$\left[ \frac{1 + \alpha^2 \int_0^{\infty} g(\Delta\omega) \left[ (1 - (\tau \Delta \omega)^2)^2 + 4(\tau \Delta \omega)^2 \right]^{-1/2} d\Delta\omega}{1 + \alpha^2 \int_0^{\infty} g(\Delta\omega) \left[ (1 + \alpha^2 \omega^2 + (k^2 - (\tau \Delta \omega)^2)^2)^{-1/2} d\Delta\omega \right.} \right]^{-1/2}$
Area per period	$0 \pi$	$2\pi$	$2\pi$	$0 \pi$
Area per half-period	$4 \sin^{-1}(k)$	$\pi$	$\pi$	$4 \sin^{-1}(k)$
Energy per period	$\frac{8 E_0}{k} \left[ \bar{E}(k) + (1 - k^2) K(k) \right]$	$4 E_0 E(k)$	$\frac{4 E_0}{(1 - k^2)^{1/2}} E(k)$	$\frac{8 E_0}{k (1 - k^2)^{1/2}} \left[ \bar{E}(k) - (1 - k^2) K(k) \right]$

Table I

## SELF-INDUCED TRANSPARENCY EQUATIONS

Table I. Summary of results for the four real Jacobi elliptic function solutions to the self-induced transparency equations.

Let us start by examining what parameters are subject to experimental measurements. In principle the cnu and sdu solutions can be distinguished from the dnu and ndu solutions by a time-resolved intensity measurement as the former solutions have electric field envelopes which pass through zero while the latter solutions do not. The same measurement could also yield the period of oscillation  $T$  and the energy  $\text{per period } W$  carried by the pulse train. The pulse propagation velocity  $V$  could be determined by observing the propagation velocity of an infinitesimal perturbation to the field. The initial population inversion density  $\eta_0(\Delta\omega)$  which is characteristic of the medium could be measured by determining the gain or attenuation of a weak frequency-tunable probe beam before the electromagnetic wave was incident on the medium. The steady-state population inversion density  $\eta(\Delta\omega, t)$  could be determined in the same manner after the steady state had been established. The modulus  $k$  can be uniquely determined from the  $\Delta\omega$ -dependence of  $\eta_0$  (see Table I). From a knowledge of  $T$  and  $k$  the characteristic time can be unambiguously determined.

So far the only quantities which are not identical for the cnu and sdu solutions or for the dnu and ndu solutions are the energy per period, the intensity as a function of time, and the population inversion as a function of time. Closer inspection of the expressions for these quantities indicates that  $\varepsilon_0$  must be known in order to be able to use them for distinguishing between the different solutions. From a knowledge of  $\tau$  and  $k$ ,  $\varepsilon_0$  can be predicted. A different value of  $\varepsilon_0$  is predicted for each solution, but the differences are such that using the predicted values leads to identical values of the energy per period, etc. for the cnu and sdu solutions and for the dnu and ndu solutions. Thus, to use  $\varepsilon_0$  to discriminate among the solutions it must be both measured and predicted and the measurement compared with the predictions.

Unfortunately,  $\varepsilon_0$  cannot be measured. The reason for this lies in the fact that although  $\varepsilon(t)$  can be inferred from a time-resolved intensity measurement,  $\varepsilon(u)$  cannot be precisely specified. The problem that arises is one of where to place  $u = 0$ . Since a steady state solution is one that has propagated for an infinite amount of time through an infinite distance and is infinite in extent, an arbitrary assignment of  $u = 0$  implies a knowledge of one's absolute position in space-time, which violates special relativity. The same considerations prevent one from fixing the position of  $u = 0$  within a single cycle (i.e. specifying the phase). Since the definition of  $\varepsilon_0$  depends on knowing where  $u = 0$  is,  $\varepsilon_0$  cannot be measured.

One parameter which can be unambiguously determined is the maximum value of the electric field envelope  $\mathcal{E}_{\max}$ . Comparing the four solutions we find

$$\mathcal{E}_{\max}(\text{cnu}) = \mathcal{E}_{\max}(\text{dnu}) = \mathcal{E}_0 ,$$

and

$$\mathcal{E}_{\max}(\text{sdu}) = \mathcal{E}_{\max}(\text{ndu}) = \mathcal{E}_0 / (1 - k^2)^{1/2} .$$

Using the measurable quantity  $\mathcal{E}_{\max}$  we find

$$\mathcal{E}_{\max} \tau = 2k \quad \text{for both sdu and cnu ,}$$

$$\mathcal{E}_{\max} \tau = 2 \quad \text{for both ndu and dnu .}$$

Similar results obtain for all other quantities dependent on  $\mathcal{E}_0$ . In other words, we are unable to find any measurable quantity which can distinguish between cnu and sdu or between dnu and ndu.

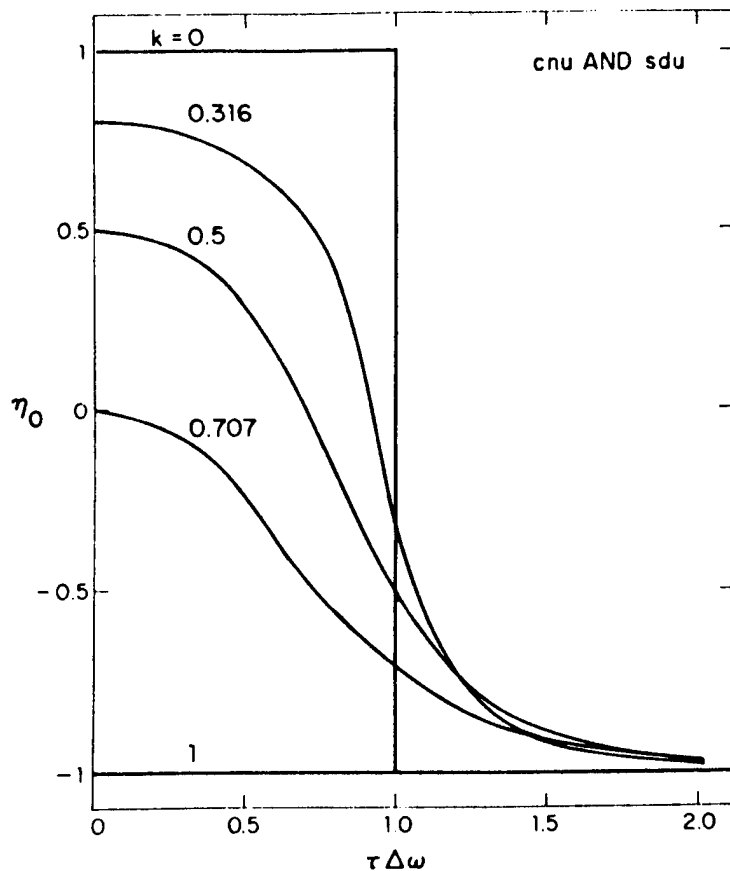


Fig. 2. The initial population inversion density  $\eta_0$  as a function of  $\tau\Delta\omega$  for cnu and sdu solutions. The curves correspond to values of  $k = 1.0, .707, .5, .316$ , and  $0$ .

## SELF-INDUCED TRANSPARENCY EQUATIONS

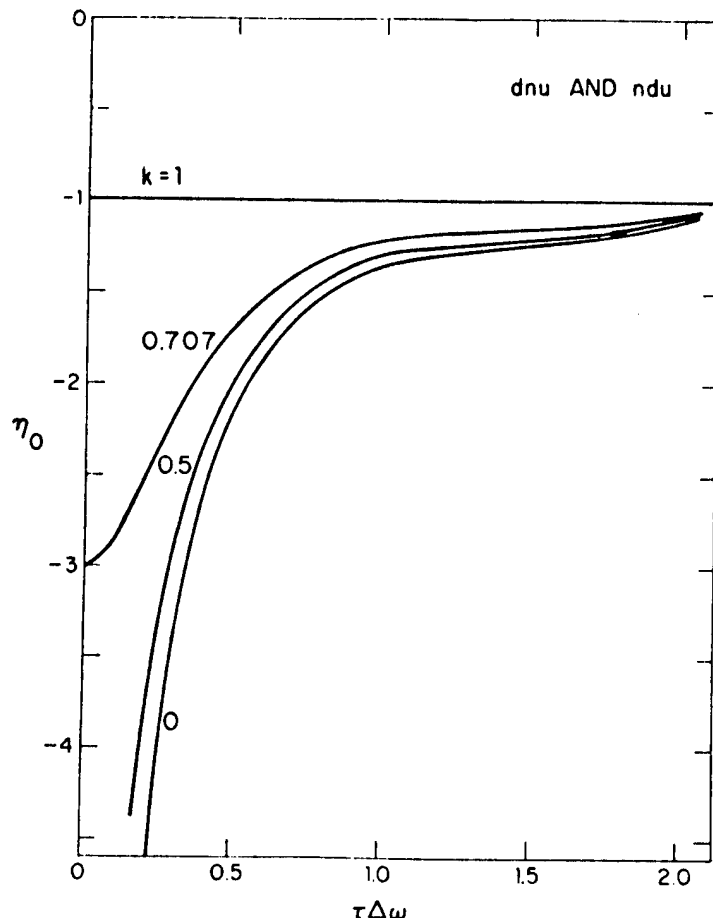


Fig. 3. The initial population inversion density  $\eta_0$  as a function of  $\tau\Delta\omega$  for the dnu and ndu solutions. The curves correspond to values of  $k = 1.0, .707, .5$ , and  $0$ .

The preceding discussion sheds some light on the physical significance of the argument transformations. The transformation  $u \rightarrow u + K$  is just a displacement in space-time which would correspond to the addition of a constant phase factor. However, because the initial phase cannot be specified, the physical situation is unaltered. The modification of  $\varepsilon_0$  by the factor  $(1-k^2)^{-1/2}$  simply expresses the fact that only  $\varepsilon_{\max}$  has meaning physically. Viewed in this light, Mishkin's argument for four physically significant solutions is seen to be in error.

Figures 2 and 3 show initial population inversion densities as a function of  $\tau\Delta\omega$  for several values of  $k$  required for the cnu (or sdu) and dnu (or ndu) solutions to occur. It is immediately obvious that  $\eta_0$  assumes unphysical values ( $\eta_0 < -1$ ) in the dnu (ndu) solution for every value of  $k \neq 1$ . At  $k = 1$  dnu reduces to sechu just

as cnu does. However,  $k = 1$  corresponds to  $\eta_0(\Delta\omega) \equiv -1$  which implies a temperature of absolute zero. This is also an unphysical situation. Consequently, the dnu and ndu solutions are not physically significant.

In conclusion, we have examined the experimental distinguishability of the four Jacobi elliptic function solutions to the self-induced transparency equations. It was shown that sdu cannot be experimentally distinguished from cnu and ndu cannot be experimentally distinguished from dnu. In addition it was found that the dnu and ndu solutions require unphysical values of the initial population inversion density. We therefore conclude that cnu is the only physically significant steady state solution to the self-induced transparency equations.

\*This work was sponsored by the Department of the Air Force.

#### *References*

1. E.A. Mishkin, private communications and unpublished correspondence.
2. E.A. Mishkin, *Physica*, 73, 459 (1974).
3. M. Abramowitz and I.A. Stegun, *Handbook of Mathematical Functions* (Dover Publications, New York, 1964) chapters 16 and 17.
4. R.C. Harney, submitted to *Physica*.

Unpublished Meeting Speeches\*

Microwave Frequency Shifting of Infrared Laser Radiation	G. M. Carter	Presentation on Lasers for Isotope Separation, Albuquerque, New Mexico, 17-19 May 1977
Calibration of $^{14}\text{CO}_2$ Laser Lines	C. Freed	
The Radar Echo Heterodyne Technique for the Measurement of Frequency Fluctuations	T. R. Gurski	Seminar, Research Laboratory of Electronics, M.I.T., 2 March 1977
Laser Frequency Stability Limitations on a $10.6 \mu\text{m}$ Laser Radar	T. R. Gurski	1976 Annual Meeting of the OSA, Tucson, Arizona, 22 October 1976
Adaptive Optics Experiments at Lincoln Laboratory	L. C. Marquet D. P. Greenwood C. A. Primmerman	Electro-Optics/Laser 1977 Conference, Anaheim, California, 25-27 October 1977
Coherent Infrared Radar	L. J. Sullivan	Optics in Radar Systems, Huntsville, Alabama, 27-29 September 1977
Coherent Monopulse Tracking with a $10.6 \mu\text{m}$ Radar	R. Teoste W. J. Scouler D. L. Spears	IEEE/OSA Conference, Washington, D.C., 1-3 June 1977
Laboratory Experiment on Thermal-Blooming Compensation Using a Deformable Mirror System	C. A. Primmerman	Optics Seminar, M.I.T., Electrical Engineering Department, 4 November 1976
Lasers for Isotope Separation	A. Mooradian T. F. Deutsch H. R. Fetterman C. Freed G. Iseler H. Kildal N. Menyuk R. M. Osgood	Conference on Lasers for Isotope Separation, Albuquerque, New Mexico, 13-14 April 1976
Stable $\text{CO}_2$ Lasers and Some of Their Applications	C. Freed	Seminar, M.I.T., 23 March 1977
Laser Radar: Concepts and Applications	R. H. Kingston	Optics in Radar Systems, Huntsville, Alabama, 27-29 September 1977
A 10 Micron Fast Frame Rate Imaging System	R. H. Kingston	CLEA Conference, Washington, D.C., 1-3 June 1977

\* Titles of Meeting Speeches are listed for information only. No copies are available for distribution.

UNCLASSIFIED

SECURITY CLASSIFICATION OF THIS PAGE (When Data Entered)